Photochemical Characterisation of Perovskites to Inform Stability and Sustainability

Volumes: 1

Alexander James Doolin, M.Eng.

Submitted to Swansea University in fulfilment of the requirements for the Degree of Doctor of Philosophy in Materials Engineering

Swansea University

December 2023

Abstract:

This thesis utilises photochemical characterisation techniques, along with morphological measurements, to study perovskite thin films deposited from a range of alternative solvent systems and anti-solvent combinations. This work aims to enlighten the process of judicious solvent selection with a view to improving the stability of the rapidly evolving perovskite technology whilst simultaneously considering the 'green' credentials of the chemicals used. Through increased understanding of solvent contribution towards film properties, it is possible to reduce the environmental and health and safety burden of new emerging materials and shed light on the interplay between crystallisation kinetics and intrinsic film stability.

Chapter 1 aims to provide a review of literature serving as a backdrop for the analysis considered within this thesis. Solvent parameters and their respective impact on film photoluminescence, morphology, and the stability of the precursor solution are considered within this chapter. The development of a 'green' solvent toolkit, proposing multiple new chemicals for use within perovskite development is a crucial aim of this work.

The following Chapter 2 focusses on the optimisation of experimental $MAPbI_3$ perovskite precursor solutions. The goal here was to utilise a novel solvent formulation to achieve power conversion efficiencies comparable to that of the best performing solvents.

Chapter 3 aims to improve the shelf life of the precursor through the introduction of novel anhydrous 'green' solvent additives – dimethyl carbonate. The long-term stability of $MAPbI_3$ films and devices was considered within this chapter with a view to increasing sample stability through solvent parameter manipulation.

Finally, Chapter 4 moves towards inherently more stable perovskite compositions – triple cation perovskite. The newly developed solvent systems and anti-solvent were trialled against this more complex composition. Devices with significant PCE% retention were evaluated over a 7-month period highlighting the potential for engineered planar perovskite architecture as the research field progresses.

Declarations:

This work has not previously been accepted in substance for any degree and is not being concurrently submitted in candidature for any degree.

Signed: ADoolin

Date: 24/02/2025

This thesis is the result of my own investigations, except where otherwise stated. Other sources are acknowledged by footnotes giving explicit references. A bibliography is appended.

Signed: ADoolin

Date: 24/02/2025

I hereby give consent for my thesis, if accepted, to be available for electronic sharing

Signed: ADoolin

Date: 24/02/2025

The University’s ethical procedures have been followed and, where appropriate, that ethical approval has been granted.

Signed: ADoolin

Date: 24/02/2025

Table of Contents

Acknowledgements:

I would like to dedicate this thesis to all those who have supported me on my decade through academia at Swansea University. My thanks go to my supervisor – Prof. Matthew Davies – for welcoming me into the world of perovskites and whose initial vision and belief in my work shaped the foundations of this thesis. To the Applied Photochemistry Group – from whom I have learned so much over the years – Dr Catherine De Castro, Dr. Rhys Charles, Dr Rodrigo Garica-Rodriguez, Dr. Emmanuel Pean, and Dr. Karen Villalobos, it has been a great pleasure to work alongside you all. Although too numerous to name, a further dedication to the researchers and students of SPECIFIC, always happy to share knowledge and experience to the betterment of all.

To the steadfast encouragement and belief of my family (always eager to hear about the new developments within the perovskite sphere!), without which this thesis would almost certainly not exist. To my amazing grandad John – it takes a lifetime to grow a forest.

Finally, and second to none – to my partner Dr. Megan Jones. It has been the greatest pleasure to share our Ph.D. journeys together, often miles apart but together through it all.

List of Tables and Figures

Abbreviations:

1

- 1,2,3-Trimethoxypropane
  - 1,2,3-TMP · 59
- 1,3-dimethyl-2-imidazolidinone
  - DMI · 59
- 1-pentanol
  - 1-P · 48

2

- 2,2',7,7'-Tetrakis[N,N-di(4-methoxyphenyl)amino]-9,9'-spirobifluorene
  - spiro-OMeTAD · 28
- 2-methoxyethanol
  - 2-ME · 117
- 2-methylpyrazine
  - 2-MP · 48
- 2-methyltetrahydrofuran
  - 2-MeTHF · 30

A

- acetonitrile
  - ACN · 48
- air mass
  - AM · 8
- aluminium
  - Al · 26
- atomic force spectroscopy
  - AFM · 42

B

- Band gap
  - E_G · 5
- bis(trifluoromethane)sulfonimide lithium salt
  - Li-TFSI · 33
- bismuth
  - Bi · 28

C

- cadmium selenide
  - CdS · 10
- Cadmium Telluride
  - CdTe · 11
- caesium
  - Cs · 26
- Caesium iodide
  - CsI · 172
- caesium lead triiodide
  - $CsPbI_3$ · 25
- carbon dioxide
  - CO_2 · 1
- carcinogenic, mutagenic and reprotoxic
  - CMR · 49
- Copper Indium Gallium Selenide
  - CIGS · 10
- critical raw materials
  - CRMs · 28
- current-voltage
  - JV · 30

D

- diethyl ether
  - DE · 118
- dihydrogen monoxide
  - H_2O · 30
- Dihydrolevoglucosenone
  - Cyrene · 60
- dimethyl carbonate
  - DMC · 30
- dimethyl propyleneurea
  - DMPU · 30
- dimethyl sulfoxide
  - DMSO · 30

Prifysgol Abertawe
Swansea University

Chapter 1 - Introduction

The effects of global warming on planet Earth are numerous and severe, driving further food and water insecurity[1], and threatening devastation to the survival of multiple species through habitat and biodiversity loss[2,3]. This warming has been intrinsically linked to an increase in anthropogenic carbon emissions resulting from the burning of fossil fuels such as oil, natural gas, and coal for energy generation[4]. Some of the most harmful gases released from these processes include carbon dioxide (CO_2), nitrous oxide (N_2O), methane (CH_4), and fluorinated gases[5]. Particularly pertinent is the high global warming potential (GWP) for these pollutants. GWP describes the ability of the gas to contribute to planetary warming over set time periods – relative to the longevity of the pollutant. Values for the aforementioned values over a 20 year period have been estimated by the IPCC as 1 – CO_2[6], 264 – N_2O[6], and 84 – CH_4[6].

The absorption of sunlight into the Earth's atmosphere is vital to determining the climate present on the surface. These gases populate the atmosphere and absorb infrared (IR) radiation. By preventing the escape of this radiation, as the volume of these gases increases, they serve to create a 'greenhouse' effect (Figure 1) – warming the Earth. This issue then exacerbates due to limited ability to remove greenhouse gases and reverse the effect. Due to a lack of remediation potential, global focus has been to minimise these emissions through technological advancement.

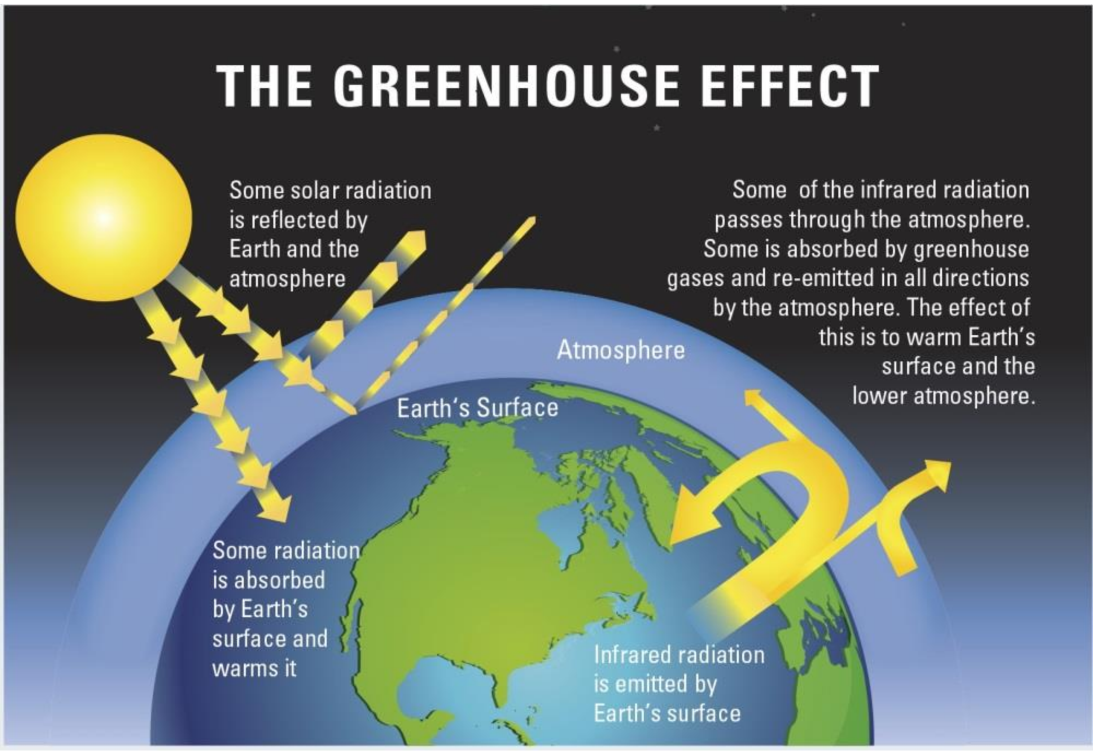

Figure 1 – Visual Representation of the greenhouse effect[7]

1.1 The Need for Renewable Energy

Simultaneously, the world is currently facing an energy crisis, with demand expected to continue rising as the global population increases[8]. Primary energy consumption (PEC) has risen from 12.62 gigatonne of oil equivalent (Gtoe) to 14.21 Gtoe over a 10 year period between 2012 and 2022[9]. Further complexity to the overall picture includes a decrease within the EU from 1.51 Gtoe to 1.44 Gtoe during the same period[9], with the rise in demand coming primarily from non-organisation for economic cooperation and development (OECD) countries[9]. This rise is particularly acute in non-OECD countries due to electricity generation from non-renewable sources such as coal[9]. Consequently, the rise in energy demand coincides with the release of greater volumes of GHGs, progressing global warming.

The IPCC have stated that global temperature should be held below a 1.5°C increase, on preindustrial temperatures, to avoid an increased occurrence of climate related disasters[10]. Drastic change to global energy ecosystems is required to both decarbonise and provide increased capacity to meet energy demand through greener technologies. Renewable energy technologies include solar, wind, and hydroelectric along with targeted renewable solutions such as biofuels[11]. Renewable electrical energy generation, however, has risen year by year, especially within OECD and EU member states, with a total electricity production of 7.4% in 2016 to 12.8% in 2021[9].

Sovereign governmental policy globally has focussed, in recent years, on incentivising and promoting the growth of the renewable sector. United Kingdom (UK) government policy sets out a strategy to achieve net zero carbon emissions by 2050[10], including the aim to meet UK wide energy demand through clean electricity generation by 2035[10]. Major investment in renewable technologies is needed to meet these aims. IRENA predicted that annual investment in solar PV needed to increase by 68% between 2018 and 2050 – reaching 192 billion per year[12]. As a percentage increase, solar PV and wind power represent the two areas experiencing the most growth over recent years[11], however, this capacity requires a large step change to meet predicted future demand. Solar PV represents a great opportunity to harness the readily abundant resource of sunlight, whilst maintaining a low production cost, relative to other renewable technologies (wind and hydro-electric). As of 2018 the levelized cost of energy (LCOE) for solar PV was already competitive with fossil fuels at 0.85 USD per kilo watt hour (kWhr)[12], with aims to further reduce this as low as 0.05 USD/kWhr by 2050[12]. Whilst wind energy remains a competitive option for renewables, the shear potential of solar PV should not be overlooked. The estimated annual solar energy potential across Earth is 23,000 terawatts per year (TWy) [13,14], with 100 years of global energy consumption (based on energy consumption circa 2009) estimated at 1,600 TWy[13,14]. The fossil fuel reserves of the planet have also been approximated at 1,655

TWy[13,14] with best case scenario for non-solar renewables, in terms of annual generation, at 94 TWy[13,14]. Harnessing the vast potential resource of sunlight provides one of the only avenues to future independence from fossil fuels.

1.1.1 Predicted PV Deployment

Photovoltaic (PV) deployment is vital to ensuring that renewable energy targets are met. It has been estimated that the global weighted average LCOE for solar PV decreased by 77% from 2010 to 2018[15]. This represents a fantastic, if not vital opportunity to factor large scale PV installation into future projections for renewable energy expansion.

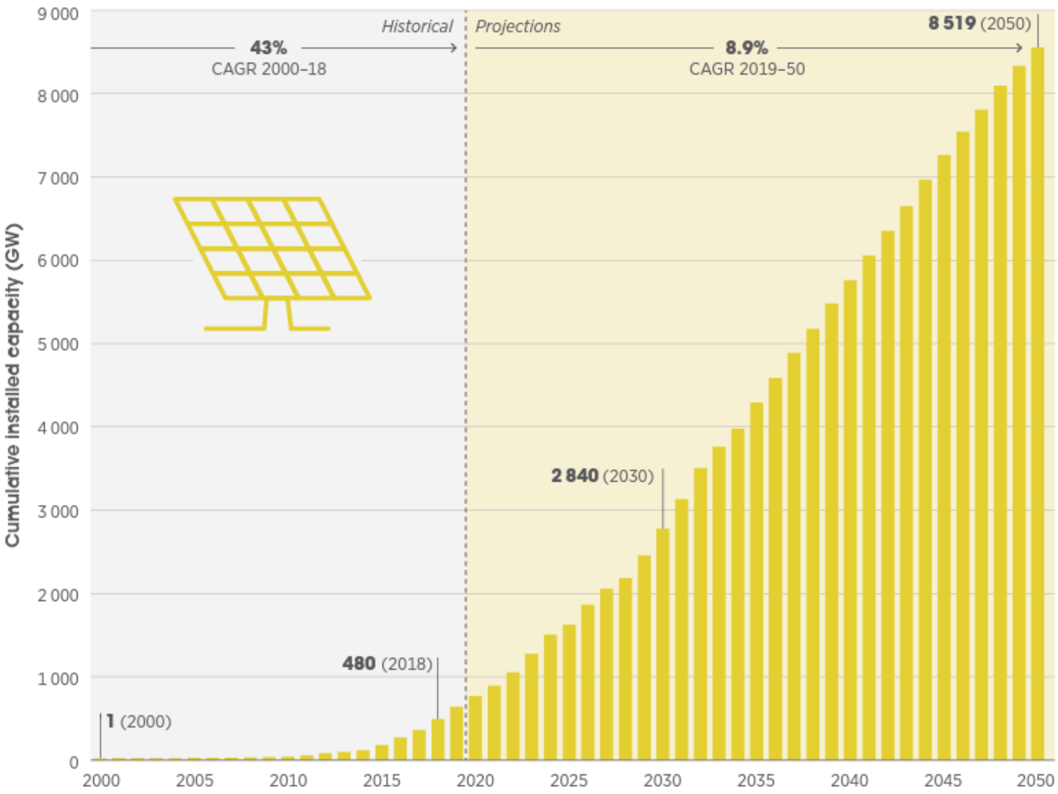

Sources: Historical values based on IRENA's renewable energy statistics (IRENA, 2019c) and future projections based on IRENA's analysis (2019a).

Figure 2 - IRENA PV projections showing the compound annual growth rate (CAGR), estimated to be 8.9% through to 2050[15].

The IRENA Remap analysis (Figure 2) estimates a huge compounding growth rate from PV installations by 2050 to meet increasing demand for clean energy[15]. This projection is further supported by studies into global renewable energy outlook. Yolcan (2023) estimated that PV capacity reached 942 GW at the end of 2021[9], in line with the IRENA projections. This is a 842% increase in capacity over a 10 year period[9].

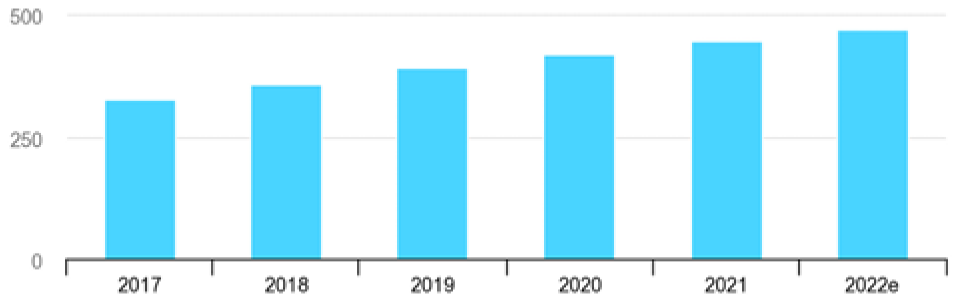

Figure 3 – Global investment in renewable energy technologies (billions $ per year – 2022 estimated value)[16]

Figure 3 shows investment approaching 500 billion dollars per year from 2022[16] directly into the transition to renewable energy sources. Global research aims have pivoted to improving this technology to maximise the LCOE and sustainability of solar PV, in anticipation of rapid large scale high value deployment in the near future.

1.1.2 Sustainability Issues at Scale

Given the scale of predicted PV deployment, sustainability becomes a more prominent issue. IRENA have predicted the deployment of PV to be around 60-80% utility scale installations and 20-40% rooftop/domestic[15]. This produces a wide range of potential environmental impacts associated to this PV use. These adverse impacts include land use, water use, pollution, hazardous materials, and visual and noise pollution[17]. The production of current PV technology at scale therefore includes a greenhouse gases (GHG) burden in terms of mining materials, manufacturing devices and ancillary equipment needed, and running the PV installation itself. There are also many competing PV technologies each with their own associated material sustainability concerns that need to be addressed.

1.2 Photochemistry and Photovoltaic Concepts

Photochemistry is the study of the interaction between light and matter. Ordinarily this is distinguished by a chemical change in one or more species. This defines the basic principle of a photovoltaic device, a material that facilitates the absorption and conversion of light into an electrical current.

1.2.1 Light Absorption

Sunlight, that is incident on the Earth, is represented as a spectrum of electromagnetic (EM) radiation. This ranges from high frequency UV to low frequency radio waves. Visible light accounts for *ca.* 40% of this incident spectrum and as such most PV technologies have been designed to absorb over this range. This spectrum contains quantitative energy carriers in the form of photons. The range of the EM spectrum is represented by the characteristic frequency of these photons as defined below.

$$E = hv = \frac{hc}{\lambda} (1)$$

$h = Planck's\ Constant$

$v = frequency$

$c = speed\ of\ light$

$\lambda = wavelength$

Consequently, photons have a characteristic energy directly linked to the wavelength of the light emission. This principle can be harnessed to both study and characterise photoactive materials.

1.2.2 Excitation

If photons of light provide the energy, excitation provides the mechanism to effect a chemical change within an absorber. Excitons are quasi-particles consisting of an electron hole pairing formed through Coulomb interactions[18]. Photons, of a characteristic wavelength, interact with an electron in the valence band of the semiconductor. The electron has sufficient energy to move into the conduction band leaving behind a charge correlated hole in the valence band. These excited electrons are then bound to respective holes and an exciton pair is formed. The existence duration of the exciton is then defined by the binding energy, within perovskites, this energy is reported to be very low at ambient conditions, <50 milli electron volts (meV), resulting in the formation of free charges at room temperature, negating the need for an interface to facilitate charge separation[19,20]. Excited electrons in the conduction band are then free to move within the material. Perovskites can, therefore, create free carriers following the absorption of light and the rapid dissociation of excitons. These free carries are extracted as current in a PV device. Under these operational conditions the perovskite structure alone can absorb energy from photons, effectively exciting electrons within the material, which can be extracted as a useable current.

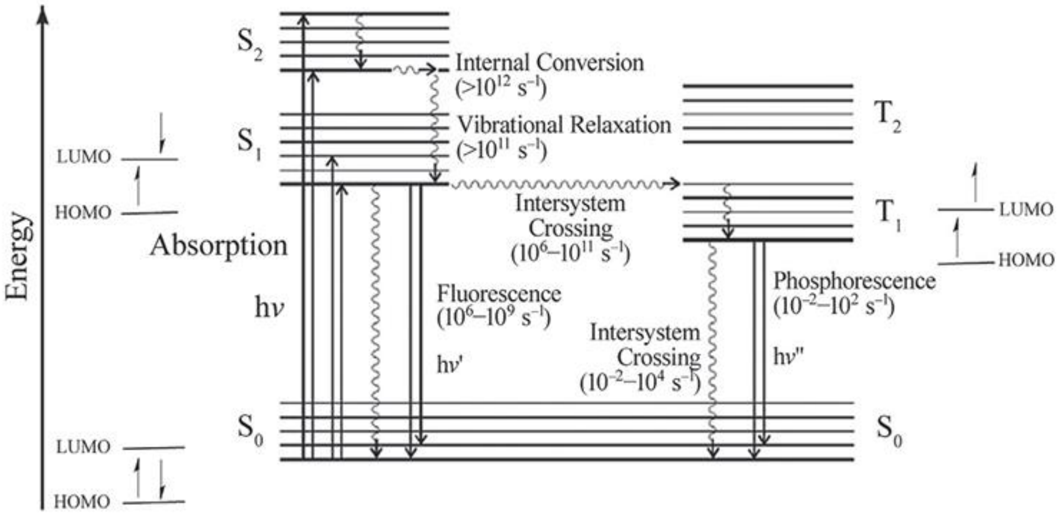

Figure 4 - Jablonski diagram showing the excitation of an electron from the valence band to the conduction band following the absorption of an incident photon. Image adapted from De Castro et al, 2017[21]. Radiative transitions are depicted as straight lines, with wavy lines denoting non-radiative transitions[21]. Predicted timescales for the transitions are included in the labelling (s^{-1}).

Figure 4 provides an in-depth illustration of excitation and subsequent relaxation pathways with magnitude timescale. To understand the nature of light absorption for perovskite materials we first need to define the energy transition between the valence band and the conduction band, *i.e.* - the band gap.

1.2.3 The Band Gap (E_G)

Semiconductor materials are characterised by the relative position of the valence band and the conduction band. The maximum energy of the valence band and the lowest energy of the conduction band define the relative position of the band gap. Whether these maxima or minima occur at the same electronic momentum also characterises the nature of the band gap and the recombination process itself. A direct band gap semiconductor is defined as a material by which the maxima of the valence band and the minima of the conduction band have the same electronic momentum. In Figure 5, a direct recombination pathway is visible as the electronic momentum is equal, a photon can be emitted characteristic of the band gap energy without a need for a change in momentum. Conversely if the maxima and minima are located at different momentum values, this process requires additional momentum retrieved through lattice vibrations in the form of phonons. Figure 5 b, shows two possible photon emission pathways for an indirect band gap, with phonon assisted momentum modifications.

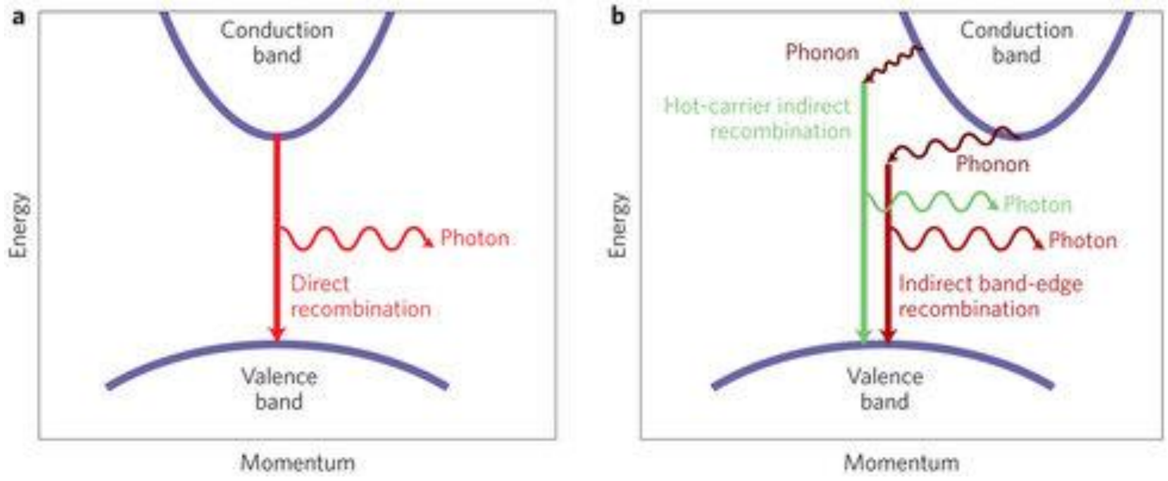

Figure 5 - Direct and indirect band gap recombination processes[22]

Perovskites themselves, as a potential competitor to silicon (Si), are direct band gap semiconductor where silicon are indirect – thus, silicon PV has to be relatively thick to absorb significant amounts of light. Perovskites tend to have high extinction coefficients due to in part being direct band gap materials - meaning they can be made into thinner PV devices. This culminates in a drastic decrease in material usage for the technology.

1.2.4 Radiative and non-radiative recombination

To further understand the potential recombination mechanisms within photoactive semiconductor materials, a distinction must be made between radiative and non-radiative recombination methods. Electrons excited into the conduction band exist in a meta-stable state[23]. To move to a more favourable electronic condition, the electron will move towards an empty state, characterised by the electron-hole. Direct band to band recombination, by which an excited electron relaxes to the edge of the conduction band before recombining with a corresponding hole in the valence band and emitting a photon of light, is known as radiative recombination. However, this assumption of band-to-band recombination usually requires a direct band gap material with little to no defects to allow the transition and release of the photon.

A second major type of recombination may be characterised as non-radiative recombination, also known as Shockley-Read-Hall (SRH) or trap-assisted recombination. In this instance, defects to the crystal structure can lead to the presence of additional energy levels within the band gap. In this instance, during recombination the electron may lose energy in the form of photons or commonly phonons and traverse the band gap before becoming ‘trapped’ at an energy level within the band gap (Figure 6). Defect levels equidistant to the valence and conduction bands can serve as recombination centres due to the finite possibility of trapping both carrier types leading to electron hole annihilation. The consequent recombination releases a smaller amount of energy usually in the form of phonons or lattice vibrations contributing to heating the material, generally considered to be greatly detrimental to device performance[23].

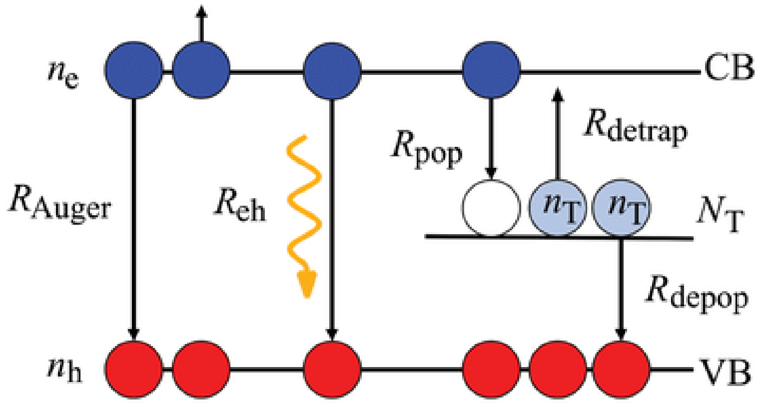

Figure 6 – Radiative and non-radiative recombination processes including trapping and de-trapping of electrons[24]

The final recombination type to be considered is known as Auger recombination. This phenomenon typically involves 3 carriers, with the electron-hole annihilation providing energy, not in the form of phonons or photons but as a transfer to another electron within the conduction band. This electron is then excited to a higher energy level within the conduction band before relaxing back to the band edge and emitting energy in the form of phonons[23]. This phenomenon is favoured under high levels of light illumination due to the accumulation and propensity for interaction of electrons within the conduction band edge. Under typical operational conditions (incident light of significantly lower intensity), however, this recombination pathway is not relevant for the perovskite technology.

Radiative recombination rates are therefore favoured for optimal photovoltaic performance. Non-radiative recombination rates, such as Shockley-Read-Hall and Auger recombination, play a crucial role in determining the photoluminescent properties of semiconductor thin films such as perovskite and should be understood as the debate around the nature of the perovskite excited state characteristics continues.

1.3 The Historic Development of PV

The Photovoltaic Effect:

‘The production or change in potential between two electrodes separated by a suitable electrolyte or other substance when the electrodes are unsymmetrically illuminated’[25]

The origins of the discovery of the photovoltaic effect are attributed to the French physicist Alexander Edmond Becquerel in 1839[25], who made the discovery through observing the electric current produced during experimentation using similar metal electrodes in a weak acid under illumination[25]. Following on from this initial observation, in 1873, the English electrical engineer, Willoughby Smith, discovered the electrical resistance of selenium was prone to change under different illumination intensity. This discovery, in conjunction with work completed by William Adams and Richard Day discovered that illuminating the junction between selenium and platinum also produces a photovoltaic effect[26].

Ultimately it would take the work of the American inventor Charles Edgar Fritts to produce the first solar cell module using selenium. This architecture utilised a copper backplate topped with selenium and gold leaf[26]. This work demonstrated the capability of solid materials to effectively produce a continuous current under illumination, laying the building blocks of future PV devices. This era of research highlights the efficiency requirements for viable solar cells, as the technology remains under-utilised with efficiencies <1% through this period[27].

It wasn't until the 1940s that the researcher Russel Ohl discovered the potential of doped silicon layers to generate a current under illumination[28]. This discovery suggested that when doped with impurities, two silicon slabs, one with an excess of electrons within the bulk, and the other with an excess of electron vacancies (holes), could produce a current when the surface between the slabs was illuminated. The structure has become known as the p-n junction.

1.3.1 The p-n Junction

The first functional solar cells made from doped silicon work on the premise of a photoactive p-n junction. This is the connecting region of two layers of doped silicon. Silicon may be doped according to the valency of the dopant relative to silicon. To create an n-type silicon, dopants typically have 5 valence electrons (e.g. antimony), providing a negative nature to the material. Conversely to create p-type silicon, dopants with a valency of three are commonly used (e.g. boron). This provides a positive charge to p-type materials. The p type material is considered an acceptor with the n-type layer the donor. Layering the n- and p- type materials on top of each other produces a large density gradient. This results in the migration of electrons from the n-type donor across the junction to the p-type material producing negative ions in the outer region of the p-type silicon. Holes from the acceptor material then migrate in the opposite direction, into the region of free electrons. The population of charge at the boundary increases in density until equilibrium is reached due to repulsive forces preventing further charge migration. This creates a depletion zone or space charge region, where a potential difference is present between the two charged regions.

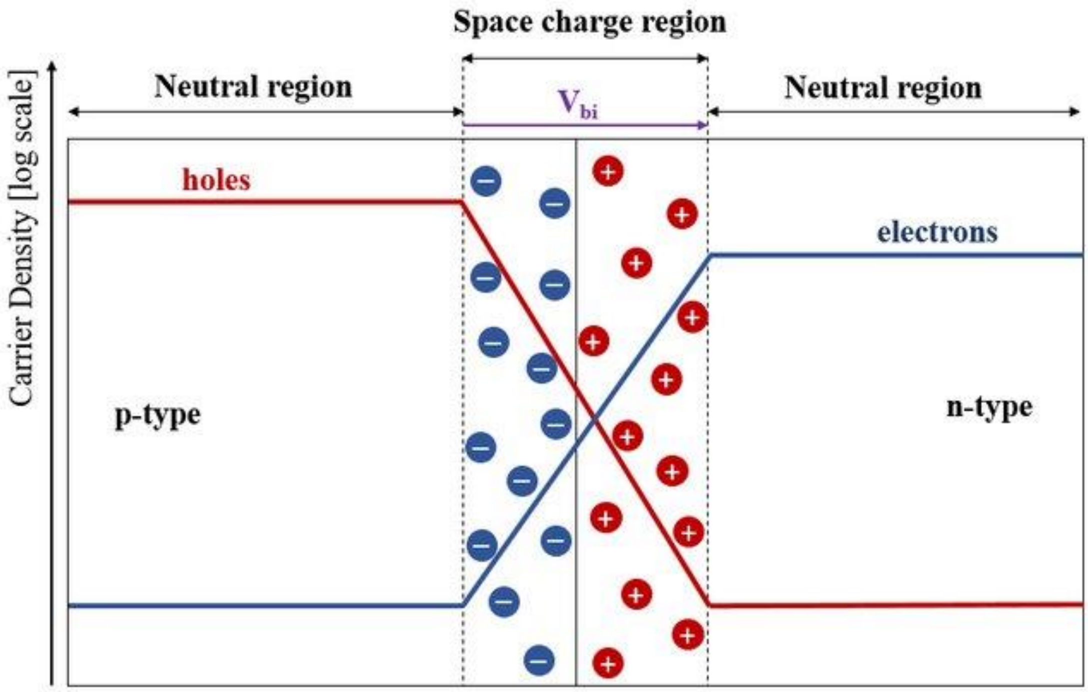

Figure 7 - Schematic of a p-n junction[29]

The p-n junction, illustrated in Figure 7, provides the basis for the photovoltaic operation of a silicon solar cell. Under illumination, electrons within the p-n junction are excited and are free to migrate through the n-type layer upon connection of the anode and cathode. The free hole migrates to the back contact, with an electrical current resulting.

William Shockley and Hans Queisser first proposed the idea that the conversion efficiency of a single junction solar cell under 1.5 air mass (AM) illumination with a band gap of 1.4 eV is limited to a maximum efficiency of 33.7% due to inherent losses during the conversion of incident photons into usable electric current. Background radiation, recombination losses, and photons below the required band gap energy all contribute to the reduction of this figure.

1.3.2 1st Generation PV – Crystalline Silicon

After the discovery of alternative valence doped silicon by Russel Ohl, the p-n junction was first manufactured into a working solar cell by Bell laboratories in 1954[28]. This cell operated with an efficiency of 6%[28], and represents the transition from the early photoactive selenium to silicon.

Since this initial device, a large-scale optimisation process has been undertaken for silicon as a PV material. Researchers have experimented with various dopants for the p and n type silicon layers, along with different thicknesses, with the aim of improving the efficiency closer to the Shockley-Queisser limit.

Huge efficiency gains were made during the early development stage linked to improved understanding of semiconductor processing[27]. The quality of the silicon crystals was rapidly improved, reducing impurities and improving performance[27]. Later advances through the late 1970s and early 1980s related to metal contact passivation and surface passivation, increasing silicon efficiency to above 20%[27].

Silicon cells historically fall into three categories:

(i) Monocrystalline cells

These are also known as single crystal silicon cells due to the use of a single extruded silicon crystal. These cells have high efficiency due to a reduction of defects associated with polycrystalline structures, however, have higher costs associated with the precision manufacturing process.

(ii) Polycrystalline cells

These cells contain multiple layers of silicon crystals, with boundaries representing regions for efficiency loss. The primary advantage has traditionally been lower cost for more widespread domestic application. The reduction in the cost of monocrystalline cells decreases the popularity of polycrystalline silicon.

(iii) Amorphous cells

Commonly used for low-cost small energy applications, such as solar panels on a handheld calculator, amorphous films are thin film silicon devices with high absorption in the visible spectrum. The thin film nature of this silicon device type provides alterative applications to crystalline silicon; however, they suffer from a large reduction in efficiency. Amorphous silicon cells, due to their thin film nature, are part of the second generation of PV, a generation focussed on low-cost thin film manufacturing with a minimal amount of material usage.

1.3.3 2nd Generation PV – Thin Film PV

As previously discussed, amorphous silicon represents the first attempt to manufacture solar cells using thin film processes with reduced material demand. The reduction in efficiency for these devices lead to a search for new materials within the film category.

(i) Copper Indium Gallium Selenide (CIGS)

This group I-III-VI$_2$ 2nd generation PV technology has roots in lab scale $CuInSe_2$ devices manufactured by Bell laboratories in 1974[30], doping with gallium an advancement on this initial composition. A challenge facing all 2nd generation solar is to achieve high absorption at film thicknesses ≤1 µm. This is achieved in the CIGS structure with a direct band gap and high absorption coefficient[30].

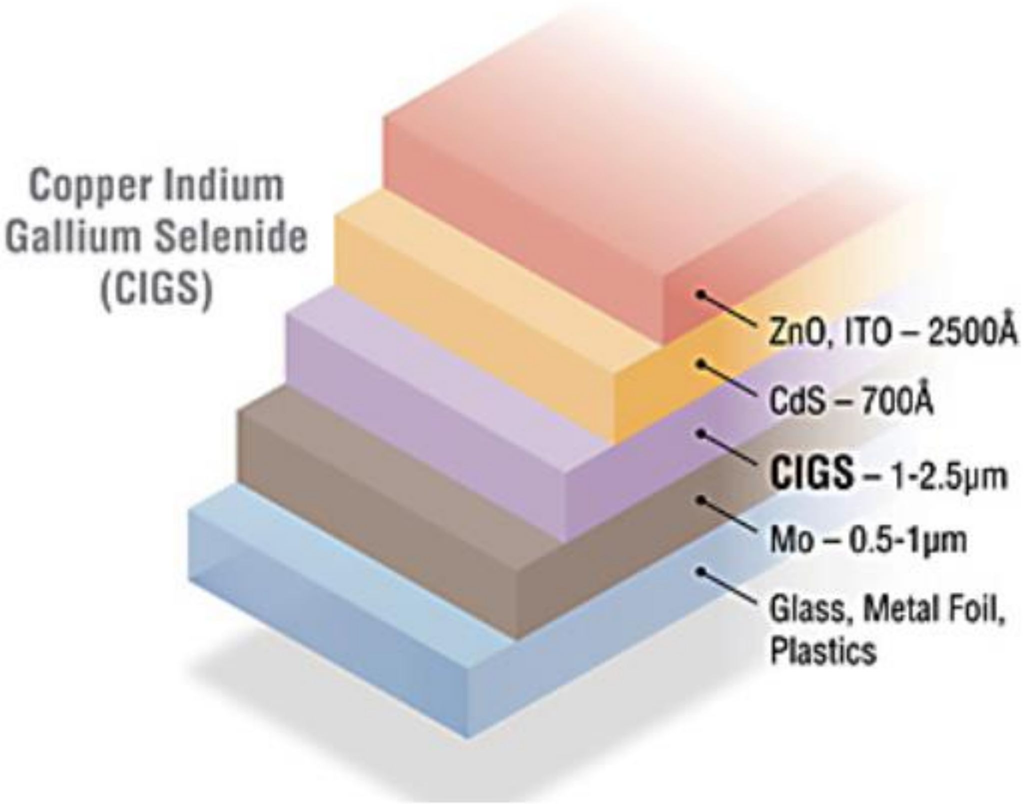

Figure 8 – CIGS Typical architecture[31]

A p-n junction is utilised in this architecture between the p-type CIGS and the n-type cadmium selenide (CdS) layer. Figure 8 shows the typical layers composing the multilayered structure of the CIGS architecture. Alteration to the copper concentration regulates the copper deficient region at the CIGS-CdS interface, providing surface passivation[30]. Advances to the structure, substituting the Cd component for Se, have achieved lab based efficiencies of up to 23.4%[32], with the current record slightly higher at 23.6%[33]. This record is lower than conventional silicon panels (26.7%[34]), albeit competitive for thin film technologies.

(ii) Cadmium Telluride (CdTe)

CdTe solar cells are currently the second most abundant architecture globally (following crystalline silicon) representing 5% of the PV market share, the most abundant 2nd generation technology[35]. With a direct band gap, tuneable in the optimal range of 1.4-1.5 electron volts (eV), this technology benefits from cheap and comparatively facile manufacturing processes.

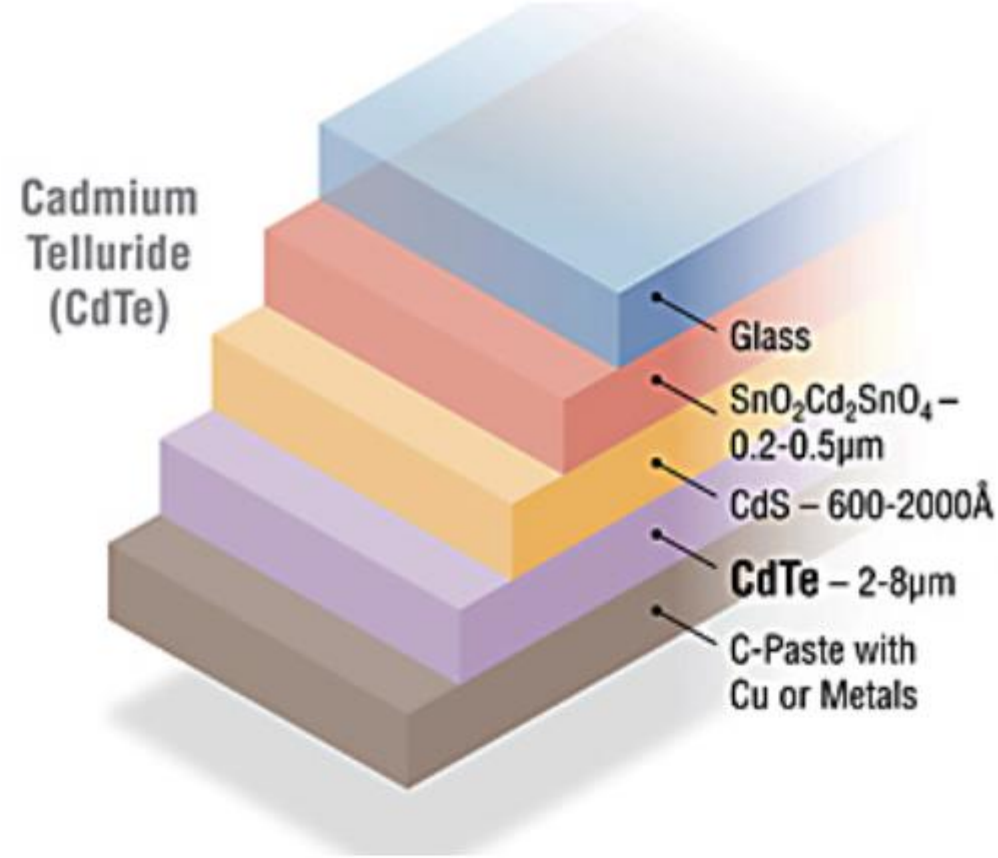

Figure 9 – CdTe Typical Solar Cell Architecture[36]

Despite these advantages, the efficiency of CdTe solar cells is limited to a lab record of 22.1% by Frist Solar[35], with a typical panel averaging 18%[35]. Again, a p-n junction provides the mode of operation for this material with the p-type CdTe combined with a CdS n-type layer. In Figure 9, the operational arrangement of the layers can be seen set on a glass substrate.

(iii) Gallium Arsenide (GaAs)

Gallium arsenide solar cells represent a deviation away from traditional second-generation cells. A group III-V semiconductor material, with a direct band gap of 1.42 eV[37], this material exhibits good thermal stability for use in high temperature environments[37]. With a record efficiency of 27.6% for a single junction device[38], GaAs holds a prestigious position amongst PV technologies – the highest efficiency. However, the production costs for this cell type are very high, limiting use to high intensity and space applications[36]. A key research aim within this area is to lower the production cost to a level more comparable to competitor 2nd generation technologies such as CdTe or CIGS, paving the way for a highly efficient low-cost thin film architecture.

1.3.4 Chasing Efficiency - Multijunction Solar Cells

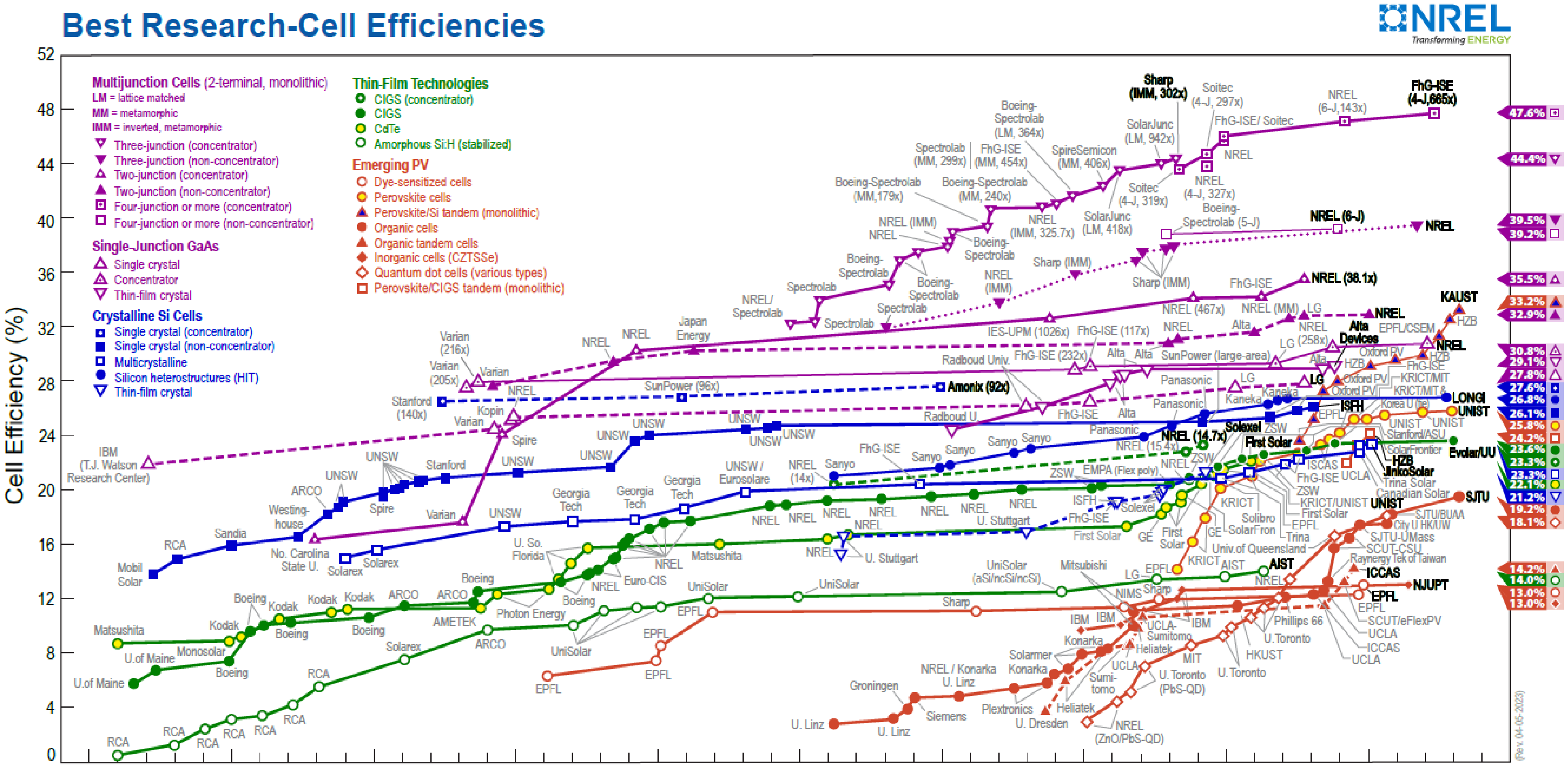

Figure 10 – National renewable energy laboratory (NREL) Record PV Efficiency Chart[33]

The competition between efficiency and cost of manufacture has dominated the first and second generation of PV development. This has been an ever-changing picture with the cost of crystalline silicon dropping over the years, influenced by multiple competing factors. This technological learning curve is typical of a technology in the stage of continual improvements and optimisation. As evidenced by the history of PV development, efficiency is a vital parameter to the success of a solar technology. Figure 10, the NREL efficiency chart, depicts PV technology record efficiencies against time. This is continually updated and shared by researchers, highlighting the wide interest in the use of efficiency as a benchmark for technologies competing for commercialisation.

The Shockley-Queisser limit defines the theoretical maximum efficiency for a single junction device. A major way of improving the efficiency past this standalone limit is the use of multiple junctions within a single device. Traditionally, this method involves the use of multiple p-n junctions each set to harvest a different region of the EM spectrum to produce current. By utilising more of the energy available in sunlight, the efficiency can be drastically increased. A crucial aspect of this method is to fabricate multiple p-n junctions capable of harvesting photons of different energy at high efficiency without a significant drop in the performance of the other junctions. This requires each layer (junction) within the device to have a different band gap energy. The top device in the series connected stack exhibits a wide band gap, harvesting light from the shorter wavelength range of the spectrum[39], photons of shorter wavelength possess higher energy, needed to activated the wide band gap transition. Light of longer wavelengths will conversely pass through this layer. This light is the target of the middle layer, with a reduced band gap, optimised for harvesting light in the middle of the spectrum[39]. Again longer wavelength light will not be absorbed by this material with a bottom layer utilising this light to activate a narrow band gap[39]. In this manner, the total light absorbed at each junction covers a large range of the visible spectrum, providing higher efficiency for the total conversion.

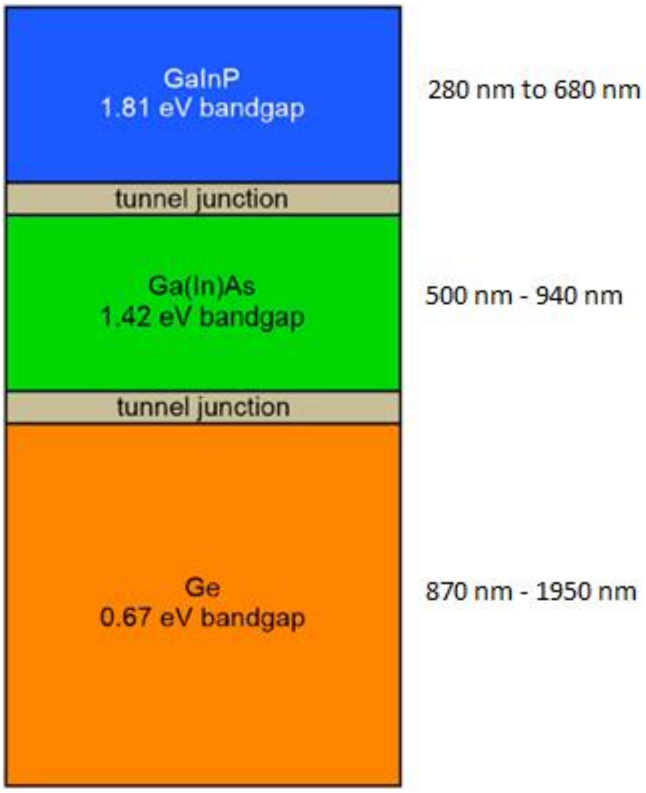

Figure 11 – Basic diagram showing a type III-V three junction multi-junction solar cell[39,40]

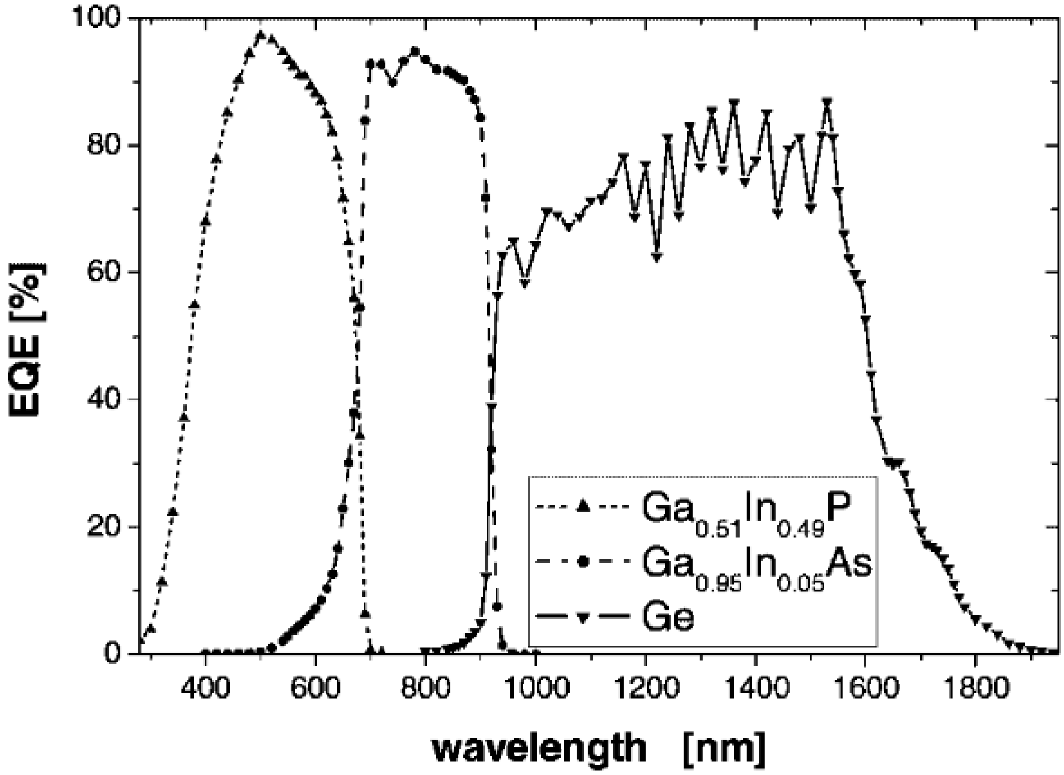

Figure 12 – External quantum efficiency (EQE) sample data from Meusal et al, 2003. EQE for a 3 junction III-V solar cell shows the wavelengths of greatest current generation for the three complementary band gap materials[41].

Figure 11 provides a basic three junction multi-junction cell utilising III-V direct band gap semiconductor materials. The approximated band gaps are shown[39], highlighting the reduction in bandgap through the layers. Figure 12 provides a sample of EQE data from a three-junction cell of the same material composition, this provides a visual representation of how the current is generated from each of the layers. The individual efficiency of each layer contributes to the additive total for the multi-junction structure.

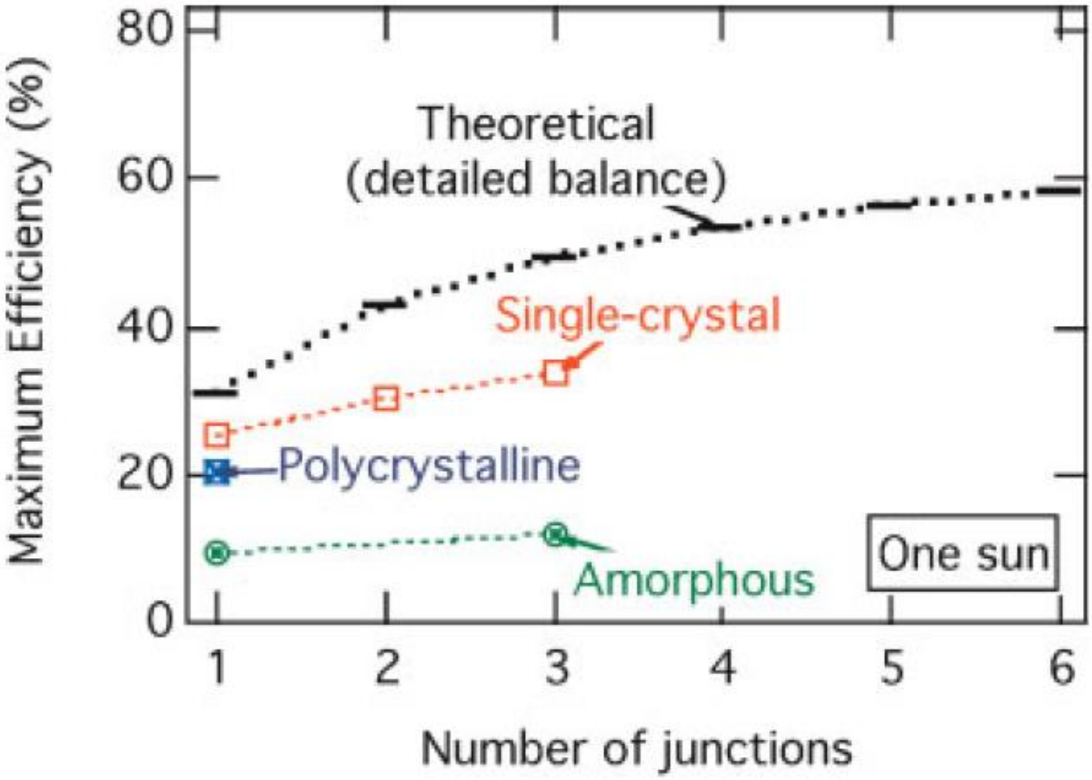

Figure 13 – Graphical depiction of the theoretical maximum for a solar cell compared to the number of junctions[42]. Actual recorded efficiencies for each type are shown with both the theoretical and experimental data taken under 1 sun illumination.

Figure 13 shows the theoretical efficiency for solar cells against the number of p-n junctions. This is above 40% for two junctions and approaching 50% for a three junction stack connected in series[39,42]. The record efficiency of a multi-junction solar cell (MJSC) is 47.1%, with this parameter dominating progress over the years of technological development[39]. The niche occupied by these cells is, however, small. With long device lifetime and stability contrasted with a higher cost of production than silicon-based panels. This results in applications where surface area is a more important consideration that cost, which for now limits the deployment of MJSCs.

It is also clear that alternative factors have had a large impact on PV development including the search for more cost-effective manufacturing and alternative PV materials. By pursuing efficiency alone, these factors can snowball into large issues for burgeoning technologies, as has been seen for MJSCs.

1.3.5 Sustainability Issues for 1st and 2nd Generation PV

Silicon PV, whilst dominant in the PV market with high efficiency, lifetimes, and reliable performance, also suffers from traditionally high costs associated with manufacture along with environmental, health and safety concerns linked to the production of the silicon modules.

With the metric for solar PV measured in cost per Watt, the price of silicon PV has decreased drastically as reported by Frauenhofer Institute for Solar Energy Systems (ISE), by as much as 87% since 2004[43]. The efficiency of manufacture, the amount of silicon needed to produce 1 Watt of energy is also reported to have seen an 8-fold decline since 2004[43]. This is in spite of a huge increase in the cost of silicon during the early days of mass silicon PV roll out. This was followed by a plunge in prices as the Chinese government prioritised solar power as part of future energy considerations. The market has remained quite steady at a low cost since these interventions with the competitive price of silicon pushing further constraints to emerging technologies.

In terms of environmental impact, the improved efficiency of silicon manufacture is vital to reducing the GHG burden of silicon PV. Silicon is manufactured through the high energy reduction of silica and coke in industrial arc furnaces. Silica is a readily available element within the Earth's crust; however, mining is an intensive process damaging to the environment both in terms of land use and associated emissions. The postproduction processes also have an associated energy burden as refinement and high-tech extrusion processes are also required to form photovoltaic grade silicon. The cost of silicon PV per Watt produced is therefore heavily dependent on the price of silica along with the cost of precision production equipment.

As the research sphere has focussed primarily on improving the cost and efficiency of solar cells, sustainability concerns have arisen given the increasing scarcity of rare earth elements used in the manufacture of a range of second-generation PV. Unlike silicon based cells, 2nd generation PV utilises rare earth metals such and indium (0.052 ppm – Royal Society of Chemistry (RSC) [44]), cadmium (0.08 ppm – RSC[45]) and germanium (1.3 ppm – RSC[46]).

CIGS utilises copper, indium gallium and selenium, and is considered by some studies to be more environmentally friendly than several competitor PV technologies[47]. An analysis by Stamford et al, 2019, concluded that CIGS, evaluated over 18 impacts against CdTe, multi-crystalline silicon, and mono-crystalline silicon, shows a reduction of 8-60% across 16 of the 18 categories[47]. The two outstanding categories highlight the major issues surrounding CIGS as an environmentally friendly PV, metal depletion and land use. Metal depletion was found to be 5 times higher than competitors[47], with land use greater by between 12-31%[47], with this result expected due to lower efficiency of CIGS. This result suggests that the raw materials used in the manufacture exhibit a particularly high environmental burden. Other studies have suggested that CIGS manufacture is unlikely to be hampered by indium material availability concerns into the future[48].

The same study evaluated the impact of CdTe manufacture and concluded that material availability issues are also unlikely to impact CdTe future growth, with the noted exception of excessive price variation[48]. This finding is reinforced by the lower metal depletion result for CdTe and the production of cadmium, in particular as a by-product of Zinc manufacture, with creation of product outstripping predicted usage for PV applications[49].

For GaAs solar cells, life cycle analysis (LCA) evaluations have shown that using PV generated power over fossil fuels significantly decreases the environmental impact[50]. However, the same study suggests that the reduction in toxicity over the lifetime is negligible, though comparable to multi-silicon PV[50].

1.3.6 PV Development Summary

The 1st generation of PV, thick film crystalline silicon, currently dominates installed PV capacity globally, exhibiting a high efficiency and long lifetime. There have been problems identified relating to the cost of production along with technological requirements to manufacture high purity silicon single crystal panels.

2nd generation PV has focussed on thin film technologies, attempting to reduce manufacturing complexity and achieve a higher ratio of power generation per gram of material used. Though lower than crystalline silicon (CIGS, CdTe), these technologies exhibit high efficiency and great device stability, with GaAs breaking records for efficiency with a single p-n junction. Research has consequently identified issues with both the vapour deposition processes along with material demand constraints, limiting the deployment of 2nd generation PV.

Where research has targeted high efficiency as a crucial parameter, MJSCs have eclipsed single junction device efficiencies. The drawback being prohibitively high manufacturing costs, limiting this technology to niche applications where surface area for power generation is restrictive (aerospace, high intensity applications).

1.3.7 The drive for low-cost PV – Solution Processed Solar Cells

Moving forward, the research sphere has attempted to innovate novel solar materials that can be processed and manufactured through cheap methods – solution processed solar cells. These materials are thin film in nature, limiting resource use per Watt generated. The mechanism of power generation has also been refined, moving away from traditional p-n junction architectures. This generation includes organic solar cells, dye sensitised solar cells and the now highly coveted perovskite class of materials.

1.3.8 The Dye Sensitised Solar Cell

Since introduction into the PV research sphere in 1991, in a publication authored by Brian O'Regan and Michael Gratzel, dye sensitised solar cells entered the race for development in a new 3rd generation of solar cells – those designed to use low purity abundant chemicals and very low cost manufacturing techniques[51]. This device architecture utilised a thick film of titania (10 µm) with a sensitiser dye impregnated into the film[51]. This development created a fundamental difference in mode of operation to a conventional p-n junction, separating the process of light absorption to the sensitiser dye, with the n-type titania film facilitating charge extraction. The process has been detailed into four basic steps by Sharma et al, 2018[52]:

Light absorption – The sensitiser dye absorbs photons within the visible spectrum. (typically below 700 nm, corresponding to a band gap of 1.72 eV[52]). Electrons within the dye are thus promoted from the ground state (S^+/S) into the excited state (S^+/S^*)[52]. Many dyes were, however, developed to harvest across the visible spectrum using combinations of different dyes – generally red - optimised for the peak of AM1.5 light at around 550 nm.

Electron injection – The excited electrons within the dye, exhibiting a short carrier lifetime in the order of nanoseconds relative to the quicker injection process, are then injected into the conduction band of the n-type titania structure, which lies at a lower energy value than the excited electron[52].

Carrier transportation – The injected electron is then transported through the titania into an external circuit, diffusing through to the transparent conductive oxide (TCO) back contact[52]. Consequently, the dye is oxidised.

Carrier extraction – The electrons are carried through the back contact to the counter electrode through and external circuit, reducing I_3^- species to I^-, regenerating the dye to the ground state[52].

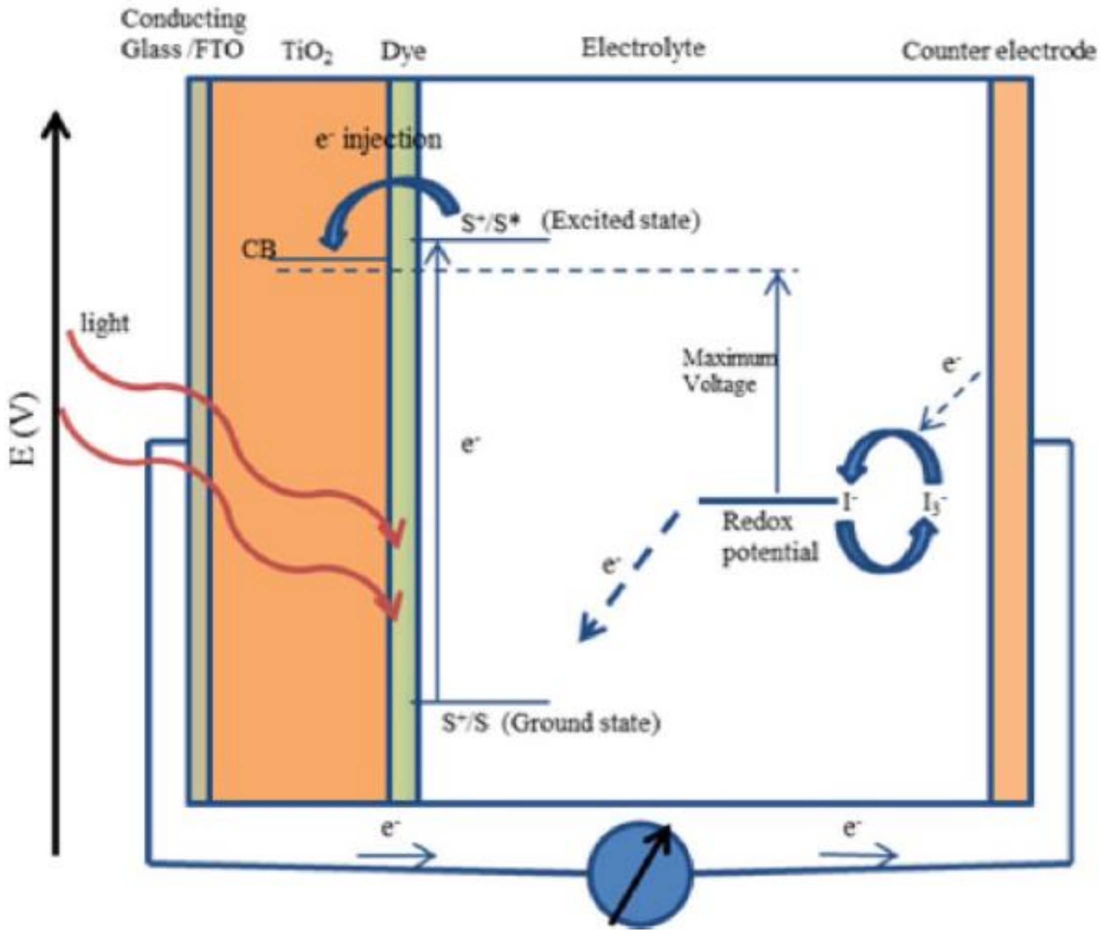

Figure 14 - Visual representation of a dye sensitised solar cells mode of operation, image adapted from Sharma et al, 2018[52]

Figure 14 provides a graphical representation of this process. Whilst an incredible breakthrough within the field, ultimately the use of a liquid electrolyte (dye) to implement the iodide tri-iodide redox couple, led to a reduced device lifetime and degradation issues[53]. This related primarily to degradation of the electrode and the possibility of electrolyte leakage impacting device operation[53].

The solution to these issues came in the form of a solid-state dye sensitised solar cell, by which the liquid electrolyte is replaced by a solid medium. This p-type semiconducting hole transporting material negates the need for a liquid electrolytic medium, effectively encapsulating the dye-adsorbed titania structure and providing a mechanism for hole extraction and dye regeneration without the need for a redox couple[54].

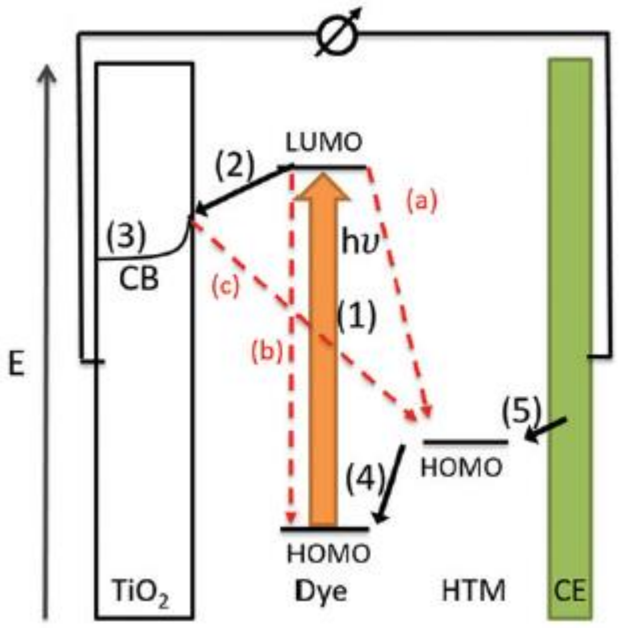

Figure 15 - Operating principle of a solid state dye sensitised solar cell (ss-DSSC)[54]

The to the solid state dye sensitised solar cell (ss-DSSC), depicted in Figure 15, provides the basis for the next generation of solar materials, solid state, low cost, defect tolerant, and highly efficient. This was achieved in 2009 with the development of the novel perovskite structure, utilising a similar mode of operation[55]. Within this material structure the process of light absorption, carrier excitation, and charge extraction can occur simultaneously, with a majority of the functional layers deposited through cheap solution processed methodologies.

1.4 The Rise of Perovskite Solar Cells

Since their inception in 2009, perovskite solar cells (PSCs) have undertaken a meteoric rise to prominence with power conversion efficiencies (PCEs) climbing from 3.8%[55] to 25.2%[56] in 2021 and 26.0%[57]. This record surpasses other thin film photovoltaic (PV) technologies[58] and is approaching the theoretical limit of 33% for a single junction device, rivalling monocrystalline silicon (Si), the PV market leader with record PCE of 26.7%[34].

Simple solution-based processing and the potential printability of perovskites to create uniform films with reduced defects at low-cost and high throughput gives appeal to manufacturers seeking to commercialise PSCs, including within tandem modules. With record efficiency of up to 29.1%[56] as of 2021. Rapid progress in this area has seen a new record of 33.9% achieved by Longi in November 2023[59] with tandem devices show great promise as a commercial application for perovskites[60]. Figure 16 shows the current record efficiencies for each device type along with the manufacturer of the device. Previous studies estimate manufacturing costs for standalone perovskite devices to be half that of Si-PV[61]. These economic advantages over alternative PV technologies may be further enhanced through lifecycle optimisation and design for circular economy enabling remanufacturing of cells and recovery of cell components at lower cost than purchasing new ones, which will afford lower cost devices over successive product generations[62–64].

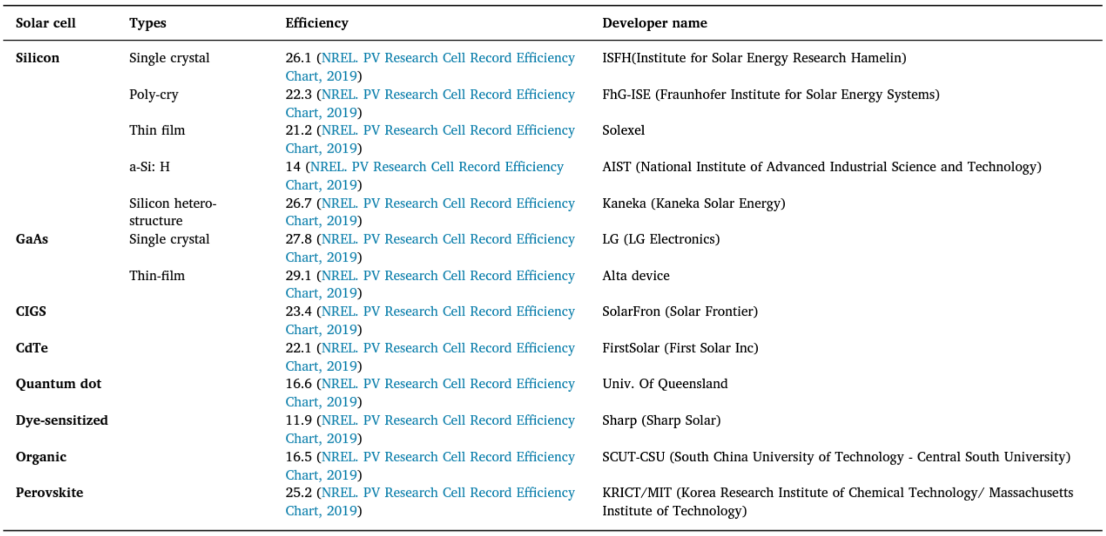

Solar cell	Types	Efficiency	Developer name
Silicon	Single crystal	26.1 (NREL. PV Research Cell Record Efficiency Chart, 2019)	ISFH(Institute for Solar Energy Research Hamelin)
	Poly-cry	22.3 (NREL. PV Research Cell Record Efficiency Chart, 2019)	FhG-ISE (Fraunhofer Institute for Solar Energy Systems)
	Thin film	21.2 (NREL. PV Research Cell Record Efficiency Chart, 2019)	Solexel
	a-Si: H	14 (NREL. PV Research Cell Record Efficiency Chart, 2019)	AIST (National Institute of Advanced Industrial Science and Technology)
	Silicon hetero-structure	26.7 (NREL. PV Research Cell Record Efficiency Chart, 2019)	Kaneka (Kaneka Solar Energy)
GaAs	Single crystal	27.8 (NREL. PV Research Cell Record Efficiency Chart, 2019)	LG (LG Electronics)
	Thin-film	29.1 (NREL. PV Research Cell Record Efficiency Chart, 2019)	Alta device
CIGS		23.4 (NREL. PV Research Cell Record Efficiency Chart, 2019)	SolarFron (Solar Frontier)
CdTe		22.1 (NREL. PV Research Cell Record Efficiency Chart, 2019)	FirstSolar (First Solar Inc)
Quantum dot		16.6 (NREL. PV Research Cell Record Efficiency Chart, 2019)	Univ. Of Queensland
Dye-sensitized		11.9 (NREL. PV Research Cell Record Efficiency Chart, 2019)	Sharp (Sharp Solar)
Organic		16.5 (NREL. PV Research Cell Record Efficiency Chart, 2019)	SCUT-CSU (South China University of Technology - Central South University)
Perovskite		25.2 (NREL. PV Research Cell Record Efficiency Chart, 2019)	KRICT/MIT (Korea Research Institute of Chemical Technology/ Massachusetts Institute of Technology)

Figure 16 – Record efficiencies for competing solar PV devices[65]

1.4.1 Crystal Structure of Lead Halide Based Perovskite

Lead halide perovskites for use in solar cells have an ABX_3 crystal structure where A is an organic cation (methylammonium $CH_3NH_3^+$), B is a metal cation (Pb^{2+}, Sn^{2+}) and X is a halogen anion (I^-, Cl^-, or Br^-) (Figure 17).

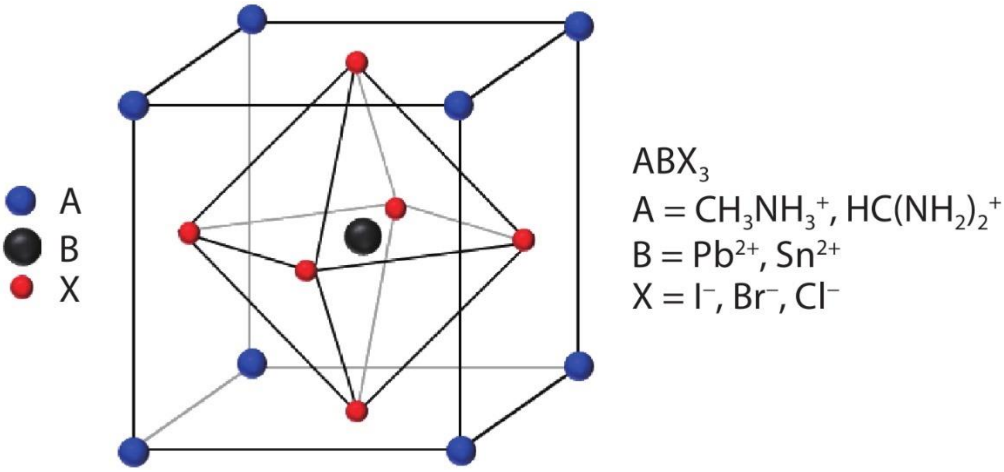

Figure 17 - Diagram of the perovskite crystal structure[66]

Tuning the double and triple cation compositions can increase the stability and PCE *e.g.* through the addition of caesium (Cs^-), rubidium (Rb^-) and formamidinium (FA^+) ions into the perovskite crystal lattice (Figure 17). This compositional flexibility results in the ability to tune the band gap (E_g)[67], which is generally minimised for optimised light harvesting across the visible-near infrared (NIR) spectrum[68].

The perovskite structure can be quantified by the Goldschmidt tolerance factor. This factor was developed to assess the stability of various perovskite structures. By computing the atomic radii of the atoms within the structure where R_A, R_B, and R_X, the factor can be calculated using the formula:

$$t = \frac{R_A + R_X}{\sqrt{2}(R_B + R_X)}$$

The tolerance factor for perovskite is usually considered stable between 0.8-1.0[69].

1.5 Structural Defects in Perovskite

The perovskite structure is known for its tolerance of defects within the material structure. Such defects are generally classified based upon their formation pathway[70]. Perovskite defects can be caused by atomic vacancies, interstitial defects, and anti-site, substitutions, Frenkel, Schottky, and substitutional impuritites[70]. Broad categories for further defects include point defects, defects aligning with a single lattice parameter[70], and line defects, with grain boundaries an important consideration for multi-crystalline perovskite films[70].

1.5.1 Vacancies

The vacancy is considered a point defect, and an important consideration for perovskite materials. Vacancies, a missing atom at a lattice point, resulting from thermal fluctuations, can cause charge differences between crystals due to the missing atoms charge contribution[70]. Crucially, these vacancies can act as deep level traps within the crystal, some of which may function as recombination centres, negatively impacting the photovoltaic performance of the layer (depicted in Figure 18).

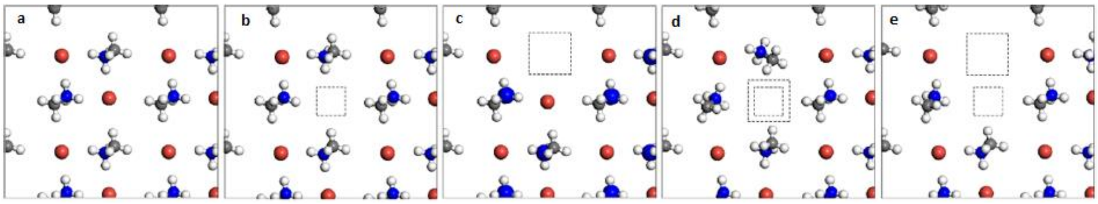

Figure 18 - Representation of common vacancies present within a methylammonium lead tribromide ($MAPbBr_3$) film. a) Complete film b) Br vacancy c) MA vacancy d) a Br-Pb double vacancy e) Br-MA double vacancy (Image adapted from Liu et al, 2017[71]).

1.5.2 Schottky Defect

A special case of vacancy defect occurs (Figure 19) when both the anion and cation leave the structure at equivalent stochiometry[70].

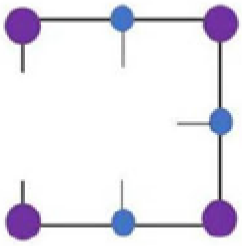

Figure 19 – Schottky defect representation with the stochiometric loss of anion and cation in the same lattice structure (image adapted from Maiti et al, 2020[72]).

1.5.3 Interstitial

Whereby a vacancy represents a missing atom at a specified lattice point, an interstitial defect represents an inclusion of an additional atom resulting from a neighbouring vacancy (Figure 20).

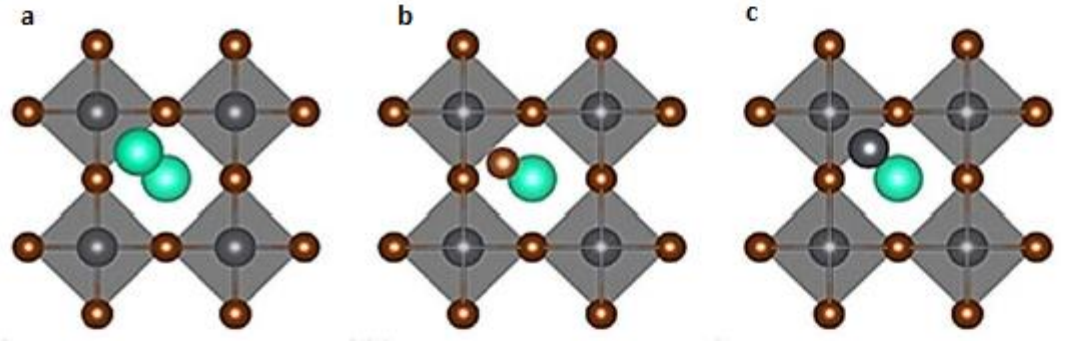

Figure 20 - Examples of interstitial defects a) A-site interstitial b) X-site interstitial c) B-site interstitial (Image adapted from Ye et al, 2021[73])

1.5.4 Frenkel Defect

A further special case of defect, known as a Frenkel defect (Figure 21), occurs when an ion exits the crystal lattice leaving a vacancy and occupies an interstitial site within the same lattice structure[70].

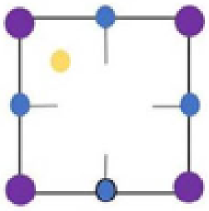

Figure 21 – Representation of a Frenkel defect within a single lattice structure. (Image adapted from Maiti et al, 2020[72])

1.6 Compositional Flexibility

1.6.1 $MAPbI_3$, $MAPbBr_3$, and $MAPbCl_3$

A promising characteristic of the perovskite structure revolves around the ability to tune the material band gap (E_G). This parameter can be altered through the modification of the halide anion within the crystal structure. Three commonly used halides are iodide (I^-), bromide (Br^-), and chloride (Cl^-). Using Iodide in the orthorhombic structure gives a band gap of approximately 1.62 eV[74], with pure bromide giving 2.21 eV[74], and pure chloride yielding the widest band gap at 2.75 eV[74]. In conjunction different ratio combinations of these halides may be used to attain specific band gap values as required for light absorption. Theoretically the $MAPBX_3$ can therefore be tuned to reach any desired band gap between 1.62 eV and 2.75 eV.

Issues arise with the mixing of halides due to phenomena such as phase segregation. For a mixed iodide-bromide system, fabrication challenges include avoiding iodide or bromide rich phases within the film.

1.6.2 Compositional Engineering for Advanced Stability ($Cs_xMAFA_{1-x}PbBr_xI_{1-x}$)

When utilised correctly, the iodide and bromide combination can allow for light harvesting over a wider range of the spectrum, utilising more available photons in typical 1 sun illumination.

A further issue with methylammonium (MA) based perovskites is the instability of the resulting films. The organic component (MA^+) tends to evacuate the film over time, resulting in defects and cation excess within aged films. This leads to a rapid declination of performance for $MAPbX_3$ films under realistic operating conditions.

The research field has tackled this issue with the inclusion of more stable cations to the perovskite structure such as formamidinium and caesium. Replacing the MA component with FA serves to improve both the thermal stability and the optical band gap of the absorber layer[75,76]. For the band gap to be activated by longer wavelengths of light, meaning a greater range of photons comprising the visible spectrum, the band gap energy needs to decrease. For formamidinium lead triiodide ($FAPbI_3$) this has been reported as 1.48 eV[77], a noticeable decrease from that reported for methylammonium lead triiodide ($MAPbI_3$) (albeit the precise value is actively debated).

The efficiency of these pure $FAPbI_3$ films was initially lower than $MAPbI_3$, with higher values attained for the mixed cation composition either utilising formamidinium (FA)/ MA blends[77], or missed halide compositions[77]. This is due to the fact that the photo-active α-phase is only stabilised at high temperatures, with the photo-inactive yellow phase stable under expected operating conditions[77]. With reference to the previously discussed Goldschmidt tolerance (t) factor, $FAPbI_3$ tends towards 1 and is ultimately unstable in the desired phase at room temperature. Through application of compositional engineering this tolerance factor can be reduced through the addition of the caesium cation. caesium lead triiodide ($CsPbI_3$) tends towards a t value of 0.8, with the inclusion of Cs into the $FAPbI_3$ structure enabling the formation of the α-phase at room temperature. Through the application of the MA/FA blend, the mixed halide composition, and the inclusion of the caesium (Cs) cation, highly efficient and crucially stable films are possible under ambient conditions[78].

1.7 Coordination and Physical Chemistry of Perovskites

As discussed, a key factor in the success of a 3rd generation PV technologies lies within the facile nature of the fabrication process. Efficient thin films can be crystallised after dissolution of the precursor materials in an appropriate carrier solvent. The selection of this carrier solvent is, however, not a trivial issue. The nature of the interactions between the solvent and the solute, along with any potential solute-solute interactions, places a large emphasis on the selection of a solvent.

A wider concern also surrounds the manufacturing technique used to fabricate these perovskite devices. Each manufacturing methodology requires customised solvents to enable high efficiency devices. Despite the record lab scale performance of perovskite, there is still a significant drop off in efficiency as devices are scaled up[79].

The perovskite precursors, particularly lead iodide – common as a high weight percent for most highly efficient perovskite films, requires a level of coordination within the precursor solution. This serves to inhibit precipitation and control the subsequent nucleation and crystallisation processes. An understanding of the coordination chemistry relevant to perovskites is needed within the research sphere, particularly as the technology reaches commercialised avenues of production.

1.8 Perovskite Device Architectures

Within the perovskite literature, there exists countless examples of different architectures used to manufacture devices in a lab setting. In the early days of development, with a nod to the conception of perovskites from the DSSC, mesoporous structures were mainly used as electron transporting, including alumina[80] and titania[67]. Planar architectures have gained a lot of traction in recent years, with new materials such as tin oxide (SnO_2) exhibiting high transparency and electron mobility. The planar structure operates without the use of a sintered mesoporous layer, improving the environmental efficiency of the manufacturing process.

For both the planar and mesoporous structures, these layers are solution deposited, typically via spin coating or spray pyrolysis, onto a transparent conductive oxide (TCO) substrate with high optical transparency – ordinarily indium or fluorine doped tin oxide. The ETL layer then is deposited as a compact layer, to sequester the two electrodes. An additional step involves the mesoporous scaffold, which is spun from a colloidal paste onto the top of the compact layer prior to high temperature sintering. Both structures then require an absorber layer of perovskite prior to the deposition of a hole transporting material to extract holes to the top contact, typically an evaporated metal (gold (Au), silver (Ag), aluminium (Al)) layer (Figure 22).

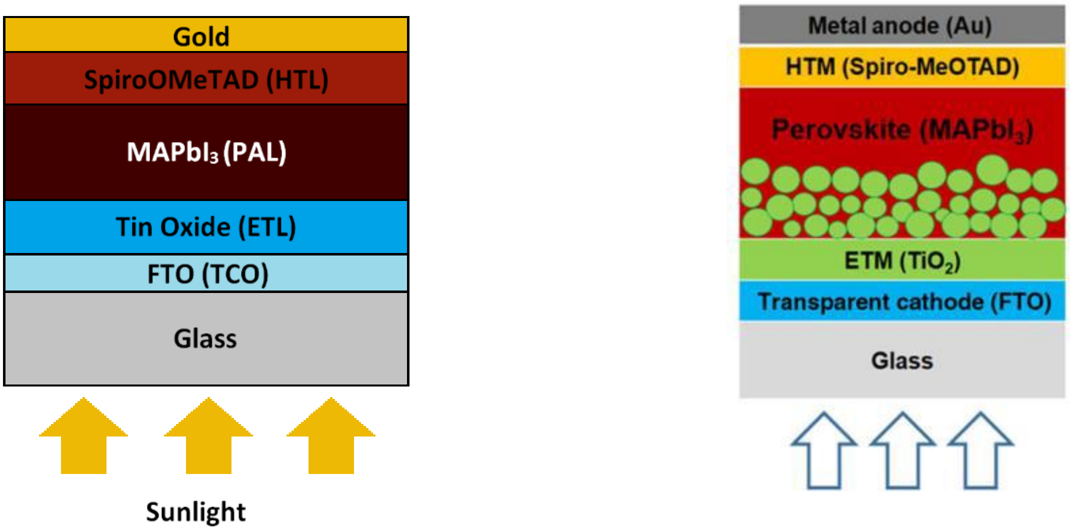

Figure 22 - a) n-i-p planar perovskite solar cell (PSC) architecture b) mesoporous structure utilising titania as the electron transporting layer (ETL)[81].

1.9 Device Mode of Operation

The working principle of a perovskite device can be best described in term of the relationship between the highest occupied molecular orbital (HOMO) and lowest unoccupied molecular orbital (LUMO) within each layer of the device.

When a photon of light with the energy equal to or higher than that of the band gap energy of the perovskite, is absorbed into the active layer, an exciton pair is formed. This process results in the promotion of an excited electron from the valence band into the conduction band, with an electron vacancy – or hole – left behind. In the absence of transport layers this electron would relax to the bottom of the conduction band before recombining with the hole in the valence band, emitting a photon of light with an energy value equal to the band gap (in the case of ideal band to band radiative recombination). In a device of the structure TCO/ETL/perovskite active layer (PAL)/ hole transporting layer (HTL)/ Au, the excited electron is free to enter the LUMO level of the ETL material at a lower energy level than the bottom of the conduction band, this effectively extracts the charge through the tertiary process of the electron being injected into the TCO for transport *via* an external circuit. This process can be seen in Figure 23. Simultaneously, the HOMO level of the HTL lies above that of the perovskite, with the hole free to migrate towards the top contact through the HTL material.

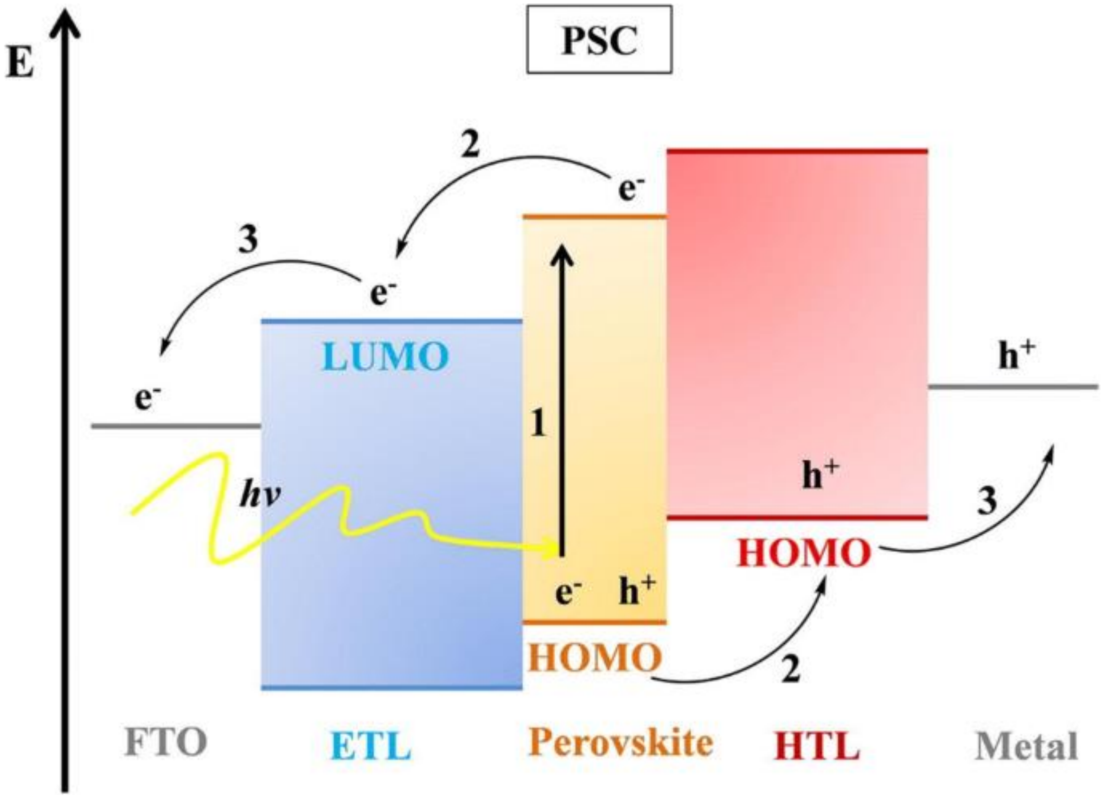

Figure 23 - Device mode of operation[82]

1.10 The Sustainability of Perovskite Materials

In the interests of eco-design, the use of hazardous and high environmental impact materials must be minimised throughout PV lifecycles[62,83]. Access to critical raw materials (CRMs) may also limit the deployment of renewable energy technologies and so where possible these should be substituted for more abundant materials or secondary raw materials, which don’t raise the same materials security or conflict mineral issues and may be obtained with considerably lower environmental impact[64,84–89]. On this basis, multiple components present in highly efficient PSCs reported to date require substitution e.g. gold and indium; as well as the solvents used to deposit thin-films during manufacture and potentially recovering those same materials in future recycling processes e.g. N,N-dimethylformamide (DMF) for perovskite and chlorobenzene for 2,2',7,7'-Tetrakis[N,N-di(4-methoxyphenyl)amino]-9,9'-spirobifluorene (spiro-OMeTAD) [90–92].

The presence of lead of in perovskite compositions is a hotly debated sustainability issue within the perovskite sphere. Lead, as a toxic chemical with a propensity to bioaccumulate, especially in aquatic ecosystems, may require substitution for an alternate metal cation. However, currently there are no alternatives that have replicated the high power conversion efficiencies of lead based perovskites. Several alternatives have been identified as potential replacements for lead (Pb^{2+}), including germanium (Ge^{2+}), bismuth (Bi^{3+}), and tin (Sn^{2+}). Of these competitor cations, Sn^{2+} is the most promising with a recorded certified efficiency of ~13%[93]. However, the oxidation of Sn^{2+} to Sn^{4+} remains a significant issue with $MASnI_3$ perovskite compounded by low defect tolerance, juxtaposed to the unique highly defect tolerant $MAPbI_3$[94]. Life cycle assessment (LCA) studies have also questioned the perceived benefits of a substitution from lead to tin[95], with lead presenting a lower embedded energy than tin and problems associated with the toxicity of tin to aquatic environments. Aside from substitution, effective module encapsulation has been posited as a means for mitigating any potential release of lead from future devices, with the expectation of lead based encapsulated devices becoming a commercialised technology. We believe that the issues from the use of lead can potentially be managed through circular economy approaches to mitigate potential impacts arising from the use of perovskite modules throughout their entire lifecycle[89]. Given the current lack of alternatives to lead, and the superior performance of lead-based perovskites, significant environmental and sustainability gains could be made from developing alternatives to the DMF solvent system, especially given the likely commercialisation of this technology in the near future.

1.11 Introductory Abstract

This introductory chapter provides a history of perovskite solar cell development. Describing the background to this highly efficient technology, detailing barriers to the potential commercialisation of these devices, and potential stability improvements as the research field progresses. Following this is a methodology chapter detailing the technical aspects relevant to the characterisations present within this thesis, the operating principles of the equipment, and the fabrication methods for the films studied. The first results chapter presents a methodology to identify more sustainable and lower toxicity alternative dipolar aprotic solvents of use for $MAPbI_3$ perovskite solar cells. The culmination of this work is an alternative 'DMF-free' solvent system, from which we deposit novel perovskite films for further photochemical and morphological characterisation. Subsequent results chapter 2 takes these solvent systems and attempts to improve the performance of the system and film formation. This is achieved through the use of additional sustainable solvent substitution, improving the long-term stability of the precursor solution. Antisolvent engineering is then introduced to further modify the deposited films. Chapter 3 proposes competing alternative solvent systems, utilising solvents prioritising low toxicity and green credentials. A characterisation of this solvent system is presented followed by the application of these solvents to alternative manufacturing processes. The final results chapter strives to analyse the relative stability of the novel perovskite films and precursor solutions when. For this more advanced perovskite compositions have been studied, providing an insight into the long-term potential of planar perovskite films.

Prifysgol Abertawe
Swansea University

Chapter 2 - Methodology

2. Introduction

This chapter aims to provide detailed information regarding the equipment, characterisation and analysis presented within this thesis. For perovskite devices, a generic build procedure is detailed here, with specific device and film fabrication customised with the chapter methodologies as appropriate.

2.1 General Procedure for the Manufacture of devices

All full perovskite devices were manufactured in a glovebox environment unless otherwise specified. This was done to limit the influence of environmental variables such as H_2O and O_2 and ensure reproducibility and comparison based on solvent content only. Furthermore, a glovebox environment is conducive to producing devices with the highest efficiency. Commercialised devices are anticipated to require >20% efficiency for industrial uptake and alternative solvent combinations need to be capable of achieving such efficiencies for adoption within the research sphere. Chapter 4 contains a comparative study of films cast inside a nitrogen environment and in ambient conditions, where the impact of environment is considered to be minor for the $MAPbI_3$ condition. Though scalable, ambient condition manufacturing techniques are beyond the scope of this thesis, the solvent methodologies presented within could be applied where solvent specifications can be determined.

Standalone perovskite films for PL characterisation were manufactured in either ambient conditions or under N_2 depending on the nature of the investigations and should be specified on a case-by-case basis. Generally, the PSCs evaluated within this thesis were fabricated with n-i-p planar configuration (doped-SnO_2/SnO_2/Perovskite/Spiro/Au). This was chosen due to planar SnO_2 exhibiting high electron mobility, reduced annealing temperature (<150°C), and optical transparency – ensuring high light transmission to the absorber material. For the evaluation of novel solvent systems using strong organic solvents, the deposited base layer should remain unaffected by such solvents during perovskite deposition. The chemical resistance of SnO_2 further justifies the use of the n-i-p architecture. However, as the p-i-n structure improves in performance and material versatility – future work towards stability may be made switching p-i-n. It is hoped that an increased use of greener solvents will speed up adoption within p-i-n sturtcures. The planar architecture was selected as preferable for evaluating novel solvents. Mesoporous structures were considered to hinder the comparison of more strongly coordinative solvents due to infiltration differences and limitations on the growth of large or uniform crystals. SnO_2 has low surface roughness and was deemed an ideal base for the growth of larger crystals – typically known to produce devices with the greatest potential.

Both fluorine and indium doped SnO_2 were utilised as the transparent conductive oxide substrate, specified where applicable. Tin oxide was also used as an electron transport layer unless otherwise specified, with spiro-OMeTAD as the hole transporter, utilising doping strategies as specified. For HTL dopants the concentration and composition were maintained through Chapters 1-3 with FK209 used in Chapter 4. Gold was used as the top contact – deposited using the same procedure in all cases.

2.1.1 Precursor Solution - General $MAPbI_3$ Fabrication

The control solvent system consisted of DMF (Acros Organics extra dry $HCON(CH_3)_2$ 99%) and dimethyl sulfoxide (DMSO) (Acros Organics extra dry $(CH_3)_2SO$ 99%) in a 4:1 ratio. This solvent provides a benchmark for the investigation of new solvent combinations throughout.

Precursor powders were weighed on a four-figure balance. Generally, a 1 mL $MAPbI_3$ solution consists of 576 mg of lead iodide (PbI_2, Tokyo Chemical Industries (TCI) Chemicals 99.99%), 199 mg methylammonium iodide (CH_3NH_2•HI 98%). This represents a stoichiometry of 1.25:1.25 M solution. This was chosen as the standard $MAPbI_3$ composition due to debate within the community on the impact of unequal stoichiometry. An excess in PbI_2 (typically around 5%) has been thought to increase the immediate performance of devices[96], with current-voltage (JV) measurements usually completed within 24 hours of fabrication. However, a decrease to performance over time is also noted as lead iodide (PbI_2) is photoinactive, and can lead to losses through increased trap concentration and parasitic absorption losses[96]. In all cases, heating at 60°C and rigorous mixing was applied until dissolution.

For the experimental solutions the bulk cosolvent system of DMSO and dimethyl propylene urea (DMPU) (Sigma Aldrich, absolute, over molecular sieve, dihydrogen monoxide (H_2O) ≤0.03%, ≥99% GC) with solvent additives 2-methyltetrahydrofuran (2-MeTHF) (Sigma Aldrich, bio-renewable, anhydrous, ≥99%, inhibitor free), dimethyl carbonate (DMC) (Sigma Aldrich, anhydrous, ≥99%), and EtOH (Sigma Aldrich, absolute, 99%, extra pure, SLR) were mixed in various ratios to investigate solvent system performance. Heating was generally required at 80°C to dissolve all material at a 1.25 M concentration with variations specified in each chapter.

2.1.2 Precursor Solution Preparation – $Cs_{0.066}(MA_{0.17}FA_{0.83})_{0.934}Pb(I_{0.83}Br_{0.17})_3$

The $Cs_{0.066}(MA_{0.17}FA_{0.83})_{0.934}Pb(I_{0.83}Br_{0.17})_3$ solution was manufactured at a mole ratio of 1:1.1:0.2:0.2 FAI:PbI_2:$PbBr_2$:MABr using 22.4 mg of methylammonium bromide (Sigma Aldrich, ≥99%), 73.4 mg of lead bromide (Sigma Aldrich, 99.999%), 172 mg of formamidinium iodide (Sigma Aldrich, 99%, anhydrous), and 507.1 mg of lead iodide (TCI Chemicals, 99.99%). The solvent system utilised DMF (Acros Organics extra dry, 99%) and DMSO (Acros Organics extra dry, 99%) in a 4:1 v/v ratio, 987 µL of which was added to the above precursor materials. Subsequently, 53 µL of caesium iodide (Sigma Aldrich, 99.999%) was added using a stock solution (390 mg/mL in DMSO - Acros Organics extra dry, 99%), which had been previously heated to 100˚C and then cooled to ambient conditions. This represents 6.6% Cs addition in a 1.25M solution, chosen to reduce the risk of suboptimal CsI levels within the film. Previous studies have shown High performance of compositions between 5% and 10%[78].

This composition includes a PbI_2 excess, with encapsulated film stability analysed based on this more efficient composition.

Table 1 - Molarity of the experimental solutions with respect to the measured weight of each perovskite precursor powder.

	mg/mL	Molar mass (g/mol)	M/mL	M/1040 uL
FAI	172	171.97	1.00	0.96
CsI	20.67	259.81	0.08	0.08
PbI2	507	461.01	1.10	1.06
PbBr2	73.4	367.01	0.20	0.19
MABr	22.4	111.97	0.20	0.19

To dissolve and adequately coordinate the precursor solution, heating was applied at 80˚C until total dissolution. Directly before perovskite deposition a 10-minute UV-ozone treatment was conducted on the ITO substrates which were then transferred to a N_2 glovebox.

100 µL of perovskite precursor was used along with 250 µL of the anti-solvent ethyl acetate or dimethyl carbonate, which was dropped dynamically onto the centre of the sample 10 seconds from the start of the spin cycle. Spin coating settings of 4000 rpm and 4000 acceleration for 30 seconds were used. The films were then annealed on a hot plate at 100°C for 30 minutes prior to characterisation.

For the evaluation of new solvent systems using this composition an adaptation to the original published methodology was used, allowing new solvent combinations to be added in one step. The only exception to this was the caesium iodide, added as a minor addition from a stock solution, controlling Cs content within the final film and giving increased flexibility to the fabrication method. The utilised Cs fabrication method first proposed by Saliba et al (2016)[78] uses an excess of PbI_2 in solution, giving a stoichiometric weighting to PbI_2. This was maintained within this thesis to attempt to achieve comparable performance. The concentration was, however, decreased from 1.5 M to 1.25 M to aid in the search for alternative solvents by minimising the amount of PbI_2 to solubilise whilst still allowing for dense thin film deposition.

2.1.3 Solvent coordination theory for triple cation perovskite

Due to the employment of the A01 and B01 systems for triple cation perovskite, it is relevant to consider the effect of enhanced coordination with the range of precursors. Caesium iodide (CsI) is the only component dissolved within a stock solution (1.5M) and added per requirement in DMSO. This leads to additional DMSO within this system along with the DMF/DMSO control.

Solvent System	Composition (µL) – 1040 Total
DMF/DMSO	250 DMSO, 789.6 DMF
A01	440 DMSO, 300 DMPU, 200 2-MeTHF, 100 EtOH
B01	440 DMSO, 300 DMPU, 300 DMC

PbI_2

For triple cation inks at a 1.25M concentration, the reduced requirement to dissolve lead iodide (507 mg compared to 576 mg for $MAPbI_3$) marginally decreases the potential for PbI_2 precipitate for the A01 and B01 systems. Some precipitate is, on occasion, observed from the A01 system over time (24 hours), suggesting this mechanism is relevant due to solvent precursor interaction, and not simply due to insufficient coordination ability.

$PbBr_2$

Dissolves adequately in all tested solvents.

This precursor solution can be created as a series of stock solutions utilising the core cosolvent combination of DMPU+DMSO or DMF/DMSO.

Table 2 – Triple cation solution manufacturing method.

Stock Solutions (1.5 M)			
Precursor		DMSO/DMPU (1:1 v/v)	DMF/DMSO (4:1 v/v)
PbI_2		1 g in 1.466 mL	1 g in 1.466 mL
$PbBr_2$		1 g in 1.816 mL	1 g in 1.816 mL
CsI Stock Solution			
CsI		1g in 2.566 mL	1g in 2.566 mL
$FAPbI_3$ Solution			
FAI	0.1 g in 0.468 mL PbI_2 stock	+ 0.001 mL	+ 0.001 mL
$MAPbBr_3$ Solution			
MABr	0.1 g in 0.704 mL $PbBr_2$ stock	+ 0.016 mL	+ 0.016 mL

Triple Cation Solution (6.6% Cs)		
$FAPBI_3$ Stock	**$MAPbBr_3$ Stock**	**CsI Stock**
0.250 mL	0.050 mL	0.0211 mL

The resulting solutions can then be diluted as needed through the addition of 4:1 v/v DMF/DMSO or with aliquots of the fluid modifiers, azeotropic 2-MeTHF:EtOH blend or DMC, to formulate a precursor at the desired concentration (1.25M – PbI_2 excess). General build procedure utilised the previously described one-vial solution with the Cs addition through a 1.5 M stock.

2.1.4 Electron Transport Layer Preparation – SnO_2

Tin oxide was chosen as the ETL for a majority of builds within this thesis due to its superior electron mobility[97], deeper conduction band[97], low temperature (less energy intensive) deposition procedure, and planar device structure. The planar device structure has been selected as the perovskite/ETL interface is simpler in nature than in mesoporous architectures. The need to alter nucleation and crystal growth dynamics during alternative solvent system design requires an architecture most well adapted to changing morphology.

A tin oxide solution was prepared from a commercially available 15% tin (IV) oxide colloidal solution (Alfa Aesar) which was diluted by a given ratio (specified for each use) with deionised water and sonicated for 30 mins. The dilution ratio ultimately provides an indication of SnO_2 film thickness, with thinner films attained from more dilute solutions.

Prior to coating, the spin-coater (in the class 6 environment), was wiped with deionised water to ensure higher humidity[98]. 150 µL of tin oxide solution was spin coated onto substrates dynamically at 3000 rpm and 3000 acceleration for 30 seconds with solution dropped onto the sample after 5 seconds. Immediately after, a swab was used to remove a strip of the SnO_2 down the middle of the substrate before annealing at 150 °C for 30 minutes on a hot plate to remove all moisture.

Published procedures for the use of SnO_2 as an ETL on fluorine doped tin oxide (FTO) recommend chemical bath deposition[99]. In this study the ETL was spun on FTO from a nanoparticle solution. It was postulated that due to the inherent surface roughness of the FTO (FTO having a root mean square value of 16 nm in comparison 0.63 nm for indium doped tin oxide (ITO) [100]), the ETL exhibited poor surface coverage. This led to erratic open circuit voltage between pixels on the same sample. A recommendation is to use ITO in this build procedure when surface roughness cannot be altered by modification methods. As the lower cost indium-free alternative to ITO, FTO may still be used in this architecture provided that a consistent, pin hole free, tin oxide transport layer be deposited.

2.2 Substrate Cleaning

This section details the procedural use of ancillary equipment during device build procedures.

2.2.1 Sonication

For substrate cleaning, the doped SnO_2 – either pre-cut laser etched 2.8 cm^2 pieces of XOP FTO Glass (tec15 – 2.2 mm thick) or 2.8 cm^2 Kintec chemically etched ITO - were initially cleaned with 2% hellmanex solution using a toothbrush. Sonication was then conducted for 30 minutes at 70°C in a 2% hellmanex solution, followed by sonication for 5 minutes in deionised water at 70°C. Substrates were then transported to a class 6 clean room environment for 30 minutes sonication in acetone and isopropyl alcohol (IPA) respectively prior to drying with a nitrogen flow.

2.2.2 Plasma Cleaning

A 10-minute treatment in a plasma cleaner at maximum power using oxygen at 0.3 mbar prior to SnO_2 deposition.

2.2.3 UV-Ozone Treatment

Generally, a 5-minute ultra-violet (UV)- ozone treatment was applied prior to SnO_2 deposition to increase solution wettability and improve surface contact. After ETL annealing, a one hour UV-Ozone treatment was applied to the ETL substrate to reduce hysteresis[101] and improve perovskite wettability upon coating. Time between treatment and solution deposition was generally minimised where possible to maintain treatment efficacy.

2.3 Films for Characterisation

Thin perovskite films were manufactured in a variety of architectures for optical (UV-Vis-NIR), photochemical (fluorescence spectroscopy), and structural (X-Ray diffraction (XRD), scanning electron microscopy (SEM)) analysis to complement full device performance. Due to minor variation in experimental methods per Chapter and experiment, detailed film preparation is available within the methodology for each thesis chapter. In general, films were manufactured on bare FTO or ITO substrate along with evaluated devices to achieve the greatest mimic to the evaluated devices where characterisation was used to contrast with device performance.

2.3.1 Perovskite Deposition - Glovebox Devices

All perovskite devices were manufactured in a glovebox unless otherwise specified. The one step deposition method was used to spin coat $MAPbI_3$ solutions onto substrates with an anti-solvent drip of ethyl acetate (EA) to initiate nucleation and crystallisation growth of the film. For the reported control solution (DMF/DMSO 4:1 v/v), spin coating setting of 4000 rpm, 4000 acceleration for 30 seconds were used. For $MAPbI_3$ samples, 100 µL of precursor solution was spread onto the ETL substrate. The spin regime was then initiated, with 200 µL of ethyl acetate dropped onto the sample 7 seconds from the start of the spin cycle. Samples were then placed on a hot plate at 60°C and ramped rapidly to 100°C for 10 minutes to anneal. For the experimental solutions, a prenucleation method of spin coating was used, harnessing the antisolvent drip stage during spin coating to induce nucleation and crystallisation. This method was used to form dense, pin hole free, specular films given the difference in solvent system properties to the control solution. It was thought that the standard control spin coating methodology leads to high defect levels if a transparent intermediate phase is formed from the candidate solutions due to over-coordination and poor solvent evacuation from the film. A specular layer was formed using a two-stage spin setting of 10 seconds at 1000 rpm with 200 acceleration, followed by 30 seconds at 6000 rpm 2000 acceleration. In this case 200 µL of anti-solvent was dropped five seconds from the end of the cycle by application of slow continuous pressure to the pipette for ~2 seconds resulting in a semi-transparent brown sample post spin-coating, which was immediately annealed on a hot plate at 100 °C for 10 minutes.

The general procedure for $Cs_{1-a}(MA_xBr_{1-x})_aPb(I_xBr_{1-x})_3$ films was customised for the glovebox conditions in use, with these samples exclusively manufactured under N_2 due to increased material sensitivity to environmental conditions. Again 100 µL of precursor solution was spread onto the sample prior to spin initiation. However, standard DMF and DMSO based devices required 250 µL of the antisolvent – dropped dynamically 10 seconds from the start of the cycle. For experimental solutions, the prenucleation strategy was also used with the anti-solvent volume increased to 300 µL and deposited 5 seconds from the end of the spin regime. Annealing requirements for $Cs_{1-a}(MA_xBr_{1-x})_aPb(I_xBr_{1-x})_3$ films also suggest a longer duration[78] with 30 minutes selected as an annealing time for the general procedure.

2.3.2 Hole Transport Layer

Generally, 85 mg of 2,2′,7,7′-tetrakis-(N,N-di-4-methoxyphenylamino)-9,9′-spirobifluorene (Spiro-OMeTAD – Merck Millipore – Sigma Aldrich) was dissolved in 1 mL chlorobenzene (anhydrous, 99.8%). 34 µL of 4-tertbutylpyrridine and 20 µL of bis(trifluoromethane)sulfonimide lithium salt (Li-TFSI) in acetonitrile (520 mg Li-TFSI in 1 mL acetonitrile (anhydrous, 99.8%)) were added as dopants with any changes to the amounts of dopant used specified in each chapter methodology. In later chapters the additive FK209 (tris(2-(1*H*-pyrazol-1-yl)-4-*tert*-butylpyridine)cobalt(III)tri[bis(trifluoromethane)sulfonimide]) was added when specified to improve the performance of the HTL layer in glovebox conditions, 8 µL was used generally and specified if altered.

The completed HTL solution was then filtered with 0.2 µm PTFE (polytetrafluoroethylene) membrane filter before deposition. The general procedure includes a period of 30 minutes to 1 hour post HTL solution manufacture.

To form the HTL layer, 100 µL of spiro-OMeTAD solution was dropped on to the device stack dynamically, 10 seconds before the end of the 4000 rpm, 30 second spin cycle. A further static method was also utilised adding 100 µL of the completed solution onto the substrate prior to spin initiation at 4000 rpm for 30 seconds to increase reproducibility. This is referred to as the static method. Oxidation of the HTL was achieved through leaving the device in a dark, ambient environment for 12 hours.

2.3.3 Top Contact Evaporation

Gold wire (Au, 99.99% purity 1.0 mm thick Sigma Aldrich) was used to deposit top contacts on devices using an Edwards bell jar evaporator at a pressure of 10^{-5} mbar. Before deposition, a thin line of perovskite was removed directly down the centre of the device, following the swab taken after SnO_2 spin coating. This allows for the middle gold strip to contact bare FTO completing the device circuit. A shadow mask was used to define the measurement area for 8 pixels per 2.8 cm^2 device. The pattern can be seen illustrated in Figure 24.

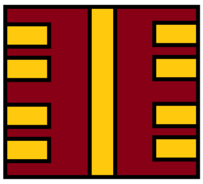

Figure 24 – Device representation with the approximate location of the gold top contact.

2.4 UV-Vis-NIR Spectroscopy

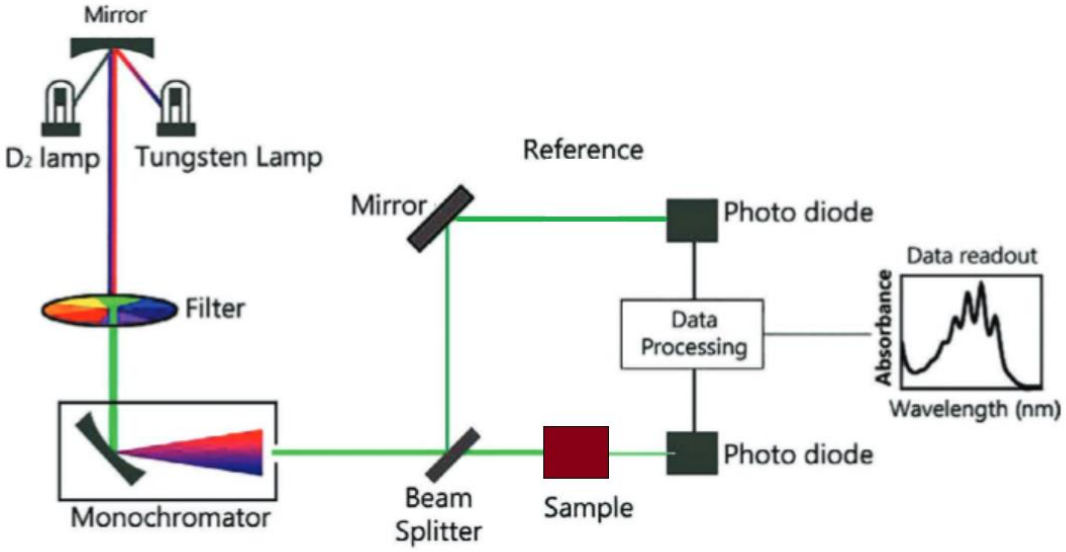

Figure 25 - Schematic for UV-Vis spectrophotometer setup adapted from Soni et al, 2021[102].

UV-Vis-NIR spectroscopy utilises a beam of light, filter wheel and monochromator to expose a given sample to a range of light wavelengths (Figure 25). The technique is used in this thesis to record the transmittance of perovskite thin films. The monochromator regulates the wavelength of the light dependent on the range of the scan. This light is then fed through a beam splitter to generate two identical beams of light. One of these beams in then impinged onto the thin film sample, before entering into a photodiode detector. The detector measures the amount of light received and contrasts this with the blank measurement taken on the non-sample beam, extrapolating the amount of light transmitting through the sample over a range of wavelengths. The absorbance of the sample can then be calculated based upon the light transmitted by the sample in equation 1. This technique, therefore, cannot account for the reflectance of the sample independently, and any scattered or reflected light represents a data loss with this method.

Within this thesis absorbance measurements for thin films were taken on a Perkin Elmer Lambda 9 UV-Vis-NIR spectrometer. Generally, the scan range was set between 200-800 nm, with a scan speed of 960 nm/s and a step change of 1 nm. Data was recorded in transmittance mode unless otherwise specified and converted into absorbance via application of the beer lambert law (equation 1).

$$\mathrm{ABS} = 2 - \log_{10}(\mathrm{T\%})(1)$$

2.5 Steady State Photoluminescence (Edinburgh Instruments FS5)

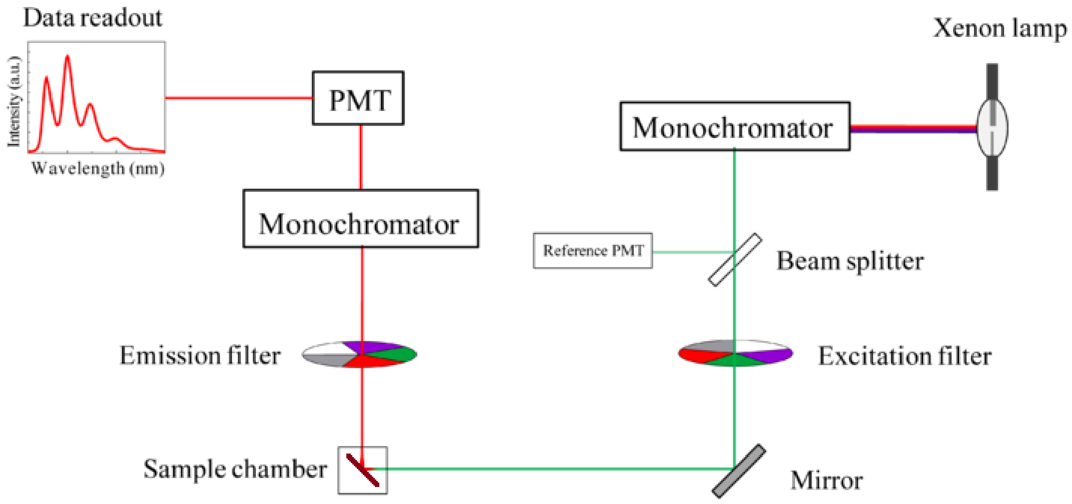

Figure 26 – Schematic showing the principles of fluorescence spectroscopy.

Figure 26 provides the mode of operation for a fluorescence spectrophotometer, designed to assess PL at steady state. Steady state photoluminescence (SSPL) measurements of thin films were made using an Edinburgh instruments FS5 spectrofluorometer, with the standard thin film sample holder; the integrating sphere unit was used to measure absorptance and is discussed in section 2.3.2.2. Fluorescence excitation was changed depending on the study (specified in each chapter for the results reported). This is known to have a large influence perovskite fluorescence and should be noted. A further parameter specific to the measurement set up includes the regulation of the excitation and emission monochromator slit widths. The excitation slit width determines the area of the sample illuminated and consequently the intensity of the characteristic emission. For all studies presented the excitation and emission slit widths were maintained at the same value as for steady state photoluminescence measurements. These are determined on a case-by-case basis as the relative intensity of fluorescence varies depending on the exact build procedure. Generally, samples manufactured in ambient air exhibited lower fluorescence than those manufactured in a nitrogen (N_2) atmosphere. For ambient air build utilising standard 1.25 M 1:1 stoichiometry a slit width of 3 nm was sufficient to achieve close to 1 million counts with high variability.

For $Cs_{1-a}(MA_xBr_{1-x})_aPb(I_xBr_{1-x})_3$ samples, fabricated in a N_2 environment exclusively, higher fluorescence intensity was generally achieved. The slit widths are modified accordingly, with 1.5 nm generally sufficient for optimisation at 1 million counts.

The FS5 spectrophotometer was optimised to 1 million counts for the most emissive sample of a sample set for each study to reduce variation as much as possible. Large differences in the fluorescence emission for samples within a set may lead to increased noise interference for the samples with the lowest emission. This is due to reduced sensitivity for samples with low emission under the given slit width conditions. This trade off was deemed necessary in order to properly compare novel perovskite films in terms of their fluorescence emission.

To ascertain the fluorescence properties of perovskite films, measurements were taken on films in the absence of the transport layers and contact (*i.e.* FTO or ITO/Perovskite/PMMA). This stack was manufactured with the poly(methyl methacrylate) (PMMA - Sigma Aldrich, average molecular weight ~120,000 by GPC) layer spin coated onto the perovskite film to prevent environmental degradation during the measurement. PMMA (1M in toluene unless otherwise specified) was deposited *via* spin coating at 3000 rpm (3000 acceleration) for 30 seconds, followed by a 3 minute anneal at 70°C. For consistency, samples were placed in the dark sample holder prior to measurement for 2 minutes. Three films per solution were evaluated with repeat measurements under constant illumination to mitigate the effect of photobrightening[103]. To achieve this, measurements were taken with a 2.5 minute delay of light exposure between scans until the scans converged and were deemed 'stable' (see Figure *39* for candidate A solution multiple scan results). The uncorrected 'stable' scan for each sample was used when calculating the average data shown along with the standard deviation range from the mean shown by the shaded region.

2.5.1 Additional Filters

An additional set of filters was used where specified to obtain clearer spectra (dependant on the excitation wavelength used and the perovskite composition). This involved the use of a 520 nm (green) band pass filter on the excitation light, and a 611 nm long pass filter on the sample emission prior to the signal entering the emission monochromator and detector.

2.5.2 Absorptance Measurements Within the Integrating Sphere

Absorbance measurements have been discussed previously in 2.3 Films for Characterisation. The absorbance value, as stated, cannot account for sample reflectance. Film measurements of absorptance were also taken using the FS5 spectrofluorometer to account for both sample absorbance and reflectance (absorptance).

Absorptance scans were taken using the same sample architecture in the integrating sphere. Slit widths were dependent on the properties of the deposited perovskite and as such were defined in each chapter. The same width was used for both the blank sphere scan and with the sample in the direct position. A synchronous scan was completed first on the blank sphere over the wavelength range 600-900 nm providing a baseline measurement. Subsequent to this, with the sample in the direct position within the sphere, a further synchronous scan was completed over the same range. The fluoracle software can then be used combining the blank and direct position scan and providing analysis to attain reflectance and absorptance curves. The presented absorptance curves were attained through linear interpolation between the original data points, then smoothed using the Savitzky-Golay method with 6 points in window and a polynomial order of 3 (on OriginPro, 2020b).

2.6 X-Ray Diffraction (XRD) Analysis

X-ray diffraction is a technique which operates according to Bragg's law of diffraction (Equation 3). Incidence x-rays are imposed onto the sample over a range of angles (θ) – as depicted in Figure 27. Corresponding ray reflections are detected providing quantitative data on the crystal structure of the material.

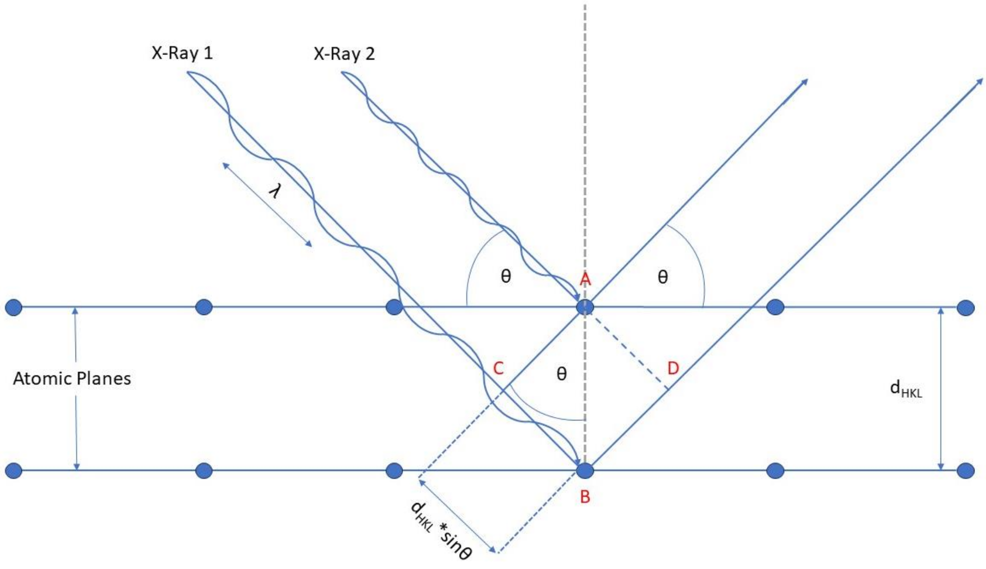

Figure 27 – XRD Mode of Operation Diagram.

Mode of Operation:

Figure 27 shows two incident x-rays striking parallel atomic planes within a material. The technique relies upon the path length difference between these x-rays. Using the nomenclature in Figure 27:

$$CB = BD = d * \sin(\theta) \quad (1)$$

The difference in path length between the two rays can be defined as:

$$\varDelta = CB + BD = 2 * d * sin(\theta) \quad (2)$$

The maximum path difference for 1st, 2nd, and 3rd order conditions is defined as:

$\varDelta = n * \lambda$

Where $n = 1, 2, 3$, with Bragg's law of diffraction as:

$$n * \lambda = 2 * d * sin(\theta) \quad (3)$$

XRD measurements were performed using a Bruker D8 Discover in a standard divergent slit set-up. Within chapter 2, the sample architecture used FTO/SnO_2/$MAPbI_3$/PMMA, with the SnO_2 deposited in class 6 clean room conditions followed by $MAPbI_3$ deposition in a nitrogen glovebox environment. The build procedure mimicked the device manufacture simply omitting the HTL for PMMA. The scan range was set from 5-60° and the measurements taken using a 40kV, 40mA Copper source with a step size of 0.04°, at 1 second per step. Origin peak analyser (OriginPro, 2020b) was used to find the full width at half maximum for the 110, 220, and 310 characteristic tetragonal $MAPbI_3$ peaks. This was done by subtracting the baseline and integrating 0.5 degrees either side of the peak.

Studies within chapter 5 and 6 utilise similar architectures with analysis provided through the Origin software (OriginPro, 2020b). Specific details of the method for each figure provided are within the individual chapter methodology.

2.7 Scanning Electron Microscopy (SEM) Imaging

Scanning electron microscopy utilises a high energy beam of electrons directly impinged onto the surface of the sample in order to generate an image of the sample surface. The technique focusses the electron beam on samples and scans the area requiring magnification. As the electrons interact with the material, secondary electrons are emitted, characteristic of the sample morphology. The secondary electrons are then detected and measured in order to create an image of relative depth, highlighting sample morphology in a digestible contrast-based image format. Unit operations within the column of the SEM and ancillary equipment are shown in Figure 28.

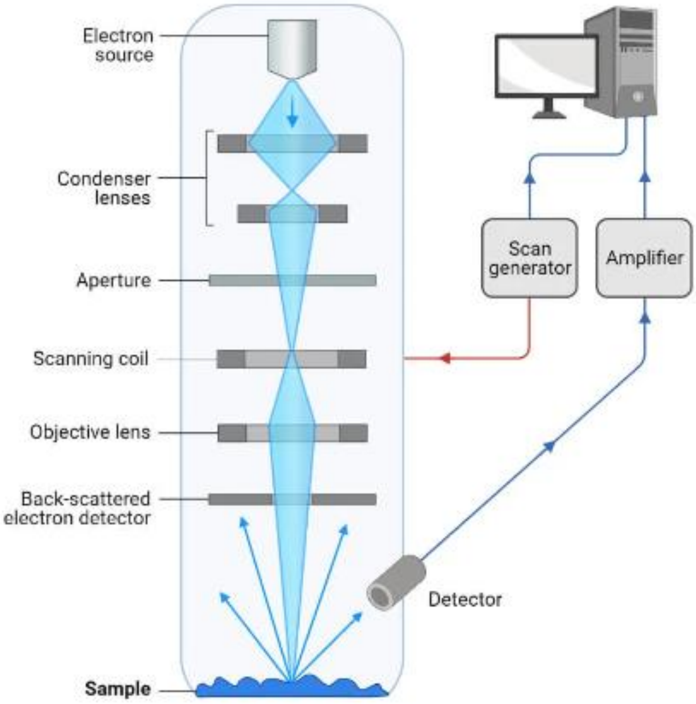

Figure 28 – SEM Mode of Operation Diagram[104]

For this thesis SEM images were taken using a JEOL 7800F FEG-SEM with 30,000× magnification. 5,000×, 10,000×, 15,000× images. Specific scan parameters are specified in each chapter as appropriate.

2.7.1 Zen Blue Intellesis – Machine Learning Based Segmentation Analysis

Image segmentation was attempted during chapter 4 of this thesis utilising the Zen Blue Intellesis segmentation software. The purpose of this software package was to find a reproducible AI analysis of SEM images to compare crystal size and structural parameters.

The procedure involved the use of 30,000× magnified images. These images show sufficiently large crystal to attempt segmentation, with lower magnification increasing the analysis segmentation error, rendering the technique unusable. The 30,000× images were used to manually train the module to segment the image as the perovskite crystal (object) and the respective grain boundaries (the background). This was done based on the contrast of the image, with darker regions suggesting greater depth from the SEM and indicating the grain boundary between the crystals. As a result of this the images were enhanced to increase contrast enabling the software to segment the image for further analysis (Figure 32). The 30,000× images were enhanced in the imaging software GIMP to achieve high contrast difference at the grain boundary.

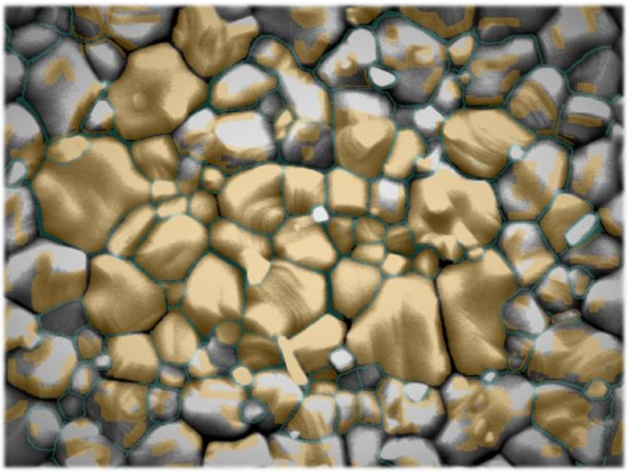

Figure 29 - Manually training the Zen Blue Intellesis Software to segment Perovskite Crystals

Figure 29 provides a sample showing the manual highlighting required to train the module. On a pixel level basis, the images were coloured to identify the lighter crystal, seen in yellow, from the darker grain boundaries, seen in blue. The software then 'learns' this differentiation. Once the programme was trained a segmentation was then run on each of the films with the result shown in Figure 31.

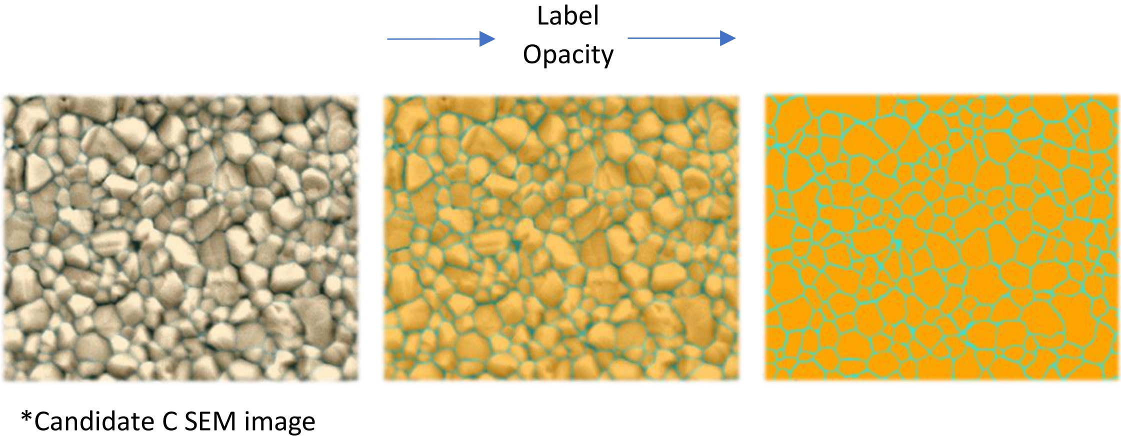

Figure 30 - Post processing opacity imaging showing the software segmenting the image.

Figure 30 shows the segmentation result with an overlay increasing in opacity. The final image then needs a post processing treatment to ensure accuracy. Segmentation may be poor at grain boundaries which exhibit poor contrast.

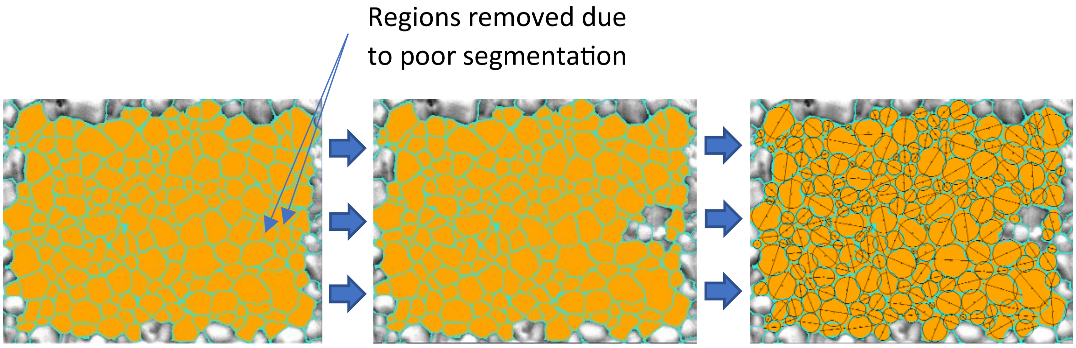

Figure 31 - Images showing the final removal of incomplete crystals before final analysis.

Once the image analysis software segmented the crystals, incomplete crystals or those with no clearly defined boundary were manually extracted during the analysis phase defining measurement regions. Parameters including area, perimeter, diameter, roundness, and maximum Feret diameter were taken for each complete segmented crystal available using the Zen Blue image analysis module with the results presented in Table 13. Errors given for crystal size parameters represent 1 standard deviation in size from the mean in nm. Figure 32 shows the fully segmented image set for candidate A films prior to analysis.

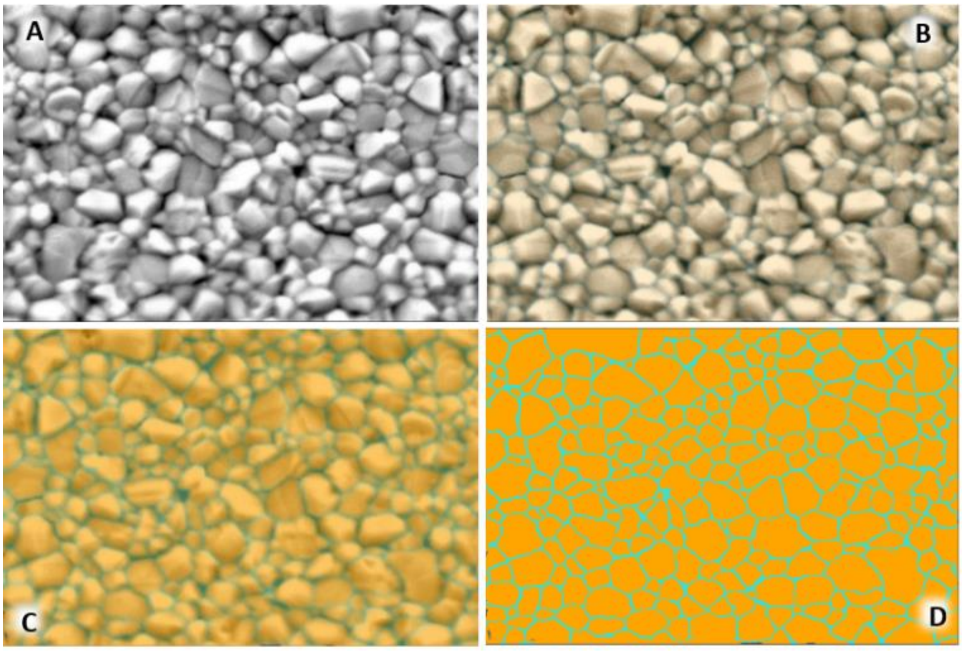

Figure 32 - SEM of $MAPbI_3$ thin-film deposition from Candidate A solvent system with 30,000× magnification (A) and the Zen Blue image analysis segmentation (B-D). A - mirrored image of the base data for the image analysis software to segment. To illustrate the accuracy of the segmentation the label opacity is increased (B-D) with the final result (D) typical of the segmented data analysed to extrapolate crystal size characteristics.

2.8 Profilometry

Profilometry as a technique was harnessed to measure film thickness and ascertain any difference in perovskite film thickness resulting from alterations to both the solvent system for deposition and the spin coating regime. This technique uses a finely tuned stylus tip to trace the surface of a sample and measure relative depth. To measure film thickness, a sharp razor blade was used to create a line along the sample contacting bare substrate. The stylus tip was moved along the sample over the gap, generating a film profile depth. Multiple measurements were taken across the sample corresponding to ‘left’, ‘middle’ and ‘right’ allowing investigation of film thickness and uniformity.

Film thickness was measured using a KLA Alpha-Step D-600 stylus profiler. Films were manufactured in a nitrogen glovebox on FTO after 10 minutes of UV-Ozone treatment and cleaning as per the manufacture method. A thin strip was manually scraped from the middle of the film to allow step down measurement of the surface. Each measurement was taken step down over a 3 mm distance with the average results presented in the Table 12. Figure 48 provides a graphical representation of the base data attained for the measurement of a ~500 nm thick film deposited using the candidate A solvent system.

2.9 Device Performance Evaluations

A crucial parameter for solar materials is the device performance efficiency, calculated as a percentage of incident light on the material that is converted into electrical current within the device. Measurement of this efficiency requires a prescribed method for comparable results between devices, a calibrated solar cell to regulate light intensity (typically an accredited silicon cell), and a solar simulator to measure both the incident light and electrical output. The current-voltage (JV) curves for devices measured within this thesis were recorded using an Oriel Sol3A solar simulator, under simulated AM1.5 sun illumination. Figure 33 shows the AM 1.5G reference spectrum used for device measurement compared to the AM0 spectrum.

To perform device measurements the completed devices were placed into a cradle with electrical contacts touching both the individual top contact for the pixel to be measured, and the gold contact touching the bare transparent conductive oxide. An electrical circuit can then be made across the device during operation.

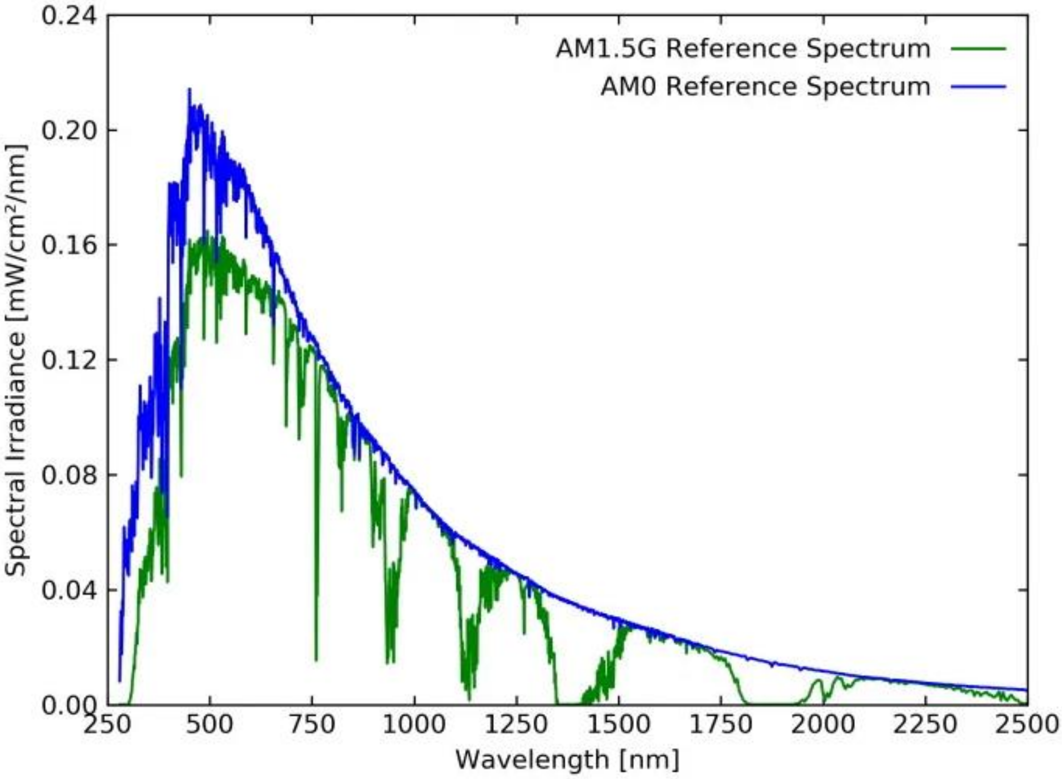

Figure 33 – AM 1.5 Solar Irradiance.[105]

In operation, the solar simulator applies a voltage to the device and records the current output – commonly known as an IV sweep. This sweep begins at open circuit voltage and decreases in pre-programmed increments – known as a reverse sweep. The voltage is then increased for a second sweep in identical increments until open circuit voltage representing the forward sweep and completing the data set. An equivalent method of presenting this data within the solar simulator is to generate a J-V curve. Where I represents the total current (milli amps (mA)), J represents the current per unit area (mAcm^{-2}). To do this the current is divided by the active area of the pixel undergoing measurement. A shadow mask defined an active area of 0.09 cm^2 for each evaluated pixel. Sequestering the incident light within predefined aeras located above the top contact. For all scans used to determine efficiency within chapter 3, 4 and 5 of this thesis a total of 8 pixels were evaluated (where possible – excluding the event of equipment failure) per sample with a pre-sweep delay for light exposure of 1s, and a sweep time of 9.8s through the range 1.2 volts(V) to -0.1V. For chapter 6 the pre-sweep delay was increased to 5 seconds. The data presented was obtained from the reverse scan set up unless otherwise specified. Thus, a J-V curve was generated for each pixel along with an internal calculation of efficiency, calculated using three major photovoltaic factors. These interrelated factors are the open circuit voltage (V_{oc} – V), the fill factor (FF - %), and the integrated current (J – mA cm^{-2}).

Open circuit voltage (V_{oc}) :

This factor represents the voltage by which the cell produces a positive current value, opening the circuit.

Short circuit current (J_{sc}):

This is determined from the J-V curve as the current output from the device at zero voltage – effectively short circuit conditions.

Fill factor (FF):

This requires the full J-V sweep and knowledge of the maximum point. Defined as the point on the J-V sweep that generates the maximum power output (the point where J×V is the largest) with J_{MPP} – current for maximum power and V_{MPP} – voltage for maximum power. From this point an integration of the area filling a rectangle, with the vertex situated on the maximum power point, yields the fill factor as a percentage of the theoretical maximum power. The relationship can be defined mathematically as

$$FF = \frac{J_{MPP}V_{MPP}}{J_{SC}V_{OC}} \quad (5)$$

Power conversion efficiency (PCE):

PCE can then be calculated through the three major photovoltaic parameters as:

$$PCE = \frac{P_{out}}{P_{in}} = \frac{J_{sc}V_{oc}FF}{P_{in}} \quad (6)$$

The PCE is therefore calculated through the generation of JV curves for each pixel of a device and provides an indication of how much current the device can produce relative to the radiant power of the AM 1.5 G light source and device active area.

2.10 Internal Photon Conversion Efficiency (IPCE)

A downside of the JV curve analysis for device performance is that the amount of light reflected, scattered, or otherwise lost is not accounted for. Neither is the effect of different wavelengths of light on device efficiency. To measure the internal photon conversion efficiency, light at individual wavelengths is shone onto the sample, under and operating voltage. The output current can then be used to ascertain the IPCE based on precise knowledge of the energy of photons actually interacting with the sample.

Prifysgol Abertawe
Swansea University

Chapter 3 - Sustainable Solvent Selection for the Manufacture of $MAPbI_3$ Perovskite Solar Cells

Part of this work has been published in the journal *Green Chemistry* titled:

'Sustainable Solvent Selection for Methylammonium Lead Triiodide ($MAPbI_3$) Perovskite Solar Cells[106]*'*

A. J. Doolin, R. G. Charles, C. S. P. De Castro, R. G. Rodriguez, E. V. Péan, R. Patidar, T. Dunlop, C. Charbonneau, T. Watson and M. L. Davies, *Green Chem.*, 2021, **23**, 2471–2486.

3.1 Introduction

3.1.1 A history of Solvents for Perovskites

Traditionally, methylammonium lead triiodide ($MAPbI_3$) has been one of the most commonly used perovskite materials for the light absorber layer in PSCs, deposited as a solution of the precursor compounds, MAI and PbI_2, in DMF[107]. During the early stages of perovskite development, in addition to DMF, several alternative dipolar aprotic solvents have been used including γ-butyrolactone (GBL) [91,108], dimethyl sulfoxide (DMSO)[107,109], n-methyl-2-pyrrolidone (NMP) [110], and dimethylacetamide (DMAc) [111] with final film morphology and device performance varying due to differences in crystallisation dynamics between solvents[109]. Solvent system optimisation for the $MAPbI_3$ composition has been a continuing process over the last 14 years. Despite the range of solvents from which $MAPbI_3$ can be successfully deposited, highly efficient devices still rely on DMF based precursor solutions. Reproductive toxicity issues and a workplace exposure limit of 15 mg/m^3 hinders the scalability of DMF for low-cost manufacturing[90,112]. It has also been proposed that the role of DMSO in lab scale cosolvent systems is vital for high efficiency devices due to enhanced system coordination effects[113]. A crucial challenge of solvent system engineering to support PSC development is to advance understanding of dissolution and coordination of $MAPbI_3$ precursors[114,115]. The impact of solvent fluid properties and colloidal metal-ligand configuration on device PCE should be ascertained to inform the selection of appropriate alternative sustainable solvents and improve the potential for large scale manufacturing.

Several guides evaluating the validity of solvent selection have previously been reported[116–122]. Solvent selection based on environmental, health and safety (EHS) considerations in the absence of full lifecycle assessment has been conducted by numerous large chemical and pharmaceutical firms in the last decade including Sanofi, GSK, AstraZeneca and Pfizer[120,123–126]. Subsequently, researchers have created unified guides consolidating this information, in part due to differences in the priorities of the organisations producing them[122,127–129]. A major effort in this field was the creation of the innovative medicines initiative (IMI)- CHEM21 selection guide[130], which has been used to guide this research. In addition to EHS considerations, solubility parameters help to identify suitable solvents for dissolution of perovskite precursors. The Hansen solubility parameter (HSP) has been applied in previous attempts to screen alternative solvents[108,109], to identify solvents similar in Hansen space to DMF, DMSO, NMP, and DMAc. HSP attempts to quantify the solvating power of a solvent in relation to a specific solute by analysing the physicochemical properties of the system with respect to; molecular dispersion (δD), dipolar interactions (δP), and hydrogen bonding (δH)[131].

Wang *et al.* (2017) compiled HSP data for commonly used $MAPbI_3$ precursor solvents and calculated the distance in Hansen space between the solvent and the assumed parameters of the lead iodide solute[109]. However, current theory indicates that HSP fails to account for ionic interaction between perovskite precursors and complexation in solution which prevents accurate application of the Hansen model to $MAPbI_3$ precursor dissolution[109]. Higher solvent polarity has, however, been linked to greater PbI_2 salt miscibility[108], potentially aiding an increase in the concentration of precursor solutions. However, several notable highly polar solvents such as ethylene carbonate do not dissolve PbI_2 in contradiction to this theory, indicating influence from multiple solvent properties[114]. Hamill *et al.* (2017) indicated a distinct correlation between the Gutmann donor number (D_N), a basicity measure of the solvent, and the ability of the solvent to coordinate Pb^{2+} from PbI_2 in solution[114]. Dissolving and retaining adequate concentrations of PbI_2 in solution for coating requires solvents which act as strong metal ligands[132]. DMSO was first proposed as a ligand additive with the poorly coordinating solvent GBL to retard crystallisation through the formation of an intermediate phase[133]. Lee *et al.* (2016) expanded on this theory suggesting that $MAPbI_3$ dissolution and deposition is dependent on Lewis acid-base interactions, where PbI_2 acts as a Lewis acid with a dipolar aprotic solvent Lewis base donor ligand[107].

Previous investigations of alternative solvent systems for spin coating, employed to improve sustainability, uniformity, and decrease defect densities have been reported. These include utilising methylamine gas as a post-treatment[115]; DMSO, 2-methylpyrazine (2-MP), and 1-pentanol (1-P) based inks[109]; and GBL, alcohol, cyclic carbonate and acid systems[108] (Table 3). Novel engineering solutions to this problem have been demonstrated, such as dissolving methylamine gas into an appropriate carrier solvent such as acetonitrile (ACN) to successfully deposit functional perovskite films[132]. This utilises strongly basic methylamine which in turn acts as the solvating agent for PbI_2. A further application of this method bubbles methylamine through ethanol, which is subsequently mixed with tetrahydrofuran (THF) [134], a common low-cost solvent with high vapour pressure at room temperature, allowing rapid crystallisation over relatively large areas. Both of these systems use volatile bulk solvents and have found application in lab-based roll to roll (R2R) manufacture. Due to limited options for DMF alternatives and understanding of the impacts of solubility parameters and crystallisation kinetics in these solvents, further investigation of $MAPbI_3$ deposition with available ‘green’ and safer solvents along with life cycle impact consideration is required to identify suitable and sustainable alternatives.

A crucial factor to consider is the deposition method used to coat precursor solutions onto substrates. Currently, the highest PCE devices are spin-coated at lab scale, with typical active areas of <1 cm^2,[58] whereas alternative methods with superior deposition efficiency are used for scaled-up production such as slot-die coating, spray deposition or inkjet printing for R2R production. Each technique requires specific consideration of the solvent parameters along with the physical and rheological properties that may differ from those of solvent systems developed for spin-coating[135,136].

3.1.2 Issues Regarding Solvent Use

Evidence suggests the reaction mechanism between Pb^{2+} ions and a dipolar aprotic solvent results in effective dissolution of trihalide perovskite layers[36]. Due to the required dissolution of lead iodide, alternative dipolar aprotic solvents were shortlisted preferentially as Lewis basic ligands for solvation. When selecting solvent substitutes, primarily driven by EHS concerns, a balance needs to be achieved between performance and 'green' credentials. This requires a methodology to accurately rank respective solvents both in terms of EHS concerns and lifecycle impact considerations, whilst also performing characterisation of the perovskite layer as utilised within a competitively efficient device. DMSO is commonly used as a co-solvent and shows promise in sustainable precursor formulations due to its lack of carcinogenic, mutagenic and reprotoxic (CMR) properties. However, a high boiling point and low vapour pressure limit its use in doctor blading and R2R slot die manufacturing, where more volatile non-coordinating solvents are favoured for near room temperature annealing[137]. A candidate list of commercially available alternative 'green' solvents, regardless of their polarity or hydrogen bonding affinity, was compiled. Consideration of boiling point and flash point was undertaken with these solvents pending industrial evaluation and mitigation by added cosolvents. The aim of this study was to identify commercially available 'green' solvents with desirable properties for the spin coating deposition of $MAPbI_3$ precursor solutions and evaluate their performance. We present a solvent screening methodology based on Hansen solubility metrics, donicity, and EHS considerations. Utilising this method, an alternative solvent system consisting of DMSO, 1,3-dimethyltetrahydro-2(1H)-pyrimidinone, also known as dimethylpropyleneurea (DMPU), 2-methyltetrahydrofuran (2-MeTHF) and ethanol (EtOH) is presented and analysed. Furthermore, solvent engineering techniques have been applied to spin coat highly efficient films *via* a prenucleation method, optimising the candidate systems of different % compositions showcasing the potential versatility of a 'green' solvent toolbox[107,114]. Structural and optical studies were undertaken to elucidate the crystalline and photoluminescent nature of this novel perovskite. The manufacture and characterisation of full devices based on the optimised DMF-free solvent system aims to shed light on the link between solvent properties and PSC performance.

3.1.3 Alternative DMF-Free Solvent Systems and their Record Efficiencies

Table 3 - Previously published power conversion efficiencies for $MAPbI_3$ solar cells produced from non-DMF $MAPbI_3$ precursor solutions.

Solvent System	Configuration	PCE%	Active Area (cm^2)	Ref.
Acetonitrile/methylamine	FTO/c-TiO_2/C60/PAL/Spiro-OMeTAD/Ag	18.0% Stabilised	0.09	[132]
		15%	0.7	
Dimethylsulfoxide/2-methylpyrazine/1-pentanol	ITO/c-TiO_2/PAL/Spiro-OMeTAD/Au	16.0% Stabilised	0.09	[109]
µ-butyrolactone + alcohols/carbonate/acid	ITO/c-TiO_2/PAL/Spiro-OMeTAD/Au	15.1%	N/A	[108]
		11.9%	4	
Tetrahydrofuran + ethanol/methylamine	FTO/c-TiO_2/m-TiO_2/PAL/Spiro-OMeTAD/ MoO_x/Ag	20.0%	0.1	[134]
		15.6%	10	
2-Methoxyethanol	ITO/PEDOT:PSS/TANP/PCBM/LiF/Al	15.3%	0.09	[138]
N-methyl-2-pyrrolidone	ITO/NiO_{x-}/PAL/$PC_{61}BM$/$Zr(acac)_4$/Ag	16.0%	N/A	[110]
N-methyl-2-pyrrolidone/dimethylacetamide	Unknown	17.38%	N/A	[139]
Dimethylpropyleneurea - 10 vol% additive in DMF/DMSO	Unknown	~2% increase	N/A	[114]

3.2 Methodology

All devices manufactured for this chapter were made in accordance with the general methodology (2.1 General Procedure for the Manufacture of devices). All chemicals were purchased from Sigma Aldrich unless otherwise stated.

3.3 Results and Discussion

3.3.1 Selection of candidate solvents

To facilitate the design of alternative solvent systems for perovskite, the boundaries for chemical substitution needed to be defined. $MAPbI_3$ was chosen for initial investigations as a highly efficient, defect tolerant composition. Solution deposition can be achieved through the combination of only two precursor compounds, PbI_2 and methylammonium iodide (MAI) respectively, limiting the complexity of the solution coordination chemistry. A robust justification for chemical substitution was also necessary. As previously discussed, the IMI-CHEM 21 methodology was utilised to provide a justification for solvent use based on the best available recommendations provided by researchers and industry. Tertiary aims of this research include improving understanding of the effect of solvent properties on the properties of the final film. This has been evaluated using a range of spectroscopic and structural characterisation techniques. To fulfil our initial aim, a screening process was implemented to identify sustainable solvents with a broad range of parameters which may be of use for perovskite dissolution and subsequent film formation.

The process used for screening candidate solvents is outlined in Figure 34. Initial screening to identify dipolar aprotic solvents with similar properties to DMF was conducted. Polarity, as described by the dielectric constant was considered in initial screening to filter candidates as a majority of known solvents for use in perovskites have dielectric constants above 30, however, high polarity alone is not sufficient[114]. A further indicator used in screening was HSP. Although calculation of the Hansen distance was done using assumed parameters for lead iodide. More recently, the Hansen sphere of lead iodide was described using Hansen Solubility Parameters in Practice (HSPiP) commercial software by Babaei et al. (2018)[140]. A table showing the results of Hansen distance (HD) calculations using these updated parameters can be seen in Table 4, with the Hansen distance[109] a function of the parameters relative to the lead iodide salt given by Equation 7[141].

$$\mathrm{HD} = \sqrt{4(\delta \mathrm{D1} - \delta \mathrm{D2})^2 + (\delta \mathrm{P1} - \delta \mathrm{P2})^2 + (\delta \mathrm{H1} - \delta \mathrm{H2})^2} \quad (7)$$

Table 4 - Reference data for the Hansen solubility parameter evaluations used to identify candidate DMF alternative aprotic polar solvents for perovskite (CH3NH4PbI3 – $MAPbI_3$) film deposition.

Perovskite Precursor Solute (Babaei *et al.* (2018))	δD ($MPa^{1/2}$)	δP ($MPa^{1/2}$)	δH ($MPa^{1/2}$)				
Lead iodide (PbI_2)[140]	17.76	21.41	14.46				
Solvent				HD [109]	HD *(this work)*	Gutmann Donor Number[142] (kcal/mol)	Dielectric Constant
dimethylformamide (DMF) [109]	17.4	13.7	11.3	1.8	8.4	26.6	38.25
dimethylsulfoxide (DMSO) [109]	18.4	16.4	10.2	1.8	6.7	29.8	47.00
diethylformamide (DEF) [109]	16.4	11.4	9.2	5.0	11.6	30.9	29.02
2-methylpyrazine (2-MP) [109]	18.3	12.3	10.5	2.9	10.0	Unknown	Unknown
γ-butyrolactone (GBL) [109]	18.0	16.6	7.4	3.7	8.6	18	41.70
acetonitrile (ACN) [109]	15.3	18.0	6.1	7.6	10.3	14.1	36.64
dimethyl carbonate (DMC) [109]	15.5	8.6	9.7	8.1	14.4	17.2	3.17
dimethylacetamide (DMAc) [143]	16.8	11.5	10.2	4.2*	11.0	27.8	38.85
dihydrolevoglucosenone - Cyrene [116,128]	18.8	10.6	6.9	6.2*	13.4	Unknown	37.30
dimethylpropyleneurea (DMPU) [143]	17.8	9.5	9.3	5.7*	13.0	33.0	36.12
2-methyltetrahydrofuran (2-MeTHF)[144]	16.9	5.0	4.3	12.1*	19.4	18.0	7.53

*calculated using the same assumed parameters and method as Wang *et al.* (2017) [109]

3.3.2 Bulk solvent selection chart for $MAPbI_3$ dissolution

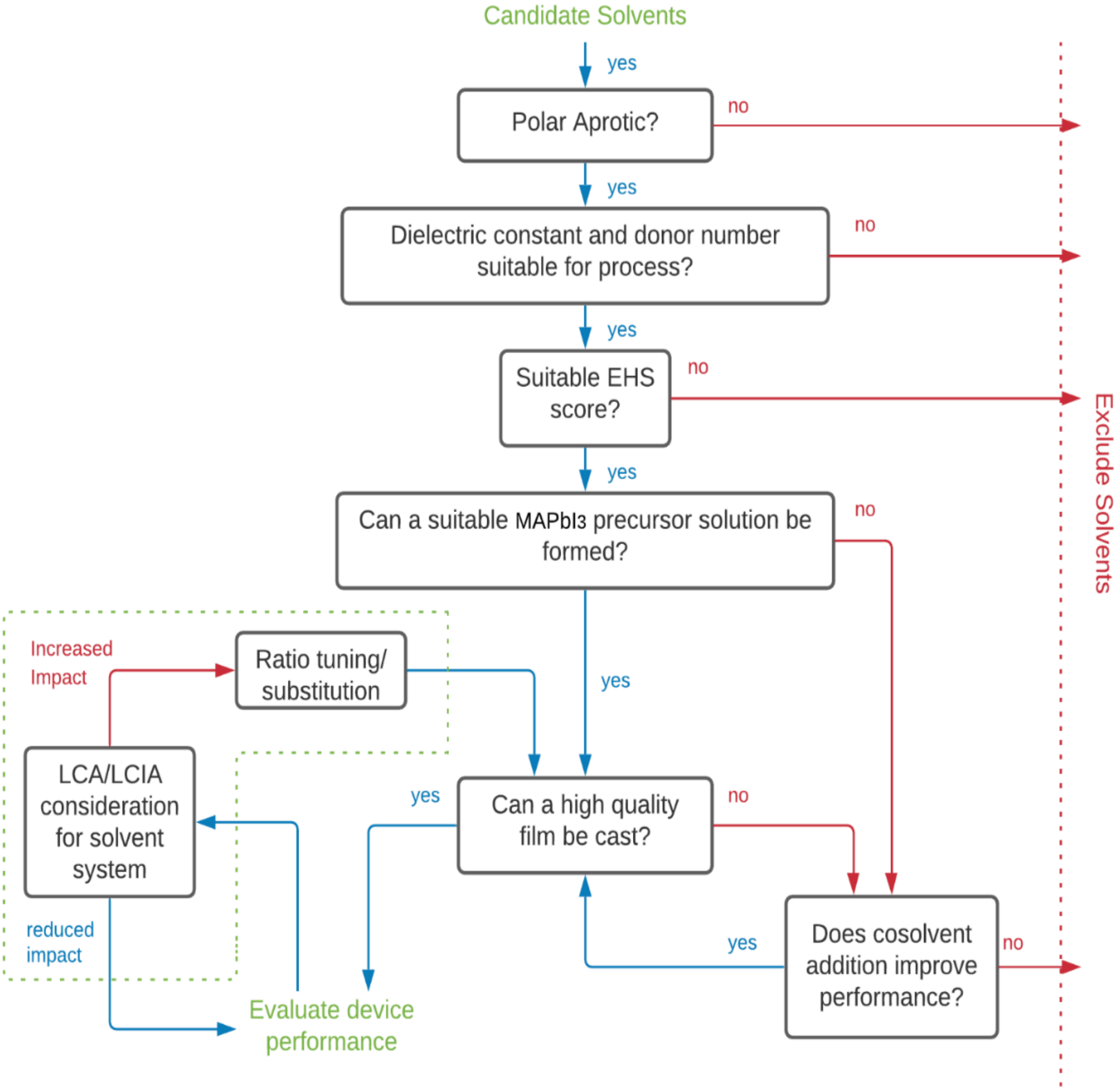

Figure 34 - Solvent selection decision tree for screening and evaluation of alternative solvents. LCA/LCIA evaluation highlighted as a section that requires significant improvement and implementation when considering solvent systems. EHS – environmental, health and safety, LCA – life cycle assessment, LCIA – life cycle impact assessment, $MAPbI_3$ – methylammonium lead triiodide.

3.3.3 Screening based on environmental, health and safety considerations (EHS)

EHS concerns were used to grade candidate solvents using the IMI-CHEM21 guide (

Table 5). The methodology for the derivation of the EHS scores can be found on the ACS Green Chemistry Institute Pharmaceutical Roundtable website[145]. Solvents that scored either ‘hazardous’ or ‘highly hazardous’ were excluded. Solvents which scored ‘problematic’ or ‘recommended’ status as the outcome of the evaluation were included as a potential improvement on DMF which is determined to have ‘hazardous’ status.

The task of evaluating solvents on their ‘greenness’ is complicated by a lack of available lifecycle impact assessment (LCIA) data for emerging green solvents, an issue that is commonly encountered attempting to conduct lifecycle assessment (LCA) on green solvents[146]. For DMPU this data remains unavailable due to limited industrial application. Full consideration of the trade-offs in environmental impacts at different stages of product lifecycles resulting from solvent substitution is not possible without it, or a better picture of all processes involved in manufacturing, distribution, use, collection, and end-of-life stages of PSC products. However, consideration of available LCA data showing cradle to gate impacts of solvents has been considered.

3.3.4 Technical evaluation of candidate solvents

Following EHS screening, remaining candidate solvents were purchased from Sigma-Aldrich (anhydrous solvents where possible, used as received) and 1st generation precursor solutions were made by adding PbI_2 (~580 mg) and MAI (~200 mg) in 1 mL of candidate solvent by heating to 60°C with stirring. If the precursors remained undissolved, temperatures were increased until complete dissolution was achieved, or the solvent could be excluded for failing to dissolve precursors to a sufficient extent to achieve a 1.25M solution. In such cases, undesirable reactions often resulted from solvent-solute or solute-solute interactions.

Table 5 - Traffic light scores of classic PSC solvents vs alternatives and components (comp) of proposed novel solvent system evaluated via CHEM21 method[130]. S – safety: H – health: E – environment.

Solvents	S	H	E	Outcome
Classic PSC solvents				
DMF	3	9	5	Hazardous
Chlorobenzene	3	2	7	Problematic
DMSO	1	1	5	Recommended
Ethyl Acetate	5	3	3	Recommended
Potential alternative aprotic solvents				
2-MeTHF	6	5	3	Problematic
Acetonitrile	4	3	3	Problematic
Cyrene	1	2	7	Problematic
Dimethyl carbonate	4	1	3	Recommended
Ethylene carbonate	1	2	7	Problematic
NMP	1	9	7	Hazardous
Propylene carbonate	1	2	7	Problematic
DMPU	1	6	7	Problematic
Our System				
DMSO (Comp 1)	1	1	5	Recommended
DMPU (Comp 2)	1	6	7	Problematic
2-MeTHF (Comp 3)	6	5	3	Problematic
EtOH (Comp 4)	4	3	3	Recommended

Table 6 - Previously used solvents for successful $MAPbI_3$ deposition with relevant safety information and concerns

Solvent	Health and Safety Information	B.P (°C)	F.P (°C)	Cost (GPB/L)	GHS Hazard statements	Operational Exposure Limits (OEL)		Commercial Consideration	
						STEL	TWA	Advantages	Disadvantages
Dimethylformamide (DMF)	Candidate for immediate substitution from Sanofi, GSK, and Pfizer [120,123,124] GHS02, GHS07, GHS08 Known Reproductive Effects REACH registration as SVHC	153	58	£81.90	H226-H312 + H332-H319-H360D P201-P210-P261-P280-P308 + P313-P370 + P378 [147]	30 mg/m3 or 10 ppm[147]	15 mg/m3 or 5 ppm [147]	Has been used to produce the highest efficiency devices in lab environments.	Synthesised by a distillation process which is highly energy inefficient. Toxic substance which requires expensive equipment and processing.
Dimethyl Sulfoxide (DMSO)	Known to permeate the skin enhancing the absorption of chemical species[148]	189	89	£108.00	H227 P210, P280 [149]	N/A	N/A	One of the least concerning of the currently used organic solvents rated as problematic by the IMI-CHEM21 study, GSK, and Sanofi [120,123,130]	Percutaneous absorption, especially in a lead containing solution could render use of this chemical more hazardous
γ – Butyrolactone (GBL)	GHS05, GHS07 REACH Registration	204	98	£50.00	H302-H318-H336 P261-P280-P305+P351+P338 [150]	N/A	N/A	Reduced toxicological impact Found application in carbon stack based printable PSCs due to low coordinating ability and strong scaffold infiltration	GBL is a precursor to regulated drug GHB. Legality issues are a major barrier to any potential commercialisation of processes using GBL. DMF and DMSO based solutions also increased efficiencies past those

									achieved with this solvent.
Acetonitrile (ACN) w/methylamine	Methylamine – Highly flammable substance Acetonitrile – REACH Registration; GHS02, GHS07	82	5.5	£105.00	H225-H302+H312+H332-H319 P210-P280-P305+P351+P338 [151] H220-H280-H315-H318-H332-H335 P210-P280-P305+P351+P338+P310-P377-P410+P403 [152]	ACN – 102 mg/m3 or 60 ppm[151] methylamine – N/A	ACN – 70 mg/m3 Or 40 ppm [151] Methylamine – N/A	Good potential method for pilot scale manufacturing. Acetonitrile is an economically viable solvent	Safety issues associated with the storage of flammable methylamine. Requirement of additional step bubbling methylamine through solution
Dimethylacetamide (DMAC)	Reproductive Toxicity GHS07, GHS08 REACH Registration as SVHC	165	69	£31.90	H312-H332-H319-H360D P201-P261-P280-P305+P351+P338-P308+P313 [153]	72 mg/m3 or 20 ppm[153]	36 mg/m3 Or 10 ppm [153]	Has been used in conjunction with NMP to formulate highly efficient perovskite films without annealing requirements	Toxicity, and health and safety concerns Recommended for substitution by several company's corporate solvent selection guides with a focus on green solvent use.
N-Methyl-2-Pyrrolidone (NMP)	Reproductive Toxicity REACH Registration 1907/2006 (SVHC)	202	91	£107.00	H315, H319, H335, H360D P201, P280, P305+P351+P338 [154]	80 mg/m3 or 20 ppm[154]	40 mg/m3 or 10 ppm[154]	Induces instant crystallisation upon interaction with antisolvent drip. This along with superior coordination ability allow highly efficient films at room temperature	REACH registration as SVHC Some uses of NMP are restricted under Annex XVII of REACH[155]

The process of solvent selection is complicated by competing concerns relating to sustainability, health and safety, and cost; ultimately this relates to the viability of cost-effective manufacture. Current theory suggests that competitively efficient perovskite films (*c.a* 25%) rely on strongly coordinating organic solvents. Conversely these solvents tend to grade low in terms of both sustainability and health and safety factors. Industrial manufacturing concerns may also alter the emphasis where solvent cost may be mitigated by effective solvent capture and reuse. However, where solvent capture is applied, large capital expenditure (CapEx) costs can be anticipated for more toxic chemicals. It is also worth noting that the cost of alternative solvents is much higher than traditional solvents (Table 7 and Table 6). Currently, this cost disparity becomes even greater at high volumes as traditional organic solvents have more developed production routes benefitting from economies of scale, whereas emerging solvents may have more complex synthesis, and are manufactured at smaller scale with higher associated costs. Considering the relative CapEx requirement, a low toxicity solvent system could end up a more cost-effective option in the intermediate and longer term as the alternate solvent production routes develop and also benefit from economy of scale. Table 7 reports the ‘greener’ aprotic polar solvents i.e., those that scored ‘problematic’ or ‘recommended’ following EHS evaluation with the CHEM21 method, along with further a justification for their consideration for application in PSC production. Recent advances in perovskite solvent impact include the analysis provided by Vidal *et al,* 2020. This research considers the health and environmental impact of several commonly used perovskite solvents in terms of both solvent production and energy demands alongside application of the ‘USEtox’ method to assess the wider health impact of each solvent[156]. This work highlights the importance of the comparatively benign organic solvent DMSO and underlines the toxicity concerns surrounding most other commonly used solvents including DMPU. These concerns are relative to the placement of DMF on the candidate list of substances of very high concern (SVHC) as part of the registration, evaluation, authorisation, and restriction of chemicals (REACH) initiative headed by the European Chemical Agency[156]; however, there is a clear need for comprehensive frameworks to aid in the design of genuinely green and low toxicity solvent systems that attain high PCE.

Based on Hansen parameter evaluation (Table 4), several solvents were considered as promising candidates, creating a close position in Hansen space relative to the estimated HSP sphere of PbI_2. Whilst none of the evaluated solvents provided a perfect match, the Hansen distance (HD) of DMSO is 6.7, the smallest evaluated distance. DMF and GBL both show the next closest HD values.

Qualitative experimental data suggests that all three of these solvents are able to dissolve the PbI_2 precursor in the presence of MAI, despite the low coordination ability of GBL. This provides justification for continued use of DMSO as part of a co-solvating system. EHS solvent screening showed the newly developed solvent cyrene to be a possible dipolar aprotic replacement for DMF. However, our HD evaluation, along with that performed by Wang, *et al*. (2017), suggests that cyrene is relatively far away from lead iodide in Hansen space which may explain the poor performance of cyrene in generation 1 testing, with precursors precipitating out of solution. This is probably due to insufficient polarity and a comparatively low δH value – representative of hydrogen bonding affinity.

Table 7 - Candidate solvent selection table used to shortlist potential green solvents based on a literature review of green solvents along with varied solvent characteristics.

Solvent	Cost* (GBP/L)	Health and Safety Codes	b.p (°C)	f.p (°C)	Justification for Solvent Use
Cyrene	£171.00	H319 P305+P351+P338 P337+P313	203	108	Developed as a green solvent by the Circa Group in conjunction with the Green Chemistry Group[116]. Boiling point is higher than DMF but not drastically and the route of production is far more environmentally friendly as a bio-based solvent. Cost is a potential concern as production is currently small scale.
Dimethylpropyleneurea (DMPU)	£333.00	H302, H317, H318, H361 P280, P305+P351+P338	247	120	Classified as a 'greener' alternative solvent by Byrne 2016[122]. Lacking popularity in industrial applications with concerns regarding cost and the health and environmental impact of the solvent.
2-methyltetrahydrofuran (2-MeTHF)	£146.00	H225, H302, H315, H318	78	-11	Created as a green replacement solvent for tetrahydrofuran (THF). Derived from biomass processes, this solvent exhibits a greener production than THF with far lower toxic effects[128].
Sulpholane	£198.00	N/A	282	166	Touted as a green solvent with a high boiling point and corresponding flash point. Some issues noted due to high toxicity, with sources citing mitigation through low skin penetration effects [118].
Cyclopentyl methyl ether (CPME)	£132.00	H225, H302, H315, H319, H412	106	-1	Classified by GSK metrics as a substance with 'some issues', despite substitution been requested by Sanofi[122,123]. Issues with sensitivity to light have precluded this solvent from

					testing in a fume cupboard environment.
1,2,3-Trimethoxypropane (1,2,3-TMP)	No Data Available	No Data Available	143	42	Created as a trimethyl ether of glycerol, the green qualities of the feedstock are attractive. Synthesised for CO2 capture, little is known about the physical properties to date[157]. Due to low boiling point and green feedstock, appears to be a promising candidate on paper. Unavailable for testing due to lack of commercial manufacture.
γ – valerolactone	£374.00	H227	207	81	A bio derived solvent from cellulose feedstock, this represents a promising green solvent in certain industries. Production route is linked to the emergence of the green hydrogen economy[128].
1,3-dimethyl-2-imidazolidinone (DMI)	£258.00	N/A	225	120	A homolog of DMPU, this solvent has similar characteristics to hexamethylphosphoramide (HMPA), a carcinogenic solvent, and has been used as a green alternative in certain synthesis pathways. This is mainly due to reduced toxicological effects[122].
Ethylene carbonate	£112.00	H302, H319, H373	248	143	Previously used as an additive in GBL based solutions. The solvent itself cannot fully solvate the precursors or form the appropriate complexes. The high boiling point excluded this from further investigation.
Propanenitrile	£131.40	H225-H300+H310-H319-H332	98	6	Included in the candidate list to contrast the acetonitrile-based mixtures. The low boiling point suggests a potential co-solvent to aid in solvent removal. Huge toxicity issues surround the use of this from a health and safety perspective.

*The cost of these solvents was taken from Sigma Aldrich at equivalent grade/purity where available. b.p – boiling point, f.p – flash point.

A low δH value is hypothesized to result from the hydrogen accepting ability of the $C = O$ bond present within the cyrene molecule. The properties of the candidate solvent DMPU are not encouraging based upon this metric. Although the effective use of DMPU in cosolvent systems relies specifically upon its ability to coordinate the metal ion and form a complex, a major aspect of dissolution not accounted for in Hansen evaluation. However, Hansen solubility provides a useful benchmark showing the importance of polarity in relation to the lead iodide salt while pursuing a 'like dissolves like' approach to dissolution. HSP gives a point of reference for selecting solvents with similar parameters as substitutes[108,109]. Despite the limits to the HSP model, a centralised theory of polarity and coordination impacting effective $MAPbI_3$ precursor dissolution was used to define ideal parameters. The candidate solvents were therefore used in a second level of experimentation incorporating Gutmann donor number theory as a crucial parameter. Figure *35* depicts the chemical structure of solvents utilised within this research that form part of the ‘green’ solvent toolkit.

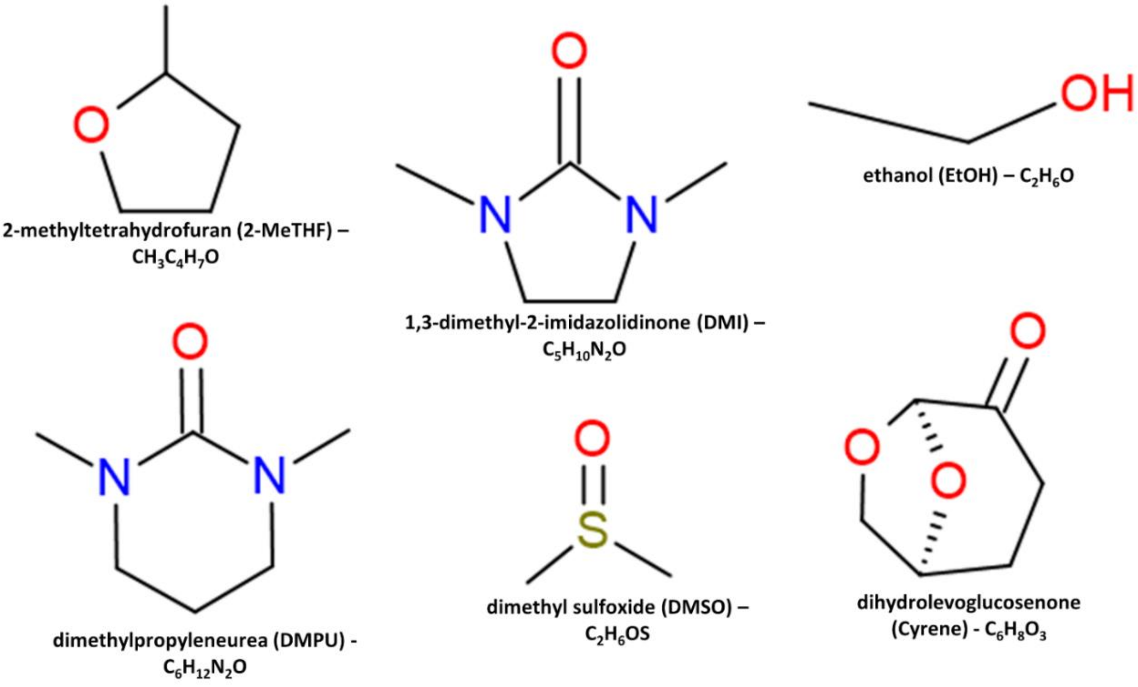

Figure 35 - Chemical structures of solvents evaluated for perovskite deposition in this study.

3.3.5 Identification of Solvent Specific Parameters for PbI_2 + MAI Dissolution

To design a new solvent system several competing concerns were identified. Initially, the concern is to solubilise the precursor at concentrations appropriate for spin coating. Secondarily, the system needs to be able to deposit high quality perovskite films. With a focus on sustainability, the solvent properties that can be utilised are limited to those presented within the green solvent toolkit. This leaves a narrow path to select not only sustainable, inherently more safe solvents, but to imbue the solvent system with the properties necessary to compete with the highly optimised DMF/DMSO system. The first stage towards this goal was to undertake a review of literature to identify which solvent parameters lead to high quality perovskite deposition.

3.3.6 Technical Properties for $MAPbI_3$ Perovskite Precursors

As discussed in section 3.1.1, solvent polarity is the first parameter of importance to enable the dissolution of lead salts. As previously covered in the literature, the donor number serves as a quantitative measure of Lewis basicity[158] and has been linked to coordination of the perovskite precursor[114] metal centre Pb^{2+}. The challenges inherent to PbI_2 dissolution and coordination within a solvent system have been previously studied and were found to be independent of the counterion present[41] (methylammonium in this case). A reduction in the coordinating capacity of the solvent causes an increase in iodine ion concentration which in turn leads to iodoplumbate ion formation[159] of PbI_3^- and PbI_4^{2-}. This behaviour enlightens the dissolution process and informs solvent selection further, as inhibition of these mechanisms by increasing the coordinating ability of the solvent may lead to customisation of the resulting morphological effects[114].

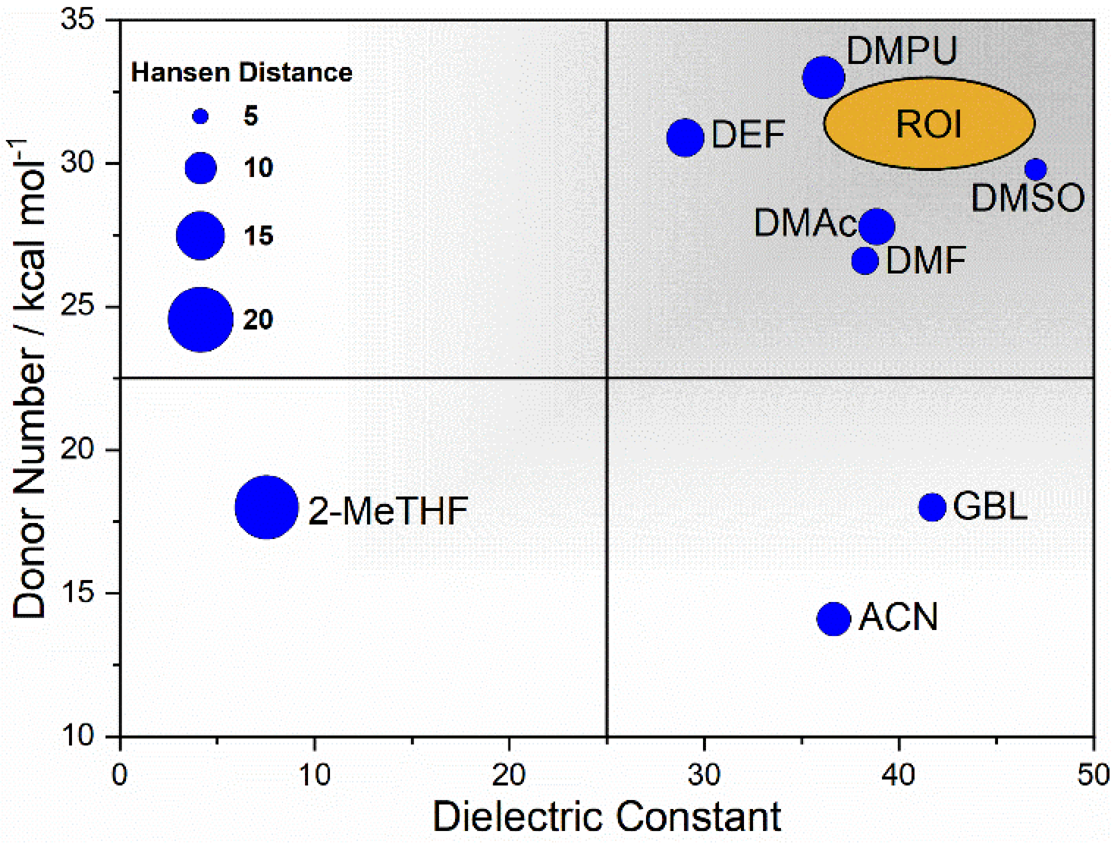

Figure 36 - Graphical representation showing both the dielectric constant and donicity of several solvents analysed in this study. The selected combination of DMSO and DMPU aims to combine the highest polarity and most strongly coordinating solvents available to dissolve high concentrations of PbI_2 needed for spin coating highly efficient $MAPbI_3$ films. The region of interest (ROI) defines the combined donicity and dielectric constant range for the chosen cosolvent system (DMSO/DMPU).

DMPU was chosen as a major constituent, effectively replacing DMF, due to the high donor number, along with an adequate dielectric constant – similar in magnitude to DMF. DMPU has previously been studied as a solvent additive with the observation that when used alone to dissolve the precursor materials the coordination of Pb^{2+} leads to a precipitate forming at room temperature[114]. We report this finding through our own studies but found the effect mitigated by adding as little as 10 vol% of DMSO. In order to capitalise on the increased coordinating ability offered by DMPU, the coordination chemistry of the solvated Pb^{2+} complex and the resulting colloidal configuration regarding the space demands of the solvent require further study. Studies suggest DMPU is a particularly space demanding solvent that coordinates lead in a holo-directed octahedral manner, whereas DMF preferentially coordinated in a hemi-directed configuration[160]. Figure 36 shows a graphical representation combining the desired properties of high donicity and dielectric constant with the region of interest (ROI) highlighted for a DMSO/DMPU cosolvent system.

In developing an alternative solvent system, we have utilised solvent characteristics ranging from the dielectric constant and HSP, the fluid properties of vapour pressure and boiling point, to the Gutmann donor number (D_N) and consideration of solvent space constraints and colloid configuration.

3.3.7 Laboratory Solution Manufacture – Qualitative Analysis

Having evaluated the literature and collected a toolkit of ‘green’ solvents. Attempts began to evaluate the efficacy of each solvent as a perovskite processing solvent. The aim of this stage was to mix perovskite precursor inks appropriate for spin coating functional $MAPbI_3$ layers.

3.3.8 Precursor Dissolution

Our initial solvent screening (1st generation) yielded negative results, with all solutions culminating in a perovskite precipitate, suggesting insufficient ability to dissolve and hold the precursor materials. These solvent candidates were used alone and in combination in several stages of testing to ascertain their ability to dissolve $MAPbI_3$ precursors. Table 4 provides qualitative data evaluating four generations of cosolvent systems. DMPU, showed promise during 1st generation testing, with 1mL solutions completely dissolved at 1.25 M concentration. Observations over time found that DMPU is inherently unstable, forming a solid phase[114].

Dimethylimidazolidinone (DMI), a homolog of DMPU, was also evaluated with lower observable dissolution of the precursor materials along with a precipitate forming after time exposure. Cyrene (Table 3) was also considered for cosolvent testing due to its promise as a bioderived alternative to traditional dipolar protic solvents. The results for cyrene, 2-MeTHF, and propanenitrile were similar in that black crystalline precipitate formed indicative of $MAPbI_3$ perovskite. These solvents were then excluded from individual use due to an inability to coordinate the PbI_2 and prevent the ‘crashing out’ of perovskite crystals in solution.

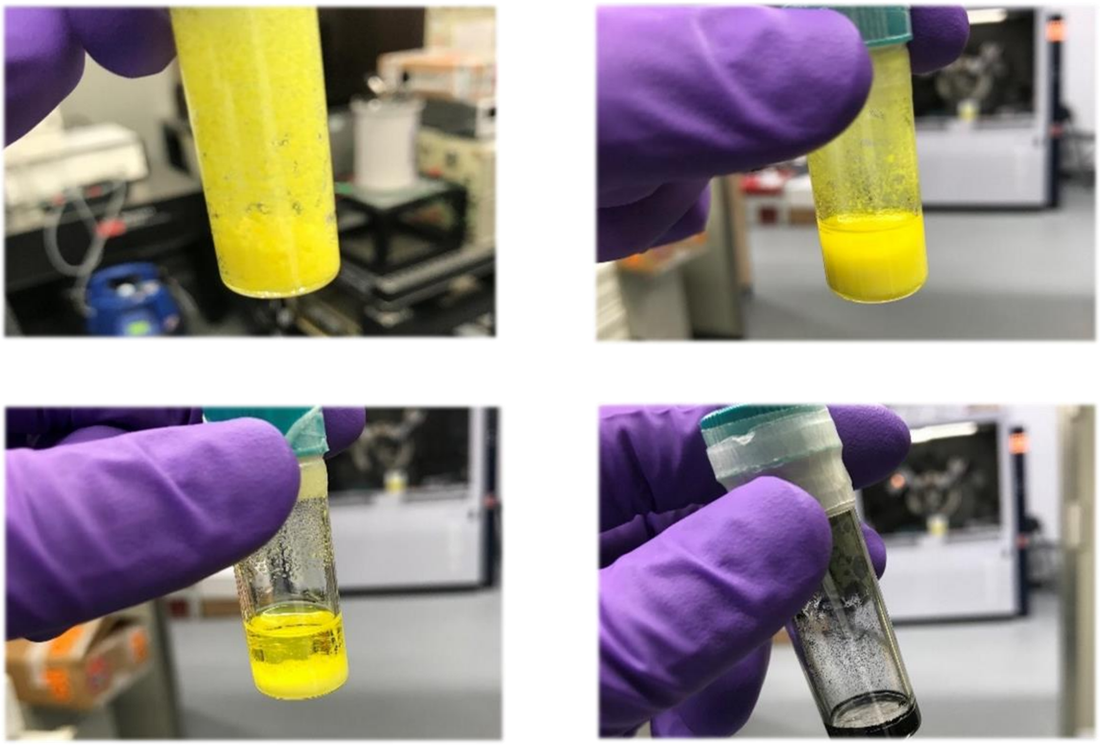

Figure 37 - Sample images showing unsuccessful attempts to formulate a 1.25M $MAPbI_3$ precursor solution through various undesirable reaction mechanisms.

Based on the initial ability to dissolve the precursors in 1st generation testing, 2nd generation testing involved inhibiting the formation of a solid phase resulting from strong over-coordination of DMPU[114], by addition of a cosolvent DMSO (Figure 37). Attempts were made to improve the prospect of using the green solvent cyrene through the addition of the highly polar and strongly coordinating solvent DMSO. However, this yielded no successful solutions. The 2nd testing phase culminated in the manufacture of films and full devices where possible to ascertain which solvents combinations to pursue. 3rd generation testing proceeded with the best performing systems of DMSO and DMPU from 2nd generation testing, where a tertiary additive was selected to improve performance. Lower vapour pressure or boiling point additives were selected to balance the high boiling point and low vapour pressure of DMSO and DMPU, in alignment with the characteristics of the DMSO/DMF system.

Table 8 Solvent systems evaluated in the initial screening in this study and results of attempts to create precursor solutions (Y - Yes, N - No, DT – dissolution temperature used, PD – precursor dissolution, STP – standard temperature and pressure, control – 80/20 v/v DMF:DMSO solution).

Solvent System @1.25M (MAI + PbI2) (vol%)	PD	DT °C	System Condition at STP	Major Characteristics of the Solvent System
100% Cyrene	N	-	Black precipitate solution, highly viscous	Black solid undissolved, potentially crashing out MAPbI3 crystals
100% DMPU	N	-	Crystalline solid forms over time	Initial dissolution. Over time the solution solidifies to a crystalline yellow solid, postulated to result from over coordination of the PbI2[114]
100% DMI	N	-	Crystalline solid forms	Dissolution appears weaker than with DMPU, solid forms over time
100% 2-MeTHF	N	-	Black precipitate solution – low dissolution	Less solvating power than cyrene with a similar black precipitate solution, some orange coloured solid observed indicating lead iodide still present
100% Propanenitrile	N	-	Black precipitate solution	Similar black precipitate that is present for cyrene and acetonitrile
20% Cyrene, 80% DMF	Y	60	Deep orange MAPbI3 solution	Very visible colour change to orange
20% DMPU, 80% DMF	Y	60	Yellow MAPbI3 solution	Equivalent solution to DMF/DMSO visually
20% Cyrene, 20% DMSO, 60% DMF	Y	60	Orange colour present – solution forms	Solution does form but orange colour returns during cooling over time
20% DMPU, 20%, DMSO, 60% DMF	Y	60	Yellow solution – similar colour match to control	Equivalent solution to DMF/DMSO visually
80% Cyrene, 20% DMPU	N	-	Solid forms	Reaction system causes solid to form, cyrene susceptible to strong bases
20% Cyrene, 80% DMPU	N	-	Solid forms	Reaction system causes solid to form, cyrene susceptible to strong bases
50% ACN, 50% DMPU	N	-	Foam like solid forms – fast rate	Quickly turns into a foam like crystalline lattice when spun with vortex
70% ACN, 30% DMPU	N	-	Crystalline structure and foam like solid present	Slower reaction rate but solid and crystals still form
10% DMSO, 90% Cyrene	N	-	Polymer like solid forms over time	Reaction occurs
20% DMSO, 80% Cyrene	Y	90	Solution also dark orange in colour	No reaction observed, strong orange red colour solution, quite viscous
30% DMSO, 70% Cyrene	Y	95	less viscous than above solution – crystals form at STP	No reaction observed, strong orange red colour solution, quite viscous
10% DMSO, 90% DMPU	Y	110	Yellow solution – higher apparent viscosity that control	Visually more viscous that control solution, good colour match
20% DMSO, 80% DMPU	Y	110	Yellow solution – lower apparent viscosity than above	Visually more viscous that control solution, good colour match
30% DMSO, 70% DMPU	Y	105	Yellow solution – lower apparent viscosity than above	Visually more viscous that control solution, good colour match
20% DMSO, 60% DMPU, 20% PPN	Y	95	Yellow solution, good match to control	Visually lower viscosity, possible miscibility issues
20% DMSO, 60% DMPU, 20% ACN	Y	100	Yellow solution with fine crystalline lattice present at STP	When cooled to room temperature overnight a crystal lattice forms. Needle type crystals (likely PbI2)
20% DMSO, 60% DMPU, 20% 2-MeTHF	**Y**	**95**	**Yellow solution mimics control**	**Visibly more viscous than the control, possible miscibility issues**

3.3.9 Initial Device Builds – Optimisation

Table 9 Gives an overview of solution development from candidate solvents to initial film deposition and device builds. Qualitative observations are included, this suggests that the approach was to effectively mimic the rheological properties of DMF. Third generation testing lead to the development of three competing systems. Propanenitrile, acetonitrile, and 2-MeTHF were selected as additives and the solutions evaluated as follows:

1) **20% DMSO, 60% DMPU, 20% PPN**
2) **20% DMSO, 60% DMPU, 20% ACN**
3) **20% DMSO, 60% DMPU, 20% 2-MeTHF**

Priority was given to the green nature of solvents, leading to the exclusion of propanenitrile containing solutions. Precursor solution stability was monitored for a period of 24 hours post dissolution. Due to the precipitation of PbI_2 crystals from acetonitrile containing solvent system, this was also excluded.

3.3.10 Third Generation Testing – Device Builds

The third generation testing phase, aimed at balancing the low volatility of the highly coordinative solvent system, was chosen as the starting point for film manufacture. Films were produced in accordance with the methodology presented in 3.2 Methodology.

Solvent System:

60 vol% DMPU, 20 vol% DMSO, 20 vol% 2-MeTHF

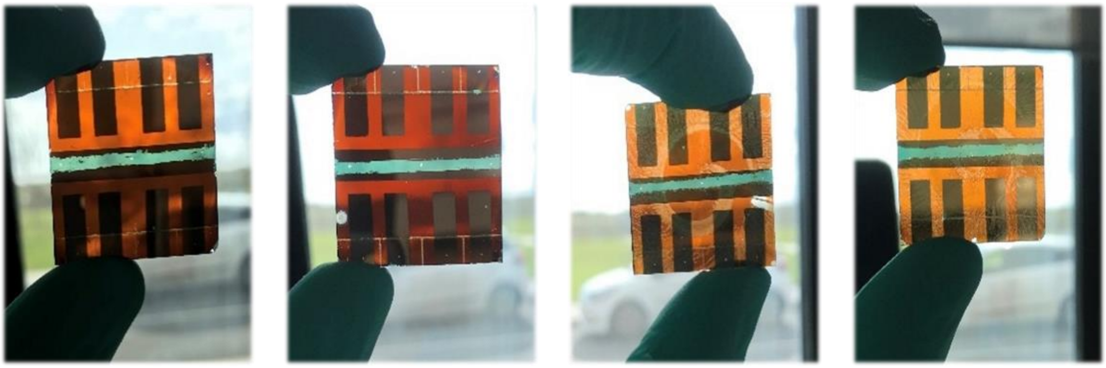

Figure 38 - Images of films cast from the DMF/DMSO system (left) and 60 vol% DMPU, 20 vol% DMSO, 20 vol% 2-MeTHF solvent system (right). The control samples show a specular finish with a characteristic spiral present on the experimental samples.

This initial spin coating system produced films with a characteristic spiral and light orange colour (Figure 38). Despite the visual defects present for these samples. A device build was able to manufacture functional films with fairly high reproducibility. Record efficiencies for these films reached 8-9% compared to a 13% DMF/DMSO device, providing proof of concept to continue the optimisation.

Table 9 - PSC performance with $MAPbI_3$ deposition using candidate solvent systems.

Solvent System	**Results/Hypothesis**
60 vol% DMPU, 20 vol% DMSO, 20 vol% 2-MeTHF	Best cell at between 8 and 9 % for all pixels. Appearance of cells more transparent and orange in colour. Poor annealing set up? Difficult to achieve a smooth finish during spin coating currently, streaks and a characteristic spiral usually present.
40 vol% DMSO, 20 vol% DMPU, 40 vol% 2-MeTHF in 1:1 mix with EtOH	New system that aims to increase miscibility of 2-MeTHF with ethanol addition – UNTESTED. Takes rigorous stirring at up to 75 °C to dissolve the precursor materials. Hopefully will lead to a more favourable evaporation of solvent.
40 vol% DMPU, 20 vol% DMSO, 40 vol% 2-MP	Efficiencies around 7% recorded for a single pixel, set against poor control cells. Appears to spin coat a much thicker and darker perovskite coloured layer with a mirror like smooth finish. System has been successfully utilised using just DMSO and 2-MP so lacking in originality unless DMPU significantly aids in device performance.
40 vol % 2-MeTHF, 30 vol % DMSO, 30 vol % DMPU	Known to dissolve precursor materials and deposit a functioning layer, low efficiency as of now.
40 vol% DMSO, 30 vol% DMPU, 30 vol% 2-MeTHF in 2:1 mix with EtOH	Known to perform to an efficiency of ~13%. Difficulty spin coating due to rapid crystallisation (this could be improved by optimising the anti-solvent drip time – earlier stage due to more rapid supersaturation?) but a promising solution none the less.
40 vol% DMSO, 30 vol% DMPU, 30 vol% 2-MeTHF in 1:1 mix with EtOH	Possible option to increase the solvating power of solution G whilst simultaneously decreasing supersaturation levels.
50 vol% DMSO, 20 vol% DMPU, 30 vol% 2-MeTHF in 1:1 mix with EtOH	Pending testing as a promising DMSO majority system. DMSO appears to evacuate the film more effectively than DMPU (see 40 vol% DMPU, 40 vol% DMSO, 20 vol% 2-MeTHF+EtOH 1:1) Also has achieved efficiencies up to 13.32% for a single pixel. Some crashing out observed as solution cools to room temperature. Higher Jsc achieved than lower 2-MeTHF higher DMPU systems.
50 vol% DMSO, 30 vol% DMPU, 20 vol% 2-MeTHF in 1:1 mix with EtOH	Pending the results of system above, could be preferential if solution crashes out at room temperature.
40 vol% DMPU, 40 vol% DMSO, 20 vol% 2-MeTHF+EtOH 1:1	Recently tested system, dissolution occurred with rigorous stirring alone at room temperature. Remains 'stable' at room temperature and deposited as such. Films formed were slightly more transparent/orange in colour compared to DMF/DMSO system. Record pixel of 13.94%, many pixels above 13% and some better consistency on several cells.
40 vol% DMSO, 30 vol% DMPU, 30 vol% 2-MeTHF in azeotropic mix with EtOH (taken from literature sources as 34 vol% EtOH and premixed essentially simplifying the system to 3 component)	As of 26/11/19 this system shows great promise due to its ability to solubilise the perovskite precursor materials at the same concentration as the control. Similar solutions tested with the MeTHF solution changing ratios – these have produced promising results. However, due to the formation of an azeotrope at 34 vol% EtOH in MeTHF, this has been used to better elucidate the solvent system crystallisation dynamics further down the line. Should a build with this system produce reproducible perovskite films of appreciable efficiency then this is the premier choice for publication.

3.4 Conclusion

Within this chapter, a review of literature surrounding perovskite solar cells has been presented. A screening methodology for green solvents has been proposed with reference to the IMI-CHEM 21 method. This EHS scoring system represents a large scale data collection effort to score solvents on a relative scale using metrics relevant to industrial adoption of green solvents[145]. The presented methodology provides ana analysis of commercially available green solvents with acceptable EHS scores as a stage in the selection process. Further stages are described – including a look into the relevant literature surrounding the technical aspects of perovskite dissolution and subsequent crystallisation. This outlines key parameters to expect from a solvent and how these parameters may be harnessed to achieve specific deposition requirements. This has been done with a focus on the most common perovskite precursor materials (PbI_2 and MAI). This provides a tool kit of green solvents and their application to perovskite development upon which the remainder of this thesis aims to expand, furthering the sustainable development of this burgeoning solar technology.

Solvents tested within this chapter include the novel ‘green’ solvent Cyrene, which ultimately failed to coordinate the PbI_2 component, DMPU and DMI – promising low volatility highly coordinative solvents, and 2-MeTHF – a replacement for the toxic tetrahydrofuran (THF). The high volatility and benign nature of 2-MeTHF along with the high coordination ability of DMPU suggested that a multicomponent system could be utilised to replace the volatile and coordinative solvent DMF – the ultimate aim of this study. The technical aspects of solvent-solute $MAPbI_3$ perovskite dissolution, including the donicity of the solvent, the partial vapour pressure, and the dielectric constant, have been discussed. The ideal $MAPbI_3$ solvent has been proposed to exhibit coordination and dissolution of the PbI_2 precursor at a minimum of 1.5M, high vapour pressure, and low boiling point for expedient solvent removal and nucleation initiation. A toolkit of solvents attempts to mimic the desirable properties of DMF as part of a multi-component system – with each contributing a desired technical ability.

To prove the concept of this methodology an application driven use case is presented, which outlines a potential set of solvents that were put through an initial screening procedure (dissolving MAI and PbI_2). This was then trialled through several iterations of cosolvent addition with the qualitative observations reported for each cosolvent combination. Through this trial-and-error method an initial set of solutions was developed and used to fabricate perovskite devices. Whilst low efficiencies were obtained initially, the results suggested promise for further optimisation.

The conclusion of this work is an application driven selection methodology – grounded in both technical and environmental, health and safety (EHS) considerations – that has been applied to successfully design an alternative solvent system with higher donicity and lower EHS concerns than the DMF/DMSO standard.

Prifysgol **Abertawe**
Swansea University

Chapter 4 – Sustainable Solvent System Optimisation and Characterisation

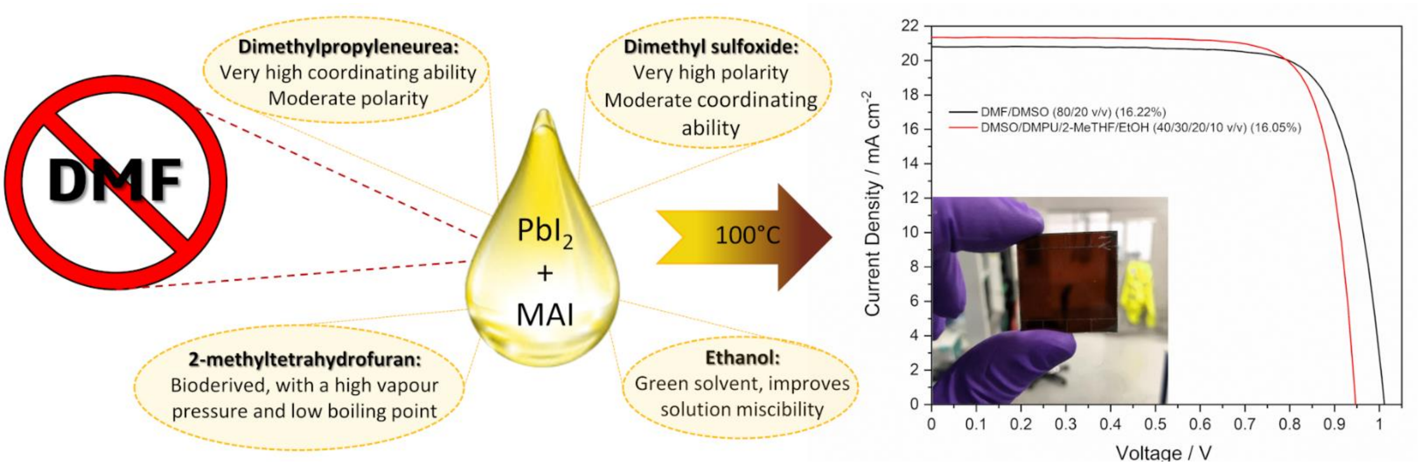

Part of this work has been published in the journal *Green Chemistry* titled:

‘Sustainable Solvent Selection for Methylammonium Lead Triiodide ($MAPbI_3$) Perovskite Solar Cells[106]*’*

A. J. Doolin, R. G. Charles, C. S. P. De Castro, R. G. Rodriguez, E. V. Péan, R. Patidar, T. Dunlop, C. Charbonneau, T. Watson and M. L. Davies, *Green Chem.*, 2021, **23**, 2471–2486.

4.1 Introduction

This experimental chapter expands on the previous chapter, focussing on the optimisation and photochemical characterisation of novel $MAPbI_3$ perovskite films cast from experimental precursor solutions. Morphological studies are also displayed with SEM and XRD analysis to assess changes the microstructure resulting from the varied solvent properties. Through optimisation of alternative systems, a greater understanding of the impact of solvent parameters can lead to rapid advancement. Adoption of alternative green methodologies hinges on the performance of the system relative to well optimised controls. Expanding on newly developed systems at an early stage of development presents an opportunity to compete with established methodologies and gain wider adoption within the research zeitgeist.

4.2 Experimental Methods

4.2.1 Manufacture of devices

All devices were manufactures in a glovebox environment unless otherwise specified. The device and film fabrication are listed in the methodology (2.1 General Procedure for the Manufacture of devices). Alternative compositions, including a 5% PbI_2 excess are specified where necessary.

4.2.2 Precursor Solution - $MAPbI_3$

Precursor preparation for the $MAPbI_3$ can be found in 2.1.1 Precursor Solution - General $MAPbI_3$ Fabrication. Heating at 60°C and rigorous mixing was applied to the DMF/DMSO $MAPbI_3$ solution to aid precursor dissolution. For the candidate A-C solutions evaluated, heating at 80°C was applied, along with rigorous mixing until the complete dissolution of the precursor materials.

4.2.3 Substrate Cleaning

Substrates were cleaned as per 2.2 Substrate Cleaning.

4.2.4 Electron Transport Layer – SnO_2

A tin oxide solution was prepared according to 2.1.4 Electron Transport Layer Preparation – SnO_2. For the final device builds presented in section 4.3, one hour UV-Ozone treatment was applied to the electron transport layer (ETL) substrate to reduce hysteresis[101].

4.2.5 Perovskite Deposition - Glovebox Devices

Cleaned substrates were transferred to a glovebox for perovskite deposition. The one step deposition method was used to spin coat $MAPbI_3$ solutions onto substrates with an anti-solvent drip of ethyl acetate (EA) to initiate nucleation and crystallisation growth of the film. For the reported control solution (DMF/DMSO 80/20 v/v), spin coating setting of 4000 rpm, 4000 acceleration for 30 seconds were used. 200 µL of ethyl acetate was dropped onto the sample 7 seconds from the start of the spin cycle.

Samples were then placed on a hot plate at 60°C and ramped rapidly to 100°C for 10 minutes to anneal.

4.2.6 The Prenucleation Strategy

The DMF/DMSO spin coating regime is a highly optimised strategy. The timing of the antisolvent drip is very precise with the aim of forming a DMSO-adduct as a wet film prior to annealing. For a new solvent system, this regime is not optimal as the solvent properties are significantly changed. The prenucleation strategy used is detailed in 2.3.1 Perovskite Deposition - Glovebox Devices.

Hole transporter encapsulation was carried out as described in 2.3.2 Hole Transport Layer, without the use of FK209 as a dopant during these investigations. 2.3.3 Top Contact Evaporation was followed to complete devices with a gold top contact.

4.2.7 UV-Vis-NIR Spectroscopy

Both unencapsulated (FTO/PAL) and Encapsulated (FTO/PAL/PMMA) $MAPbI_3$ films were measured on a Perkin Elmer Lambda 9 UV-Vis-NIR spectrometer. The scan range was set between 200nm to 800 nm, with a scan speed of 960 nm/s and a step change of 1nm. Data was recorded in Transmittance unless otherwise specified and converted into absorbance *via* application of the beer lambert law as per the methodology 2.4 UV-Vis-NIR Spectroscopy equation (1).

4.2.8 Fluorescence microscopy (Edinburgh Instruments FS5)

As these films were made in ambient conditions, the EA anti-solvent drip timing was changed to 15s from the start of the cycle (from 7s) for the control with the 'prenucleation' strategy remaining as described. Absorptance and fluorescence measurements of thin films were made using an Edinburgh instruments FS5 spectrofluorometer, with the standard thin film sample holder; the integrating sphere unit was used to measure absorptance. Fluorescence (excitation wavelength of 450 nm) was measured using an integrating time of 0.2s and 3 nm excitation and emission slits. Measurements were taken on films in the absence of the transport layers and contact (*i.e.* FTO/$MAPbI_3$/PMMA). This stack was manufactured in ambient conditions with the poly(methyl methacrylate) (PMMA - Sigma Aldrich, average molecular weight ~120,000 by GPC) layer spin coated onto the perovskite film to prevent environmental degradation during the measurement. PMMA (1:1 by weight with toluene) was deposited *via* spin coating at 3000 rpm (3000 acceleration) for 30 seconds, followed by a 3 minute anneal at 70°C. For consistency, samples were placed in the dark sample holder prior to measurement for 2 minutes.

4.2.9 Mitigating Photobrightening

Perovskite materials are known to exhibit greater levels of PL emission after they have been exposed to light. This effect is known as photobrightening. Understanding this mechanism is important for spectroscopic studies of alternative perovskite solvent systems due to differences in the photobrightening rate after films have been cast from alternative formulations. To accurately assess the PL properties of novel films, a light soak may be used – exposing the sample to light until the PL remains consistent. This is a typical approach for measuring device JV. However, multiple PL scans may also be taken to gain as much information as possible as to the PL behaviour of the novel film. This combined approach has been used in this section with Figure 39 a representative example of 3 separate films scanned until the PL stops increasing in intensity. The relative difference in intensity ratio is therefore based upon a 'brightened' film for the purpose of comparison.

To achieve this repeat measurements were used as described in 2.5 Steady State Photoluminescence (Edinburgh Instruments FS5). Measurements were taken with a 2.5-minute delay of light exposure between scans until the scans converged and were deemed 'stable' (see Figure 39 for candidate A solution multiple scan results).

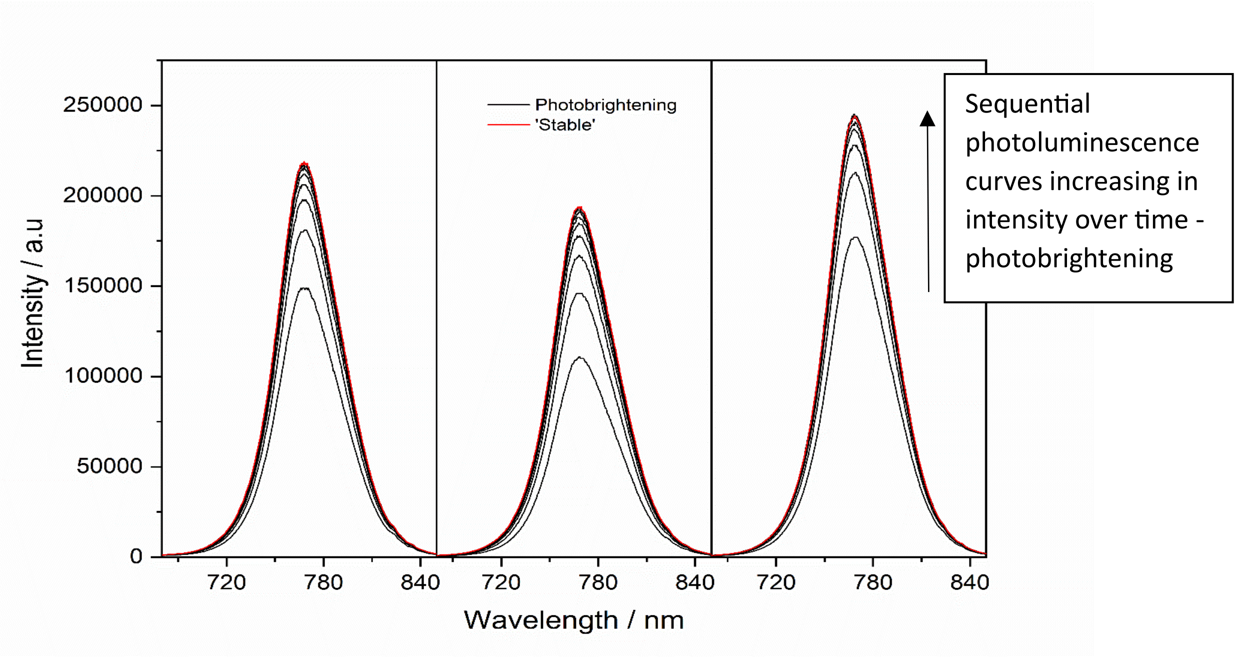

Sequential photoluminescence curves increasing in intensity over time - photobrightening

Figure 39 - Experimental SSPL data curves for the candidate A average SSPL curve and standard deviation spread. A – 9 scans taken with 'stable' curve emission scan. B - 9 scans taken with 'stable' curve emission scan 9. C – 10 scans taken with 'stable' curve emission curve 10. PL emission increases to a stable value as measurements are repeated.

4.2.10 Additional Filters

For certain scans directly into the perovskite, a 450 nm excitation is selected to mitigate the effect of varied film thickness, common for alternative solvent systems.

When exciting with 530 nm, a 520 nm band pass filter is used, with a 611 long pass for all compositions presented in this chapter (triiodide perovskite).

4.2.11 The Integrating Sphere

Absorptance scans were taken using the same sample architecture in the integrating sphere. Slit widths of 2.5 nm on the excitation and 0.25 nm on the emission were used for both the blank sphere scan and with the sample in the direct position. A synchronous scan was completed first on the blank sphere over the wavelength range 450-850 nm providing a baseline measurement. The presented absorptance curves were attained through linear interpolation between the original data points, then smoothed using the Savitzky-Golay method with 6 points in window and a polynomial order of 3 (on OriginPro, 2020b).

4.2.12 X-Ray Diffraction (XRD) Analysis

XRD measurements were performed using a Bruker D8 Discover in a standard divergent slit set-up. The sample architecture used FTO/SnO_2/$MAPbI_3$/PMMA, with the SnO_2 deposited in class 6 clean room conditions followed by $MAPbI_3$ deposition in a nitrogen glovebox environment. The build procedure mimicked the device manufacture simply omitting the HTL for PMMA. The scan range was set from 5-60° and the measurements taken using a 40kV, 40mA Copper source with a step size of 0.04°, at 1 second per step. Origin peak analyser was used to find the full width at half maximum for the 110, 220, and 310 tetragonal $MAPbI_3$ peaks. This was done by subtracting the baseline and integrating 0.5 degrees either side of the peak.

4.2.13 Scanning Electron Microscopy (SEM) Imaging

SEM images were taken using a JEOL 7800F FEG-SEM with 30,000× magnification. 5,000×, 10,000×, 15,000× images are available in Figure 52-55. Post processing is detailed in 2.7.1 Zen Blue Intellesis – Machine Learning Based Segmentation Analysis.

4.2.14 Profilometry

Film thickness was measured according to 2.8 Profilometry.

4.3 Results and Discussion - Optimised Candidate Solutions

The fourth generation of solvent system testing aimed to improve device PCE through solvent ratio and miscibility tuning. The evaluation of these solvent systems is given in Table 10. From the trials 3 candidate solutions (A, B, and C) were selected for further analysis, each contain 40% DMSO where the % composition of DMPU, Me-THF and ethanol are varied. Multiple candidate solutions were formulated based on a core combination of DMSO and DMPU, an historic alternative dipolar aprotic solvent with a high coordination ability as defined on the Gutmann scale as 33 kcal mol^{-1} compared to 29.8 kcal mol^{-1} for DMSO and 26.6 kcal mol^{-1} for DMF[142]. Of the lower coordinating 'green' solvents 2-methyltetrahydrofuran (2-MeTHF) and ethanol (EtOH), 2- MeTHF can be biologically derived[161] and was selected for high vapour pressure; with EtOH added to improve the miscibility of 2-MeTHF with DMSO/DMPU whilst simultaneously increasing solution supersaturation. This provides a degree of flexibility in developing an efficient solvent system for a given manufacturing procedure.

The concentration of the precursor solution was fixed at 1.25 M for the purpose of spin coating as this is commonly used. The dissolution and coordination of the precursors in the candidate systems is directly dependent on the DMSO/DMPU cosolvent combination. At this concentration, the lowest the DMSO/DMPU ratio possible with successful dissolution was the given ratio for candidate A and B (70% of the total volume). <70% total volume adversely impacts the ability to form a spin coat-able solution in a reasonable time window. The ratio of 2-MeTHF and EtOH has been varied to explore the impact of their respective rheological properties. Candidate C consisted of additional DMSO/DMPU to ascertain the impact of increased coordinative bulk solvent on the produced films with the benefit of increased solution stability and ease of processing. Table 10 outlines the system compositions, dissolution temperature and major characteristics.

Table 10 - Table showing optimised solvent systems for further characterisation (Y - Yes, N - No, DT – dissolution temperature used, PD – precursor dissolution, STP – standard temperature and pressure, control – 80/20 v/v DMF:DMSO solution).

Solvent System @1.25M (MAI + PbI2) (vol%)	**PD**	**DT (°C)**	**System Condition at STP**	**Major Characteristics of the Solvent System**
Candidate A (A01) 40% DMSO, 30% DMPU, 20% 2-MeTHF, 10% EtOH	Y	80	Yellow solution, improved viscosity match to control	Remains a yellow solution upon cooling. Slight stochiometric differences between PbI2 and MAI can cause PbI2 to crash out of solution
Candidate B 40% DMSO, 30% DMPU, 15% 2-MeTHF, 15% EtOH	Y	80	Yellow solution	Some lead iodide precipitate upon cooling to STP over time
Candidate C 40% DMSO, 40% DMPU, 10% 2-MeTHF, 10% EtOH	Y	80	Yellow solution, slightly higher viscosity than A and B	Precursors remains ‘stable’ in solution at ambient temperature

4.3.1 Optimisation of Manufacture and Characterisation Techniques

Beginning with the candidate A solution. This section focusses on the identification of differences between films manufactured in ambient conditions and a nitrogen filled glovebox.

4.3.2 Comparison of PL for Candidate A solution vs DMF/DMSO For Glovebox Samples vs Ambient Conditions – FTO/SnO2/PAL/PMMA

Substrates were prepared in accordance with the methodology, with differentiation starting during perovskite deposition. For candidate A, the A01 system, samples the spin coating regime remains the same between environments. DMF/DMSO samples were fabricated in ambient conditions with an antisolvent drip 15 seconds from the start of the sample. For the glovebox conditions this moves to 7 seconds from the start as per optimised procedures. For this investigation all samples were manufactured on FTO/SnO_2 substrates and subsequently coated with 1M PMMA in the respective environment (ambient lab or glovebox (GB)). This was done to mimic the build procedure typical of a device build, especially with respect to the influence of deposition on the ETL surface an opposed to glass, mitigating differences due to surface roughness, wettability etc. Three samples of DMF/DMSO $MAPbI_3$ and A01 $MAPbI_3$ were manufactured in the GB and encapsulated. Following this, two further substrates were taken into ambient conditions for perovskite deposition with the same precursor solution.

4.3.3 UV-Vis-NIR Spectroscopy

Figure 40 shows transmittance data for each of the experimental $MAPbI_3$ samples was converted into absorbance, with differences highlighted between samples fabricated in a glovebox environment and ambient conditions. Average values have been generated and plotted within Figure 41.

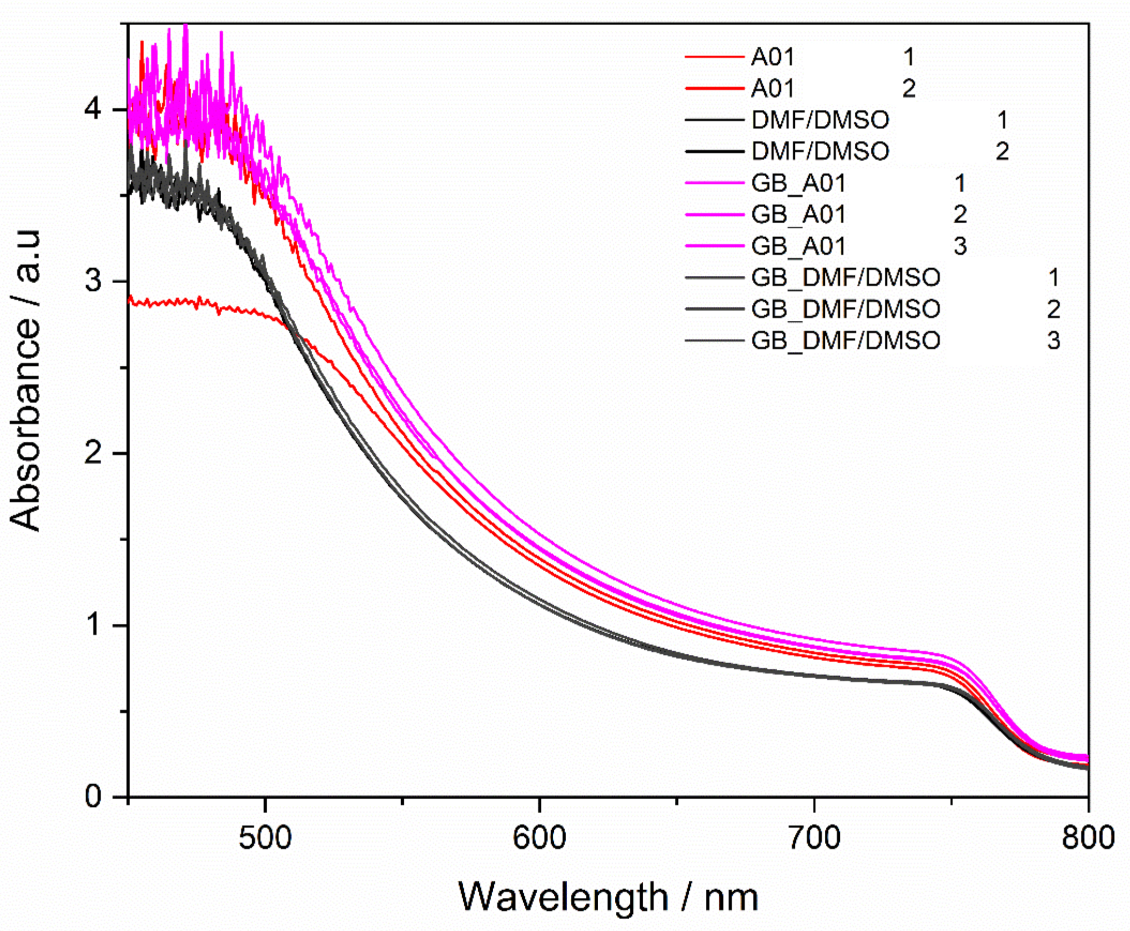

Figure 40 - Data for each $MAPbI_3$ sample was collected in transmittance before transformation using the beer lambert equation explained in the methodology (2.4 UV-Vis-NIR Spectroscopy).

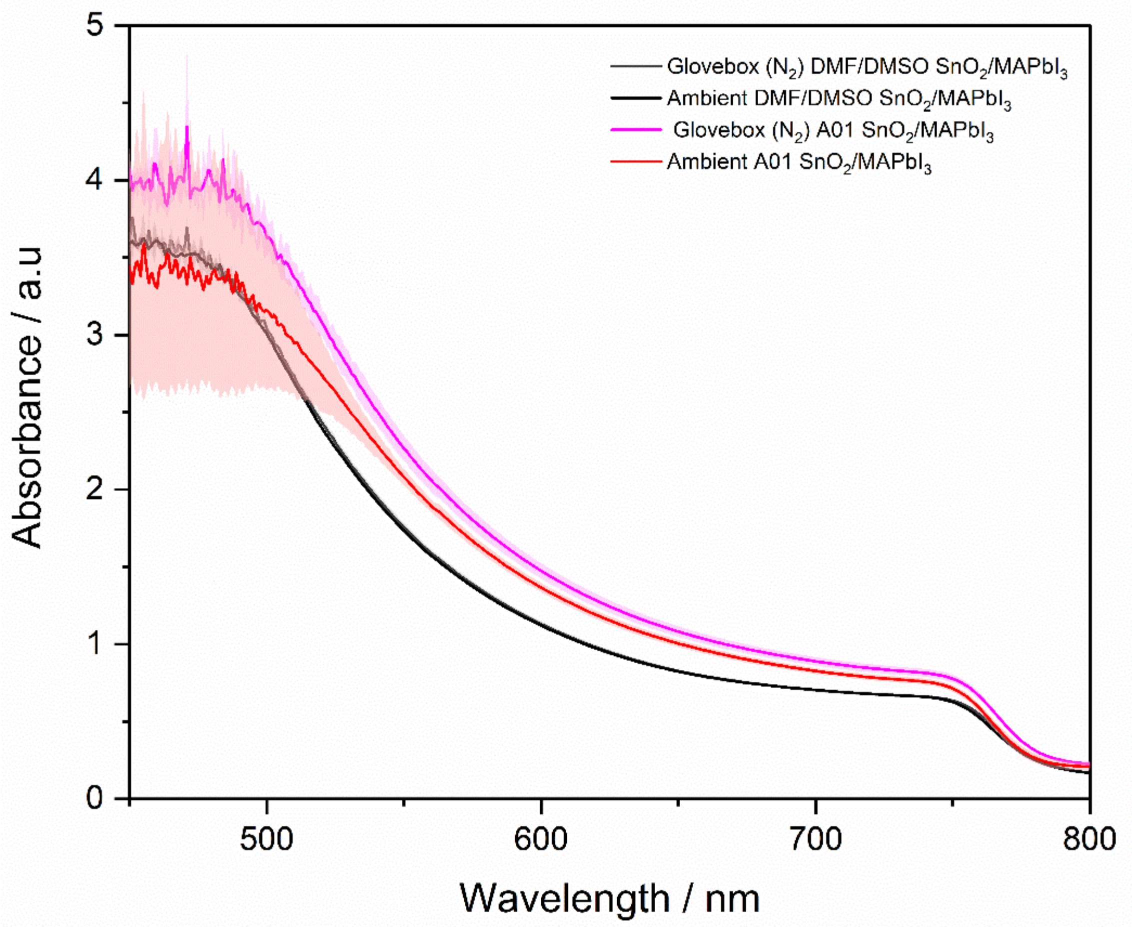

Figure 41 - Average of 5 samples of candidate A and DMF/DMSO samples. 3 samples each manufactured in nitrogen conditions in a glovebox. Two ambient films were also cast from the same solutions. STDEV is represented by the shaded area.

Analysis of this data shows little change in the absorbance properties of DMF/DMSO $MAPbI_3$ regardless of deposition technique. With A01 $MAPbI_3$ showing a higher absorbance for all samples, even when compared to specular high-quality controls, slight variations appear to be present. The glovebox manufactured A01 films have the highest absorbance overall.

Figure 41 shows this effect through average absorbance + standard deviation from the mean plots. Figure 40 does suggest that for the A01 system, an ambient sample can perform to a similar degree but may also be more likely to contain defects.

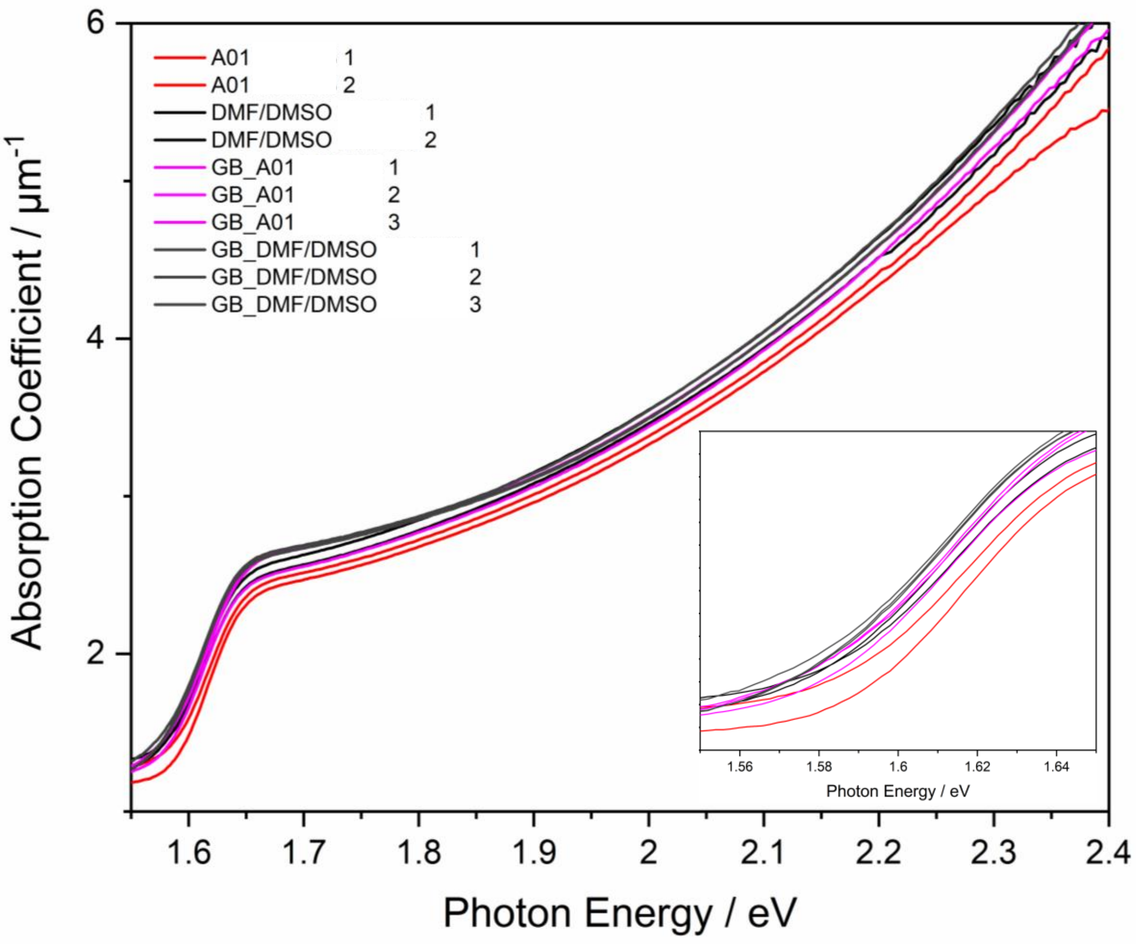

Figure 42 - Plot created through use of the Tauc relation and the respective thicknesses of $MAPbI_3$ films produced from each solvent system (as measured through profilometry).

Although only an estimate, by analysing the onset of absorption from these samples we can glean preliminary information regarding the likely bandgap of the material. Reflectance in not accounted for in this model, with the films very specular. Figure 42 shows the expected band gap (E_G) extrapolation to be marginally narrower for the DMF/DMSO solution. Higher variability, also still minor, is also observed for A01, with the control samples maintaining high levels of reproducibility. Ambient A01 samples indicate the widest E_G, with the difference measured in tens of milli volts. Charge carrier recombination from deep within the band tail, defined as a density of states extending into the band gap and caused by structural or thermal disorder[162] may be responsible for an increase in E_G of this magnitude[163]. The GB A01 samples appear to show a similar narrow E_G displayed by the DMF/DMSO film of ~1.55 eV. Overall, trends are visible highlighting minor changes to the material, both *via* changing solvent composition and fabrication environment. These changes are, however, unlikely to have a substantial impact on device or thin film characterisation.

4.3.4 Steady State Photoluminescence

As these samples were fabricated as ½ of a full device. The photoluminescence at steady state was also investigated. A functional ETL is present beneath the absorber leading to the expectation of successful quenching of the PL signal. Samples were measured through the glass/TCO side, with λ_{ex}= 560 nm.

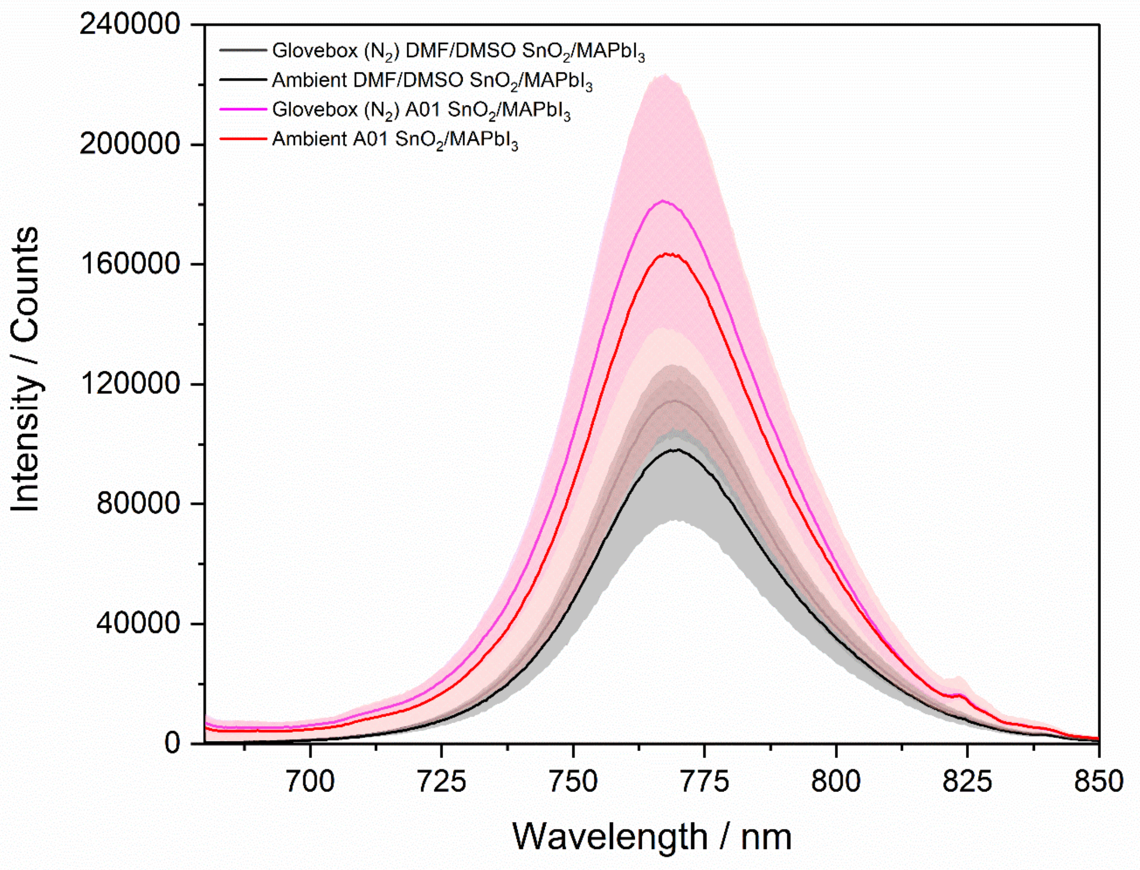

Figure 43 - Steady state photoluminescence uncorrected spectra taken from ITO/SnO2/PAL samples prepared in a glovebox (N2) environment to mimic conditions present within a device build. Curves represent the mean average with the shaded region representing 1 standard deviation from the mean. A 3.3 nm slit width was used on both the excitation and the emission.

The individual curves for DMF/DMSO remain fairly consistent for all samples, with intensity differences expected. The A01 solution again shows high variability with an ambient film showing equivalent emission (to the glovebox samples) and also the highest degree of quenching. The ½ device comparison suggests the difference in PL emission from films manufactured in a glovebox is small, with potential variation (introduction of defects) higher in ambient devices. The difference in magnitude between glovebox sample average and their respective ambient counterparts (for both A01 and DMF/DMSO) is quite reproducible, representing a shift of 10%. As these films were manufactured on SnO_2 the ambient films tend to quench to a higher degree. During the glovebox manufacture, the substrates are treated with UV-Ozone prior to deposition. This provides a charge to the tin oxide surface in the addition of hydroxyl groups which in turn improves the wettability[101]. It is possible that solvent vapours within the glovebox adsorb to the surface prior to deposition when the concentration is high (without sufficient purging prior to deposition). This should be accounted for through a rigorous purge procedure during device builds.

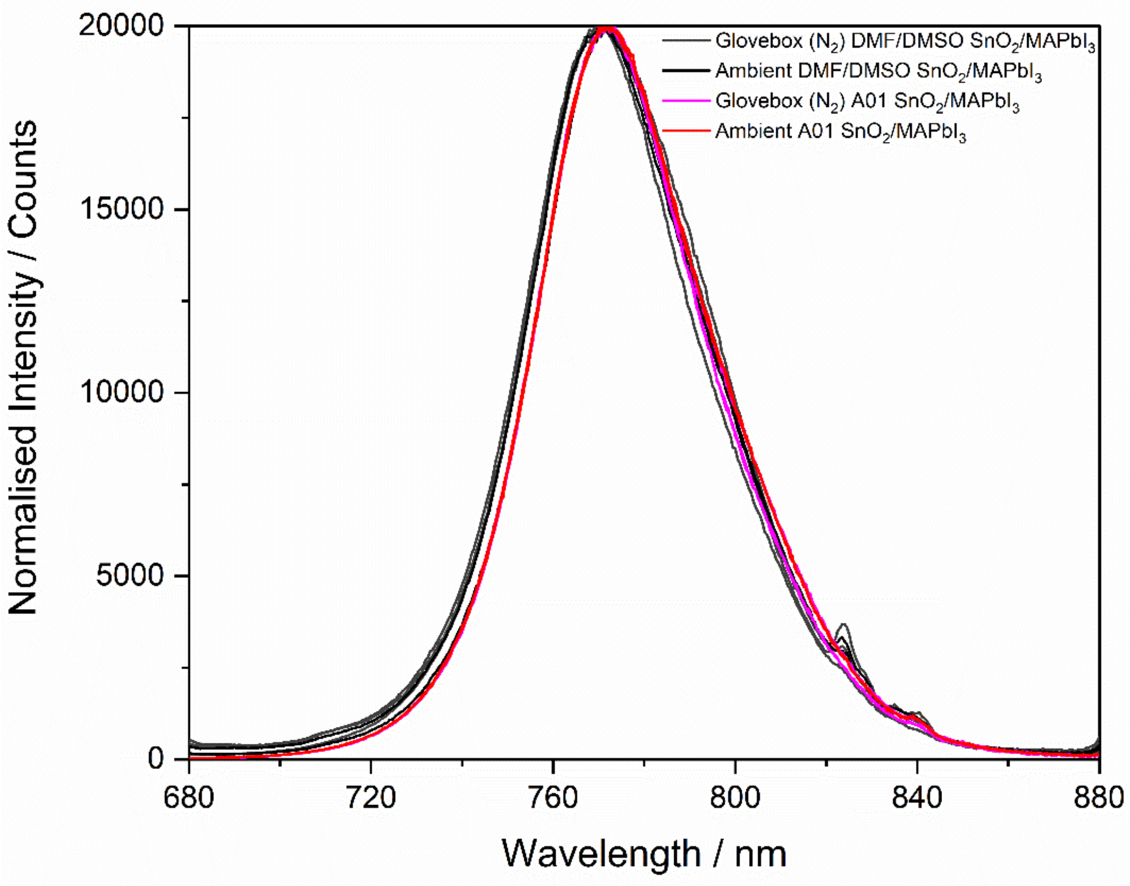

Figure 44 - Normalised spectra for the films, slight red shift observed for candidate A solutions.

The spectra were normalised to compare peak position (Figure 44). This is a compositional shift between solvent systems and appears unaffected by the manufacturing conditions. First glance suggests a minor red shift for the candidate A films, however, peak analysis agrees broadly with observations made using the absorption coefficient plot. This difference in peak position and relative curve position is due to a minor shoulder on the rise of candidate A films. Ultimately, the peaks are very comparable and show good agreement that the novel $MAPbI_3$ perovskite film possesses similar properties to that deposited from DMF containing precursors. Small peaks are present in the scan at ~825 nm. This is anticipated to be artefacts from the Zenon lamp used in the absence of additional filters. For future characterisations manual filters should be employed to avoid these effects. This will lower the excitation to 530 nm (instead of 560 nm) and employ a 520 nm band pass on the excitation along with a 611 long pass on the emission.

4.3.5 Photoluminescence Peak Analysis

Table 11, shows the results of a peak analysis to determine the full width at half the maximum (FWHM) of the peak intensity. The relative peak intensity has been calculated for each respective peak position.

Table 11 - Sample Photoluminescence Analysis for the FWHM

Sample	FWHM (1.s.f)	Peak Position (nm)	Relative Emission Intensity (a.u)
Glovebox DMF/DMSO SnO_2 $MAPbI_3$	41.2	769.5	6
	42.1	769.0	5
	40.7	770.0	9
Ambient DMF/DMSO SnO_2 $MAPbI_3$	42.0	770.0	8
	41.9	769.5	10
Glovebox A01 SnO_2 $MAPbI_3$	40.8	768.0	1
	44.1	767.0	3
	44.6	767.0	4
Ambient A01 SnO_2 $MAPbI_3$	42.3	767.5	2
	41.2	769	7

The FWHM represents the broadness of the emission peak. This has been linked with an inhomogeneous material, giving rise to an increase in defect sites, whether point defects or vacancies, or more structural disorder defects. These defect sites serve as traps for excited carriers which then may relax towards the ground state through the emission of phonons in a process known as non-radiative Shockley-Read-Hall (SRH) recombination[164]. Though small in magnitude, the A samples suggest a higher FWHM and wider E_G. This in conjunction with the previously theorised absorption band edge shift (Figure 42), further supports the slight increase in band tail states within Candidate A samples. The existence of these states would increase radiative recombination, as evidenced by increased PL and due to the thermalisation of carriers into the tail state[162]. Non-radiative SRH recombination will also be increased resulting in spectral broadening of the PL and red shift in the band gap. All samples appear to show a stokes shift when compared to the absorption band edge, with the peak height recorded widening the E_G from ~1.55 eV to ~1.61 eV. This effect appears most pronounced for GB A01 samples but is thought to be caused by the instant excitation of absorption, before lattice relaxation occurs, in contrast to emission recording a post relaxation condition in the sample[165].

4.3.6 Quenching Comparison

A final comparison was done with a sample on glass and a sample on a tin oxide substrate. Due to the properties of the ETL, it is expected that the PL will quench as the charges are extracted, lowering the magnitude of radiative recombination within the film. Candidate A $MAPbI_3$ ordinarily an emission several times higher than DMF/DMSO solutions. Figure 45 shows this case for an emissive A deposited film. With the ETL in place the PL is significantly quenched. The DMF/DMSO film also suggests a high degree of charge extraction as expected. However, due to the magnitudes involved and the degree of variability, care should be taken from a standalone analysis. While this trend is repeatable, it is also possible that the quenched PL of the candidate A film may be higher than a non-quenched DMF/DMSO film (in Figure 45 we see a marginal increase). This indicates a significant amount of radiative recombination even within a quenched film.

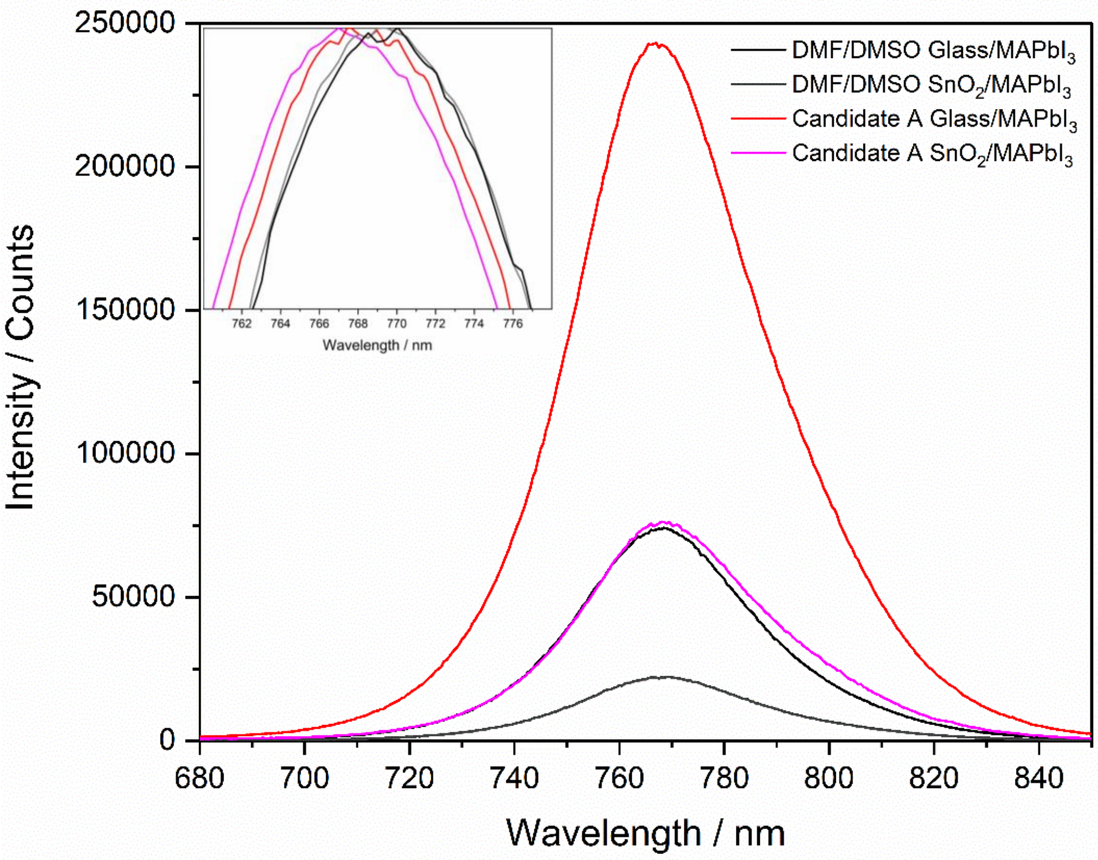

Figure 45 - Stabilised curve taken from 5 individual emission scans for samples manufactured as: FTO/ $MAPbI_3$/PMMA and FTO/SnO_2/$MAPbI_3$/PMMA. This shows high levels of quenching for both films. All films for this analysis were manufactured in a glovebox with capping under N_2.

4.3.7 Ambient vs Glovebox Fabrication - Conclusion

A further consideration for the comparison ambient vs glovebox builds is the presence of moisture and oxygen within ambient build conditions. We have already discussed issues of solvent vapour potentially causing damage and degradation pathways in glovebox conditions; however, this should be controlled in a glovebox environment. There is a lack of control over environmental impact of ambient manufacture. Evidence suggests it is possible to formulate high quality films, but that this may be less likely and the results more variable than glovebox manufacture. It is also worth noting that degradants such as moisture can also be transferred into the final perovskite film through the precursor solution as well as humid air. There is some debate over the impact of moisture on perovskite films, with initial studies suggesting this represents an avoidable degradation pathway[166]. Other studies show that moisture may be beneficial to perovskite grain formation[167]. Ultimately, with the aim of improving the stability of perovskites through solvent engineering techniques, it is vital to understand the impact of moisture on perovskite devices[168]. As a result of this investigation, the manufacture of devices will be done under N_2 to reduce variability in defects. Films for the purpose of characterisation will be made in both environments depending on the nature of the investigation; however, this will be specified. The impact of moisture should be noted for all candidate films due to inclusion within the precursor (EtOH) when compared to the anhydrous solvents used for the control samples.

4.3.8 Optical and Photoluminescent Characterisation of Perovskites

Having successfully formed stable $MAPbI_3$ precursor solutions the optical and morphological characteristics of spin coated films were studied.

Films manufactured from the 3 candidate solutions, show similar absorptance to the control (deposited from DMF/DMSO) with a very slight shift in the band gap position for films manufactured from candidates A and B (Figure 46). This is less apparent in the photoluminescence spectra; all films show a similar maximum emission wavelength (768 nm), with only ±1 nm between the average maximum emission wavelength of samples (from the measurements of 3 films per sample, see Figure 39). Care is needed in assigning significant differences between these samples to these slight changes in band-gap and maximum emission wavelength, especially given the highly sensitive nature of the photoluminescence from perovskite samples in ambient conditions[103], these slight differences are likely due to the differences in crystal size.

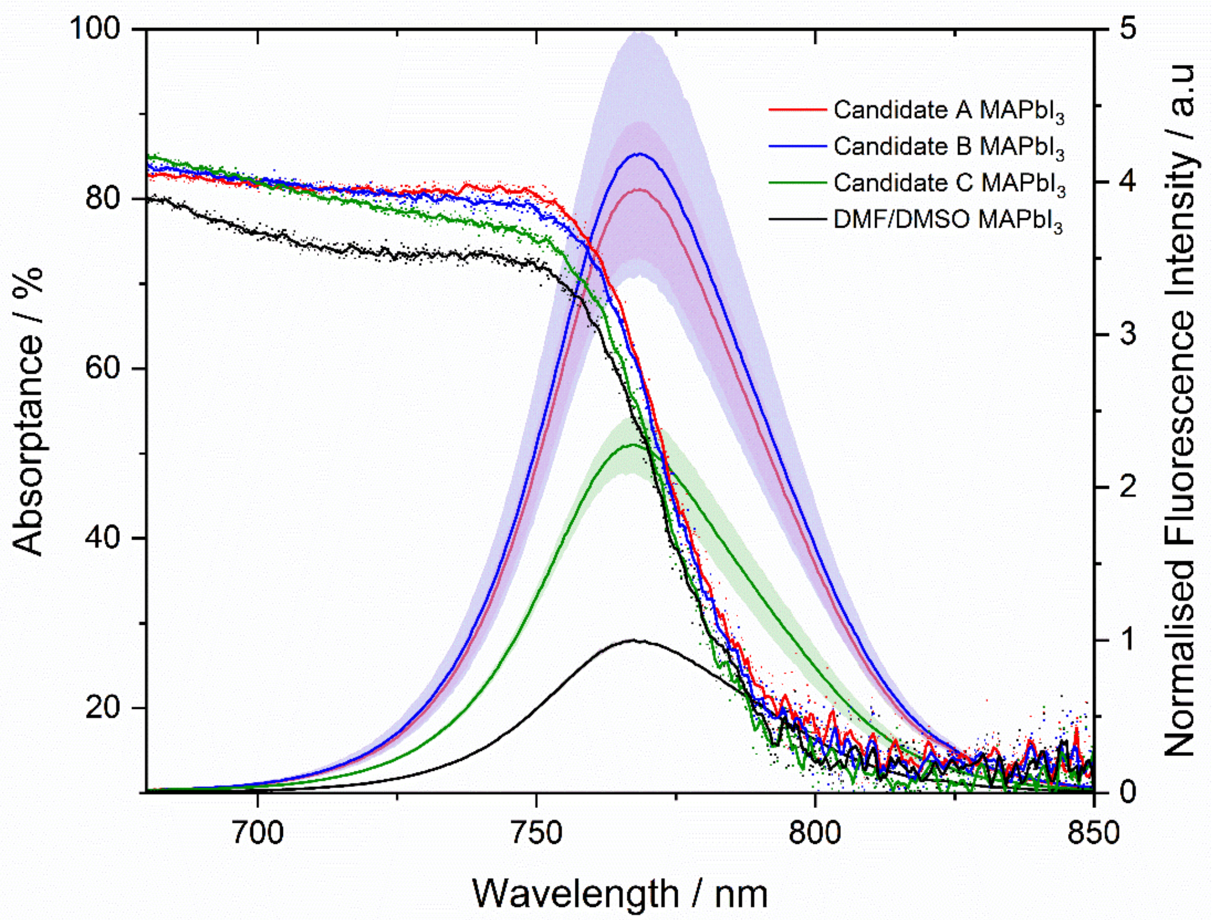

Figure 46 - Absorptance and photoluminescence - excitation wavelength (λ_{ex} 450nm) for each for films manufactured in ambient conditions from the control and candidate solvents. Three films per solution were evaluated, 3 nm excitation and emission slit widths and repeat measurements under constant illumination were used to mitigate the effect of photobrightening. All curves have been normalised to the maximum value of the control PL curve. The final 'stabilised' curve was used for each sample to create the average curve. The standard deviation of each sample set is displayed as the shaded region. (Film thicknesses were determined through profilometry with mean average values of: 366, 487, 492, and 365 nm for the control, A, B, and C).

The three candidate films show slightly higher absorptance and significantly higher photoluminescent intensity, it is worth noting that the absorptance varies less between samples at the excitation wavelength for photoluminescence (PL) measurements (Figure 47) and thus the higher PL is not only due to higher absorptance. Since these are thin-films (with no HTL present) and not full devices, higher PL is likely indicative of a lower defect concentration suggesting the candidate solution have produced higher quality films than the control. It is important to note that PL measurements are an average of 3 measurements or 3 films and so the candidate solutions produce films with higher PL consistently. Thicknesses of the films were measured via profilometry (Table 12) giving average values of 366, 487, 492 and 365 nm for the control and A, B, C films, respectively. Solvent systems A and B produce films which are approximately 25% thicker than the control or solvent system C, suggesting that the volume of 2-MeTHF directly affects the final film thickness. This could be due to the higher volatility of 2-MeTHF, which aids in the expedient removal of the solvent after coating, dramatically increasing the supersaturation level and corresponding nucleation. An excitation wavelength (λ_{ex}) of 450 nm was chosen. At this wavelength is has been shown penetration into the perovskite to be as low as 100 nm[169], giving some confidence that this emission increase is not simply due to increased sample thickness. This is also evidenced by the candidate C solution showing an equivalent thickness of 365 nm, whilst maintaining an increased fluorescence. This result suggests that the crystallisation mechanics may be more comparable between candidate C and the DMF/DMSO solution.

Despite the higher rotations per minute (rpm) during the coating process, candidate films A and B remain considerably thicker than their counterparts. The route of this appears to lie in the method of spin coating itself. In lieu of DMSO adduct intermediate phase formation, a ‘prenucleation’ method has been used for the candidate solvent systems. This leads to the formation of a phase of perovskite crystal during the spinning operation (light brown colour) with the subsequent annealing step precipitating 3D tetragonal $MAPbI_3$ from the solvent bound film above (as evidenced by XRD analysis). This method appears to lead to thicker films independent of the spin speed used.

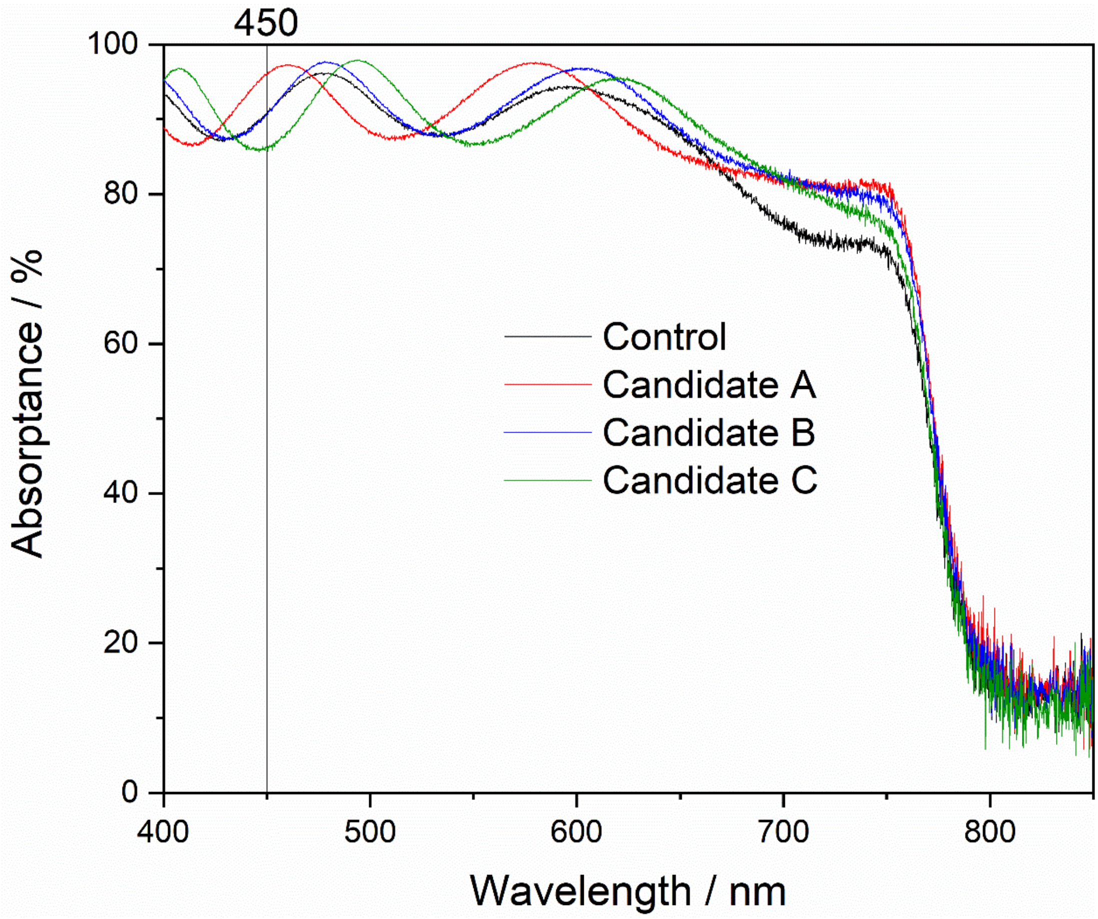

Figure 47 - Absorptance scans of films deposited from each candidate solution and the control. Fluctuations in the absorptance below 600 nm attributed to the PMMA capping layer. SSPL excitation wavelength of 450 superimposed to highlight absorptance differences.

Figure 47 shows the absorptance of candidate samples against the DMF/DMSO control. At wavelengths below 650 nm, Fabry-Perot interference fringes can be seen, this indicates a uniform film with a flat surface, little reflection, and an even thickness[170].

4.3.9 Profilometry

A determination of film thickness was undertaken for each of the candidate systems. The solvent parameters are likely to play a role in this determination, along with the spin coating regime. For the prenucleation style of spinning, where solvent bound nucleation sites are created within the wet film for conversion *via* antisolvent application to ordered $MAPbI_3$, it is important to assess thickness changes as a function of highly coordinative low volatility (HCLV) solvent. Films were prepared as for devices in a GB environment. Three measurements were taken per film to verify a uniform thickness across the film.

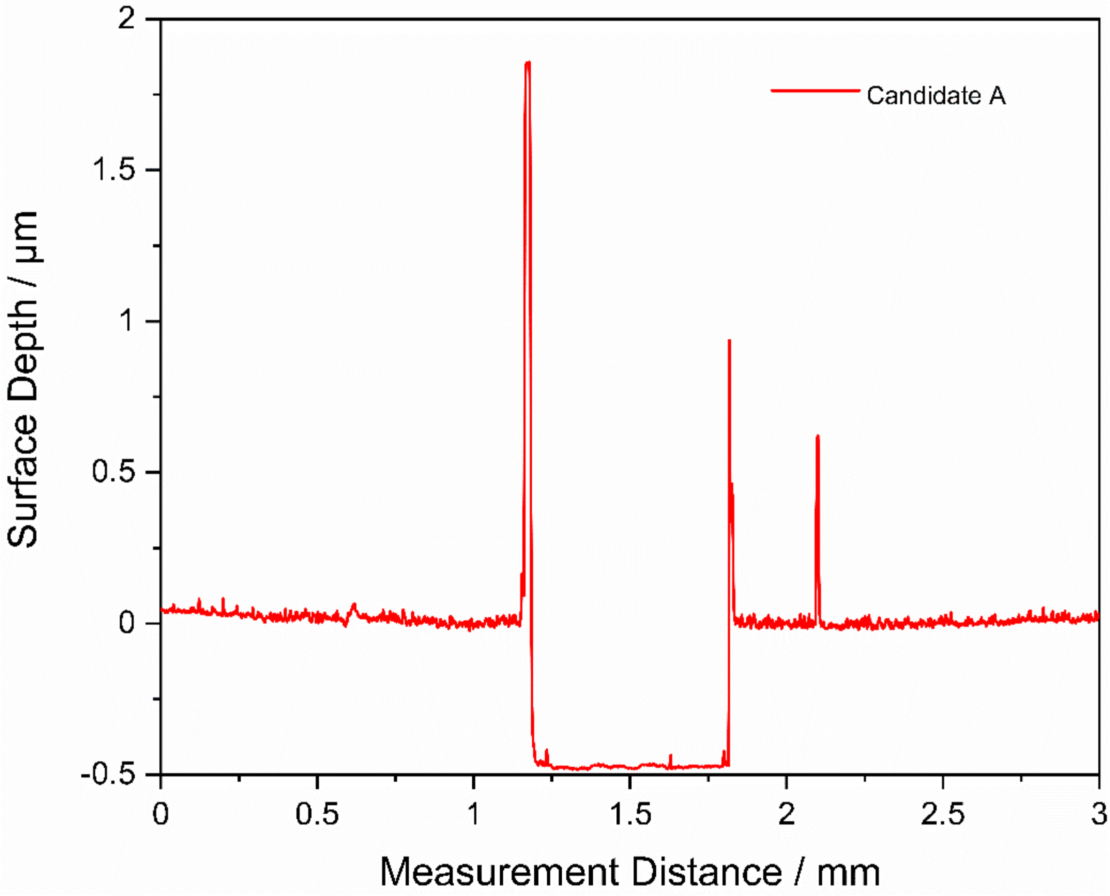

Figure 48 - Profilometry data presented graphically for a candidate A film measurement showing a film thickness ~500nm. Three measurements were taken corresponding to left side, centre, and right side.

Figure 48 is a sample of a measurement taken for a Candidate A film, with the 'trough' representing a section of the substrate with the perovskite manually removed. The results were recorded in Table 12.

Table 12 - Profilometry results for evaluated solvent systems. 3 readings were taken per film with the average thickness calculated as the mean value.

Solvent System	Recorded Thicknesses / nm	Average Film Thickness / nm
Control (DMF/DMSO)	368	366
	363	
	366	
Candidate A	475	487
	505	
	482	
Candidate B	484	492
	496	
	497	
Candidate C	370	365
	357	
	368	

4.3.10 Morphological Characteristics of Candidate A, B, and C $MAPbI_3$ vs the DMF/DMSO Solution

To verify the compact, homogenous nature of the films, SEM images were taken at 4 different levels of magnification.

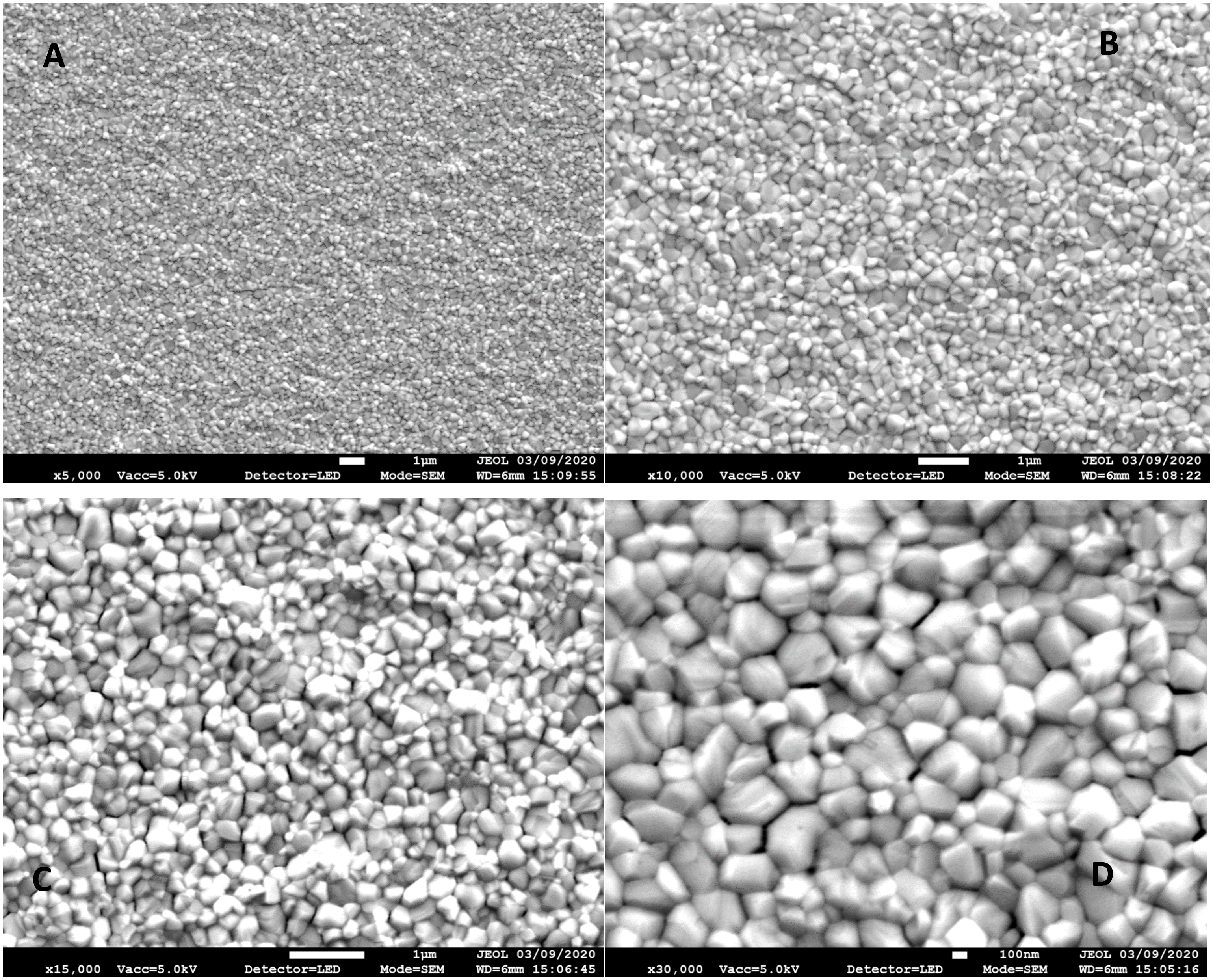

Figure 49 - Candidate A SEM images at A) 5,000× magnification B) 10,000× magnification C) 15,000× magnification D) 30,000× magnification

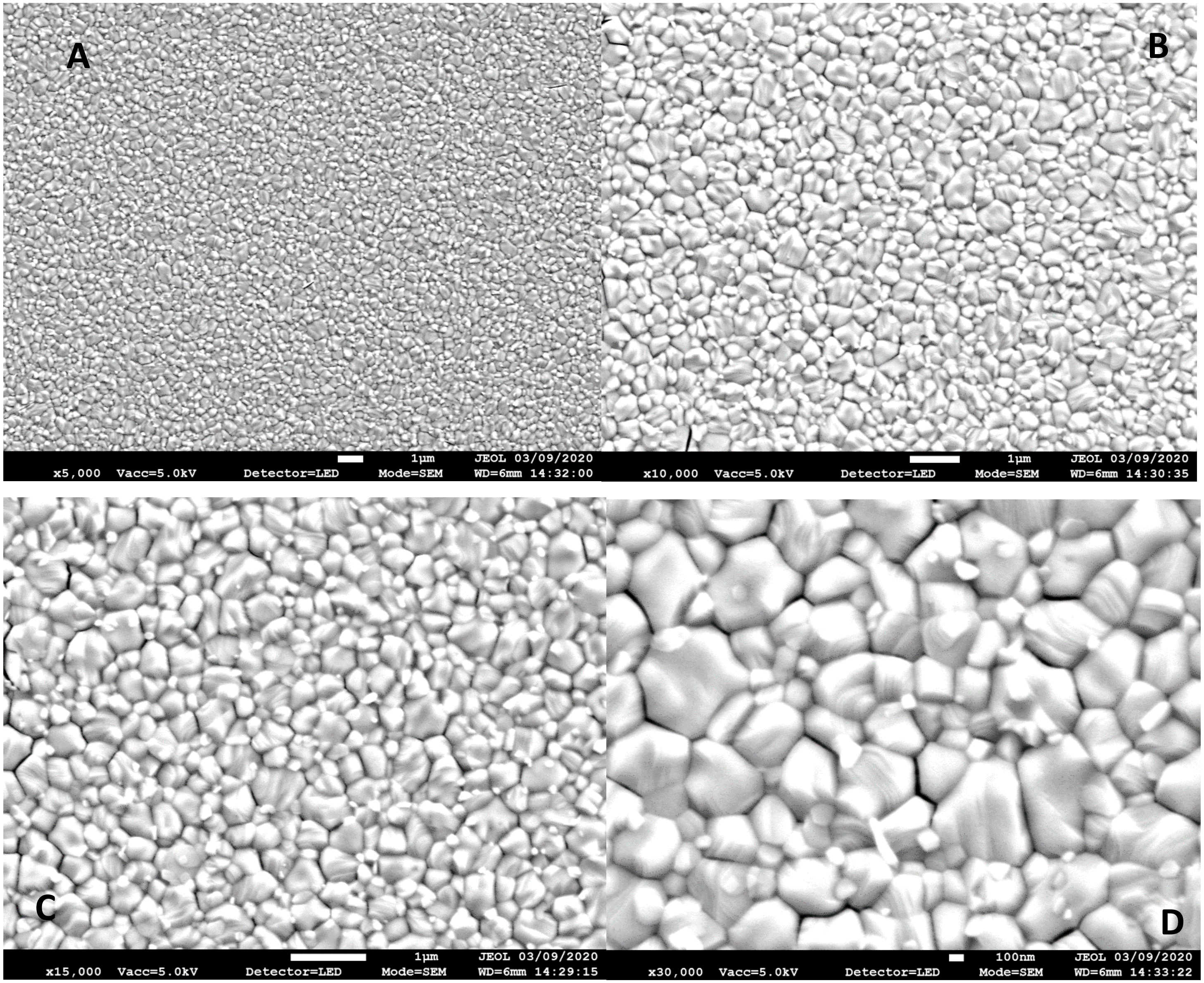

Figure 50 - Control SEM images at A) 5,000× magnification B) 10,000× magnification C) 15,000× magnification D) 30,000× magnification

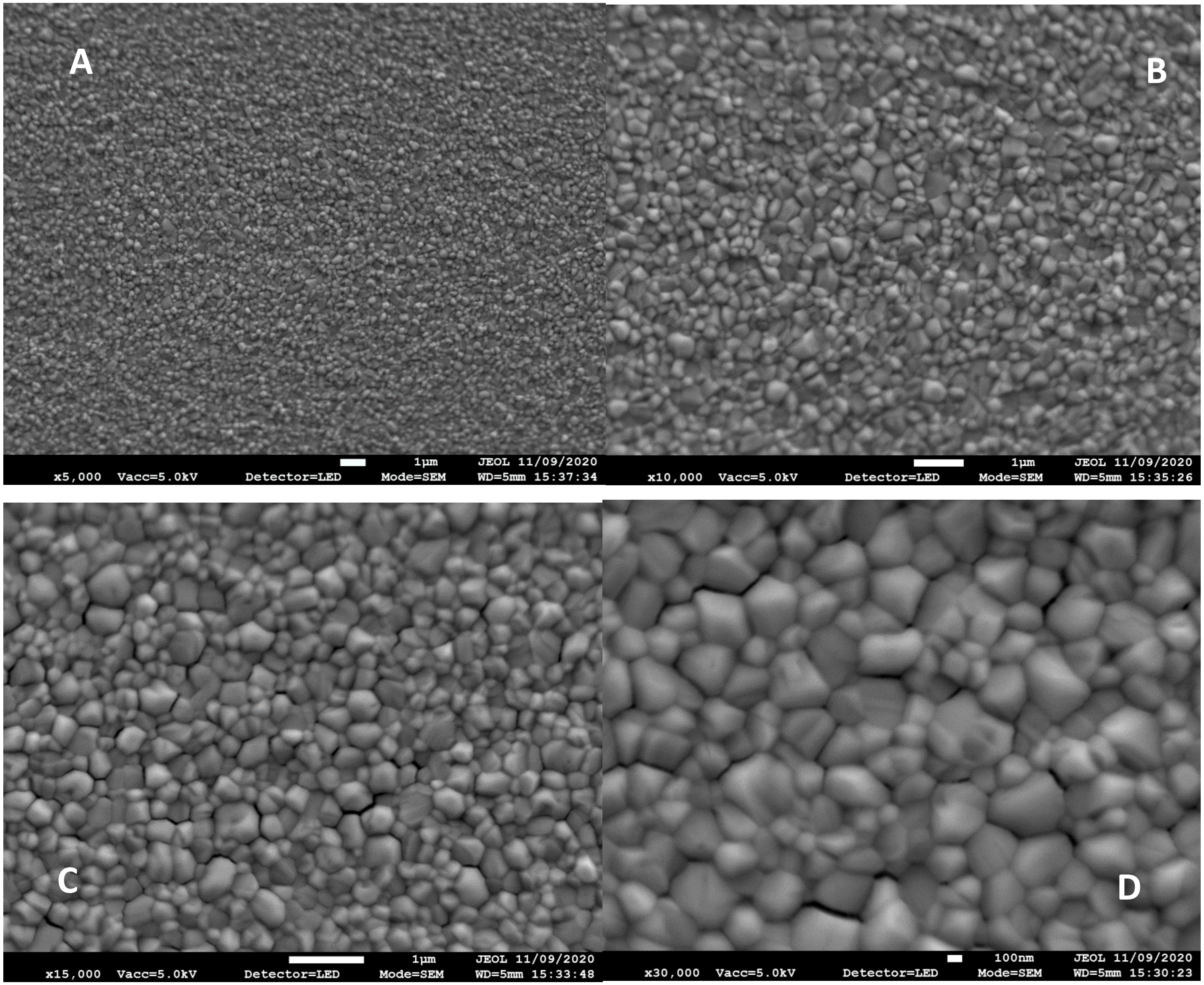

Figure 51 - Candidate B SEM images at A) 5,000× magnification B) 10,000× magnification C) 15,000× magnification D) 30,000× magnification

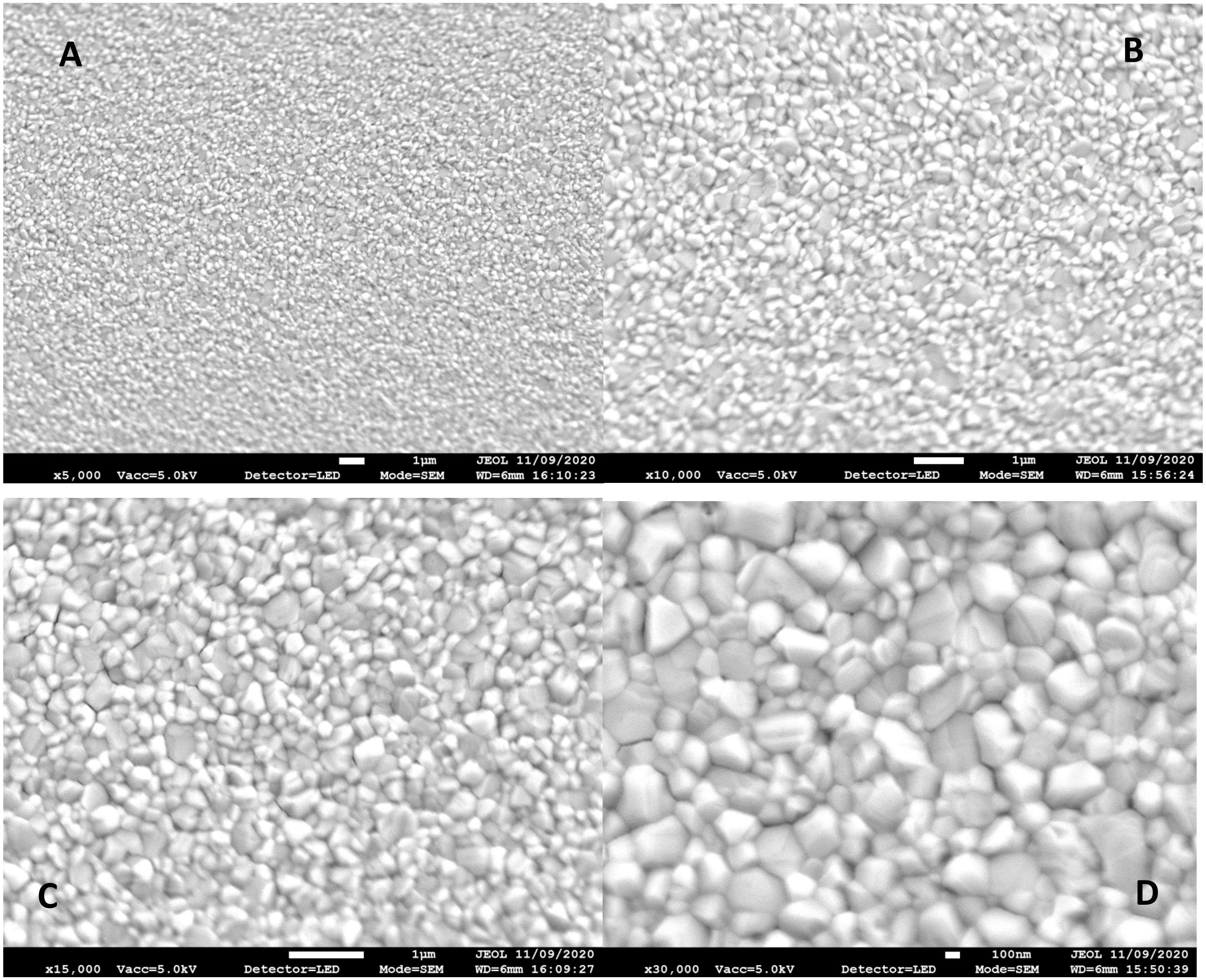

Figure 52 - Candidate C SEM images at A) 5,000× magnification B) 10,000× magnification C) 15,000× magnification D) 30,000× magnification

4.3.11 SEM, 30,000× Magnification Crystal Analysis

During the evolution of solvent systems for perovskite, emphasis has been placed on the morphology of the film in relation to the materials optoelectronic properties. Solvent engineering techniques have been utilised to improve the size of the perovskite crystallites[68,107,171–174]. This is due to the inherent recombination mechanisms of perovskite. Trap assisted recombination (SRH) is thought to be the dominant recombination mechanism in perovskites[175]. Defects are known to be present in larger numbers at these boundaries in the form of vacancies, impurities, and lattice mismatches[176]. Theory suggests that smaller domains present a higher surface area for these losses to occur. However, this has been found to only represent part of the issue, with diffusion based processes making GBs more accessible for smaller grains[177]. The relation between grain area (GA) and recombination at the grain boundaries has been described as follows[177]:

$$Defect\ Density\ \alpha\ \frac{1}{GA^{\frac{3}{2}}} \quad (9)$$

The larger the average surface area of the crystal grains, the lower level of defects with the bulk of the film relative to the total film.

Some debate exists with the literature regarding the impact of grain boundaries on recombination in full devices and ultimately photovoltaic performance. Previous work has postulated that defects can lead to recombination losses that reduce FF in devices due to increased series resistance (R_s), while suggesting a moderate crystallite size is optimsal[178]. Alternative studies suggest in full devices the effect of trap assisted recombination on PCE is negligible, due to rapid filling of these traps under illumination[175]. GBs have also been found to increase rates of degradation in perovskites while being responsible for hysteresis[176].

It is also known that the solvent system can have a large effect on the grain size. This can be from the level of coordination of the precursor[114], and also the degree of supersaturation within the precursor[167]. The number of crystallites (N) per unit area has been shown to have an inversely proportional relationship with the grain size. Burton, Cabrera, and Frank defined this relation first in 1951[179–181] as:

$$N = 1.1\left(\frac{V_1}{V_2}\right)^{\frac{1}{2}} \quad (10)$$

Where:

$$Nucleation\ Rate = V_1 \propto \exp\left(-\frac{1}{\sigma^2}\right) \quad (11)$$

$$Supersaturation = \sigma$$

$$Crystal\ Growth\ Rate = \ V_2 \propto \sigma^2 \qquad (12)$$

$$at\ \ \sigma \gg 0 \quad or \quad \sigma \gg 1$$

$$V_2 \propto \sigma \quad (13)$$

The solvent system properties dictate the nucleation rate, the crystal growth rate, and consequently, the number of crystallites per unit area. This in turn influences the size, uniformity, quality and ultimately, the morphology of the film.

Given the importance of morphology to a samples performance, and the direct link between solvent system and subsequent crystallisation, a statistical analysis was conducted on these novel perovskite films. High magnification images for films deposited from each candidate solution can be seen in Figure 53.

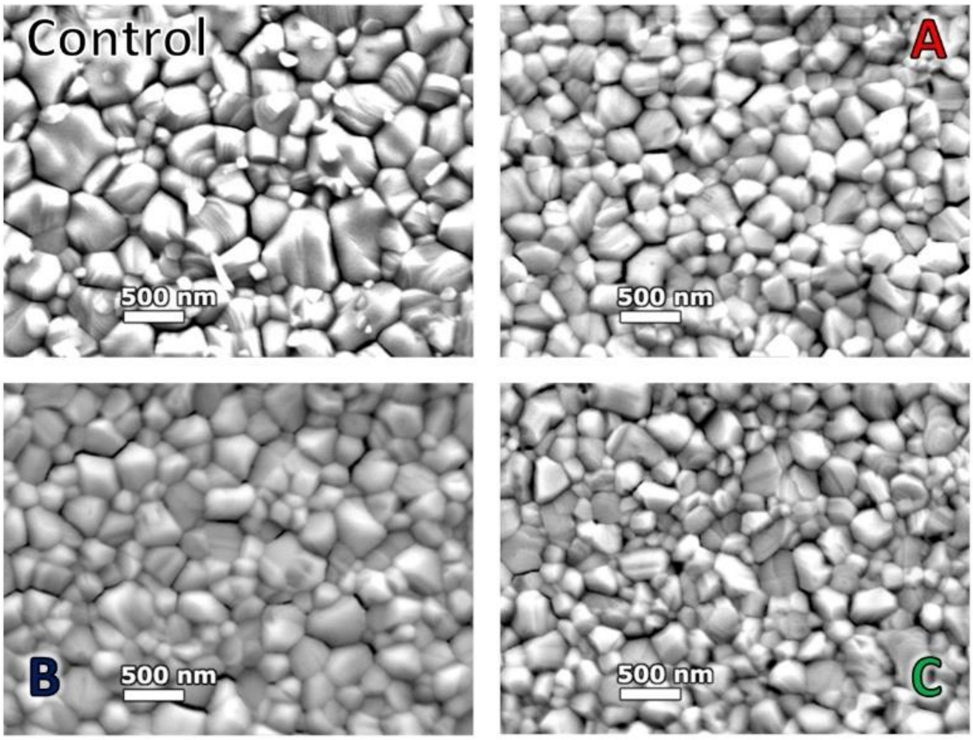

Figure 53 - 30,000x SEM Images for Candidate Solutions and the DMF/DMSO Control

SEM of the samples (Figures 49-52) show both the control and candidate solutions produce a dense, pinhole free, highly compact perovskite film. A difference in spin coating anti-solvent drip methodologies between the control and candidate solutions involves the formation of an intermediate phase as identified as a DMSO based adduct in the DMF/DMSO solution, by which the anti-solvent ethyl acetate (EA) removes the majority of the DMF and leaves a transparent adduct phase which upon annealing forms specular and large grain $MAPbI_3$ perovskite. This is suggested to be due to retardation of the crystallisation process favouring greater crystal growth over time. This is evidenced by the control sample which shows a specular film (by eye) with crystal domains visible with a mean average maximum Feret diameter of 346 ± 183 nm under 30,000× magnification. The candidate solutions utilise fluid modifiers to increase supersaturation within the solution. Using the 'prenucleation' anti solvent drip strategy, films cast from these solutions give numerous oriented nucleation sites required for the formation of the compact film upon annealing. Due to this action directly impacting the growth phase of the crystallisation, the crystal size visible for candidate solution films appears smaller. Solvent systems A and C produce films with crystal sizes of 267 ± 106 nm and 264 ± 112 nm respectively whereas candidate B shows more comparable average crystal size to the control sample with 304 ± 108 nm. Comparing the constituent solvents may suggest why these results were achieved. Of all the candidate solutions, solution B has the highest relative supersaturation (due to the additional ethanol compared to A, where C has a lower supersaturation resulting from additional HCLV solvent DMPU). This ethanol likely introduces additional H_2O into the precursor solution, as discussed in Chapter 4.

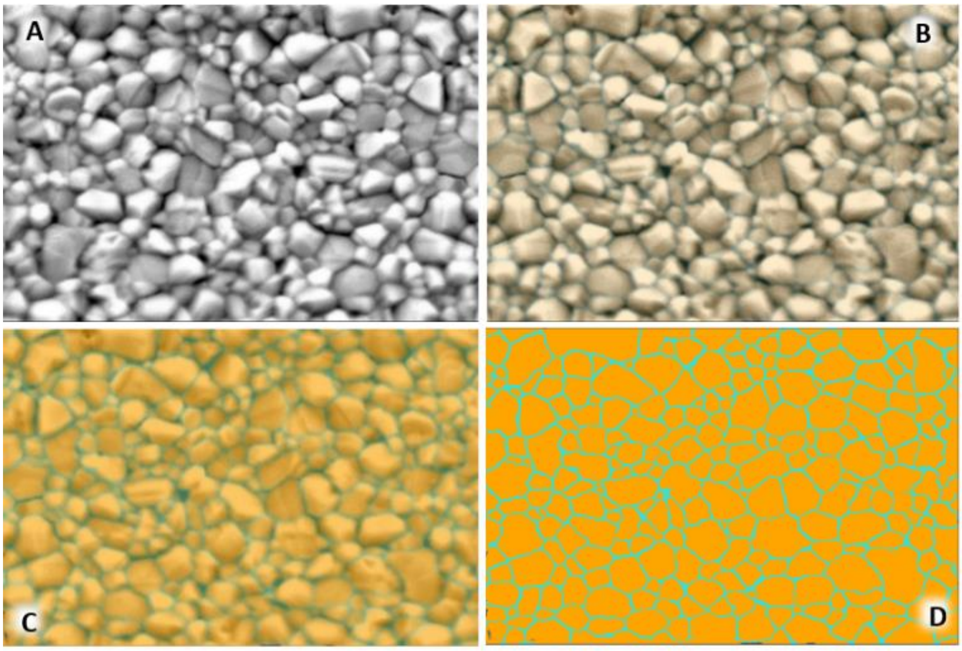

Figure 54 - SEM of $MAPbI_3$ thin-film deposition from Candidate A solvent system with 30,000× magnification (A) and the Zen Blue image analysis segmentation (B-D). A - mirrored image of the base data for the image analysis software to segment. To illustrate the accuracy of the segmentation the label opacity is increased (B-D) with the final result (D) typical of the segmented data analysed to extrapolate crystal size characteristics.

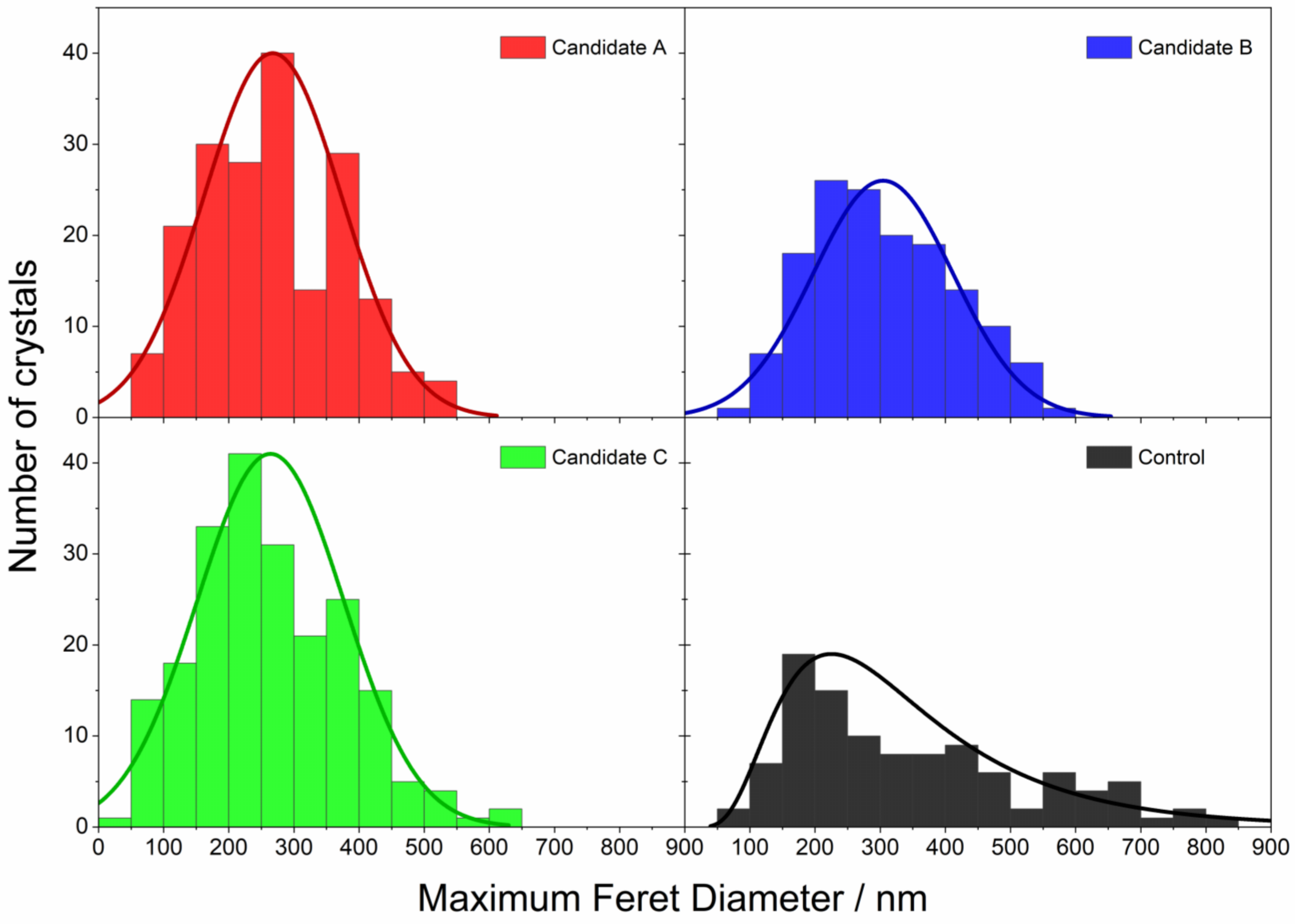

Figure 55 - Crystal size distribution histograms taken from the Zen Blue Intellesis analysis of the maximum Feret diameter for each sample. Normal distribution curves have been superimposed onto candidates A, B, and C, with a lognormal distribution applied over the control graph.

Table 13 - Crystal grain parameters for each candidate solution taken from image analysis on the Zen Blue Intellesis module software.

	Average Area / nm^2	**Average Perimeter / nm**	**Average Roundness**	**Average Diameter / nm**	**Average Max Feret Diameter / nm**
Control	73949	1111	63%	272	346
Candidate A	39429	882	61%	208	267
Candidate B	50758	1054	62%	238	304
Candidate C	38269	880	59%	203	264

This suggests that films manufactured using the DMF/DMSO control system consist of larger grained crystals on average (Table 13). However, the greater standard deviation in the data set, along with size distribution graphs (Figure *55*), show that there is a skew towards the formation of comparatively small crystals alongside the large grains for this sample. Whilst the average Feret diameter taken for candidate films A-C is lower, the grains tend to a normal distribution and a lower standard deviation from the mean. Analysis of this data, in conjunction with the XRD results suggest that size distribution, along with film compactness and uniformity, may lead to films with higher crystallinity. This difference is thought to be related to the use of the prenucleation spin coating methodology, where a homogenous spread of nucleation centres initiates the crystal growth in a highly uniform and preferentially regimented manner, tightening the size distribution seen in the final film.

Distinctive tetragonal $MAPbI_3$ peaks can be seen for all samples at 14.1°, 28.4° and 31.9° corresponding to the 110, 220, and 310 crystal planes (Figure *56*)[182]. For the DMF/DMSO sample a small diffraction peak can be seen at 12.6° attributed to PbI_2[182].

4.3.12 XRD Analysis of Candidate Solutions

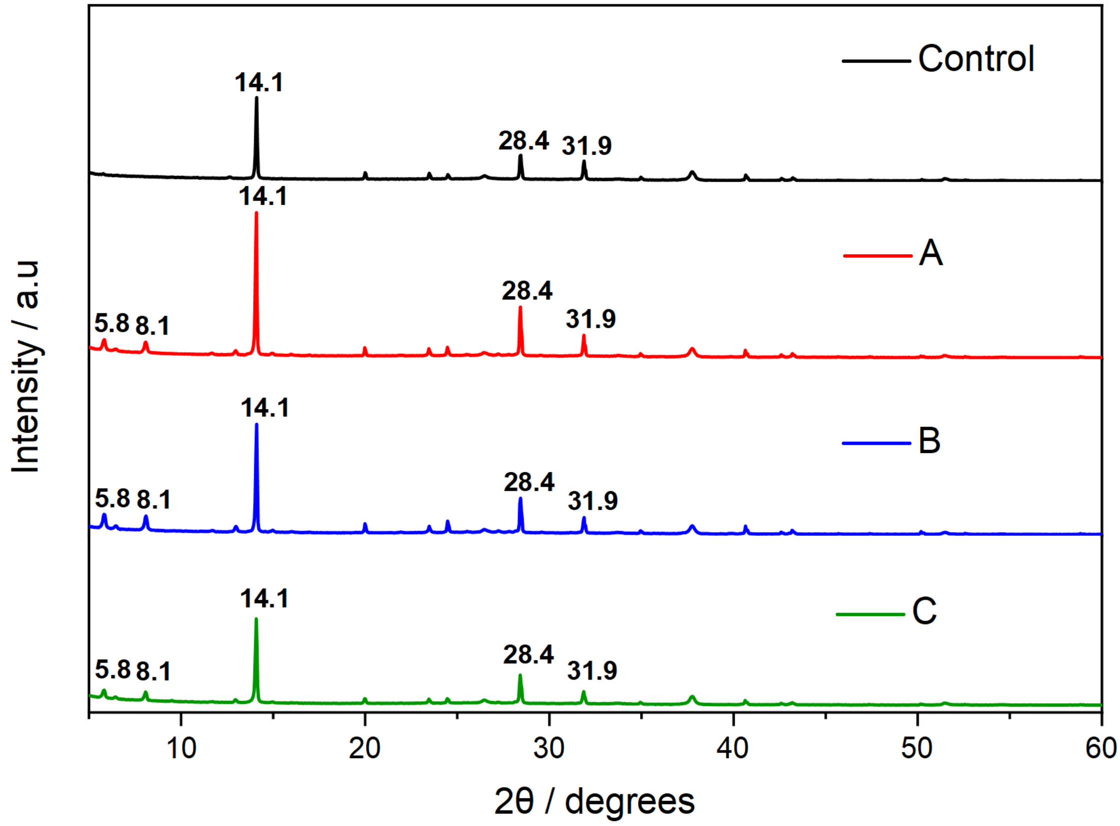

Figure 56 - XRD scans for candidate solutions A, B, C, and control (DMF/DMSO 80/20 v/v)

For the candidate solutions a new peak is exhibited at around 13.1° along with other smaller peaks at approximately 15° and 16°, these are likely due to the presence of an intermediate PbI_2, similar to those exhibited in the works by Y. Ren *et al*[183]*.* In this the MAI and solvents are interacting with the layered structure of the PbI_2 resulting in a distortion of the PbI_2 lattice, most notably in the *c* axis, which presents as a shift in the peak positions.

All candidate solutions also exhibit two prominent peaks and a smaller tertiary peak below 10°. These were identified at 5.8°, 6.5°, and 8.1° respectively. This may be due to the presence of 2D perovskite phases; the use of specific solvents and solvent additives has been reported to produce 2D lattice structures classified by the number of lattice layers n[184]. The most likely region for any 2D perovskite growth would be the ETL/PAL interface, due to the spin coating procedure. As the incidence angle is very acute, it remains unlikely that we have identified 2D $MAPbI_3$ perovskite during these XRD scans of 400-500 nm thick samples. Another possible explanation for the observed low angle (<10°) peaks is the presence of solvated phases within the sample. This could be due to an insufficient annealing step, or residual solvent present within the bulk. Although identification of the exact peak position is difficult to match, recent studies – also applying a prenucleation style of drip – identify three low angle peaks as $MA_2Pb_3I_8{\cdot}2DMSO$[167]. The XRD position reported here is shifted to the left by ~1° compared to that presented by Zhang et al, 2020. However, the relative position and intensity of the three peaks show good agreement[167].

4.3.13 XRD FWHM Peak Analysis

The full width at half maximum (FWHM) of the diffraction peaks were measured (Table S4) with the DMF/DMSO control providing the baseline for a high-quality film. Candidate A, B and the DMF/DMSO sample all show similar FWHM values for the 110 peak (*ca*. 0.09). For both the 220 and 310 peaks the FWHM for candidate A is the lowest of all samples. This, along with the higher PL intensity observed suggests higher crystallinity within the material. This is postulated to be the result of reduced impurities resulting from the use of the prenucleation method with this sample. The intensity of the 110 peak shows a higher intensity in all of the candidate solutions (order of precedence A-B-C-Control) compared to the control, with candidate C showing largest FWHM and consequently the poorest crystallinity, again this agrees with the PL measurements with C.

Producing lower PL intensity compared to A and B. In terms of peak intensity, the 310 peak is noticeably lower relative to the 110 and 220 peaks in the candidate films compared to the DMF/DMSO film. Table 14 shows the 110/310 peak intensity ratio for each solvent system. All candidate solutions show a higher ratio suggesting 110 orientation is dominant. This suggests that the candidate films form crystals with less disorder than the DMF/DMSO derived film and a preferred grain orientation[173].

Table 14 - Results for XRD Peak Analysis

Solvent System	110 FWHM	220 FWHM	310 FWHM	110/310 Intensity Ratio
Control (DMF/DMSO)	0.09796	0.13680	0.14950	4.02
Candidate A	0.09834	0.11705	0.13913	6.16
Candidate B	0.09663	0.13319	0.15377	6.16
Candidate C	0.11234	0.14174	0.16608	5.93

4.3.14 Photovoltaic performance evaluation for candidate solutions

The three candidate precursor solutions produce devices of a similar efficiency to the DMF/DMSO control devices (Table 15) with no discernible performance loss on substituting the harmful DMF-based solvent system with the ‘greener’ alternatives. Box plots, showing the four photovoltaic parameters PCE, Jsc, Voc, and FF on a pixel-by-pixel basis can be seen in figure 30. Amongst the candidate solutions (A-C) similar performance may be expected as they do not vary a great deal in composition, however, it does show a degree of flexibility which could be valuable when matching a solvent system to a particular deposition method.

Candidate A in particular matches the performance of the DMF/DMSO system extremely well with the champion devices achieving over 16% PCE matching the champion devices of DMF/DMSO (The J-V curves for all champion devices are given in Figure 59). For average values Candidates B and C produce overall similar PCE values with slightly lower J_{SC} values which may be due to slightly less uniform films as suggested by the XRD and in the case of Candidate C, lower PL intensity. Candidates B and C also didn’t produce as high efficiency champion devices compared to Candidate A and the control DMF/DMSO, although this may just be a case of needing further refinement of the spin coating cycle and anti-solvent drip. Specifically, the addition of increased amounts of EtOH in candidate B and DMPU in candidate C subsequently serves to increase solution supersaturation and reduce film evacuation respectively, both parameters expected to impact deposition.

Table 15 - Statistical Representation for 6 months of Candidate A, B, and C Devices against a DMF/DMSO Control. Four photovoltaic parameters; Power conversion efficiency (PCE%), Fill factor (FF), Open circuit voltage (Voc), and short circuit current (Jsc).

Solvent System		PCE / %	Jsc / mAcm^{-2}	Voc / V	FF / %
DMF/DMSO	Average	12.4 ± 2.0	19.4 ± 1.7	0.97 ± 0.04	65.6 ± 7.2
	Champion	16.22	22.02	0.97	75.8
Candidate A 40% DMSO, 30% DMPU, 20% 2-MeTHF, 10% EtOH	Average	12.3 ± 1.9	19.5 ± 1.7	0.97 ± 0.04	64.8 ± 7.1
	Champion	16.05	21.35	0.94	79.6
Candidate B 40% DMSO, 30% DMPU, 15% 2-MeTHF, 15% EtOH	Average	11.9 ± 1.1	17.9 ± 2.1	0.97 ± 0.06	69.0 ± 3.1
	Champion	13.32	20.79	0.92	69.6
Candidate C 40% DMSO, 40% DMPU, 10% 2-MeTHF, 10% EtOH	Average	12.3 ± 1.8	18.8 ± 1.0	0.99 ± 0.04	66.1 ± 7.6
	Champion	13.94	18.96	1.01	67.8

Based on all the evidence available to us, it seems apparent that Candidate A is the most promising, but B and C could potentially be improved further and the ability to tune the solvent composition without significantly effecting device performance could be extremely valuable to optimising the solvent system to various printing techniques. As an example, candidate solution C could be chosen for experimentation with excess PbI_2, a common strategy to increase device PCE, as it has the highest % of DMSO/DMPU (total 80%); by tuning the ratio to include more DMPU and less 2-MeTHF and EtOH blend, the solvating power of the solution is increased potentially allowing increased concentrations of PbI_2.

4.3.15 Device Performance Box Plots

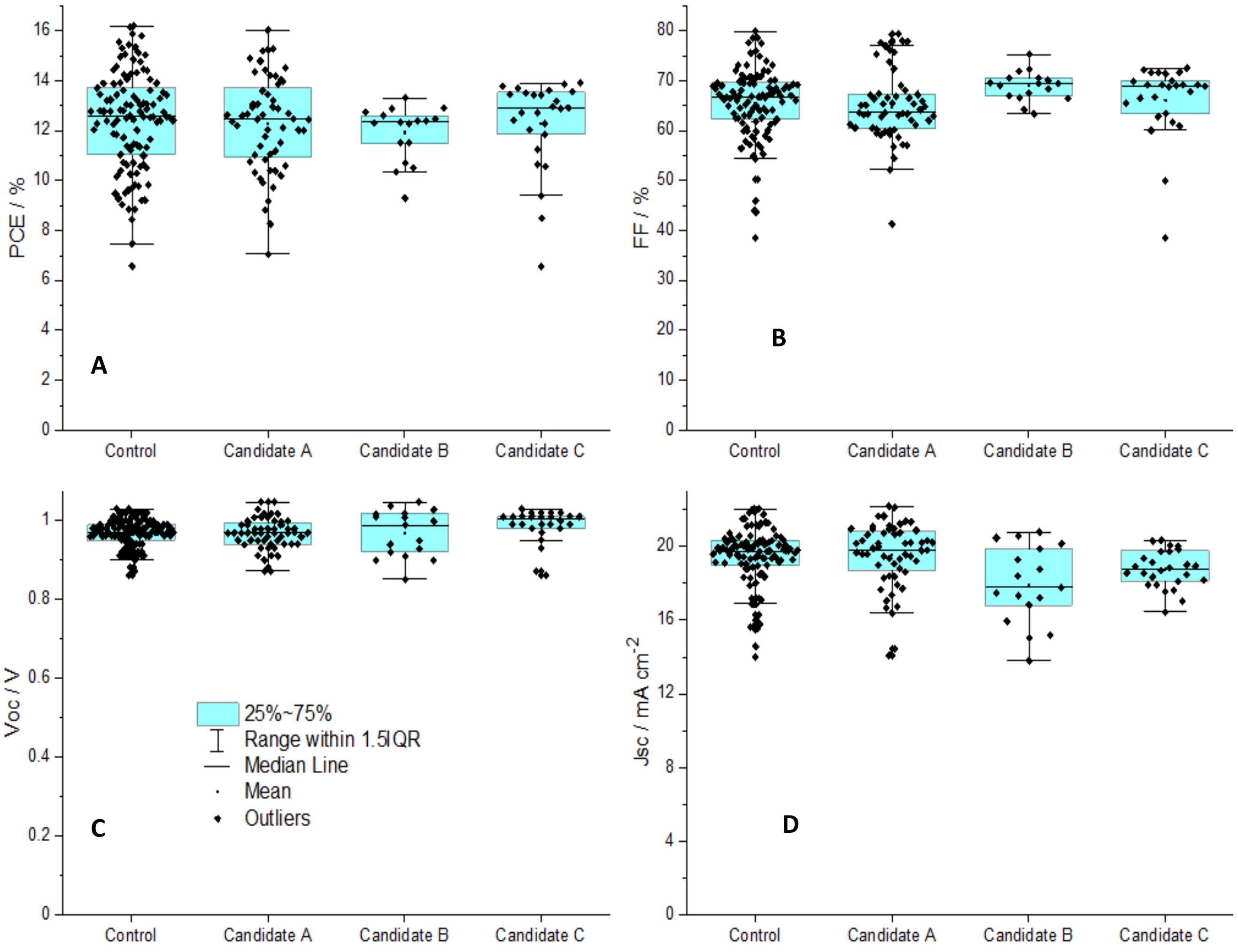

Figure 57 - Combined candidate solution box plot charts for the four photovoltaic parameters; A power conversion efficiency (PCE%), B- fill factor (FF), C - open circuit voltage (VOC), and D - integrated current (JSC)

Through the visual representation of the device statistics in Figure 57. The most trailed candidate A system competes with the DMF:DMSO cosolvent system in all key parameters most notably efficiency. To attain comparable results between systems all data was analysed and evaluated pixels with a recorded open circuit voltage below 0.85 were omitted. This was due to experimental problems while depositing the tin oxide ETL onto pre-cut laser etched FTO samples. As the ETL required a thin layer spun from a nanoparticle solution, it was postulated that poor surface coverage was present on most samples due to the inherent surface roughness of the FTO, given a root mean square value of 16 nm to 0.63 nm for ITO[100]. This led to erratic and subpar open circuit voltage results which subsequently impacted both efficiency and fill factor with minimal if any change to the integrated current drawn. This impacted both experimental and control devices. A key recommendation is to use ITO in this build procedure when surface roughness cannot be minimised by surface modification methods. As the lower cost alternative to ITO, FTO may still be utilised in this architecture provided a consistent tin oxide transport layer be deposited.

4.3.16 Substrate Comparison for SnO_2 ETL

Figure 58 shows the results of a build procedure using an SnO_2 ETL with both FTO and ITO substrates. For the SnO_2 layer, the film was made intentionally thin *c.a.* 3%, to harness higher Jsc values known to be possible with a thin ETL of this type. The same solution of DMF/DMSO $MAPbI_3$ was used to manufacture samples in both cases. The average current attained was uniformly higher in the ITO samples (between 5-10% total increase), significant in pushing the device efficiency to above 18%. Most importantly, however, we see a much higher, more uniform, and reliable Voc spread for the ITO samples with a reduction in poor ITO/ETL interfacial contact.

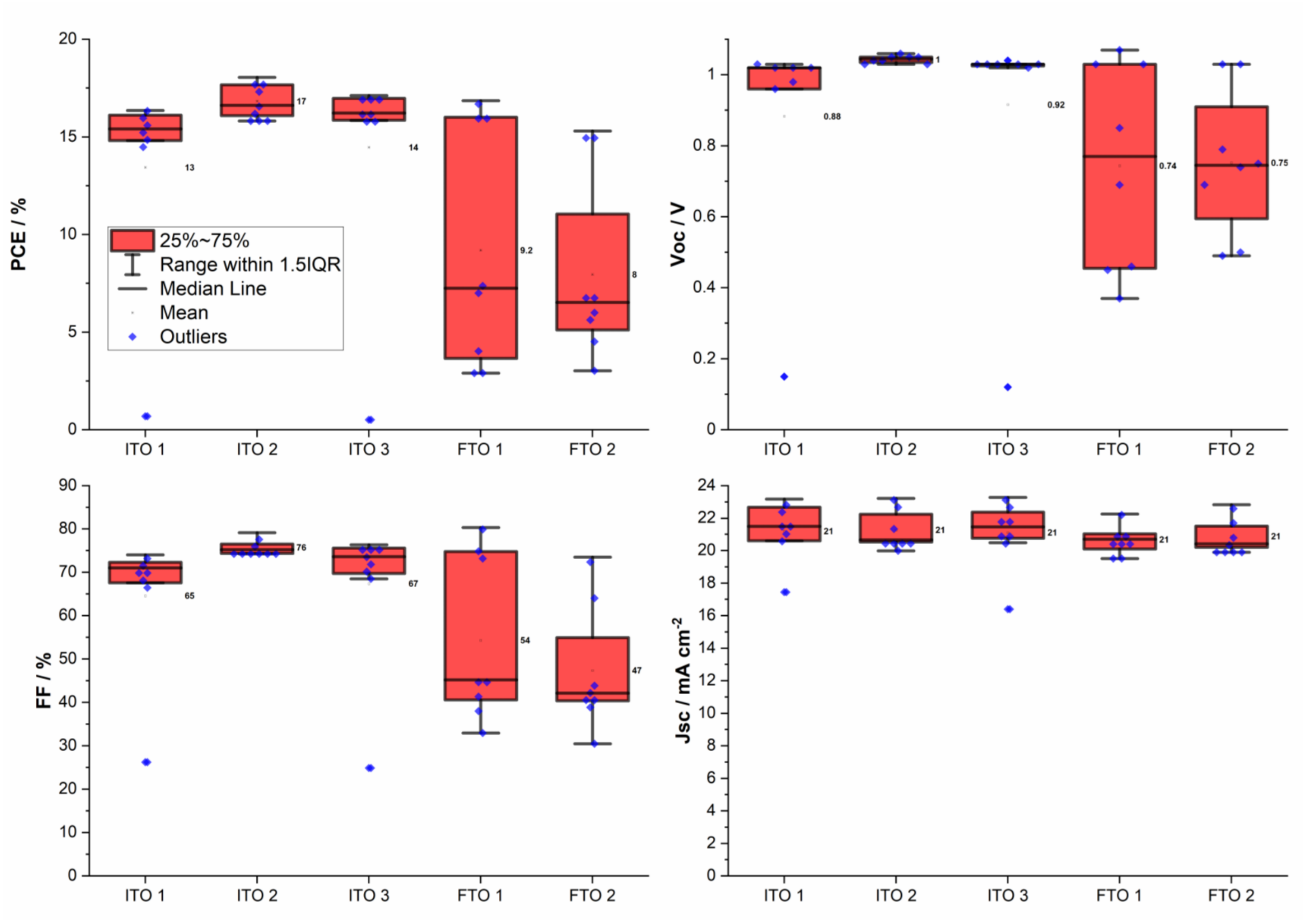

Figure 58 - Device Performance Evaluation Comparing FTO and ITO substrates for SnO_2 Deposition

4.3.17 Champion Device Pixels for the Study

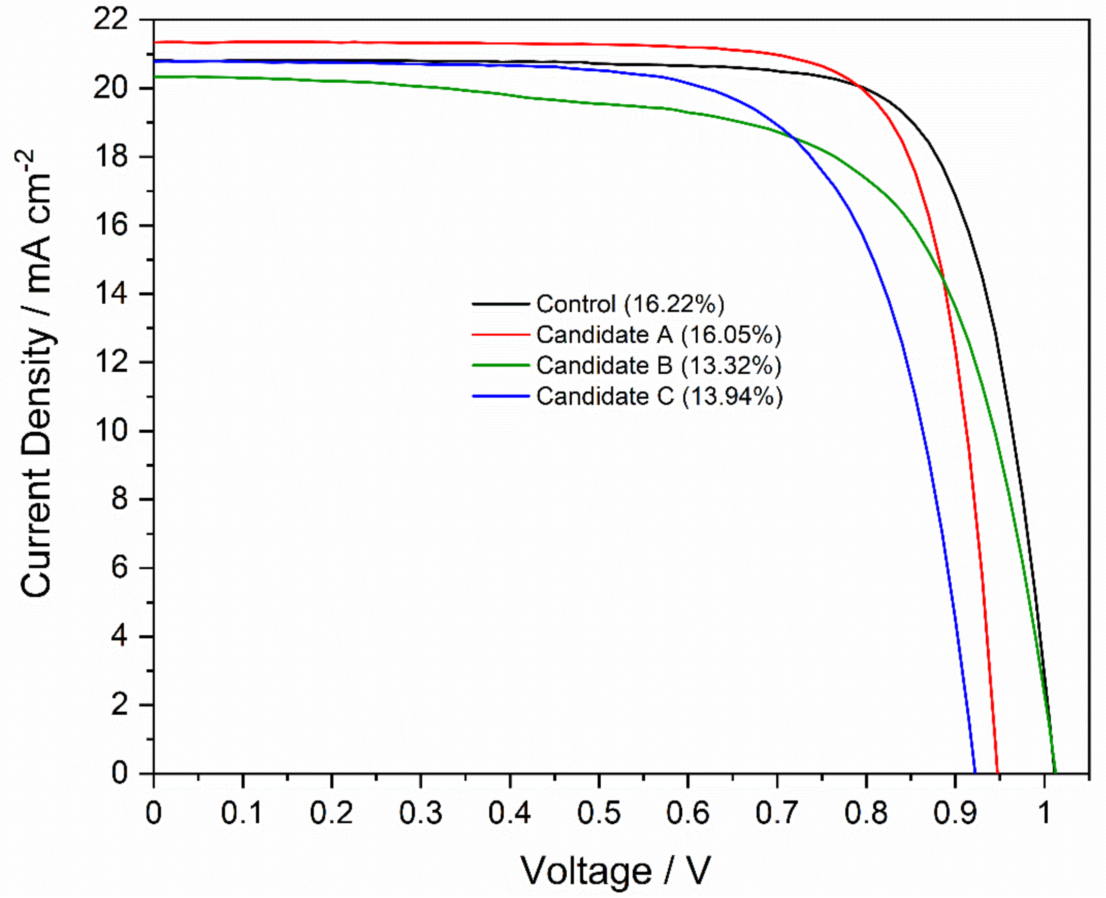

Figure 59 - Champion JV curves for candidate solutions.

The control DMF/DMSO solution achieved the highest PCE% at 16.22%. The candidate A system reached the highest PCE of all experimental solutions at 16.05% (40 vol% DMSO, 30 vol% DMPU, 20 vol% 2-MeTHF, and 10 vol% EtOH), with the candidate B solution (40 vol% DMSO, 30 vol% DMPU, 15 vol% 2-MeTHF, and 15 vol% EtOH) the lowest at 13.32. The additional DMPU candidate C system (40 vol% DMSO, 40 vol% DMPU, 10 vol% 2-MeTHF, and 10 vol% EtOH), achieves 13.94% in the study. Figure 59 provides the champion JV curves for full devices for each of the candidate solutions.

4.4 Conclusion

In this work we have identified a solvent system consisting of DMSO, DMPU, 2-MeTHF and EtOH that can match the performance of the commonly used DMF/DMSO solvent system for deposition of $MAPbI_3$. We have shown there is a degree of flexibility in the composition of this solvent system by studying three candidate solutions (A-C), with slightly different compositions of the four constituent solvents, that all achieve similar device performance to the control DMF/DMSO. 'Hero' devices produced PCE values of 16.2, 16.1, 13.3, and 13.9% for when DMF/DMSO and A-C are used to deposit $MAPbI_3$ respectively. XRD and SEM confirm that the solvent systems produce dense, crystalline, and uniform films with no observable pin-holes. We have highlighted and demonstrated the methodology for green solvent substitution which we hope will act as a framework to support further development of greener and more sustainable solvent systems for PSC manufacturing and hasten the commercialisation of this technology. We have investigated commercially available solvents and used benchmarks of basicity as represented through the Gutmann donor number, and dielectric constant to identify solvents likely to dissolve $MAPbI_3$ perovskite precursors (MAI and PbI_2). Two dipolar aprotic solvents DMSO and DMPU were identified as a cosolvent system capable of forming high (1.25M) concentration solutions suitable for spin coating. Emphasis was also placed on the increased Pb^{2+} coordinating ability of the DMSO/DMPU system to produce highly crystalline planar perovskite films. An additive cosolvent system comprising the derived 'green' solvent 2-methyltetrahydrofuran and ethanol helped to mitigate over coordination improving film quality and ease of spin coating. A prenucleation style of anti-solvent drip was utilised with a $MAPbI_3$ crystalline film forming during the spin coating process and providing a dense spread of nucleation sites for further temperature induced crystal growth from the solvated phase. Our results suggest that this solvent system results in efficient, compact films with superior fluorescence emission and improved crystallinity compared to the highly optimised DMF/DMSO cosolvent system. Solvent systems A-C produced films with significantly higher fluorescence emission compared to the DMF/DMSO system, with A and B showing the highest fluorescence intensity likely due to the higher volume % of 2-MeTHF (20 and 15% respectively) resulting in slightly thicker films (487 and 492 nm respectively vs 366 nm for DMF/DMSO) while retaining higher crystallinity and uniformity as evidenced by SEM observations. While the 3 candidate solutions presented here have similar compositions, we feel that analysis of these systems highlights the potential for customisable solvent system to alter crystallinity, reduce defects, and tune the properties of the perovskite film and could potentially be optimised for a given manufacturing method. We have used environmental, health and safety considerations (EHS) of the solvents as the first step in screening potentially 'greener' solvents producing a system significantly better than DMF/DMSO in terms of the EHS credentials.

Purely in terms of the PL properties observed during the course of this work, there appears to be some potential in further optimisation of these devices. By harnessing the evident increase in PL, and passivating or ameliorating loss pathways – the current draw from the device could reach much higher levels than we have observed. Moving forward, thorough techno-economic evaluation and extended lifecycle assessment methodologies should be undertaken to verify that solvent substitution results in reduced environmental impacts throughout the whole lifecycle of PSC devices and no unintended consequences occur from adoption of alternative solvent systems.

Prifysgol Abertawe
Swansea University

Chapter 5 - Improving MAPbI$_3$ Films and Precursor Solution Stability

5.1 Introduction

5.1.1 Precursor Stabilisation

This results chapter details developing the solvent selection process through increasing the stability of the perovskite precursor solution. Films fabricated from solution A show high levels of photoluminescence emission, and in full devices, compete in terms of PCE, when measured under AM1.5 light 24 hours after manufacture, with 16 % n-i-p pixels achieved. One limitation of this four-component system is a lack of long-term stability. At a 1.25M 1:1 stoichiometry, which is needed to achieve supersaturation, some precipitate of PbI_2 was observed after a period (24 hours). This precipitate is thought to be as a consequence of ethanol in the precursor. Ethanol, which has previously been used as a perovskite antisolvent[185], is a green solvent which is miscible with a majority of perovskite precursor solvents. It is capable of initiating nucleation within a film. This nucleation inducing ability also hampers its use in precursor formulations. For commercial production of perovskite, the precursor must remain stable, retaining specific amounts of the precursor chemicals over a long time. Although the solution may return to a useable state after a period of heating, repeated heating cycles should be avoided due to the tendency to thermally decompose the precursor materials[186]. The nature of repeated or continual heating also increases the energy cost of the process, reducing commercial and environmental viability.

Alternative solvent systems that have previously been developed have also run into issues with long term precursor stability. R2R methodologies have come to rely on the use of methylamine acting as a solvating agent within a highly volatile carrier solvent[132,187]. In this case methylamine has such high volatility that at room temperatures, it can be expected to enter the atmosphere over time, reducing the dissolution ability of the system. As previously discussed in this case, refrigeration may be considered to improve the life of the precursor, with an associated environmental and literal cost. Recent research, by Casella et al, present a novel solvent system for R2R manufacture without the need for methylamine. This involves a tuned combination of 2-methoxyethanol (2-ME) and THF[188]. 2-ME has previously been reported as a useful perovskite solvent with a high volatility[138]. In this case the ability of the solvent to coordinate to some extent the iodoplumbate complexes within the precursor solution is attributed to the hydrogen bonding affinity of the solvent. This mimics our own studies as shown in Chapter 4. By removing the methylamine component, the condition of the precursor is improved in several ways. Firstly, long term storage is possible. Secondly, the process is annealing free and simply dependent on nitrogen to aid in solvent removal, increasing potential throughput. Finally, this co-solvent combination provides an insight into the volatility requirements necessary for R2R formulations. Further room temperature ‘annealing free’ formulations have reached 23.1% efficiency in inverted architectures. These findings indicate an increased research focus on the perovskite ink formulation and associated coordination and physical chemistry requirements. An area that is often overlooked, however, remains the long-term performance of such systems.

5.1.2 Moisture within the $MAPbI_3$ Precursor

Several studies have tackled the issue of moisture degradation of $MAPbI_3$[189–194]. This has been characterised more often than not as a definitive method of degradation in perovskites, especially in conjunction with light and oxygen[193]. Film stability has been shown to be adversely effected by high (>70%) humidity environments[194]. Interestingly, for this work – informed primarily by SSPL evaluations, Kundu and Kelly (2020) postulated that high humidity environments can cause an increase specifically to the intensity of the PL emission[194]. Few studies have probed the moisture PL intensity relationship for novel films cast from alternative – potentially moisture containing precursor solutions. For the purposes of the following investigations – conducted in very low H_2O containing N_2 environments with PMMA encapsulation – the A01 solution contains residual moisture with the B01 comprised of anhydrous solvents. The impact of residual H_2O during spin coating serves to suppress the nucleation phase[195]. However, the moisture-perovskite relationship has been described as more complex, with potential improvements to the crystal growth phase of the nucleation[168,195]. Alternative degradation pathways have also been demonstrated to involve H_2O such as the formation of superoxide resulting from oxygen adsorption at active sites resulting from iodide vacancies[196]. Ultimately, water molecules are known to form hydrogen bonds with perovskite cations in solution, leading to distortion of the lattice structure and appreciable degradation[189,196], regardless of the moisture source. The experiments presented within this Chapter should be considered in relation to the uncertain picture involving moisture and perovskite precursor formulations.

5.1.3 Antisolvent Engineering

Laboratory scale perovskite manufacture, particularly for highly efficient perovskite devices, has relied on the use of antisolvents to control film formation during spin coating. To date, few research groups have developed the necessary skill, conditions, and precision to regularly fabricate 20% + devices[99]. Device PCE has always been a driving factor behind solar development, with increased research efforts directed towards the most promising efficient technologies. Higher PCE increases the LCOE for emerging technologies and dramatically improves the rate and scale of technological adoption. Highly efficient devices usually rely on solvent systems containing HCLV solvents. The properties that are required from a processing solvent to form highly crystalline, pure, large grain $MAPbI_3$, are possessed by solvents that are commensurately difficult to remove from the final film without anti-solvent.

Development of highly efficient perovskites has relied largely on toxic antisolvents, such as chlorobenzene[197] and toluene[198]. In the interest of pursuing circularity and improving the sustainability of perovskite manufacture, these solvents require substitution.

Fundamental properties required of the antisolvent are also disputed, with a wide range of parameters determining the effectiveness of various antisolvents. Previous investigations have altered spin coating regimes, drip time, volume of drip, and atmospheric conditions[198]. Some antisolvents utilise differences in miscibility between the two processing solvents DMF and DMSO for selective removal, first achieved with diethyl ether (DE), in 2015[199]. DE also exhibits a very low boiling point as opposed to the quite high value for CB (~132°C)[200]. Clearly, attempting to quantify specific properties for the antisolvent application has proven difficult. Development of new 'novel' solvent systems leads to a further antisolvent optimisation process. A 2021 study by A.D. Taylor noted that efficiencies greater than 20% may be achieved for a range of anti-solvents – both low and high boiling point – through modification of the dripping speed[198]. Antisolvents were broadly categorised with regards to the 'time in contact' required for high quality perovskite formation. This work proved that through optimisation it is possible to produce highly efficient films (~18-19%) from a wide variety of anti-solvents. As described in Chapter 4 it is noted that a longer duration drip can allow for high quality film formation depending on the characteristics of the solvent system/anti-solvent pairing[198]. This is potentially a positive development in terms of sustainability as it increases the list of candidate solvents that can be used successfully. Although anti-solvent treatments are likely to have little role in scaled up manufacturing, study of the precursor anti-solvent interaction provides a basis for the creation of anti-solvent free methods in the future.

5.1.4 Ethyl Acetate

EA exhibits a relatively low BP (~77°C)[201], hydrophobic nature, and lewis basic ability to interact with perovskite precursors[202]. EA has become the standard anti-solvent for the optimised DMF/DMSO solvent system fabricating high quality $MAPbI_3$. Previous attempts have also been made to include small amounts of antisolvent within the perovskite precursor solution[202]. In this case EA inclusion (1-10 vol% additive) within the precursor is hypothesised to with improve efficiency with larger perovskite grains observed[202]. Similar studies have also been done for diethyl ether[203], with the results consistent across both antisolvents. This method, however, usually leads to an unstable precursor formulation, as the precipitation of precursor material is thermodynamically favoured over time. Attempts were made during this research to investigate this type of synergistic optimisation strategy.

5.2 Experimental Methods

5.2.1 Chemicals

Films were fabricated according to 2.1.1 Precursor Solution - General $MAPbI_3$ Fabrication.

The hole transport layer (HTL) was prepared according to 2.3.2 Hole Transport Layer.

5.2.2 Tin Oxide ETL Fabrication – High Efficiency Build under N_2

This build procedure was followed for SnO_2 based device builds presented within this chapter, according to 2.1.4 Electron Transport Layer Preparation – SnO_2. All devices were manufactures in a glovebox environment unless otherwise specified.

5.2.3 Precursor Solution - $MAPbI_3$

Heating at 60°C and rigorous mixing was applied to the DMF/DMSO $MAPbI_3$ solution. Experimental solutions were fabricated according to Chapter 2.1.1. A 5% excess of PbI_2 was used in 5.3.16 EA vs DMC $MAPbI_3$ (5% excess) , this was done as an excess is reported to improve device performance for the DMF/DMSO solution[96]. However, we have observed no obvious difference here, in part due to the increasing complexity of conditions required to measure device peak performance which will be discussed within this chapter.

5.2.4 Electron Transport Layer – SnO_2

A tin oxide substrate was prepared according to 2.1.4 Electron Transport Layer Preparation – SnO_2 A 3:1 15% tin oxide solution to D.I water was used to achieve films with minimal pinholes.

5.2.5 Perovskite Deposition - Glovebox Devices

Samples were prepared according to 2.3.1 Perovskite Deposition - Glovebox Devices. The one step deposition method was used to spin coat $MAPbI_3$ solutions onto substrates with an anti-solvent drip of ethyl acetate (EA) or dimethyl carbonate (DMC) to crystalise the thin film. For the novel antisolvent treatments variations in volume from 200 µL to 300 µL were used and specified where applicable.

5.2.6 Spin Coating B01 $MAPbI_3$

It was anticipated that the major characteristics of the spin coating system would be a close match to A01 $MAPbI_3$. The coordinative power of the system is retained with 70 vol% of the system containing the highly coordinate, low volatility DMSO/DMPU pairing. Presented by Saliba *et. al.* as a methodology for the crystallisation of triple cation perovskite[78], and early iterations of GBL based solvent systems[204], the adapted prenucleation style of spin coating allows the formation of nucleates within the precursor, with the antisolvent applied near the end of the spin cycle, causing a rapid formation of $MAPbI_3$. Two different variations of this cycle were experimented with during investigations in B01 $MAPbI_3$ and are given as follows:

1. Step 1) 1000 rpm, 200 acceleration, 10 seconds. Step 2) 6000 rpm, 2000 acceleration, 30 seconds. → Anti-solvent applied 5 seconds from the end of the cycle. Denoted as: **1K6K.**
2. Step 1) 2000 rpm, 200 acceleration, 10 seconds. Step 2) 6000 rpm, 2000 acceleration, 30 seconds. → Anti-solvent applied 5 seconds from the end of the cycle. Denoted as: **2K6K.**

The characterisation of films in this chapter should be assumed to utilise the modified 2K6K method unless otherwise stated.

5.2.7 Back Contact Evaporation

Finally, gold wire (Au, 99.99% purity 1.0 mm thick Sigma Aldrich) was deposited following the procedure listed in 2.3.3 Top Contact Evaporation.

5.2.8 Optical and Photochemical Evaluations

Pre-cut XOP laser etched (2.8 cm^2, 2.2 mm thick, tec 15) FTO glass was cleaned with IPA and dried prior to deposition. Deposition of these films was done in ambient conditions. Films were analysed through the perovskite as FTO/PAL stacks. PbI_2 used in these ambient builds was from Sigma Aldrich (99% purity).

5.2.9 UV-Vis-NIR of Perovskite Films

$MAPbI_3$ thin films were measured on a Perkin Elmer Lambda 9 UV-Vis-NIR spectrometer according to 2.4 UV-Vis-NIR Spectroscopy.

5.2.10 Photochemical Evaluation of Thin Films Deposited from the DMC Additive System.

Steady state photoluminescence measurements were undertaken on a range of novel perovskite films to quantify differences in radiative emission from each sample at a fixed excitation wavelength. This wavelength was altered for different characterisations present within this chapter.

In section 4.3.3 Figure 65, measurements presented are uncorrected spectra taken through back of the FTO (referred to as GlassSide). Emission and excitation slit widths were set to 3.8 nm, with a larger area required due to lower emission on this side of the sample. A step size of 0.5 nm was used with a 0.2 s dwell time. A 520 nm excitation was utilised here, with each scan a single representation of the sample response under illumination. Figure 63 also measures the sample through the glass with 4 nm slit widths and a 510 nm excitation wavelength. Only 1 scan is represented for each sample. In contrast uses a 450 nm excitation wavelength on the perovskite side of the sample (PALSide), with a 2.5 nm slit width on both emission and excitation. No additional filters were used for these measurements. For this evaluation multiple measurements were taken to study photobrightening differences between deposited materials. The variation in these scans also allows for an analysis of the impact between excitation wavelength and the emissive behaviour of this novel perovskite.

Figure 65 samples were fabricated from the same precursor solution as Figure 64 after aging the precursor for 3 months. The precursor solutions had been exposed to ambient air and were sealed with parafilm for the 3-month duration. Glass/PAL was used. SSPL measurements utilised a step size of 0.1 nm, a dwell time of 0.2 s, with a slit width of 2 nm on the emission and excitation.

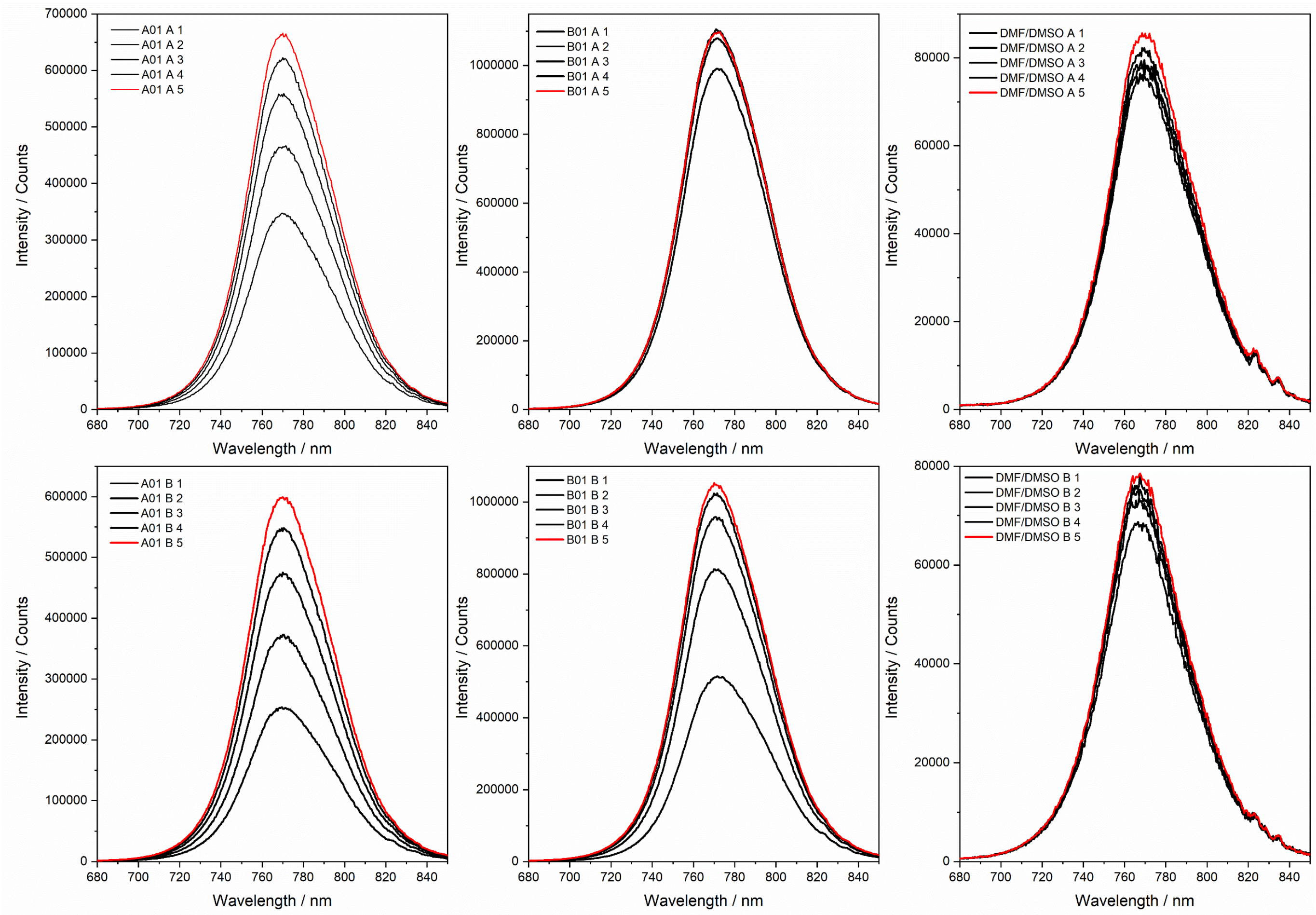

Figure 60 – Repeat SSPL measurements for Figure 64 (λ_{ex} = 450 nm).

Figure 60 is a plot showing the base spectra for the SSPL measurements. All measurements were undertaken under identical conditions with 0.5 nm step size and 0.2 s dwell time. A 1-minute delay was set up between scans with the range set to measure from 680 nm to 850 nm. These samples were left unencapsulated to observe differences in the photobrightening behaviour. The stabilised curve EM5 was taken for the plot in Figure 64 a).

5.2.11 Post Processing of SSPL Data

For Figure 63, Figure 64 a), and Figure 65 the curves were smoothed using the Savitzky-Golay method with 6 points in window and a polynomial order of 3, with the inset smoothed using 30 points in window and a polynomial order of 1. Figure 64 a) inset for the peak position uses 10 points in window and a polynomial order of 2. All data processing was conducted on OriginPro, 2020b.

5.2.12 Absorptance Scans within an Integrating Sphere

Absorptance scans were taken using the same sample architecture in the integrating sphere according to 2.5.2 Absorptance Measurements Within the Integrating Sphere.

5.2.13 XRD Analysis

XRD measurements were performed using a Bruker D8 Discover in a standard divergent slit set-up according to 2.6 X-Ray Diffraction (XRD) Analysis. The sample architecture used unencapsulated XOP (tec 15) FTO/$MAPbI_3$, with the build undertaken in ambient conditions.

5.2.14 XRD Peak Analysis

The scan range was set from 5-45° and the measurements taken using a 40kV, 40mA Copper source with a step size of 0.032°, at 2 second per step. Origin peak analyser was used to find the full width at half maximum for the 110, 220, and 310 characteristic tetragonal $MAPbI_3$ peaks. The baseline was defined manually, inputting 40-45 points. Savitzky-Golay smoothing was applied during this procedure with 3 points in window and a polynomial order of 2. The baseline was then subtracted, prior to integration with the width set to 0.7 degrees either side of the peak.

5.2.15 FWHM Analysis

FWHM values were ascertained from the peak analysis for each of the major peaks studied (110, 220, 310). Recorded values were rounded to 3.s.f. For the 110/310 peak intensity ratio, values were taken for the peak height from the peak analysis result.

5.3 Results and Discussion

5.3.1 Optimisation of the B01 system – for Enhanced Stability of the precursor solution

The purpose of this solution design is to allow for a variety of modifications to the precursor depending on the processing requirements. The candidate solutions have utilised a combination ‘fluid modifier’ of 2-MeTHF along with blending agent and perovskite antisolvent EtOH. Whilst the behaviour of this system has advantages during the deposition process, lowering the supersaturation threshold, it also limits the useful processing window for the precursor solution due to precipitate – changing stoichiometry and ink shelf life. Depending on the precise stoichiometry of the MAI and PbI_2 precursors some PbI_2 precipitate may be observed, requiring additional heating prior to deposition. To combat this undesirable effect, studies were undertaken on the efficacy of alternative ‘fluid modifiers’, with the aim of extending the useful life of the precursor solution whilst maintaining the advantageous nature of a low volatility highly coordinative solvent system. Through utilisation of the ‘green’ solvent toolkit we have looked to replace the 2-MeTHF/EtOH azeotrope with an alternative relatively volatile green solvent with a low polarity but comparable boiling point. The chemical chosen was dimethyl carbonate (DMC), a simple carbonate with low polarity[205], anticipated to have minimal interaction with the lead salts characteristic of perovskite precursor solutions. This provides fluid modification based upon miscibility with DMPU and DMSO, with a low boiling point, less viscous additive. The precursor composition is as follows:

B01 $MAPbI_3$ = 40 vol% DMSO, 30 vol% DMPU, 30 vol% DMC

For comparison against previously studied EtOH based solutions (candidates A, B, and C), this modified composition is referred to as B01. During further investigations to improve the qualities of the alternative $MAPbI_3$ films through anti-solvent engineering, this composition is designated as B01 and Candidate A is referred to as A01 and represents the 2-MeTHF/EtOH based system with greatest promise. Candidate B and C solutions were discarded after optical evaluations for comparison with the DMC containing B01 system and will not be evaluated further. These two compositions represent the best performing solutions, with A01 achieving high efficiency devices and B01 successfully stabilising the precursor and allowing anhydrous solution formulation. Due to the multi-component nature of these systems the numerical designation allows tuning of the composition for each blend, with a change to the numerical designation refereeing to a change in the ratios of solvent used in the deposition. The B01 solvent system remains stable over time, retains a 1.25M $MAPbI_3$ precursor concentration and allows for the deposition of an active $MAPbI_3$ thin film through use of an adapted prenucleation spin coating methodology. This chapter aims to evaluate the optical and photochemical properties of $MAPbI_3$ deposited from this anhydrous stable solution. Furthermore, we attempt to improve the properties of the films through antisolvent engineering techniques.

5.3.2 Optical Evaluation of B01 $MAPbI_3$

Thin films were manufactured in ambient conditions contrasting the three previously developed solvent systems against B01 and the DMF/DMSO control. Figure 61, a) shows absorbance spectra for two films fabricated from each solution. With a zoom in showing the onset of absorbance.

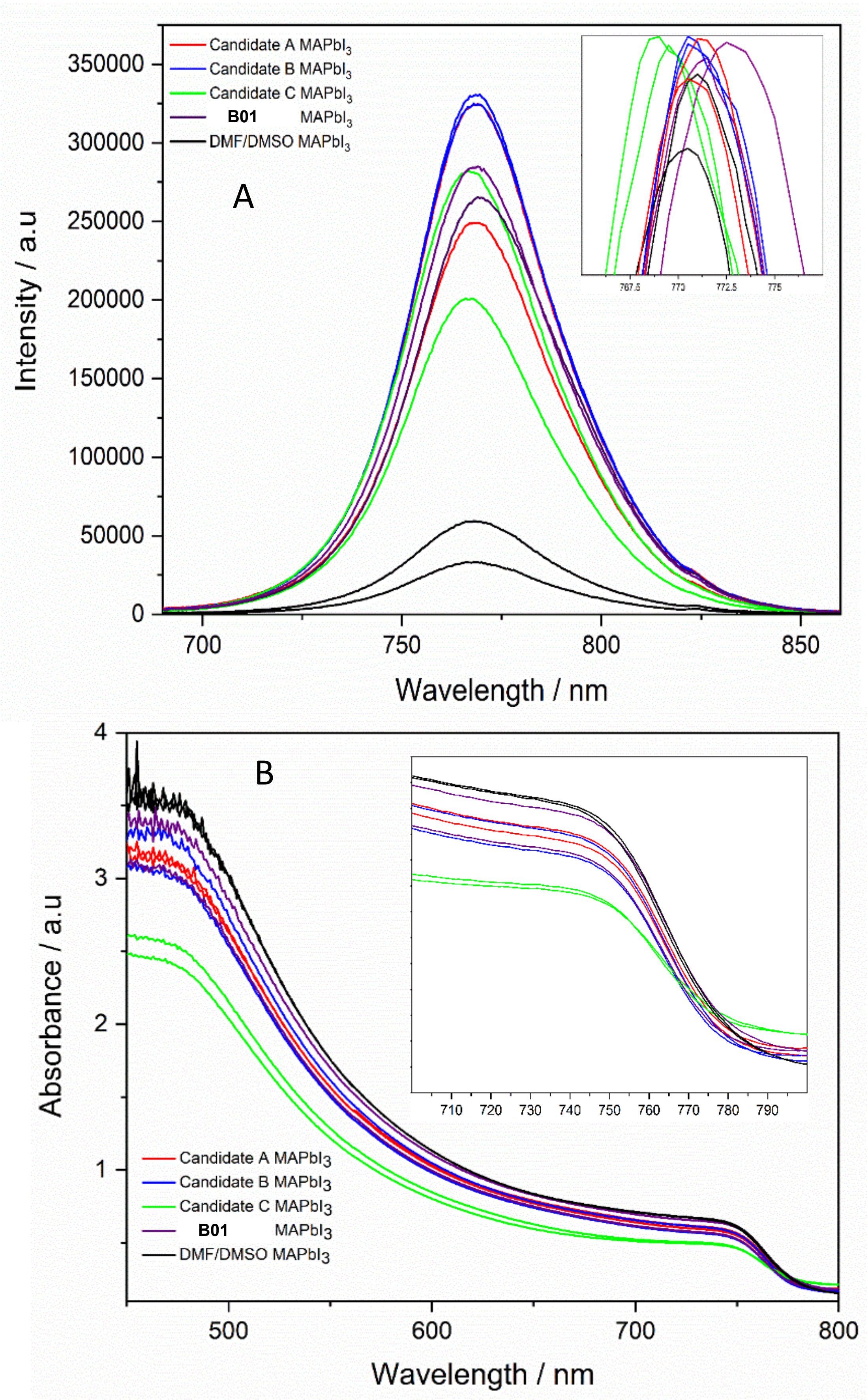

Figure 61 - A) Steady state photoluminescence spectra taken from FTO/PAL samples prepared in ambient conditions B) Absorbance spectra for Candidate solutions A, B, C, and B01 against the DMF/DMSO control. λ_{onset} of absorbance for each sample.

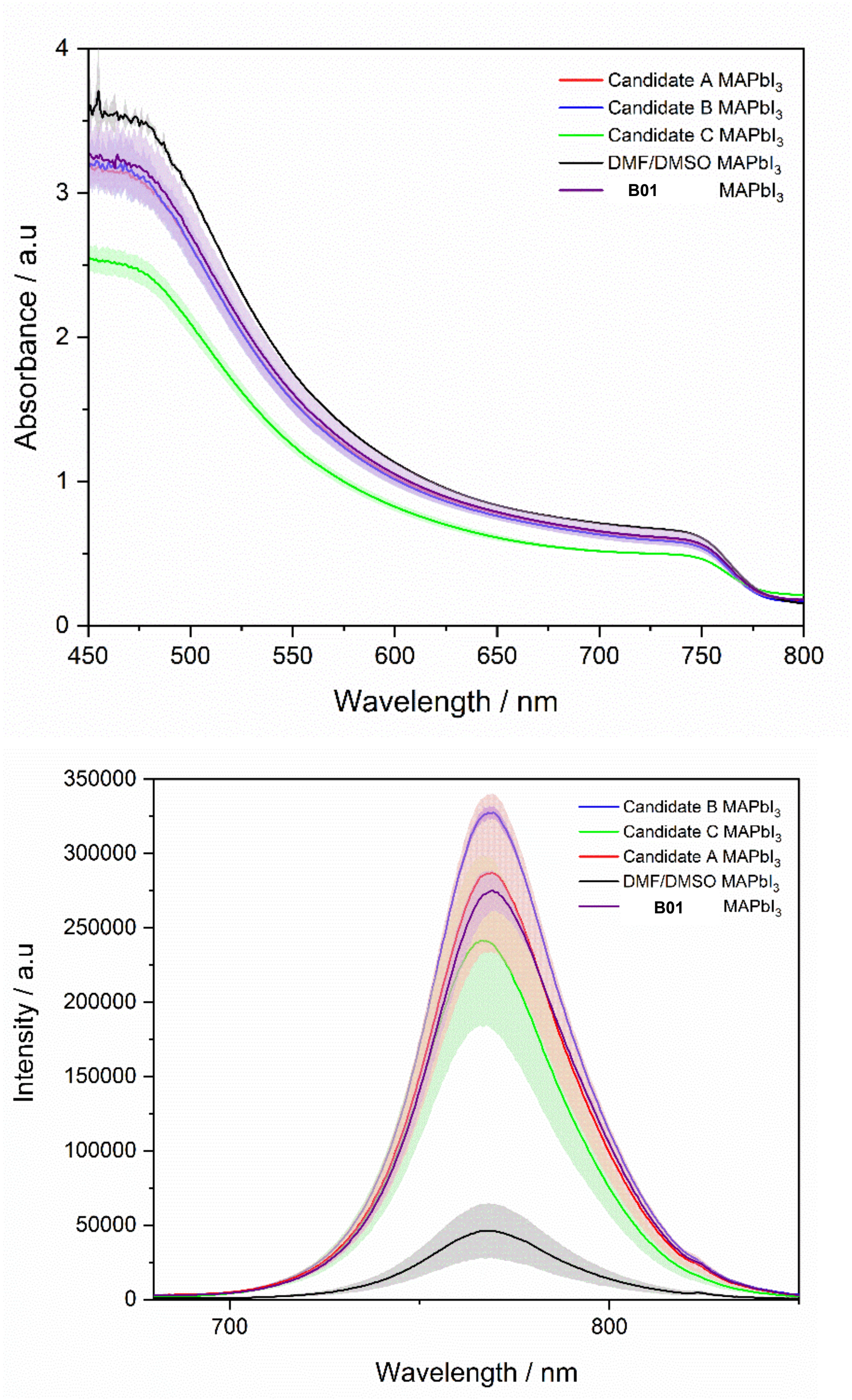

Figure 62 - Average SSPL and absorbance spectra for candidate solutions A,B,C, B01 against DMF/DMSO in ambient conditions - mean average + standard deviation.

The cast films appear reproducible, with the visibly more transparent Candidate C films exhibiting the lowest levels of absorbance. Candidate A and B show very comparable spectra with DMF/DMSO producing the highest absorbance in ambient conditions. Solution B01 shows similar characteristics Candidate A and B films as expected due to the same ratio of HCLV solvent. However, one sample in particular appears to show higher absorbance and a similar λ_{onset} as the DMF based control. Indicating a similar band gap energy.

SSPL measurements were taken to further study these films. From the peak position it is possible to see small variations in the band gap (E_G) of the material. The peaks have been processed as described in section 5.2.6. The DMF/DMSO samples suggest a characteristic $MAPbI_3$ peak at ~770 nm.

As:

$$E_G(eV) = \frac{1240}{\lambda_{Peak}(nm)} = \frac{1240}{770} = 1.61\ eV\ (3.s.f.)$$

The peaks for Candidates A and B are agreeable with this, whereas we see again a shift for Candidate C (~768) and B01 (~773). Although this shift is small it is reproducible over the two samples measured. Extrapolating likely band gap changes this equates to:

$$E_G(C) = \frac{1240}{768} = 1.61\ eV\ (3.s.f.)$$

$$E_G(\frac{D}{B01}) = \frac{1240}{773} = 1.60\ eV\ (3.s.f.)$$

This gives a difference of around ~100 meV in the determination of likely band gap energies between Candidate C and B01. Figure 62 gives average curves for each solvent system with one standard deviation from the mean expressed as the shaded region. B01 retains similar absorbance properties as the Candidate A, and B systems, with a more stable precursor formulation.

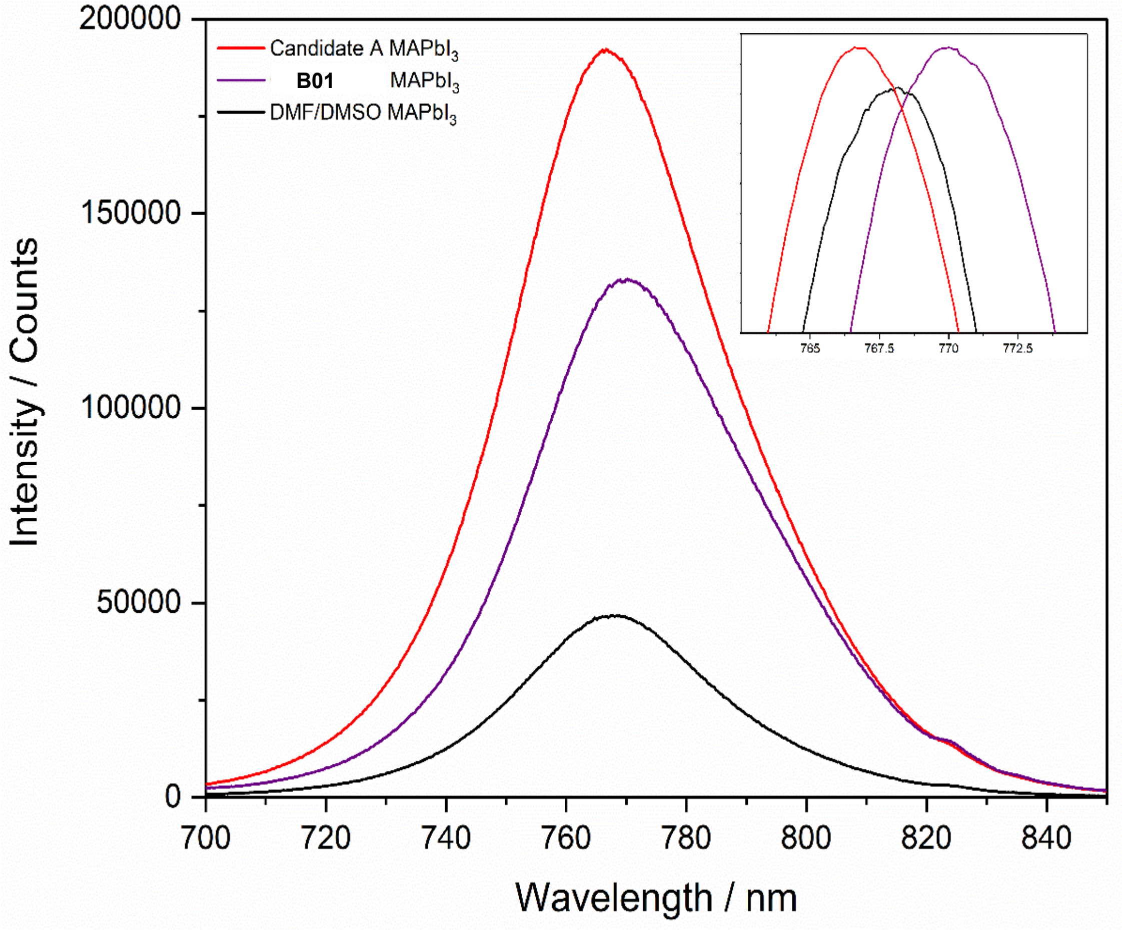

Figure 63 – B01 $MAPbI_3$ SSPL against the control and the A01 solution (510 nm excitation 3 nm slit width).

Figure 63 uses single measurements for each film, with films exposed to a light environment prior to measuring (light soaked). Measurement parameters are available in section 4.2.6. This plot shows a repeatable slight red shift for the B01 peak, observed in previously presented SSPL builds.

5.3.3 Aging the Precursor Solution

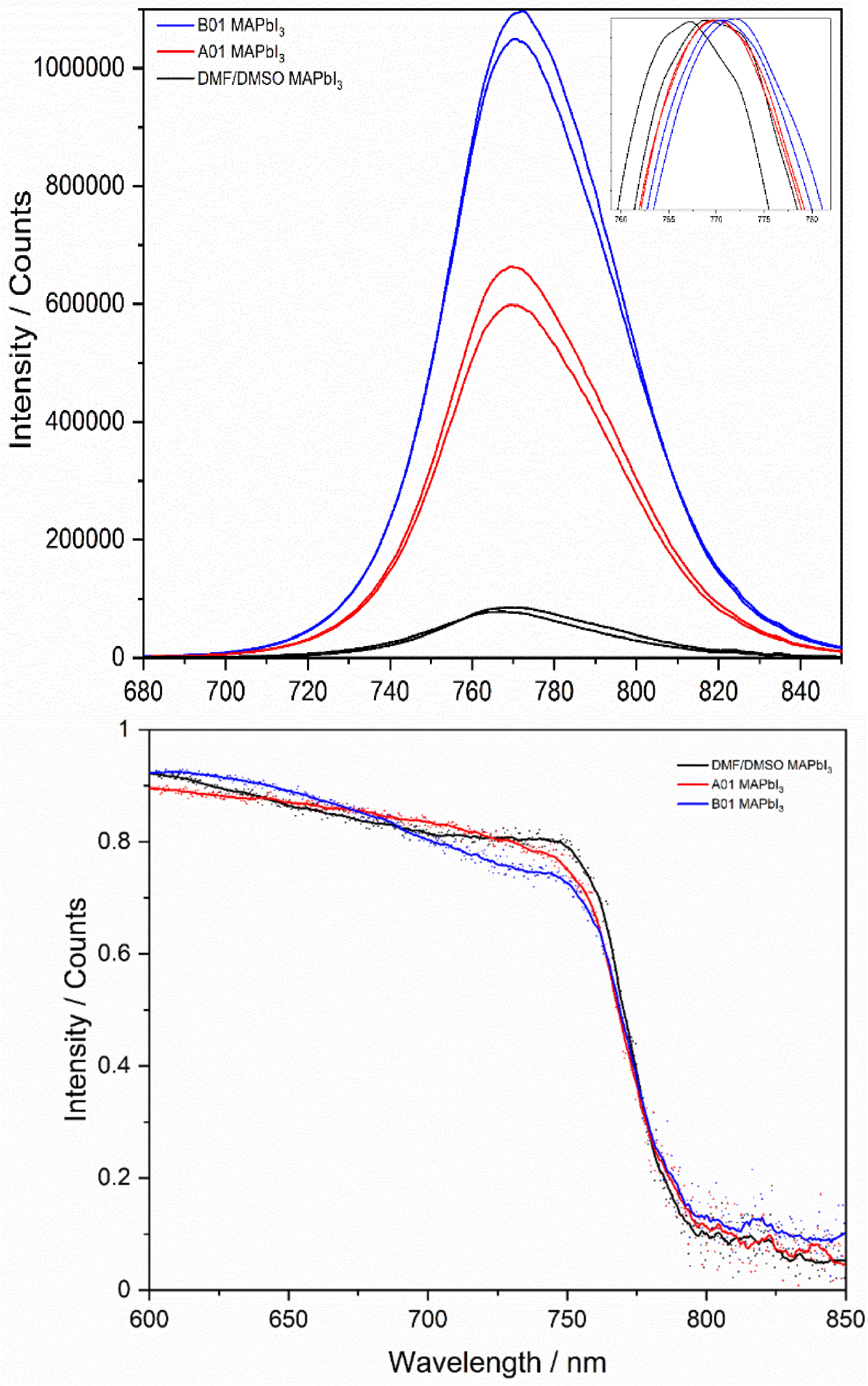

Figure 64 - a) SSPL curves for A01 and B01 films deposited in ambient conditions. A 450 nm excitation light was used with 2.5 nm slit width. b) Absorptance measurements for A01 and B01 MAPbI$_3$ thin films against a DMF/DMSO Control

A further comparison of the absorption and photoluminescence properties was conducted on films deposited from the A01 and B01 solvent systems. This was undertaken to confirm the characteristics of the 'stable' B01 solvent system.

Figure 64, b) suggests that in ambient conditions the DMF based film absorbs light to a greater extent than A01 or B01 films. A01 shows slightly higher absorptance than the B01 solution, with the λ_{onset} very similar for each film.

These films were then measured under steady state excitation, with two films measured per solvent system. The highest fluorescence emission observed was from solution B01 films, despite these films showing lower absorptance. This coincides with an analysis of the peak position, suggesting longer wavelength emission for B01. A01 samples both show a peak at ~770 nm, with DMF/DMSO samples suggesting a small shift in at least one sample of several nm. The differences in peak position are still small, with much larger differences observed in terms of PL magnitude.

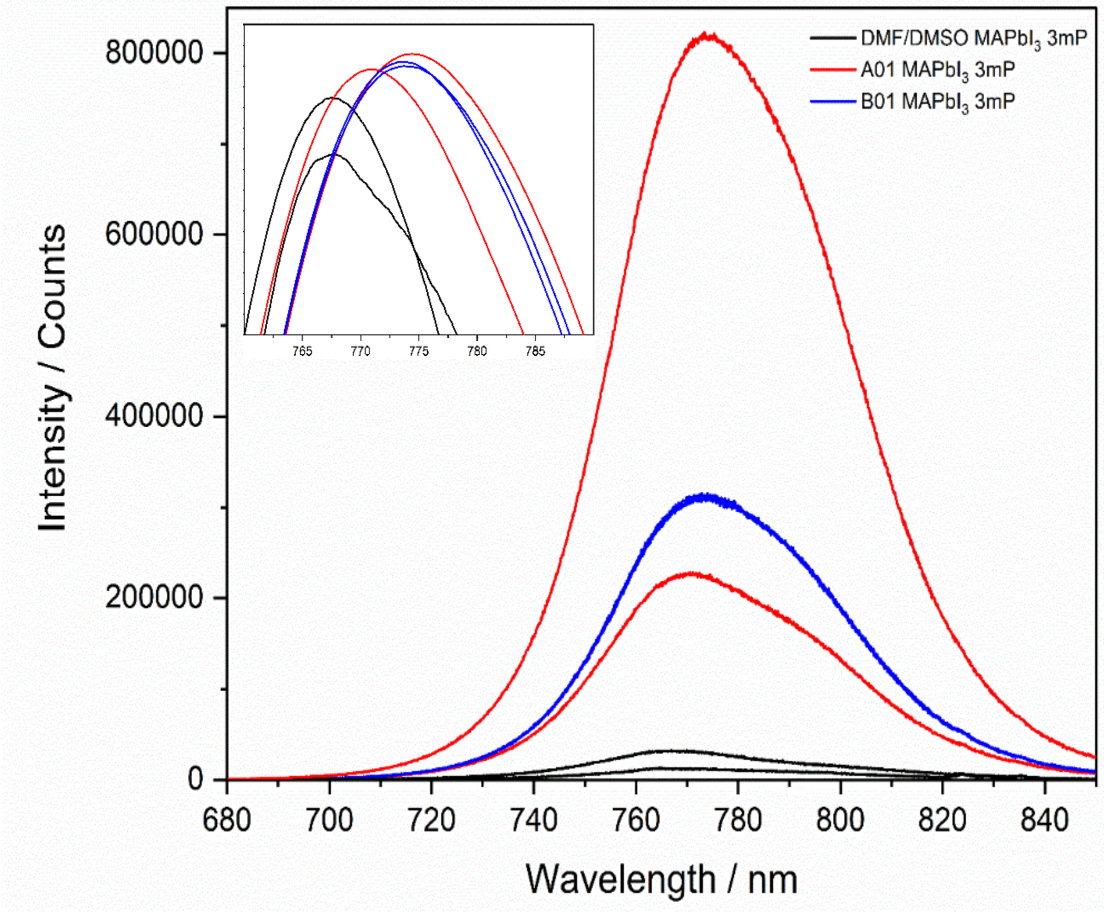

Figure 65 - Films deposited from the same A01, B01 and DMF/DMSO MAPbI$_3$ solutions as Figure 64 , after being aged for 3 months. Λ_{ex} = 450 nm.

A final characterisation of these solutions was done after a period of 3 months (Figure 65). The slit width required to measure these samples was decreased from the initial measurements, indicating an increase in the emission of the most emissive sample. A01 films show very high variability here, in contrast to the B01 films which are overlapping in the spectra. The DMF based films have a dramatically lower PL by comparison with Figure 64.

Different excitation wavelengths have been utilised throughout this study. With use of 520 nm, 510 nm and 450 nm in this results section. The emission recorded from the candidate solutions relative to the control appears to show a trend of increasing emission difference as the excitation moves to shorter wavelengths, i.e higher energy excitation.

Ultimately, both the A01 and B01 solutions for $MAPbI_3$ allow for highly emissive thin film deposition after 3 months of aging, far greater than the emission achieved for DMF based films.

5.3.4 1.5 cm^2 Samples on FTO

Small scale samples (1.5 cm^2) were fabricated for XRD analysis. This scale was chosen to better facilitate studies into the optimum crystalline structure of the material when using alternative solvents. With larger samples inevitably containing a higher degree of impurities and defects.

5.3.5 XRD Analysis

To verify the crystalline structure of the B01 films, ambient thin films were measured using XRD.

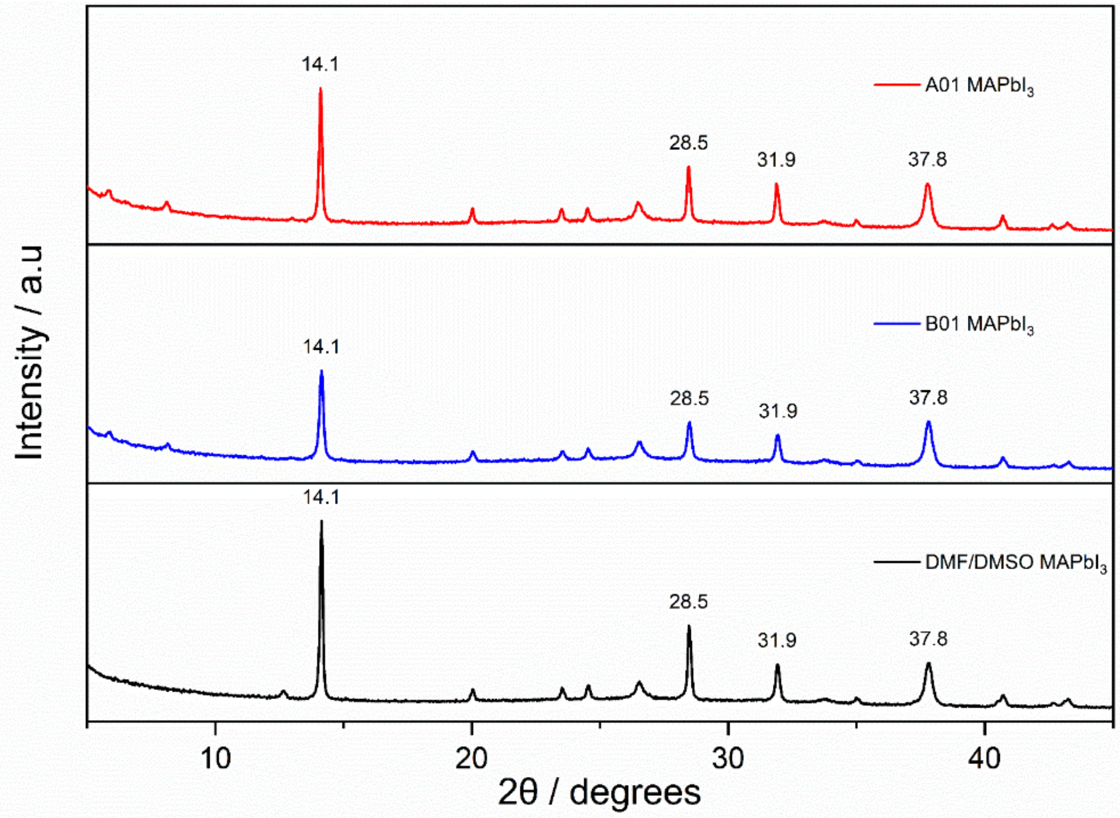

Figure 66 - XRD scans for candidate solutions A01, B01 and control (DMF/DMSO 4:1). 15 minutes scans, ambient deposition, Sigma Aldrich PbI_2.

Figure 66 displays the ambient XRD spectra. In the 110 direction, the DMF sample shows the highest peak intensity. A small peak is also present for this sample at 12.6°, attributed to PbI_2.

Table 16 - XRD Analysis for the FWHM and 110/310 Intensity Ratio

Solvent System	FWHM			110/310 Intensity Ratio
	110	220	310	
A01 $MAPbI_3$	**0.129**	**0.158**	**0.172**	**3.36**
B01 $MAPbI_3$	**0.173**	**0.203**	**0.197**	**3.36**
DMF/DMSO $MAPbI_3$	**0.124**	**0.156**	**0.189**	**4.86**

An analysis of the FWHM value for each major peak suggests a narrower peak in both the 110, and 220 directions for the DMF/DMSO $MAPBI_3$ with A01 solvent system showing a narrower 310 peak. This follows the trend of the height of the peak and in conjunction with the 110 peak intensity, indicates a higher crystallinity than either experimental sample. Assessment of the 110/310 intensity ratio provides identical values for A01 and B01 systems, with a higher ratio for the DMF/DMSO sample. This suggests during ambient manufacture, DMF/DMSO forms thin films with greater crystallinity and less disorder[173]. Small peaks below 10 degrees are also present in the B01 sample as previously reported for A01 $MAPbI_3$. This is highly indicative of $MA_2Pb_3I_8 \cdot 2DMSO$[167], trapped within the sample. For optimisation purposes we have verified the crystalline structure of the B01 $MAPbI_3$. The spectra suggest similar behaviour to the initial A01 system, with improvements needed to match the DMF/DMSO system in ambient conditions. The presence of solvated phases within the sample has also been confirmed. The removal of this inhomogeneity is an area for further improvement for the B01 solution.

5.3.6 Device Performance - Planar Architecture

To reach higher efficiencies a build was conducted under nitrogen with SnO_2 as the ETL. Three samples were manufactured with 8-pixel measurements each. Where pinoles were identified, usually indicated by PCE <1, the pixels were removed from the analysis.

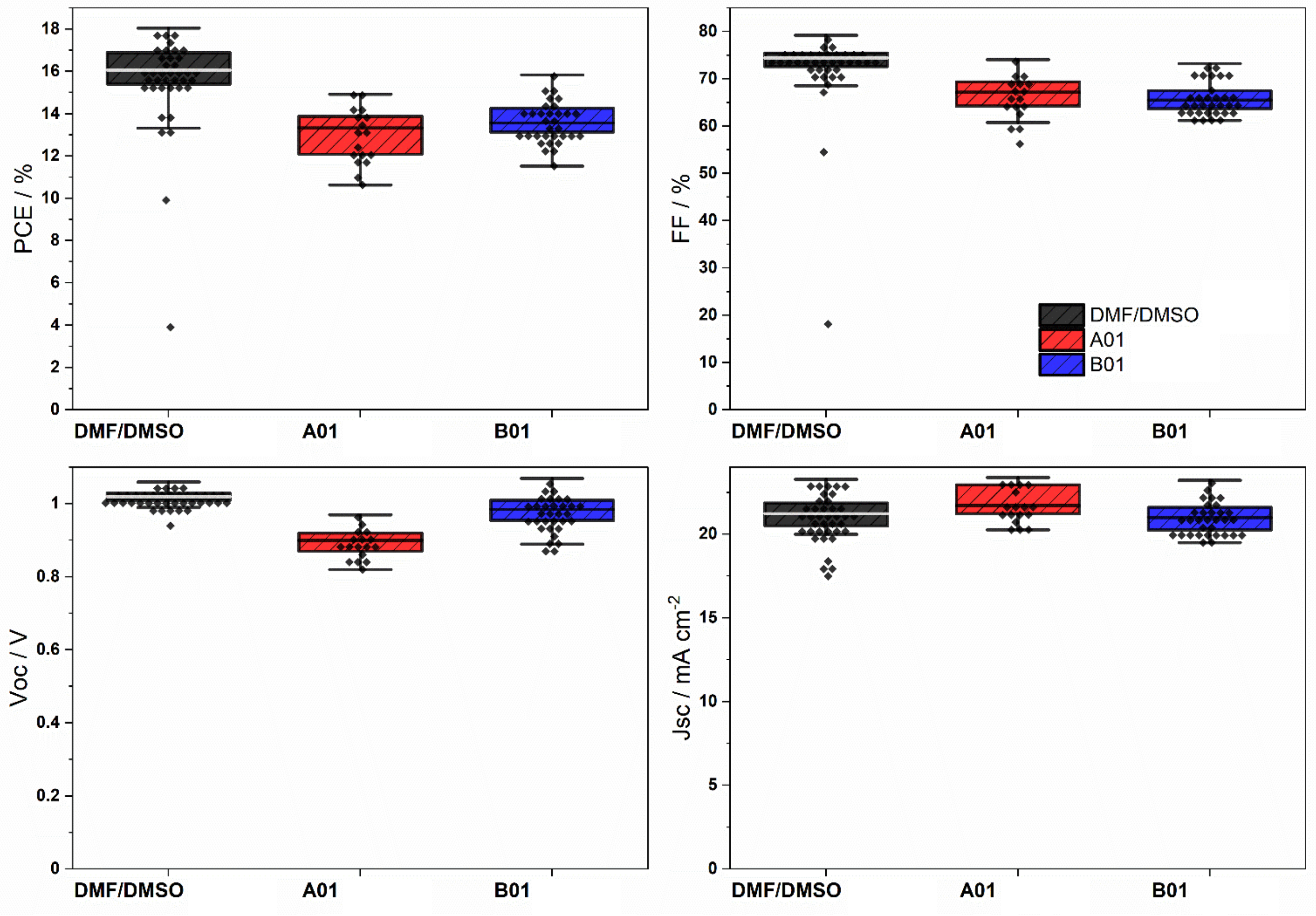

Figure 67 – Box Plots showing the performance of the A01 and B01 solvent system against the DMF/DMSO control for $MAPbI_3$.

The DMF/DMSO samples attained high efficiency during this build with high pixel to pixel uniformity (as seen in Figure 67), with B01 performing marginally better than A01 in terms of PCE averaging around 14% against 16% for DMF.

5.3.7 $MAPbI_3$ Two Week Device Aging Efficiency Study

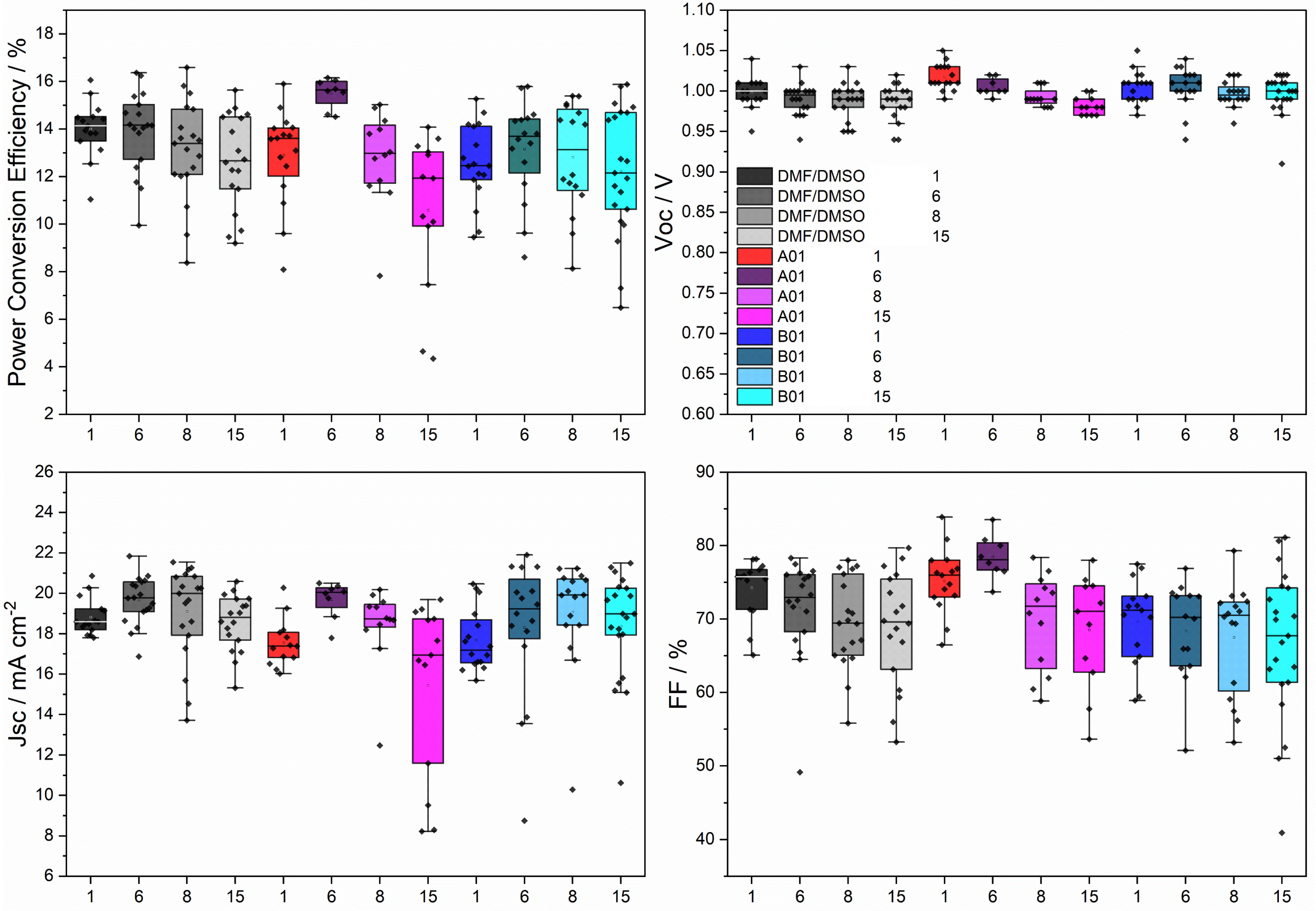

Figure 68 – Two Week Efficiency Performance for Cells Manufactured from the DMF/DMSO, A01, and B01 Systems. Four Photovoltaic Parameters are Shown

To investigate the performance of these devices over time, a two-week study was conducted with 3 samples for each solvent system (box plots depicted in Figure 68), and 4 measurements taken within a two-week period corresponding to days 1, 6, 8, and 15. Complete devices were aged for the stated period stored in dark conditions and at open circuit. Desiccant was used to reduce humidity with the storage chamber. Initial performance for the DMF/DMSO and A01 solvent system was similar with champion pixels close to 16% and an average around 14%. Initial B01 average values were slightly lower at around 12% but with some pixels achieving ~15%. 2nd stage measurements for DMF/DMSO control devices suggest a similar average value with a greater spread, including marginally improved champion pixels. By contrast an improvement in the B01 average efficiency of ~1% was observed, attributed to an increase in the J_{SC}, and small increase in V_{OC}. A01 devices show the greatest 'improvement' during this stage with efficiencies notably higher after 5 days. Both the Jsc and FF see significant improvement, with the Voc decreasing incrementally over all measurements. Some improvement may be expected after a period of device aging[190,206–211]. This is typically within the first 2-3 days of measurement. However, for A01 samples, this effect is still pronounced after 5 days. As the build was undertaken under N_2 with DMF/DMSO and B01 containing anhydrous solvents, one explanation for this dramatic increase in A01 could be the inclusion of moisture within the film. Humidity treatments have shown to improve perovskite performance through partial dissolution and recrystallisation of the outer layer of the perovskite crystal, reducing defects and grain boundaries and increasing grain size[209]. It should also be considered that at least one A01 sample had failed by this stage of the experiment, showing a high degree of variability and a possible link between the mechanism of improvement to the PCE% and degradation. This potential improvement could ultimately lead to advanced degradation pathways within the film after the initial performance boost, as evidenced by the subsequent decline in A01 samples. The H_2O-free B01 precursor maintains pace with the control DMF/DMSO solution indicative of performance degradation to be expected in ambient/humid environments[206,207,211].

5.3.8 Antisolvent Engineering for Alternative Solvent Systems

In this section the use of dimethyl carbonate (DMC) as both a precursor solvent and processing solvent was investigated. For reference, the DMF/DMSO and A01 solution provide contrast with films deposited with EA and DMC.

Table 17 – Colour Coding for the Solvent Systems and Anti-solvent Combinations

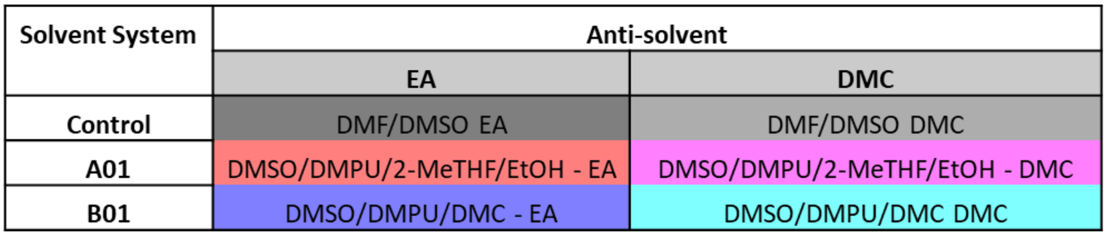

Solvent System	Anti-solvent	
	EA	DMC
Control	DMF/DMSO EA	DMF/DMSO DMC
A01	DMSO/DMPU/2-MeTHF/EtOH - EA	DMSO/DMPU/2-MeTHF/EtOH - DMC
B01	DMSO/DMPU/DMC - EA	DMSO/DMPU/DMC DMC

5.3.9 Synergistic Approach to Solvent Extraction

The formulation of these solvent/anti-solvent pairings leads to certain similarities between solvent systems. For the DMF/DMSO solution an investigation of the antisolvent DMC introduces a novel green solvent into the manufacture of lab scale devices. The A01 solution contains the same core solvent combination as B01, with DMSO and DMPU investigated with both antisolvents. B01, however, includes the anti-solvent DMC within the precursor ratio at a higher volume % than previously reported[202,203], representing 30 vol% of the solution. This solution, therefore, has a high miscibility with the tertiary component, hypothesised to create instant supersaturation of the spinning film without the undesirable side effect of precipitation. The evaluation of these six solutions was undertaken *via* optical, photochemical, and structural evaluation to assess their suitability for device manufacture.

5.3.10 Optical Evaluations

Films were deposited on FTO and coated with PMMA to prevent oxygen interactions within the perovskite. A step size of 0.5 nm, with a 0.3 s dwell time and bandwidths of 2.5 nm on the excitation and 0.25 on the emission were used. A blank sample of FTO/PMMA (1M) was used in the direct position prior to absorptance analysis.

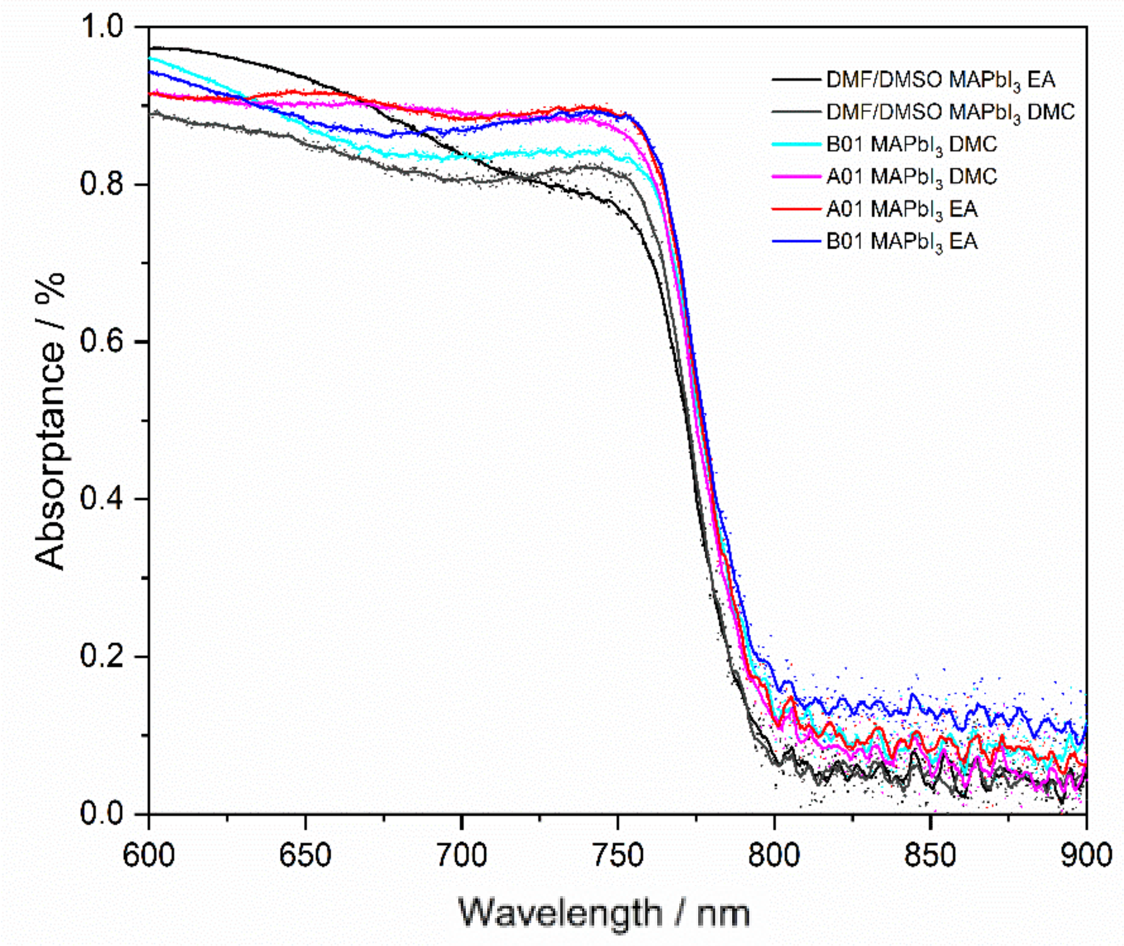

Figure 69 - Absorptance for three solvent systems using both EA and DMC as antisolvents.

Fresh samples were fabricated to analyse the initial absorptance and steady state photoluminescence of the films cast from each solvent system. The two antisolvents were utilised to crystalise the films with six unique samples for study as listed in Table 17. Figure 69 shows the 'fresh' film absorptance with the DMF-cast samples suggesting negligible difference between the absorbance onset for the films. The absorptance of the A01 and B01 systems are shifted in relation to the control and maintain good agreement regardless of the anti-solvent used.

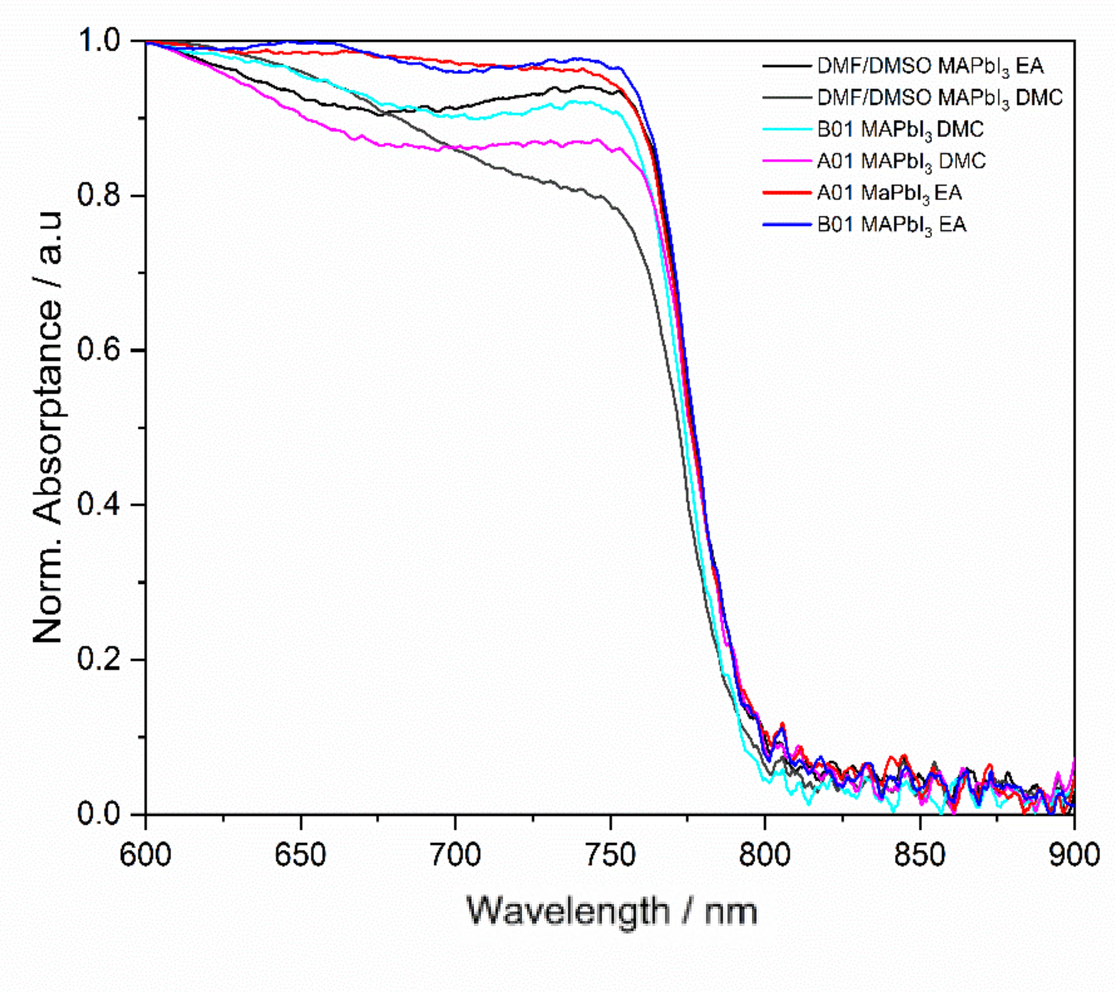

Figure 70 - Figure 69 absorptance spectra, normalised to highlight differences between the films.

Through normalising the curves differences in the absorptance spectra are enhanced (see Figure 70), Both the A01 and B01 EA cast films suggest the steepest rise in absorptance through the range 750 nm to 800 nm, with their DMC cast films both showing an initial reduction in absorptance from 750 nm to 600 nm. The same trend is evidenced for the DMF/DMSO cast films with the EA film showing greater absorbance in the 750 nm to 675 nm range before the DMC film reaches comparable absorptance. This method provides a reliable comparison due to the visual differences apparent in films cast from different solvent systems and anti-solvent pairings. Sample reflectance is accounted for within this measurement, a key parameter to control during such solvent comparisons. This data also provides an indication of the absorption properties over the material band gap range for reference in later light induced comparisons.

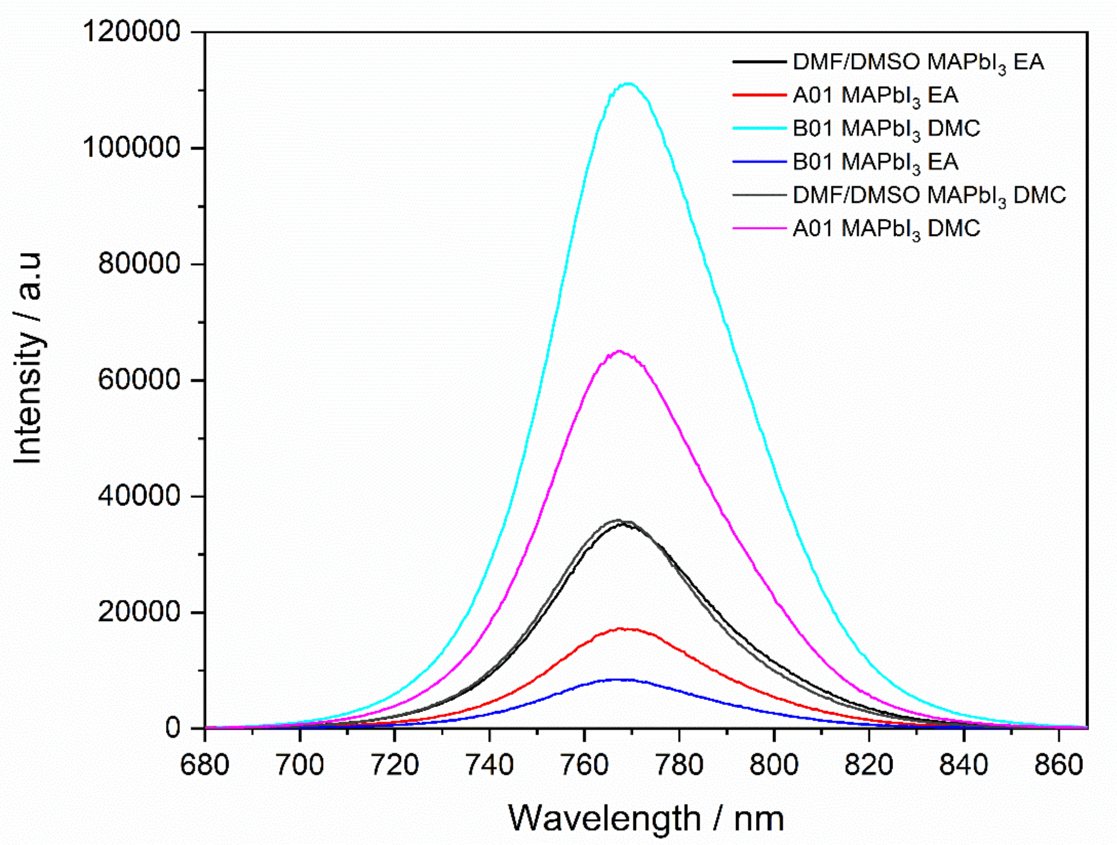

Figure 71 - Steady State Photoluminescence for the Evaluated Films (0.5 nm, 0.2 s dwell 3 scan, PMMA, 2.4 ex BW – Samples used for XRD in Figure 74)

Figure 71 shows the steady state photoluminescence of 'fresh' films cast from the competitor solvent systems and anti-solvents. The DMF system here suggests again very little difference in film PL using the alternative anti-solvent DMC. Much larger magnitude differences can be seen for the candidate A01 and B01 systems. For this study, taken in ambient conditions, the EA films suggest lower PL emission than the DMF counterparts. The DMC films, however, show a dramatic increase in PL, with the greatest difference between the B01 EA and DMC cast film. This result provides and impetus to analyse the synergistic relationship between the addition of the anti-solvent within the precursor solution. Hypothetically, the 30 vol% of DMC in the precursor solution is readily removed upon DMC anti-solvent addition. This relationship is unique to the B01 DMC sample and provides a large increase in film PL. This coincides with the qualitative observation of a more specular, less cloudy film.

5.3.11 Solution Aging 1m $MAPbI_3$ Precursor

A competitor solvent/anti-solvent system will provide additional benefit for commercial application if the precursor solution can remain stable over time. For a technology such as perovskite, in its infancy as far as commercial scale up, the reference point for performance is the highest quality system currently in use (DMF/DMSO). The shelf-life stability of this precursor ink is also under studied, however. Due to this, 'reasonable' timescales have been chosen to reflect best and worst-case scenarios encountered within industry. For the purposes of this study, it is considered likely that commercial perovskite inks will require manufacture and storage prior to deposition through screen printing or R2R. An initial benchmark of 1 month was chosen as a first stage with reactions occurring within the precursor evident after this period of storage. It is also worth noting that until these inks reach commercial benchmarks, there may be additional chemistry which requires evaluation at a later date.

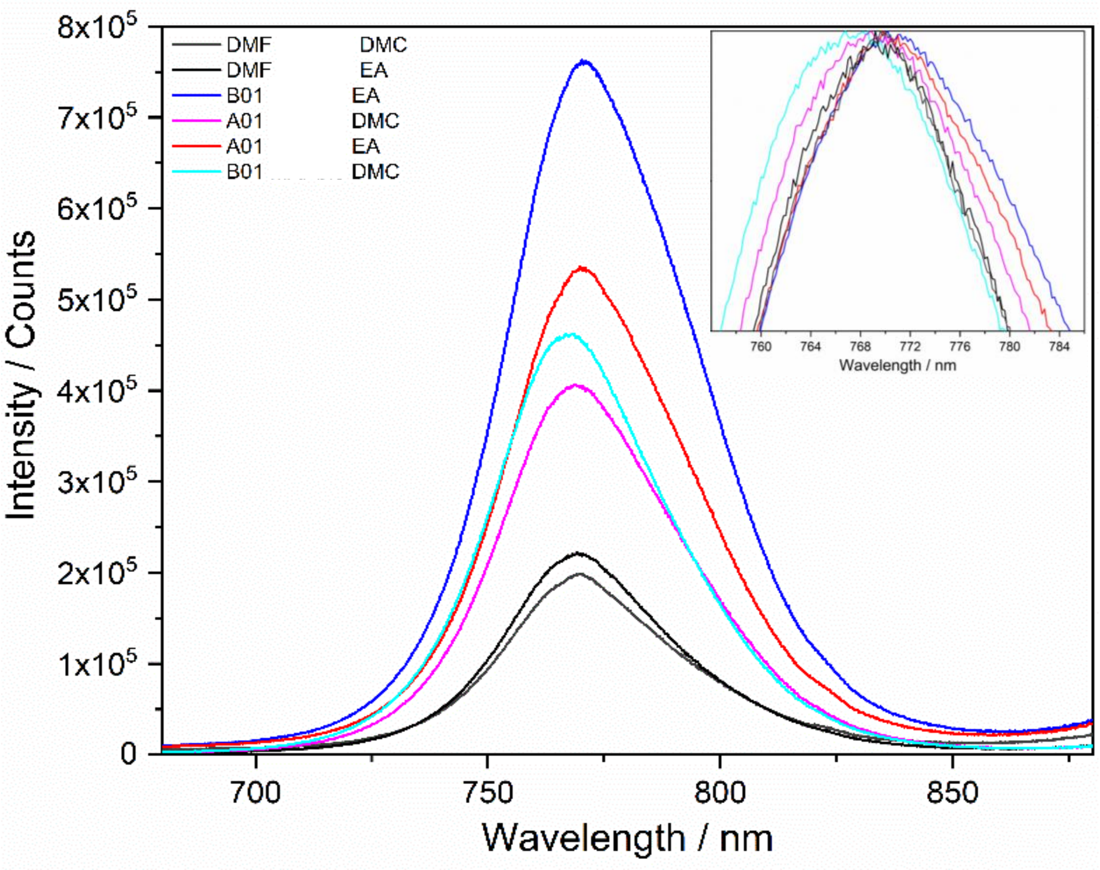

Figure 72 - Steady state PL spectra for A01 B01 and DMF/DMSO perovskite inks aged for 1 month (4nm BW, 0.2 step size 0.2 s dwell time).

Figure 72 provides the steady state PL of films cast from the candidate and control $MAPbI_3$ precursor solutions after 1 month of solution ageing. The insights provided by this study suggest that the candidate solutions can be used to cast films in ambient conditions, which exhibit greater PL than the standard DMF/DMSO solution. Both A01 and B01 show and improvement in in terms of PL magnitude alone suggesting a greater level of intrinsic solution stability. However, the greatest change is in the films cast with EA as the anti-solvent. These films have now surpassed their DMC counterparts in terms of 'fresh' film PL from the aged solution. The reaction mechanisms present within the precursor are not yet understood, leading to uncertain conclusions regarding the use of anti-solvent. The presence of additional chemicals may though serve to change the dynamics of the anti-solvent addition. This is seen to be unfavourable to a greater extent where DMC is used with the candidate A01 and B01 solutions, however, may be equally applicable to the DMF/DMSO solution with both EA and DMC usage.

The peak of the PL emission remains relatively consistent for the DMF/DMSO samples. A more significant change is noted for the candidate A01 and B01 solutions, with a slight shift to lower wavelengths noted with DMC application.

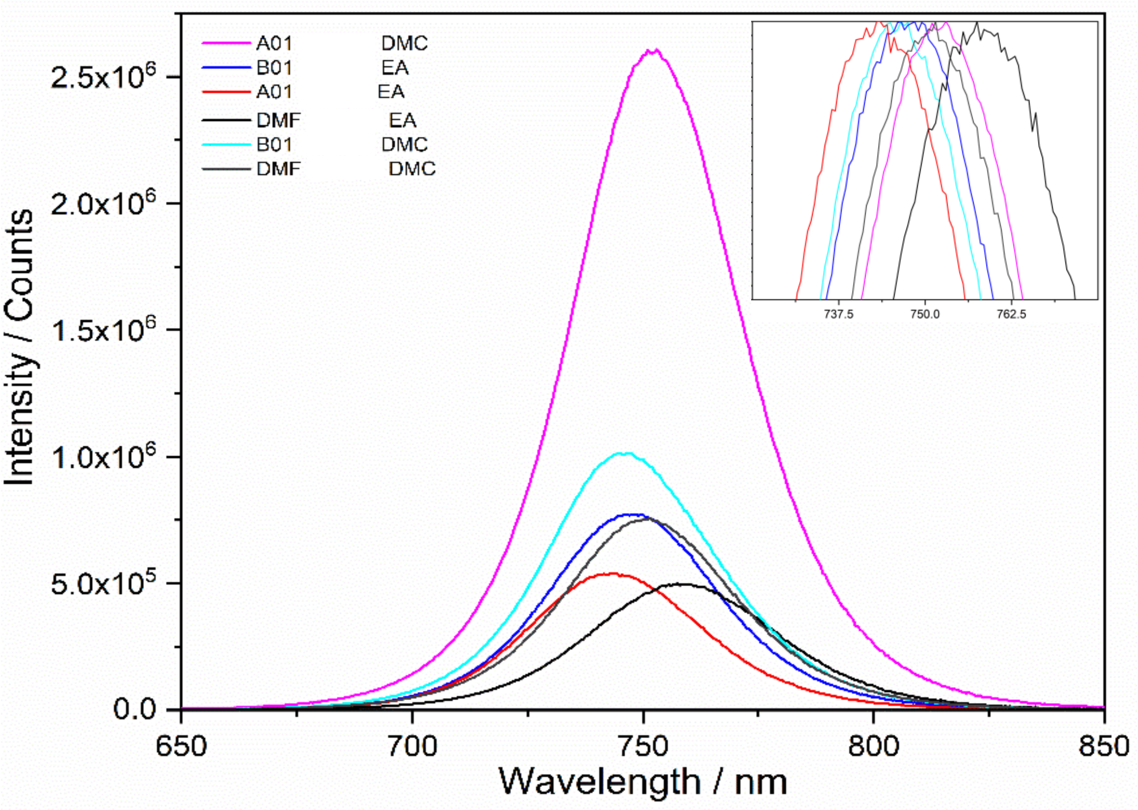

Figure 73 - The same films measured with a reduced band width after 6 days of storage.

A further consideration for commercial application is whether the cast film can remain stable over time. The introduction of additional chemicals to the colloidal ink triggers the potential for residual chemical changes to persist within the film prior to annealing and encapsulation. Any such reduction or alteration of the material represents a significant pathway reducing the lifetime of such devices. The $MAPbI_3$ composition is known to be unstable under moisture and light exposure.

Large changes are visible in the optical band gap of the material. One potential explanation for this behaviour is the re-emergence of solvated phased within the same, which have been demonstrated to cause a widening of the bandgap and subsequent band edge peak shift. The exact nature of this change is unknown but is thought to be due to inadequate solvent removal followed by a reduction to an intermediate phase over time.

In Figure 73, the magnitude and peak position of the PL emission also shows dramatic changes after 6 days of aging. All of the peak positions are shifted to lower wavelengths. For the DMF samples, the EA cast film shows the smallest peak shift at 762.5 nm. With the lowest PL magnitude measured. The DMC sample retains a higher PL, with a greater reduction in PL peak position. For the candidate solution A01, the EA film suggests the greatest change in peak position at around 740 nm. The DMC equivalent exhibits the highest measured PL magnitude, with a large shift of the peak to around 752 nm. The B01 solution still retains higher PL emission than the control, with a similarly shifted peak. In both the ‘fresh’ and ‘aged’ films, the A01 and B01 DMC samples show a higher PL, with this difference reducing after the aging period.

5.3.12 Co-solvent Anti-solvent Systems

While anti-solvents are commonly used as a standalone solvent, several cosolvent combinations have been reported in literature such as modification of EA with hexane, leading to larger grains as a result of retarded crystallisation[212]. Other studies have modified the problematic CB with additives such as EtOH[185], 2-pentanol[213], and ACN[214].

To further probe the efficacy of the novel anti-solvent DMC, a cosolvent composition, consisting of 50 vol% DMC to EA was used to fabricate films for XRD and PL analysis.

5.3.13 XRD Analysis for Antisolvent Films - Glovebox Film Study

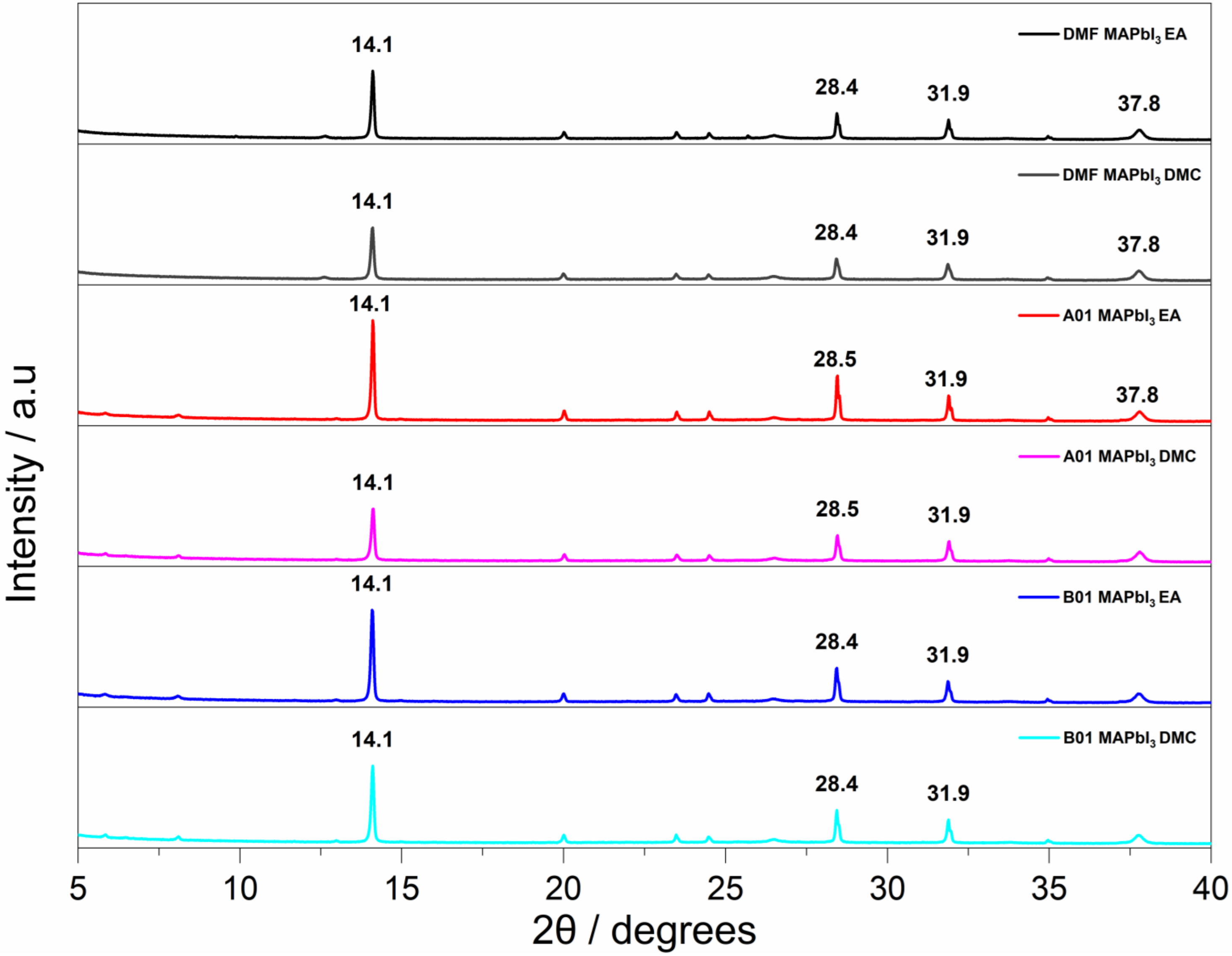

Figure 74 - XRD of films fabricated in a nitrogen atmosphere and evaluated in terms of their steady state PL in Figure 71.

XRD (Figure 74*)* provided the analysis of films deposited under nitrogen and cast with the anti-solvents EA and DMC. The visible peaks show good agreement between samples – cast from the same precursor solution. However, the 110 plane intensity decreases for all samples upon application of DMC as the antisolvent. Low angle peaks are also present for the A01 and B01 solutions. These peaks, attributed in our prior work to solvated phases within the sample, are still present regardless of the antisolvent used. This result further reinforces the nature of these peaks to the coordination of the precursor solution itself as opposed to solvent – anti-solvent interactions.

Table 18 – Samples manufactured using EA as the antisolvent. The FWHM is reported along with the consequent estimation of crystallite size utilising the Scherrer equation. The peak ratio between the 110 and 310 plane is also shown, indicative of ordered MAPbI$_3$ crystal orientation.

DMF/DMSO MAPbI$_3$ EA					
FWHM	**Peak Position**	**Peak Height**	**Scherrer Equation (k=0.94)**	**Peak Ratio**	
0.100	14.1	243	82.3	3.57	110/310
0.122	28.4	91	65.9	2.67	110/220
0.112	31.9	68	71.2	1.34	220/310
A01 MAPbI$_3$ EA					
0.093	14.1	359	88.5	4.03	110/310
0.088	28.4	159	91.4	2.26	110/220
0.086	31.9	89	92.7	1.79	220/310
B01 MAPbI$_3$ EA					
0.103	14.1	330	79.9	4.52	110/310
0.124	28.4	121	64.8	2.73	110/220
0.129	31.9	73	61.8	1.66	220/310

Analysis of the XRD data (Table 18) for the EA cast films yields highly comparable FWHM values for the DMF/DMSO and B01 solutions over the three major peaks evaulated (110, 240 and 310). Consequently the Scherrer estimation provides similar crystallite sizes. It should be noted that the Scherrer equation has limited application within perovskites due to likely crystallite sizes rangin above 200 nm. This size is where the relationship between FWHM and crystallite size begins to deconverge. The A01 solutions suggests the sharpest peaks evaluated in all directions. The 110/310 ratio is highest in the B01 analysis at 4.52, contrasting the 4.03 result for A01 and the 3.57 for the DMF/DMSO film. These values provide a benchmark to further assess the alterations to the crystal sturcture when utilising the proposed alternative anti-solvent DMC.

Table 19 – Provides the data for the samples fabricated using the alternative anti-solvent DMC, inclusive of peak height, FWHM value, Scherrer estimation, and the 110/310 ratio.

DMF/DMSO MAPbI$_3$ DMC					
FWHM	**Peak Position**	**Peak Height**	**Scherrer Equation (k=0.94)**	**Peak Ratio**	
0.109	14.1	186	75.5	3.38	110/310
0.134	28.4	73	60.0	2.55	110/220
0.15	31.9	55	53.2	1.33	220/310
A01 MAPbI$_3$ DMC					
0.108	14.1	185	76.2	2.61	110/310
0.126	28.4	92	63.8	2.01	110/220
0.139	31.9	71	57.4	1.30	220/310
B01 MAPbI$_3$ DMC					
0.099	14.1	275	83.1	3.35	110/310
0.118	28.4	116	68.1	2.37	110/220
0.125	31.9	82	63.8	1.41	220/310

Within Table 19 the DMC equivalents were anlaysed The DMF sample cast from DMC shows good agreement with the EA sample. This is evident from the 110/310 peak ratio, relative peak positions, and the FWHM of the 110 and 220 peak. A significant difference is noted in the 310 direction, with the FWHM of 0.15 the widest of the three peaks. Through Scherrer comparison, this yields a likely decrease to the crystallite size. This trend maintains, to a lesser extent, with the A01 and B01 DMC samples, with the 310 peak suggesting broadening. A decline in the 110/310 peak intensity ratio suggests a lower level of order during crystal formation for these films fabricated under nitrogen.

5.3.14 Ambient Film Study

The interplay between precursor solvent and anti-solvent during the initial stages of crystallisation is also affected by the atmosphere present. Films were then fabricated in ambient conditions, with oxygen and moisture present, to see if these factors influence subsequent film formation. To gain a deeper understanding of the mechanisms at play within co-solvent anti-solvent systems, a 50/50 vol% anti-solvent comprising both EA and DMC was also evaluated. Differences in film absorbance were first recorded, with the role of the antisolvent acting upon the film surface investigated using the XRD technique.

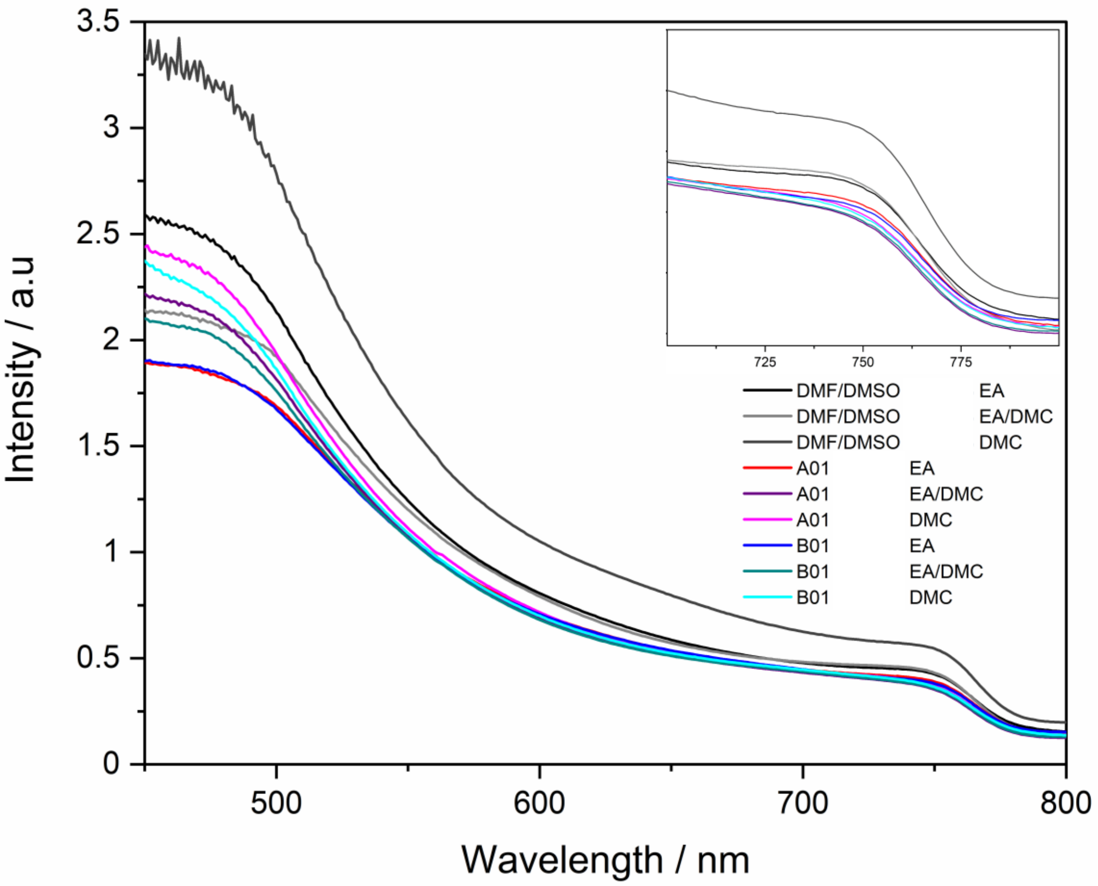

Figure 75 – Ambient films deposited for each solvent system utilising the anti-solvents EA, DMC, and a 50/50 EA/DMC combination, were assessed optically using UV-Vis-NIR spectroscopy prior to XRD analysis.

In Figure 75, during ambient deposition, the DMF films show the greatest levels of absorbance. The A01 and B01 solutions remain comparable with differences due to anti-solvent application minimal, indicating similar film absorbance.

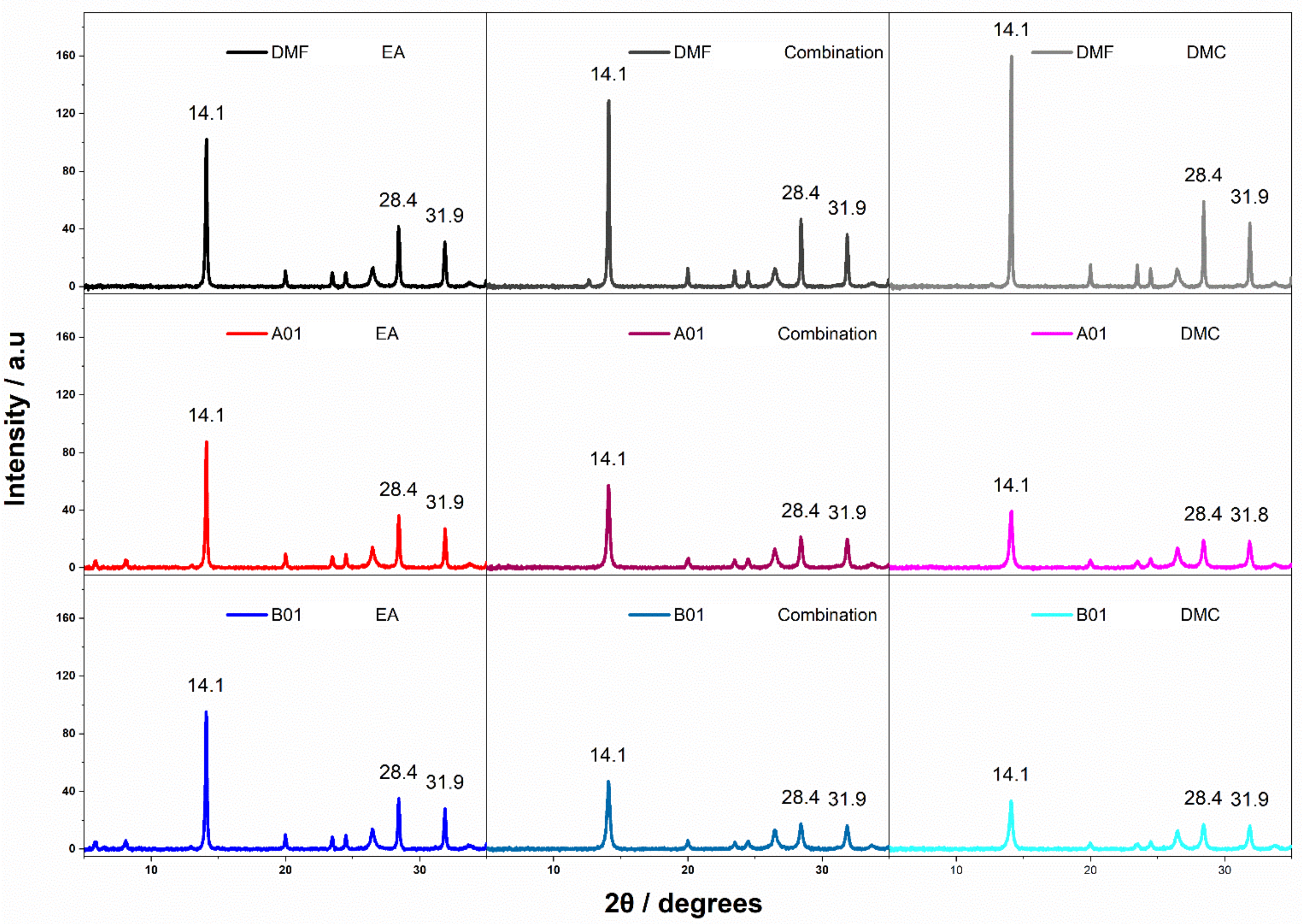

Figure 76 – XRD spectra for ambient films fabricated using the anti-solvents EA, DMC and the EA/DMC combination.

XRD spectra presented within Figure 76 show a trend of 110 peak intensity over the set of samples as the antisolvent changes. The DMF samples, under ambient conditions show an initial increase for the EA/DMC combination with the greatest intensity following on with the DMC cast film. The opposite is true for both the A01 and B01 systems, with the peak intensity decreasing in increments from pure EA treatment through to the combination and pure DMC results. A further observation for the A01 and B01 films show the presence of low angle peaks in the EA sample only, in contrast to glovebox fabricated films in Figure 74. Both the EA/DMC combination and pure DMC cast films suggest no trace of additional peaks, creating a spectrum more aligned with the often-used DMF/DMSO system.

Table 20 – Major peak positions for each of the samples evaluated in this study with the respective peak height and FWHM value.

	DMF $MAPbI_3$			A01 $MAPbI_3$			B01 $MAPbI_3$		
	Peak Position	FWHM	Height	Peak Position	FWHM	Height	Peak Position	FWHM	Height
EA	14.1	0.140	102.3	14.1	0.136	87.7	14.1	0.139	95.1
	28.4	0.166	41.5	28.4	0.162	36.4	28.4	0.160	35.0
	31.9	0.176	30.7	31.9	0.181	27.3	31.9	0.167	28.0
EA/DMC	14.1	0.130	128.9	14.1	0.221	57.2	14.1	0.252	47.0
	28.4	0.149	46.5	28.4	0.230	21.1	28.4	0.274	17.5
	31.9	0.164	35.8	31.9	0.238	19.8	31.9	0.289	16.3
DMC	14.1	0.109	159.8	14.1	0.245	39.0	14.1	0.260	33.4
	28.4	0.129	59.0	28.4	0.256	18.5	28.4	0.272	16.9
	31.9	0.155	44.2	31.8	0.251	18.4	31.9	0.256	16.2

Table 20 shows the numerical analysis of the XRD spectra for the ambient film study. When deposited in ambient conditions, the FWHM value for all films studied increases. The peaks are uniformly broader than those manufactured under nitrogen. This broadening, though linked to crystallite size through the Scherrer equation, is thought to be an indicator of film crystallite quality, with wider peaks suggesting a lower emission intensity across the sample set. The difference in environmental conditions suggests that the presence of both oxygen and moisture within ambient air influences the solvent/anti-solvent interaction. This influence determines further film quality and crystallinity, relevant to the application of alternative solvent systems to lower cost scalable production methods.

5.3.15 Device Performance

The antisolvent DMC showed greatest promise with the DMF/DMSO system, as evidenced by a greater intensity of the 110 peak. The films produced under nitrogen appear to show higher film crystallinity, whilst reducing variables likely to impact the solvent/anti-solvent interaction. To study this influence within application, The DMF/DMSO solvent system was used to manufacture high performance devices in a GB environment for optical, PL and performance evaluations.

5.3.16 EA vs DMC $MAPbI_3$ (5% excess)

The $MAPbI_3$ solution contains an excess of PbI_2 (5%), representing the most highly efficient devices for performance comparison. Alternative anti-solvents are required to compete with the established solvents currently in use, without negatively impacting device PCE or long-term stability. The DMF/DMSO solvent system was used to retain the $MAPbI_3$ precursors prior to fabrication with the traditional anti-solvent EA and the novel anti-solvent DMC.

5.3.17 GB Film Study

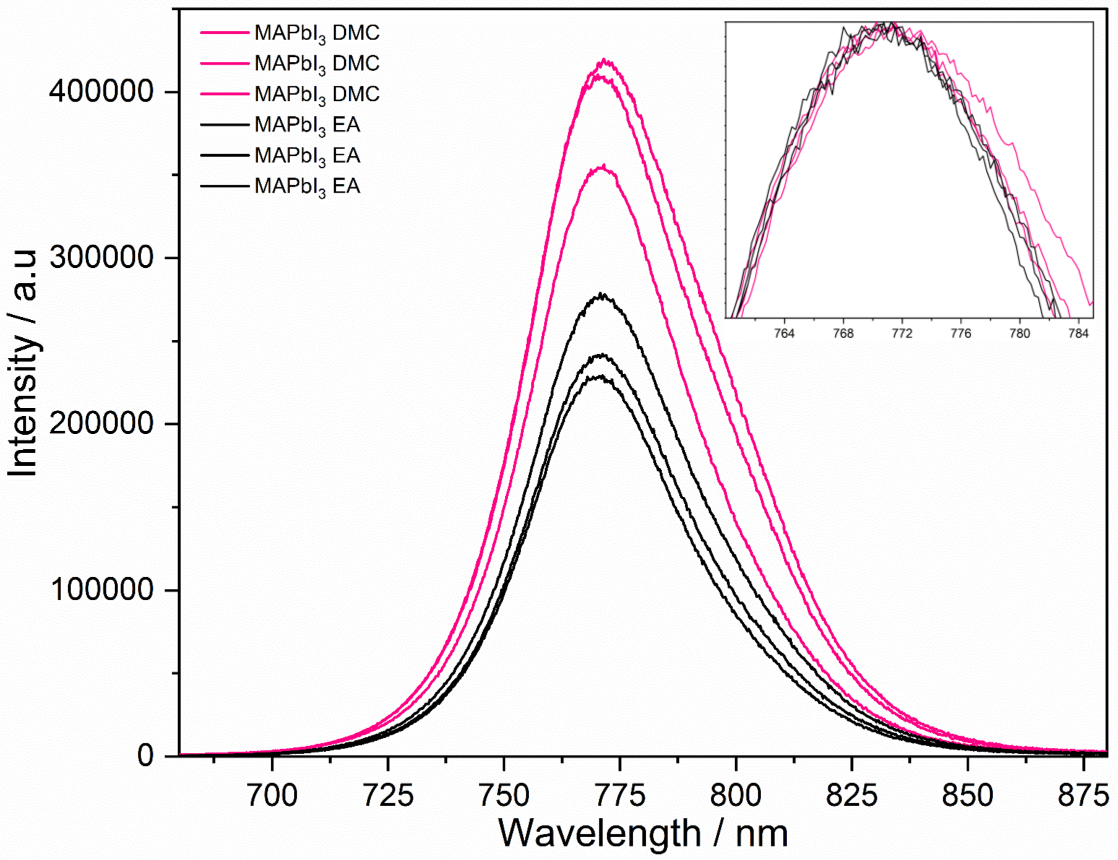

Figure 77 – Steady state photoluminesence for MAPbI$_3$ films deposited using the anti-solvent EA and the novel anti-solvent DMC (SSPL - 4.75nmBW 530ex 0.25step 0.1dwell).

For films deposited in identical build procedures, the novel anti-solvent DMC suggests a higher PL than the established EA (Figure 77). This difference is significant over the samples measured but remains a modest increase overall. The relative peak position of the films is consistent regardless of the anti-solvent used, suggesting that the material band gap is unaffected by the change in anti-solvent. As a preliminary step this indicates the potential for greater charge extraction in devices due to the higher recorded measure of radiative recombination leading to PL emission from the film. To further clarify the nature of these changes a full device build was completed to benchmark film efficiency in standard operating conditions.

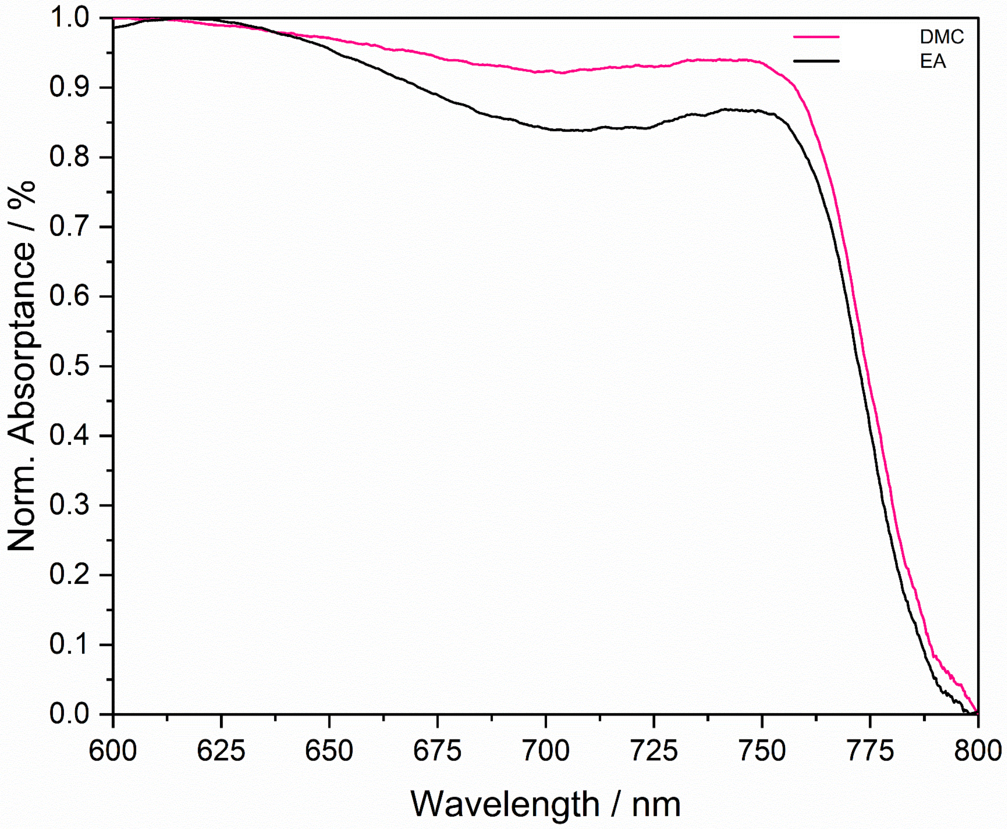

Figure 78 – Absorptance scans for the DMF/DMSO cast $MAPbI_3$ films deposited with both EA and DMC as anti-solvents.

Prior to the device build films were also analysed for their optical properties. An increase in absorption over the range 600 nm to 800 nm is noted for the $MAPbI_3$ DMC samples in Figure 78. This increase could result in part of the increased contribution to PL emission noted in Figure 77.

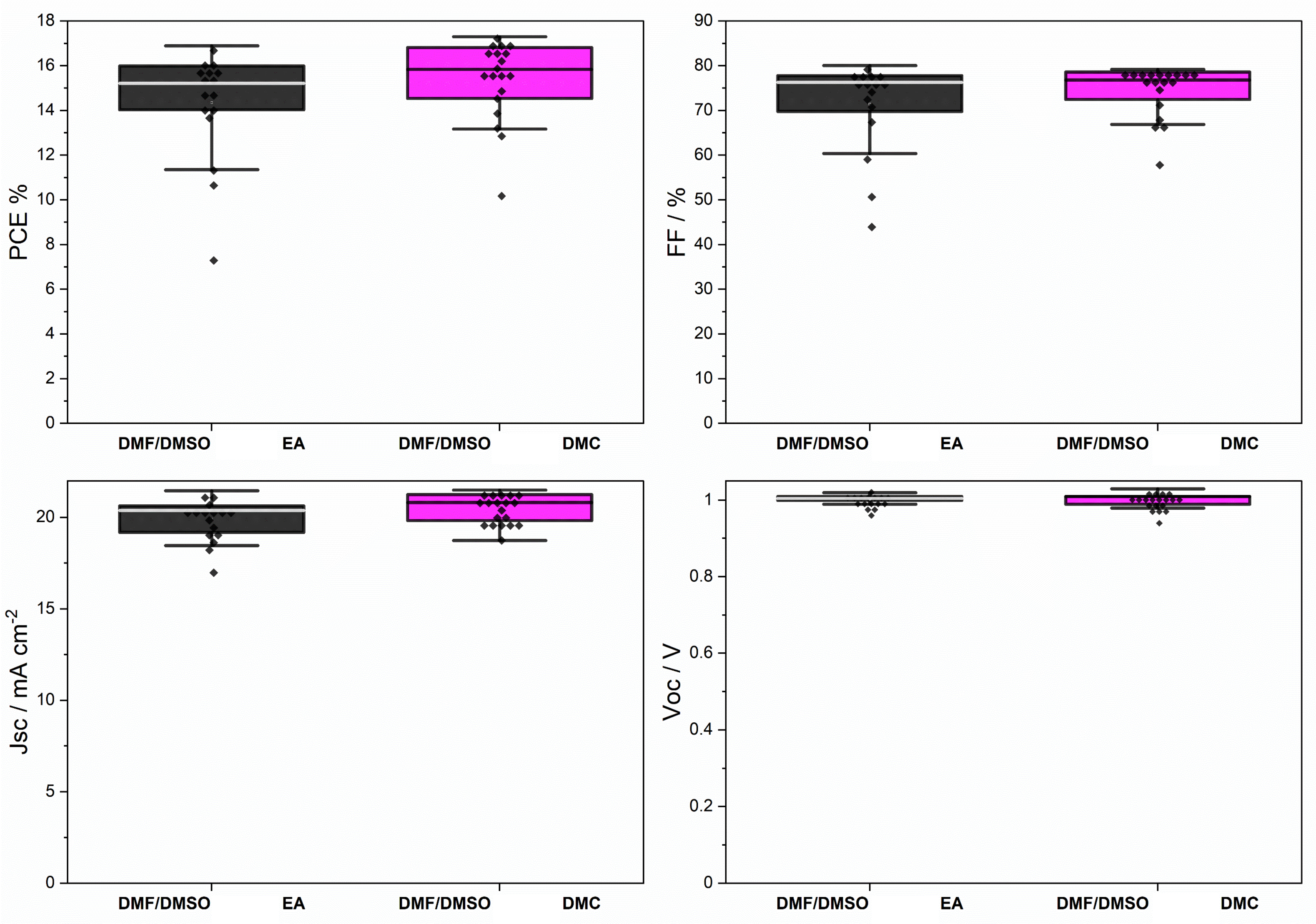

Figure 79 – Statistical box plots showing the final recorded efficiency values for the $MAPbI_3$ samples with competing anti-sovlents EA and DMC.

Figure 79 provides performance data for films cast with the anti-solvent DMC against the EA control. Whilst very comparable in terms of performance, the DMC samples achieve a higher PCE both on average and in terms of champion pixels. This suggests that the interaction between DMC and the DMF/DMSO precursor is capable of forming highly efficient films, at least on par with the most commonly used alternative anti-solvent EA.

5.4 Conclusion

In this Chapter, the precursor formulation has been modified to include the additive dimethyl carbonate, replacing the 2-methyltetrahydrofuran/ethanol fluid modifier. This was designed as an optimisation of the original solution, which exhibited evidence of lead iodide precipitate after cooling to room temperatures post dissolution. The cause of this precipitation was thought to be due to the EtOH component, a known perovskite anti-solvent capable of growing single crystals through time mediated interaction with the precursor solution. The stability of both the precursor and the film have been evaluated for the $MAPbI_3$ composition. The stability of the precursor has been seen to increase after modification with DMC, increasing the shelf life of the ink formulations within a reasonable process window (defined as at least 12-24 hours). DMC has been further proposed as an anti-solvent for perovskite films; to replace widely used toxic solvents. This has shown promise within this work, enhancing the performance of control devices – cast using the DMF/DMSO system. The stability of full devices was also assessed – using $MAPbI_3$. This was deemed a necessary step due to observations of potential DMSO trapping within the annealed films. Over a 15-day period the films showed an initial increase in PCE% followed by a decrease thereafter. The proposed alternative solvent systems A01 and B01 show comparable performance in terms of stability with this composition, with improved photoluminescence.

Solution aging has also been investigated here, in conjunction with the improved B01 proposed precursor solution. The respective solutions (A01, B01, and DMF/DMSO) were aged after mixing with the full perovskite precursor loading. This was undertaken for the period of 1-month – with the precursor fabricated in a glovebox environment and using anhydrous chemicals where possible. Both the anti-solvents EA and DMC were used to fabricate films. This work introduced the concept of the synergistically combined precursor solvent + antisolvent with the B01-DMC combination. Although no substantial improvements were noted from this additional solvent miscibility – suggesting that the miscibility with the more persistent components – in this case DMSO and DMPU.

Films were then cast and measured for PL intensity. The fresh films suggested greater intensity for the A01 and B01 EA films, however, once these films were remeasured after a period of 1-week (film aging), the A01 DMC sample had retained the greatest levels of PL suggesting less degradation within the DMC cast films. Also of note in the aged samples is a significant movement in the location of the PL peak – indicating that the material bandgap may have been modified during the film aging process and is not significantly impacted between solutions for aged precursor materials.

The crystal structure of these films has been further studied using XRD, to highlight differences in the crystalline structure resulting from these alterations to the solvent system/anti-solvent interaction. The use of an intermediate solvent combination, comprising EA and DMC in a 50/50 ratio, attempts to unravel the structural changes resulting from the choice of antisolvent. It was shown that a trend in the 110 intensity was evident for DMF/DMSO, A01 and B01. For the DMF based precursors the 110 increases with increasing DMC content in the anti-solvent. The opposite effect is observed for the A01 and B01 case films – with the 110-intensity decreasing. Using this peak intensity as an approximate measure of film crystallinity, the DMF/DMSO films suggested the greatest potential and were investigated in full devices. The full devices provided empirical evidence that the PCE% was improved through the use of DMC as an antisolvent – with this trend expected to be the opposite for the A01 and B01 systems.

As a final conclusion the novel solvent system B01 shows promise for further investigation alongside A01 and the DMF/DMSO control with more stable perovskite compositions. This strand of research informed the next level of investigations towards sustainably deposited perovskite films with increased stability.

Prifysgol Abertawe
Swansea University

Chapter 6 - Solvent Engineering for Advanced Perovskite Compositions – Towards Sustainable and Stable Devices

6.1 Introduction

The $MAPbI_3$ perovskite composition has been subject to intense research as a perovskite absorber layer due to its high efficiency, facile lab fabrication, and unique tolerance for defects. Intense research scrutiny, however, has identified issues with pure halide perovskite compositions such as $MAPbI_3$. Despite large performance gains during the early years of perovskite research, $MAPbI_3$ has increasingly fallen behind modern compositions in terms of the coveted efficiency, with a current record of 26.0%[57] for polycrystalline films as discussed in this thesis and 22.8% for a single crystal device[215]. The promise of perovskite as a commercial solar technology, has led to an increased focus on long term stability. Several degradation mechanisms have been identified for $MAPbI_3$ PSCs. As discussed in chapter 5, moisture has been identified as both a key cause of degradation for $MAPbI_3$ perovskite[189,190] as well as being beneficial in small quantities during manufacture through improving crystallinity[191]. Excess moisture within a perovskite film often does lead to a dramatic loss in performance, with several studies highlighting the synergistic effect of both moisture and light induced degradation mechanisms[193]. Work by Abdelmageed (2016) detailed the degradation mechanisms considering three major factors as a combination between light, oxygen, and moisture[193]. $MAPbI_3$ perovskite also suffers from intrinsic thermal instability reportedly as a result of its relatively low energy of formation (-0.1 eV)[216]. Buin (2015) concluded that as the enthalpy gain is so low relative to the precursor materials, the decomposition of the $MAPbI_3$ perovskite structure could be initiated by a small temperature increase[217,218]. The studies reported here conclude that a range of environmental conditions lead to a variety of different degradation pathways, nominally leading to a loss of the organic component methylammonium (MA^+)[193,216], commencing the search for more thermally stable cations. The progression of the field moved initially to formamidinium based $FAPbI_3$ perovskite, presented by Eperon (2014), exhibiting a more idealised narrow band gap of 1.48 eV[219], closer to the ideal 1-1.4 eV for a single junction PV device. $FaPbI_3$ perovskite is known to only retain the photo-active α-phase at elevated temperatures, with the photo-inactive δ-phase dominant at room temperature[78].

To overcome this issue, Seok et al combined $MAPbBr_3$, a wide band gap perovskite with the $FAPbI_3$ solution to stabilise the α-phase composition at room temperature[220]. Simultaneously, the addition of the Cs was also found to result in a stable α-phase $FAPbI_3$[221,222], resulting in an improvement in $FAPbI_3$ PCE to 16.5%[222]. These compositional improvements were capitalised on with various combinations of caesium, formamidinium, and methylammonium cations with mixed halides (I_2 and Br_2) achieving high PCE% (>20%) and superior phase stability[78,223–225].

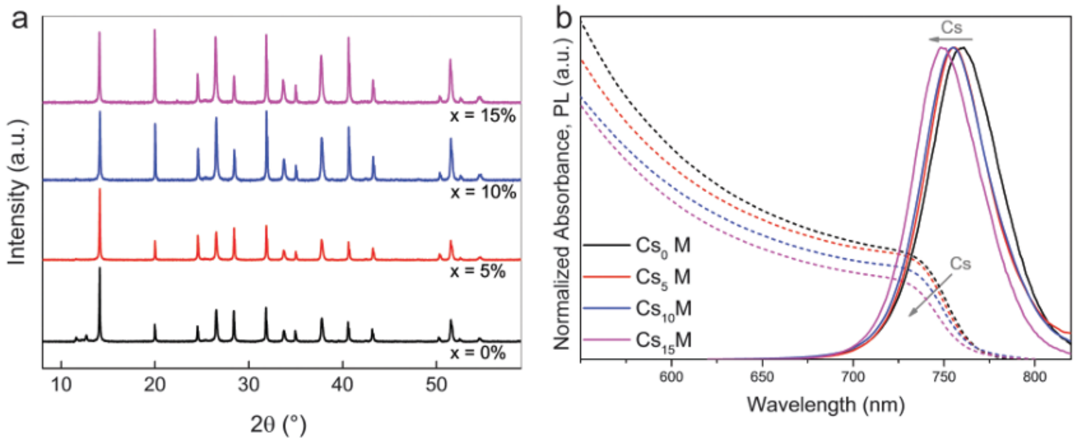

Figure 80 – XRD, SSPL, and absorbance for Cs containing MAFAPbI$_x$Br$_{1-x}$ films at different concentrations. Saliba et al, 2016[78]

Figure 80 shows experimental spectra for films with increasing concentrations of Cs cation addition. For the XRD spectra, low angle peaks can be seen with 0% Cs addition – indicating issues with the conversion of FAMAPbI$_{1-x}$Br$_x$ structure, with some PbI$_2$ residual. As the percentage increases the corresponding 220 plane ~20° peak increases relative to the 110. The absorbance and PL combined plot suggest a trend of decreasing absorbance with increasing Cs % and a shift in the peak position of the PL peak to shorter wavelengths. The shift of the PL peak suggests a modification to the band gap position. This provides a reference point for studies undertaken within this chapter analysing the effect of both solvent system and anti-solvent application on novel triple cation films.

6.2 Experimental

6.2.1 Chemicals

Lead iodide used was purchased from TCI chemicals (99.99%). With all other chemicals purchased from Sigma Aldrich unless otherwise stated.

6.2.2 Manufacture of Thin Films

Triple cation thin films were manufactured according to the thesis methodology for advanced perovskite compositions (Chapter 2.1.2). All films were fabricated under nitrogen and encapsulated with PMMA prior to exposure to environmental conditions.

6.2.3 Precursor Aging

Precursor aging is relevant to the commercialisation of perovskite technologies – defining a processing window for the fabrication of highly efficient thin films.

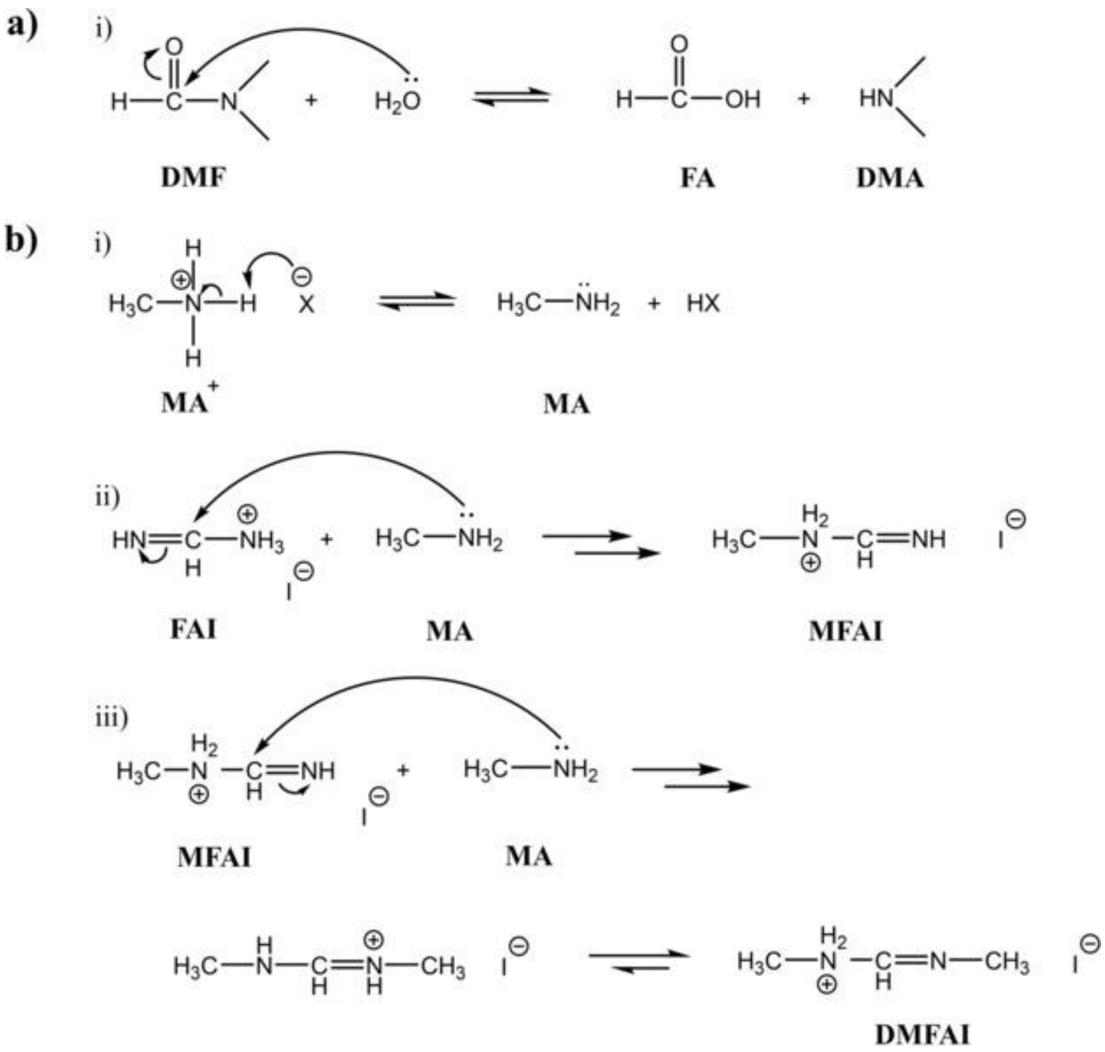

Figure 81 - O'Kane 2021[226] – Figure showing the potential degradation pathways within the standard DMF/DMSO based triple cation perovskite precursor.

Previous works have identified several degradation mechanisms resulting from chemical reactions taking place within the colloidal suspension. Figure 81 suggests how these reactions progress from initial interaction between DMF and H_2O within a perovskite ink. Several reaction products are identified. The use of novel solvent systems can be anticipated to lead to as yet unknown reactions after a period of solution aging. Within this thesis solution aging requires the perovskite ink to remain in a dark environment under nitrogen, protected from exposure to environmental contamination. It can therefore be assumed that impurities (H_2O in this case) were contained within the solvent prior to manufacture and not as a result of environmental exposure.

6.2.4 Sample Aging

Aging of samples is also required to assess long term device performance. Samples aged during these studies were left at open circuit in a dark low humidity environment (with desiccant present) without additional encapsulation – other than that present from the active transport layers.

6.2.5 Device Aging

Similarly, for device aging, devices kept in a dark low humidity environment (with desiccant present). Gold contacts were also present on these devices with ion migration notable here. Repeat measurements exposed the devices to light induced degradation for short periods of time during measurement.

6.2.6 Manufacture of Full Devices

All fabrication of triple cation perovskite was undertaken with reference to the Saliba method[227]. With the perovskite precursor preparation an adapted version of the Saliba Cs discovery methodology, suiting adaptation for alternative solvent systems without the need for extensive use of stock solutions. All precursor materials, except for CsI, were weighed into a vial prior to solvent addition on a vol% basis. CsI was then added post solution manufacture to attain the correct % of caesium. All films were deposited in a N_2 glovebox. Some variation is expected due to the extensive use of solvents within this glovebox environment, which may impact accuracy due to the sensitive nature of this material during manufacture. Attempts were made to regulate glovebox temperature to between 22-27°C. A purge of the glovebox was undertaken where possible prior to and during deposition. All films characterised in this chapter are coated with PMMA under N_2 unless otherwise stated. Unencapsulated films were used for XRD measurements, with encapsulation (PMMA) applied retroactively in ambient conditions for Figure 96. PMMA was applied from a 1M solution in toluene (heated overnight at 80°C), with 100 µL spun at 3000 rpm.

6.2.7 Precursor Solution - $Cs_{0.066}(MA_{0.17}FA_{0.83})_{0.934}Pb(I_{0.83}Br_{0.17})_3$

The triple cation precursor was manufactured in accordance with 2.1.2 Precursor Solution Preparation – $Cs_{0.066}(MA_{0.17}FA_{0.83})_{0.934}Pb(I_{0.83}Br_{0.17})_3$.

6.2.8 Electron Transport Layer – SnO_2

A tin oxide substrate was prepared according to 2.1.4 Electron Transport Layer Preparation – SnO_2 of the methodology.

6.2.9 Perovskite Deposition - Glovebox Devices

Samples were then transferred to a glovebox for perovskite deposition. The one step deposition method was used to spin coat $Cs_{0.066}(MA_{0.17}FA_{0.83})_{0.934}Pb(I_{0.83}Br_{0.17})_3$ solutions onto substrates with an anti-solvent drip of ethyl acetate (EA) or dimethyl carbonate (DMC) to help crystalise the thin film. For the DMF/DMSO (80/20 v/v), spin coating settings of 4000 rpm, 4000 acceleration for 30 seconds were used. 250 µL of ethyl acetate was dropped onto the sample 12 seconds from the start of the spin cycle. Samples were then placed on a hot plate at 100°C for 10 minutes to anneal. It is also possible to manufacture DMF/DMSO based films through the prenucleation method detailed below. This is specified where appropriate.

6.2.10 The Prenucleation Strategy for $Cs_{0.066}(MA_{0.17}FA_{0.83})_{0.934}Pb(I_{0.83}Br_{0.17})_3$

For the A01 and B01 solutions evaluated, a prenucleation method of spin coating was used. This method was used to form dense, pin hole free, specular films given the difference in solvent system properties to the control solution. A specular layer was formed using a two-stage spin setting of 10 seconds at 2000 rpm with 200 acceleration, followed by 30 seconds at 6000 rpm and 2000 acceleration (2K6K method). The amount of anti-solvent dropped onto the sample was 300 µL for experimental solutions unless otherwise stated. The HTL solution was made in accordance with Chapter 2.1.7 with the addition of the dopant FK209, 8 µL per mL of solution. The completed hole transport layer (HTL) solution was then filtered with 0.2 µm PTFE filter before deposition. 100 µL of spiro-OMeTAD solution was spread onto the PAL, a 30 second spin cycle at 4000 rpm was initiated to create the film. Oxidation of the HTL was achieved through leaving the device in a dark environment for 12-24 hours.

6.2.11 Back Contact Evaporation

Finally, gold contacts were added in accordance with 2.3.3 Top Contact Evaporation.

6.2.12 Optical and Photochemical Evaluations

Pre-cut XOP laser etched (2.8 cm^2, 2.2 mm thick, tec 15) FTO glass was cleaned with IPA and dried prior to deposition. Deposition of these films was done in ambient conditions. Films were analysed through the perovskite as FTO/PAL/PMMA stacks. For Figure 106 – Box plots showing device performance after 1 week of aging the precursor solution.- ITO/SnO_2/PAL/PMMA stacks were prepared during the course of the associated device build (Figure 106), with no removal of the SnO_2, perovskite was deposited alongside other devices.

6.2.13 UV-Vis-NIR of Perovskite Films

$Cs_{0.066}(MA_{0.17}FA_{0.83})_{0.934}Pb(I_{0.83}Br_{0.17})_3$ thin films were measured on a Perkin Elmer Lambda 9 UV-Vis-NIR spectrometer. The scan range was set between 200 - 800 nm, with a scan speed of 960 nm/s and a step change of 1nm. Data was recorded in Transmittance unless otherwise specified and converted into absorbance via application of the beer lambert law as per 2.4 UV-Vis-NIR Spectroscopy.

6.2.14 Photochemical Evaluation of Thin Films

Steady state photoluminescence measurements were undertaken on both A01 and B01 deposited films to quantify differences in radiative emission from each sample at a fixed excitation wavelength. The wavelength used in this chapter was fixed to 530 nm unless otherwise stated. The sample size was also varied for investigative purposes, though by scaling the precursor and anti-solvent relative to the area, sample thickness is assumed to be equal.

For Figure 83, measurements presented are spectra (emission correction off) taken on the PALSide encapsulated with PMMA. Range 680-880 nm. Emission and excitation slit widths were set to 2.4 nm. A step size of 0.5 nm was used with a 0.2s dwell time. A 530 nm excitation was utilised here, with each scan repeated 3 times to stabilise the sample response under illumination.

Additional manual filters were added with a band pass of 520 nm on the excitation light and a 611 nm long pass on the emission. Triple cation perovskite under PMMA exhibits drastically reduced photobrightening behaviour, in part due to a reduction in oxygen interaction and due to the compositional stability.

6.2.15 Post Processing Data

For Figure 83, Figure 88, Figure 102, and Figure 95 the curves were smoothed using the Savitzky-Golay method with 6 points in window and a polynomial order of 3, with the inset smoothed using 10 points in window and a polynomial order of 2. Smoothed curves were normalised between 0 – 1 for the inset images showing peak height.

For absorptance scans, data was plotted as individual points, with line interpolation using origin. This was then smoothed using Savitzky-Golay, with 20 points in window and a polynomial order of 1 prior to normalisation between 1-0 where specified.

6.2.16 Absorptance Scans within an Integrating Sphere

Absorptance scans were taken using the same sample architecture in the integrating sphere according to 2.5.2 Absorptance Measurements Within the Integrating Sphere.

6.2.17 XRD Analysis

Several distinct XRD studies are presented in this chapter, the substrate size varies with all scans taken on FTO. XRD measurements were performed using a Bruker D8 Discover in a standard divergent slit set-up. The sample architecture used unencapsulated XOP (tec 15) FTO/$Cs_{0.066}(MA_{0.17}FA_{0.83})_{0.934}Pb(I_{0.83}Br_{0.17})_3$.

6.2.18 XRD Peak Analysis

The scan range was set from 5-45° and the measurements taken using a 40kV, 40mA Copper source with a step size of 0.032°, at 2 second per step. Origin peak analyser was used to find the full width at half maximum for the 110, 220, and 310 tetragonal $Cs_{0.066}(MA_{0.17}FA_{0.83})_{0.934}Pb(I_{0.83}Br_{0.17})_3$ peaks. The baseline was defined manually, inputting 40-45 points. Savitzky-Golay smoothing was applied during this procedure with 3 points in window and a polynomial order of 2. The baseline was then subtracted, prior to integration with the width set to 0.5 degrees either side of the peak.

6.2.19 FWHM Analysis

FWHM values were ascertained from the peak analysis for each of the major peaks studied (110, 220, 310). Recorded values were rounded to 3.s.f. For the 110/310 peak intensity ratio, values were taken for the peak height from the peak analysis result.

6.2.20 Device Performance

Device performance was recorded according to 2.9 Device Performance Evaluations.

6.2.21 IPCE Measurements

IPCE measurements were undertaken during the 7 month of device stability testing in accordance with 2.10 Internal Photon Conversion Efficiency (IPCE).

6.3 Results and Discussion

6.3.1 Application of Developed Solvent Systems to Triple Cation Perovskite

Expanding on our previous work we have looked to implement our developed A01(40 vol% DMSO, 30 vol% DMPU, 10 vol% EtOH, 20 vol% MeTHF) and B01 (40 vol% DMSO, 30 vol% DMPU, 30 vol% DMC) solvent systems on to the more stable triple cation composition. The selected composition represents a small adaptation of one of the more well studied compositions:

$Cs_{0.066}(MA_{0.17}FA_{0.83})_{0.934}Pb(I_{0.83}Br_{0.17})_3$

This was abbreviated to CsMAFA for the purposes of graphical analysis and only this composition was studied throughout.

6.3.2 Initial Film Evaluation

The use of the anti-solvents EA and DMC were trialled to produce CsMAFA films on FTO. There are several alternative factors that can impact the transparency/specular nature of the perovskite. These include interactions between solvent vapours within the spin coater and the perovskite surface or antisolvent during the drip phase. Through initial film depsosition, using the 4000 rpm 12s drip for the DMF/DMSO system, and the 2K6K spin regime for the A01 and B01 inks, it is visually apparent that DMC creates a more spcular sample for the candidate formulations than EA. EA generally produces a greyed out perovskite upon annealing with these systems, contrasted to the control. Using DMC in these evaluations there is a noticable difference for the A01 and B01 samples, showing improved film transparency. The opposite is noted for the DMF-based film, with a cloudy appearance indicative of a poor anti-solvent drip procedure.

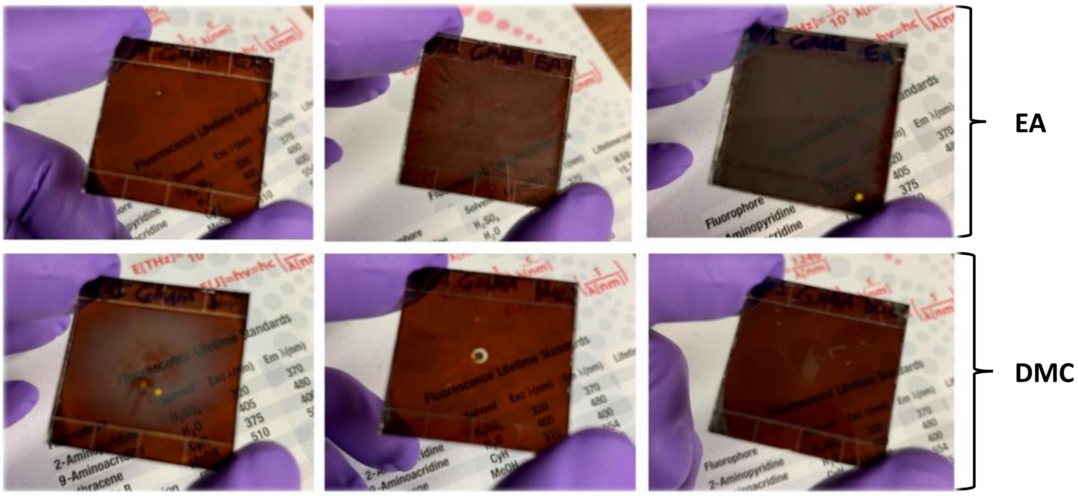

Figure 82 - CsMAFA Images - Antisolvent engineering techniques applied using DMC leading to visually more specular films.

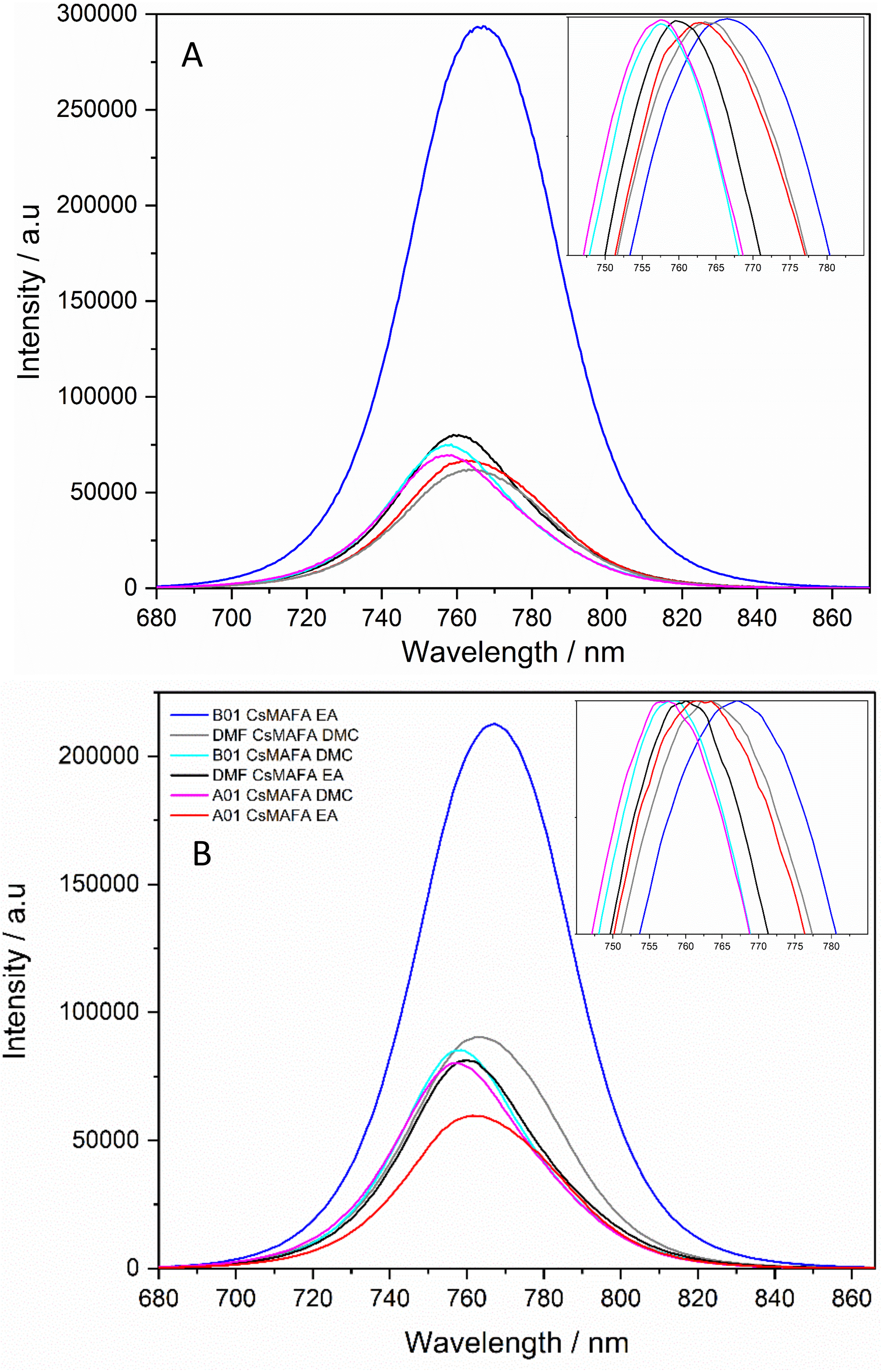

Figure 83 - Steady state PL investigation for anti-solvent engineered CsMAFA samples. a) Initial measurements of PMMA encapsulated films ($\lambda_{ex} = 530$ nm ex, 520 BP, 611 LP) b) Same samples evaluated after 8 days of aging.

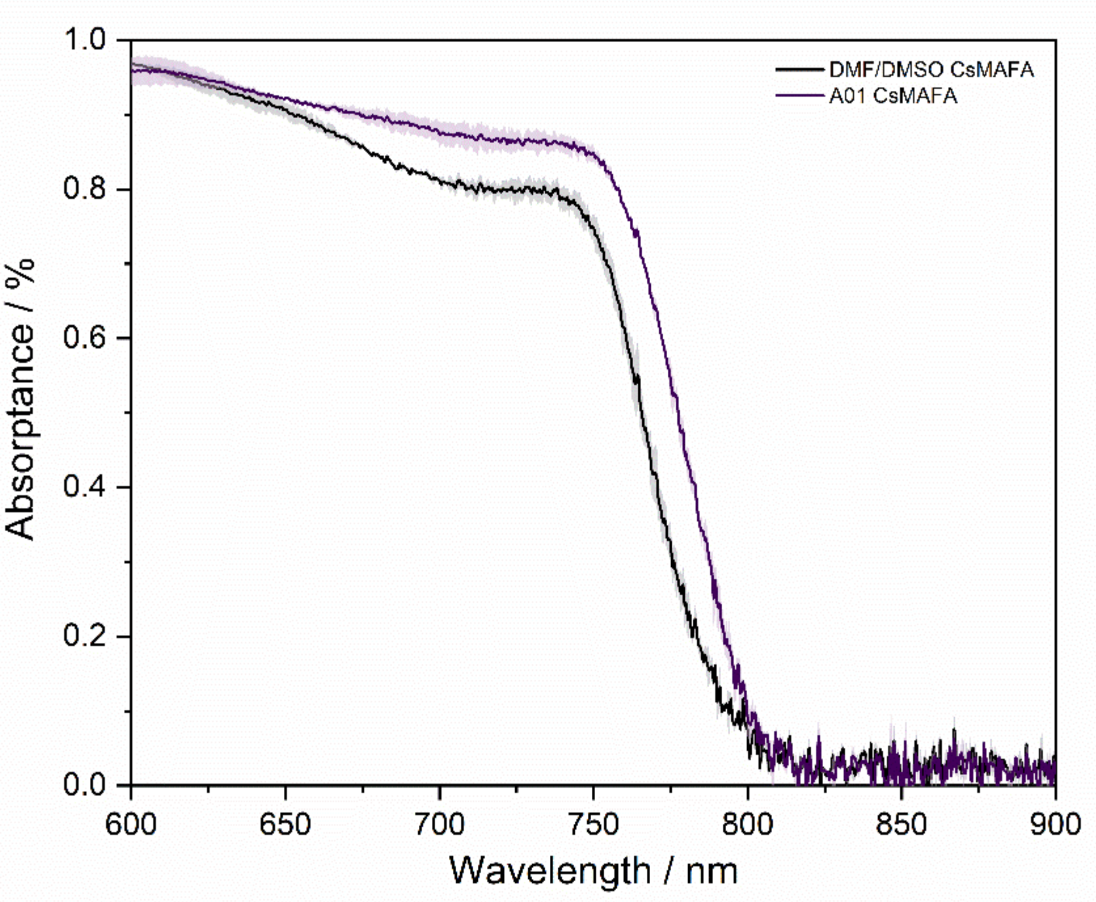

Figure 84 - Initial absorptance showing A01 vs DMF/DMSO CsMAFA EA (Average of 2 samples + 1 standard deviation from the mean – shaded region)

Steady state photoluminescence was used to provide an initial view of the thin film response under excitation (λ_{ex}=530 nm). Initial samples encapsulated under PMMA were measured on the day of fabrication and after 8 days of aging as shown in Figure 83 b). The control system (DMF/DMSO CsMAFA using EA as the anti-solvent) suggests a peak of 760 nm for this composition, in line with literature reports[78].

There are some notable changes observed in terms of peak height and position both dependent on the formulation and the antisolvent applied. The B01 solution with the EA application shows the highest PL emission of all samples. With the intensity for the other compositions similar in magnitude. Initially the DMC samples show a higher intensity for both the DMF and A01 formulations, with the exception of B01, where EA produces the film with the highest PL. The synergistically tuned B01 DMC solution was fairly comparable to the A01 DMC system suggesting a limited impact of the synergistic approach on PL intensity alone. The standard A01 sample with EA provides the lowest emission intensity here, with a significant increase in the DMC version cast from the same solution. The visual sample 'quality' discussed earlier appears to have little impact on the fluorescence emission with the scans taken from the perovskite active layer side (PALSide) showing a huge discrepancy between the

A01 and B01 EA solutions. However, limited inference can be made from the intensity alone. Of interest here is the peak position displayed for each sample. This remains consistent after 8 days of ageing with the peak intensity decreasing for the DMC samples whilst remaining consistent for the DMF/DMSO EA and A01 EA samples and increasing for the B01 EA sample. Relative to the DMF-based EA control DMC appears to cause a minor shift to longer wavelength emission, with a shift to shorter wavelengths observed for both the A01 and B01 solutions when using DMC. For EA A01 shows a small peak shift with the largest change for the most emissive B01 EA sample suggesting a peak close to 770 nm. Through these initial investigations we have observed several repeatable behaviours which may have links to both solvent-precursor interactions, solvent-antisolvent interactions and the final composition of the material. The absorptance of the A01 samples was initial considered in Figure 84, with 2 samples deposited using EA for each formulation. A higher absorptance is noted at longer wavelengths along with the absorptance onset, further confirming a significant change in the material.

6.3.3 Initial Device Builds

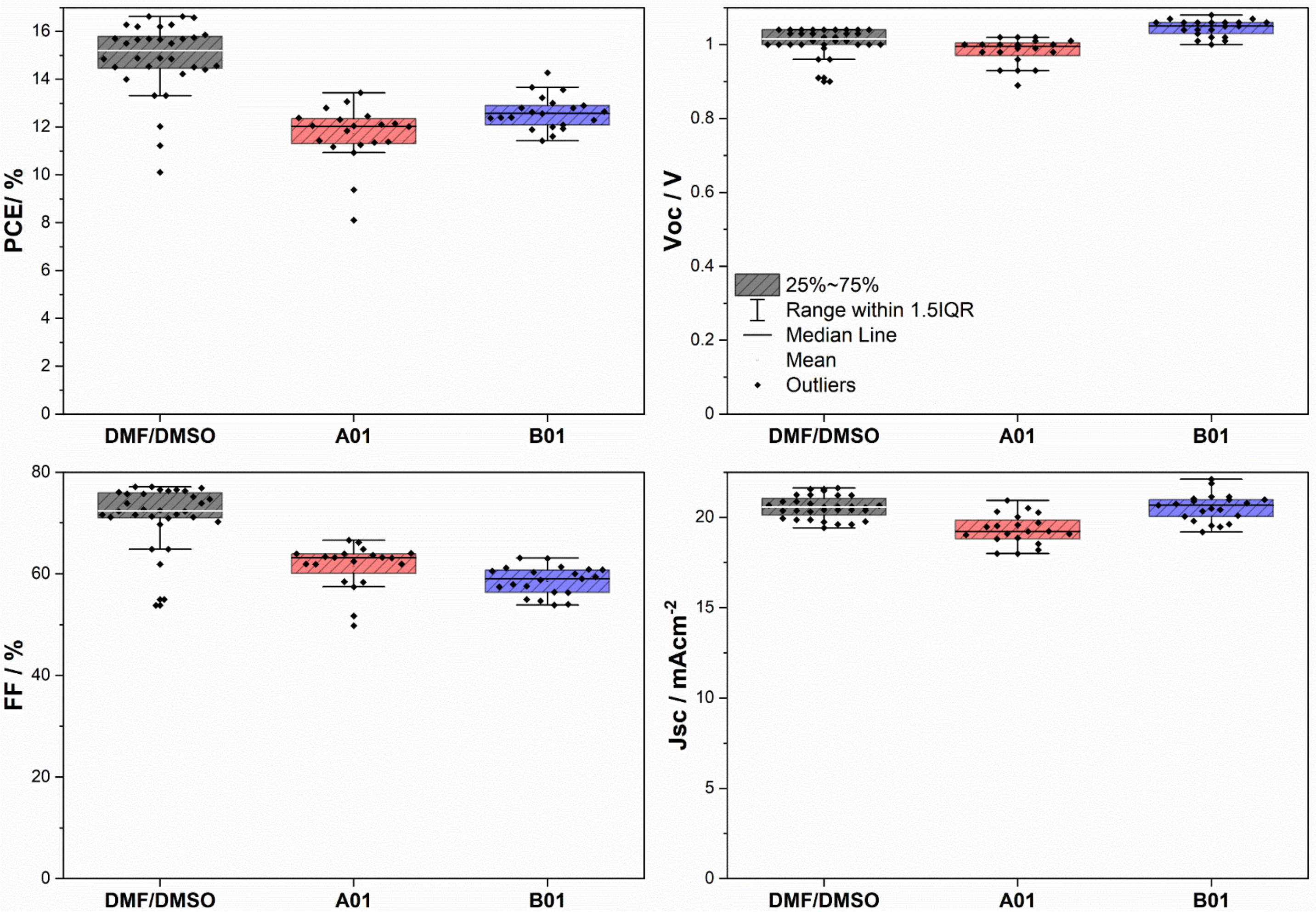

Figure 85 - Initial device builds using EA. As functional films can be manufactured from these systems an initial device build was undertaken to provide a benchmark for further improvements. This was done using 3 samples for each composition (8 pixels per sample), on identical SnO_2 transport layers. EA was used as the sole antisolvent.

Standard DMF-based CsMAFA devices achieve encouraging results averaging ~15% (Figure 85). Several underperforming pixels exhibit unusually poor V_{oc} values attributed to poor electron extraction, with a small impact on the total spread. From this we can see a slight increase in the B01 EA samples in terms of PCE attributed to high V_{oc} values despite showing quite poor FF averaging below 60% and over 10% lower than the control. Comparable J_{sc} leads to the conclusion that the FF is inhibiting the performance of these films. Strategies to improve this parameter are to be undertaken to achieve parity of performance. To further investigate the source of these issues XRD measurements were taken on EA based films along with their more specular DMC counterparts. This was done to ascertain the cause of the change to film transparency and subsequent loss of FF and performance.

6.3.4 XRD Initial Investigations Analysis

Samples for XRD were done on FTO substrates, double the thickness of ITO counterparts with increased surface roughness. This may alter the dynamics of the crystallisation process, but still provides a comparison of the solvent-antisolvent blends.

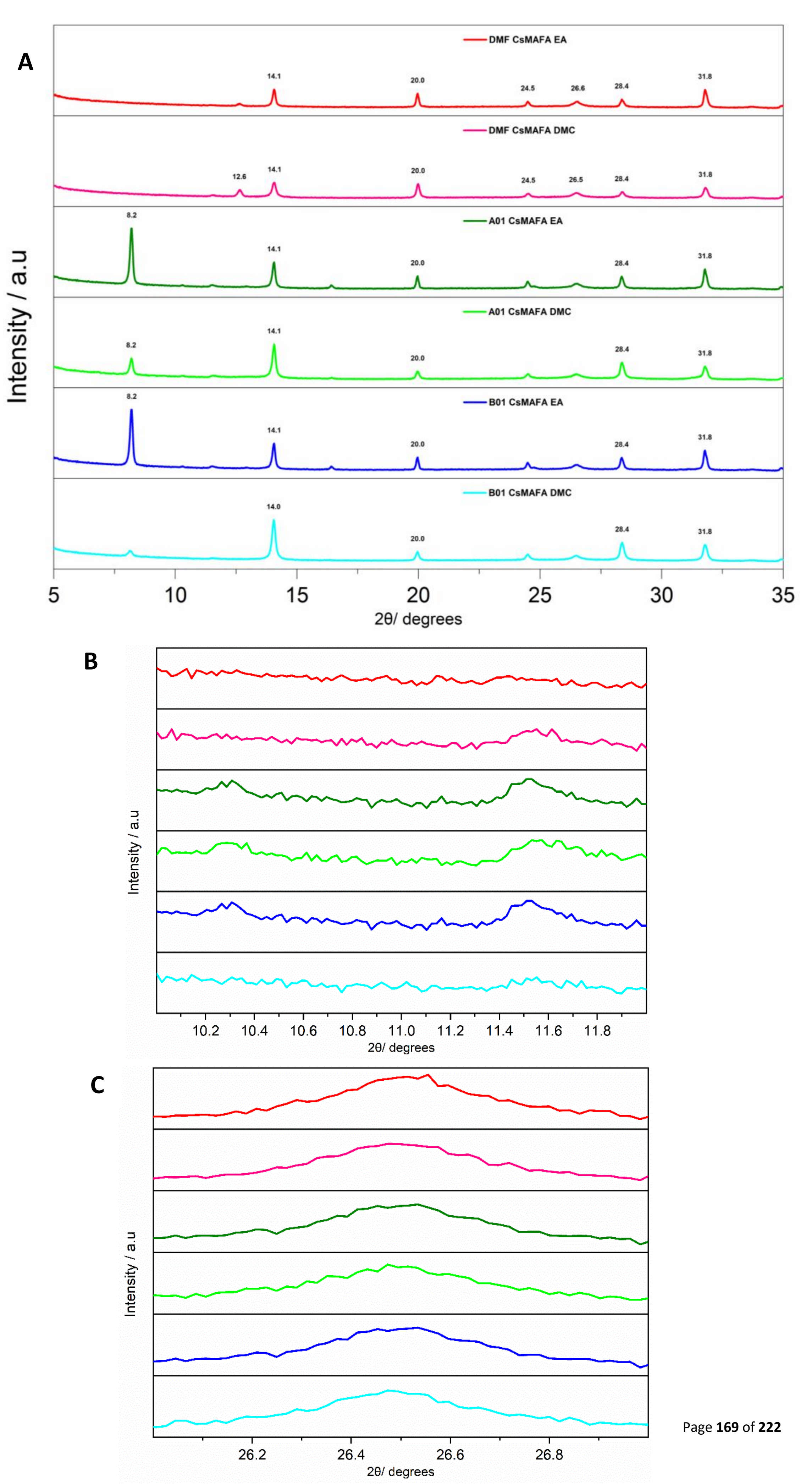
A
DMF CsMAFA EA
14.1
20.0
24.5
26.6
28.4
31.8
DMF CsMAFA DMC
12.6
14.1
20.0
24.5
26.5
28.4
31.8
A01 CsMAFA EA
8.2
14.1
20.0
28.4
31.8
A01 CsMAFA DMC
8.2
14.1
20.0
28.4
31.8
B01 CsMAFA EA
8.2
14.1
20.0
28.4
31.8
B01 CsMAFA DMC
14.0
20.0
28.4
31.8
Intensity / a.u
5
10
15
20
25
30
35
2θ/ degrees
B
Intensity / a.u
10.2
10.4
10.6
10.8
11.0
11.2
11.4
11.6
11.8
2θ/ degrees
C
Intensity / a.u
26.2
26.4
26.6
26.8
2θ/ degrees

Figure 86 - a) XRD scans for Initial CsMAFA EA DMC evaluation b) enhancement of small low angle peaks seen in A01 CsMAFA EA and DMC samples along with the B01 EA sample. c) enhanced 26.5° peak

Figure 86 displays XRD patterns from 5° through to 35°, encompassing the major 110, 220, and 310 planes (14.1°, 24.4°, 31.8°) characteristic of 110 dominant tetragonal $MAPbI_3$. Analysis of the DMF/DMSO precursor with EA, provides a benchmark for efficient CsMAFA structure. A small PbI_2 peak can be seen at the 12.6° position, with this peak more prominent after the use of DMC as the anti-solvent. No further peaks are visible below 12.6° for the 'control' solution. However, a small peak is seen for all other samples at 11.5° roughly corresponding to the 010 δ-phase $FAPbI_3$[228], shifted by 0.3° as to that reported by Zhang et al, 2018[229]. Another major $FAPbI_3$ peak corresponding to the 021 direction should be located at 26.3°[229], however, this coincides with the presence of a known 110 FTO plane at 26.6°[230], obscuring any evidence of this peak. The magnitude of these peaks may be negligible, however, with any impact on performance expected to be negative but potentially undiscernible. Of note is the B01 DMC sample, which appears to show no trace of these peaks, indicating that customisation of the solvent interactions used to fabricate these films can effect positive changes on the crystal structure. In relation to this, a significant and extremely prominent peak is visible for the A01 and B01 solutions at 8.2°. Literature suggests this to be a FAI-PbI_2-DMSO intermediate phase[228], inferred to have formed during spin coating with annealing insufficient to remove all the DMSO. Although the cause of this intermediate phase in these samples in unknown, it is interesting to note the difference between films cast from the same solutions with the anti-solvent DMC. The interaction with DMC appears to have caused a significant reduction in the intermediate phase formation through modification of the crystallisation kinetics. For both the A01 and B01 samples, judicious anti-solvent selection can be used to customise the crystalline structure of a novel perovskite, improving the intensity of the 110 direction peaks, associated with tetragonal growth, and removing undesirable structural elements, such as trapped intermediate phases. Upon switching to DMC as an antisolvent. he improvement in visual film quality appears to be linked to an improvement in film crystallinity, forming a purer tetragonal perovskite. This also provides an indication that significant customisation of the films may be possible through alterations to the anti-solvent and the crystallisation pathway more generally (substrate size, anti-solvent volume, drip pressure, time in contact).

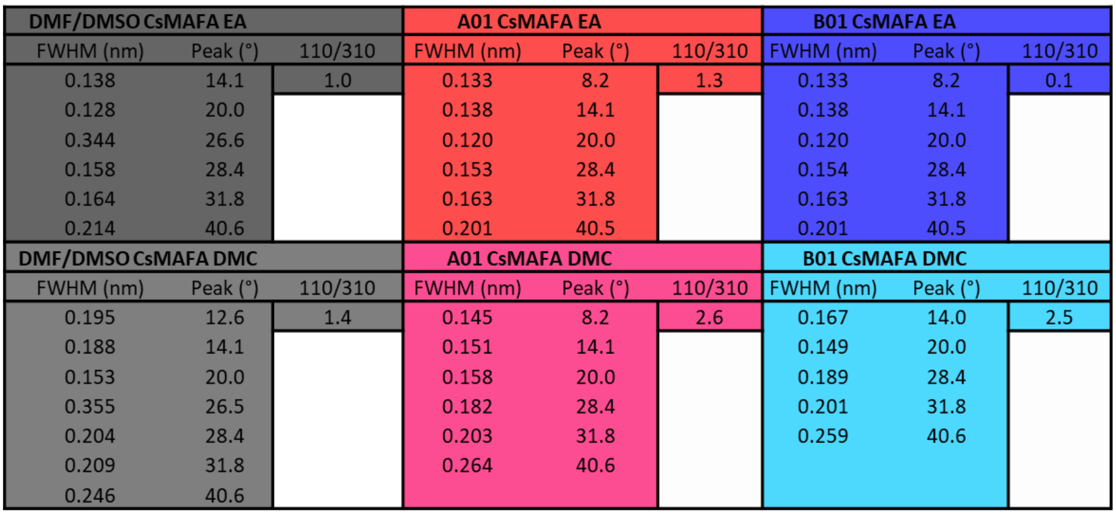

DMF/DMSO CsMAFA EA			A01 CsMAFA EA			B01 CsMAFA EA		
FWHM (nm)	Peak (°)	110/310	FWHM (nm)	Peak (°)	110/310	FWHM (nm)	Peak (°)	110/310
0.138	14.1	1.0	0.133	8.2	1.3	0.133	8.2	0.1
0.128	20.0		0.138	14.1		0.138	14.1	
0.344	26.6		0.120	20.0		0.120	20.0	
0.158	28.4		0.153	28.4		0.154	28.4	
0.164	31.8		0.163	31.8		0.163	31.8	
0.214	40.6		0.201	40.5		0.201	40.5	
DMF/DMSO CsMAFA DMC			**A01 CsMAFA DMC**			**B01 CsMAFA DMC**		
FWHM (nm)	Peak (°)	110/310	FWHM (nm)	Peak (°)	110/310	FWHM (nm)	Peak (°)	110/310
0.195	12.6	1.4	0.145	8.2	2.6	0.167	14.0	2.5
0.188	14.1		0.151	14.1		0.149	20.0	
0.153	20.0		0.158	20.0		0.189	28.4	
0.355	26.5		0.182	28.4		0.201	31.8	
0.204	28.4		0.203	31.8		0.259	40.6	
0.209	31.8		0.264	40.6				
0.246	40.6							

Figure 87 - XRD Peak Analysis for the triple cation samples.

Figure 87 shows the peak analysis calculations with the displayed 110/310 ratio suggesting large variation in crystal structure between samples.

6.3.5 Alternative Precursor Evaluation (A02, MAFA)

Due to the nature of the solvent system design, inherent tunability, there are many alternative compositions for these systems possible by ratio tuning. This is especially pertinent when considering changes to the stoichiometry or solution concentration. Ultimately a 1.25 M solution has been chosen for the triple cation evaluation, with this containing an excess of PbI_2 to attain high performance[231,232].

6.3.6 Inherent System Tunability – A02 System

An aim with this experiment was to prove the inherent tunability of such multi-component systems. Most systems find an optimal point for common precursor concentrations – however, the solvent system can be modified to handle changes to composition or additional requirements as needed. To mitigate concerns raised with respect to the oxidative nature of DMSO within such precursor systems, an alternative DMPU heavy ratio was trialled to ascertain whether DMPU could be used as the major modifier (for example for tin-based perovskites). To investigate the effect of ratio tuning a solution was prepared with excess DMPU to DMSO:

A02	300 µL DMSO, 400 µL DMPU, 200 µL 2-MeTHF, 100 µL EtOH

Investigation of these films for SSPL and absorptance was undertaken using both the EA and DMC anti-solvents. With a corresponding XRD scan for these samples.

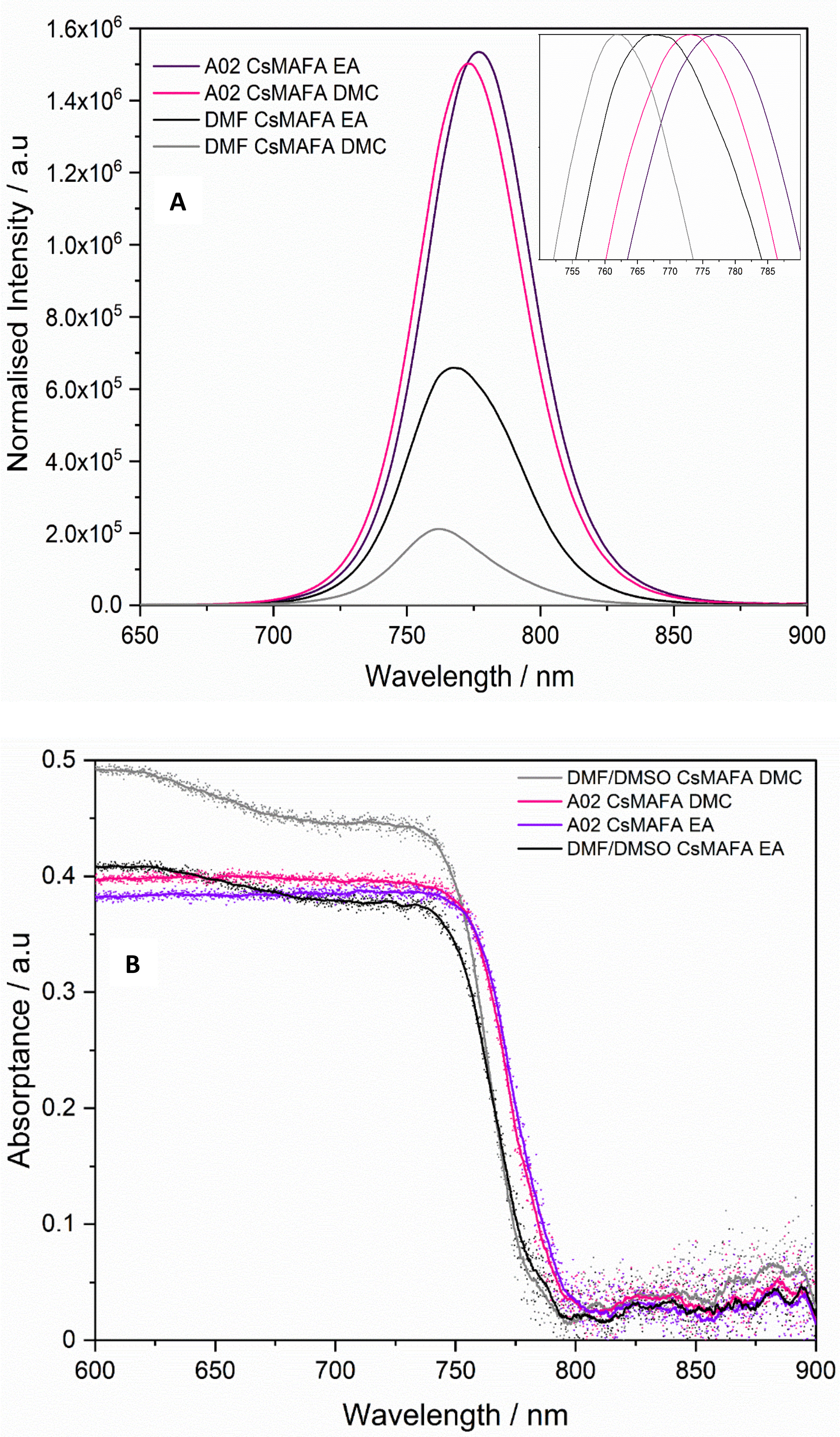
A
Normalised Intensity / a.u
Wavelength / nm
A02 CsMAFA EA
A02 CsMAFA DMC
DMF CsMAFA EA
DMF CsMAFA DMC
0.0
2.0x10^5
4.0x10^5
6.0x10^5
8.0x10^5
1.0x10^6
1.2x10^6
1.4x10^6
1.6x10^6
650
700
750
800
850
900
755
760
765
770
775
780
785
B
Absorptance / a.u
Wavelength / nm
DMF/DMSO CsMAFA DMC
A02 CsMAFA DMC
A02 CsMAFA EA
DMF/DMSO CsMAFA EA
0
0.1
0.2
0.3
0.4
0.5
600
650
700
750
800
850
900

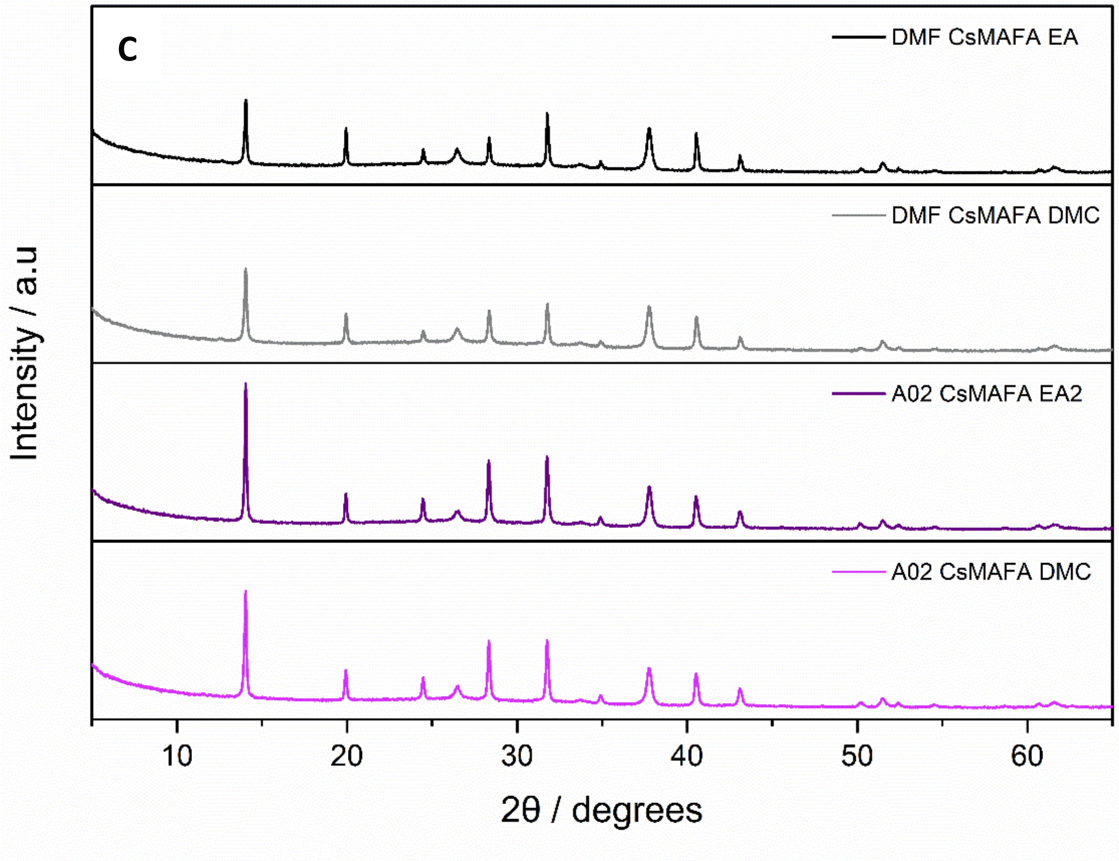

Figure 88 – Modified A02 solvent system characteristics a) Normalised absorptance b) SSPL spectra c) XRD spectra

Spin coating the A02 films was done in an identical manner to A01 films on 2.8 cm^2 samples. Increasing the amount of the highly coordinative DMPU facilitates marginally quicker dissolution of the precursor materials, enabling the higher amount of PbI_2 to be retained within solution. The subsequent supersaturation of the solution is thus anticipated to be lower than for A01, leading to a reduced nucleation during the drip of the anti-solvent. 300 µL of EA has been reported for CsMAFA samples within the literature[227], with 250 µL used within this chapter for control films. Using this amount of anti-solvent is recommended for the enhanced DMPU composition to mitigate inadequate solvent removal, such as seen in the XRD scans presented in Figure *86*. Figure 88 a) shows the absorptance spectra for the modified A02 films, with a significant improvement in absorptance over the range, with a commensurately higher λ_{onset}, more typical of a triiodide perovskite. To further confirm this potential band gap shift, SSPL measurements for each film are presented in Figure *88* b) with the inset showing the peak position, corresponding to the approximate band gap energy. These corrected scans show a higher emission peak than anticipated for this composition, with a shift up to 5 nm to longer wavelengths. In this case the A02 peaks still suggest a shift to longer wavelengths, with the A02 EA peak at ~780 nm. The application of DMC (A02 DMC) slightly shifts this peak to 775 nm, however, this is still unrepresentative of the usual position of the emission peak of CsMAFA based perovskites (750-760 nm), suggesting issues with forming the correct composition. This trend is notably not present with the initial A01 SSPL results (Figure 83), likely due to the influence of bromide and caesium on the resultant peak and extrapolated band gap energy (assuming equal film thickness). For the standard DMF-based samples the EA sample suggests a red shifted peak position from ~760 nm to ~765 nm, however, significant shouldering is present on this peak, suggesting an influence of photobrightening during the measurement or impurities within the sample. The DMC manufactured sample, previously shown to have little impact on peak position is slightly shifted to the expected 760 nm position further suggesting issues with the control sample. This is further confirmed by XRD studies showing a higher 110 intensity for the DMC sample in contrast to Figure *86* a). This inconsistency also highlights the variability during manufacture of these sensitive samples and suggests caution drawing definitive conclusions from limited data sets. Ultimately the XRD for the A02 samples, suggests a fully annealed film with no peaks visible below 12.6 (PbI_2) peak. As theorised previously, the 8.2° peak (suggested to be indicative of phase impurities and DMSO trapping) is not present within these DMPU tuned samples. This could be due to the reduced DMSO volume within the precursor, to more preferential anti-solvent drip interaction, or a combination of both factors. This experiment highlights the tunability of the provided 4 component solvent system, with this tunability able to further customise the characteristics of the film. However, compositionally this appears to result in an over coordination of the key metal cations within solution, likely with favour to the iodide component (present at excess). This appears to lead to the formation of a different iodide favoured perovskite, whilst still maintaining prominent 110, 220, and 310 tetragonal perovskite structure. Application of alternative anti-solvents, such as DMC, can also be applied to further alter the kinetics of the CsMAFA formation, albeit to a minor degree here. This result corresponds to the conclusion from the initial study, that the level of possible interactions to consider for CsMAFA deposition with alternative antisolvents is much greater than for $MAPbI_3$ with the resulting photochemical and structural results potentially tunable to a much higher degree.

6.3.7 Assessing the Impact of Solvent Engineering on the Stability of Perovskite Films

The inherent advantage of the triple cation composition is an increase in film stability resulting from the inclusion of the comparably smaller caesium ion within the lattice structure. The solvent system designed to deposit this composition must not only replicate the efficiency of DMF-based devices, but also avoid harming long term stability. Stability can be assessed for both the precursor solution, as discussed in chapter 2.1.2, with the DMF-based control solution reducing in efficacy after 1 week of storage as evaluated against the highest performing devices produced for this composition[99]. The proposed candidate solutions are evaluated after 6 days of aging within this chapter to determine the stability of this complex colloidal ink. A further stability concern is the inclusion of residual solvent within films deposited from the novel solvent systems and anti-solvent alterations. Film aging, under PMMA encapsulation, was also studied using PL techniques and structural XRD probes to identify any difference in behaviour/structure as a result of post fabrication aging. Finally, an evaluation of long-term device performance was undertaken to assess the impact of the proposed processing ink/anti-solvent pairings. Devices were aged in a dark, low humidity environment using desiccant, with exposure to ambient humidity and light during measurement.

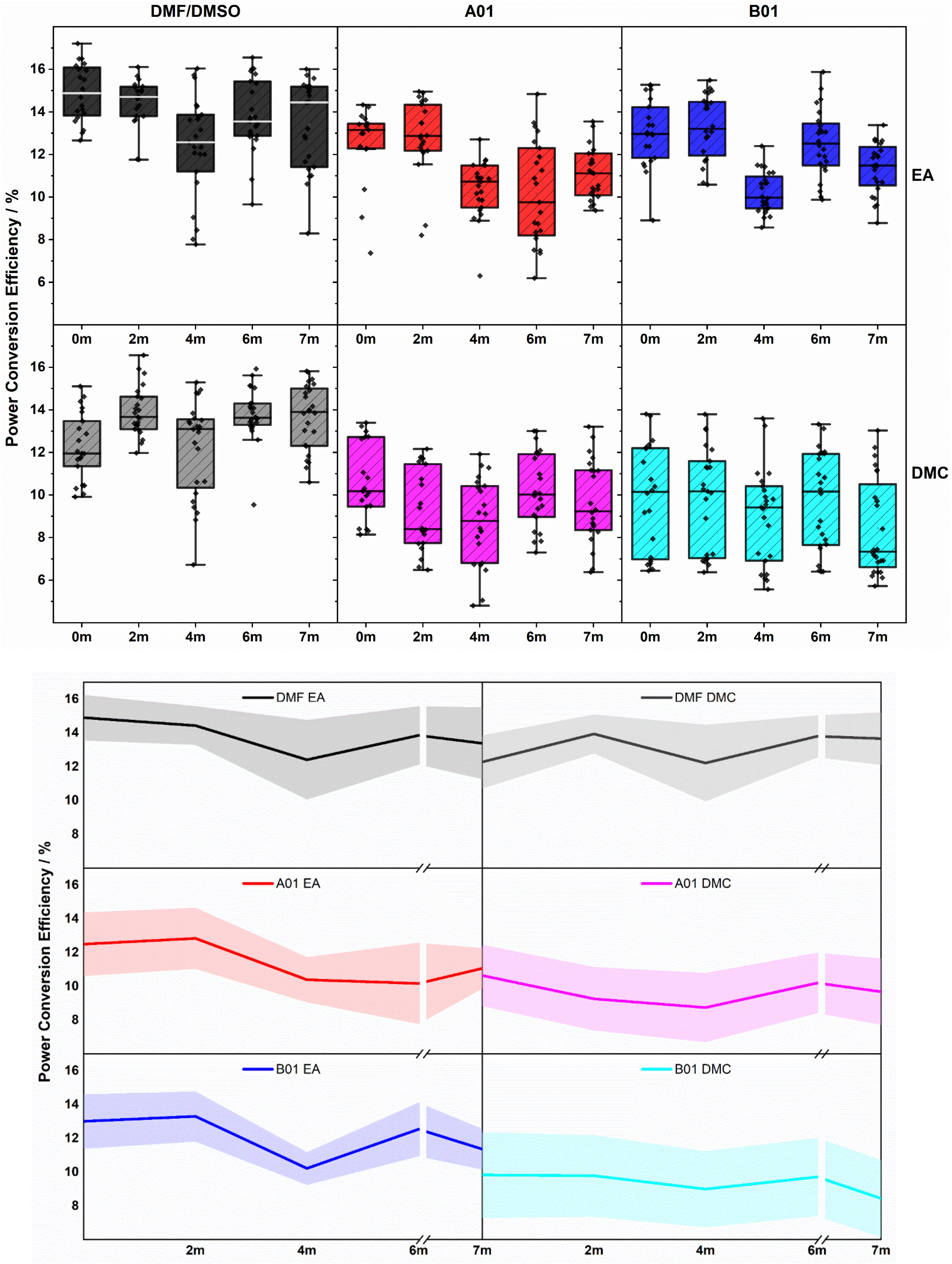

Figure 89 - Box Plots and statistical plot for device PCE over 7 months of measurement.

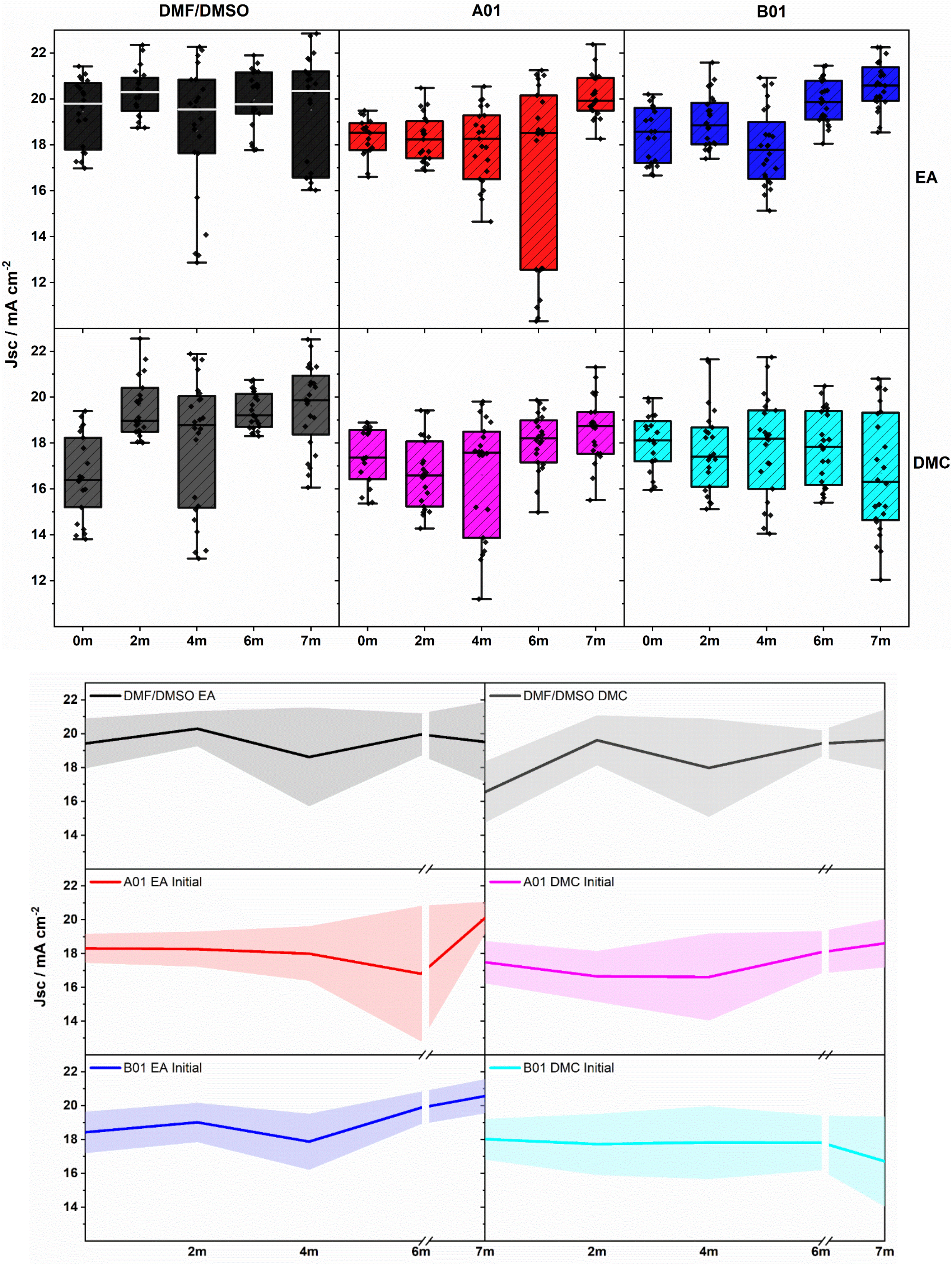

Figure 90 - Box plot and statistical plot for device Jsc over 7 months of measurement.

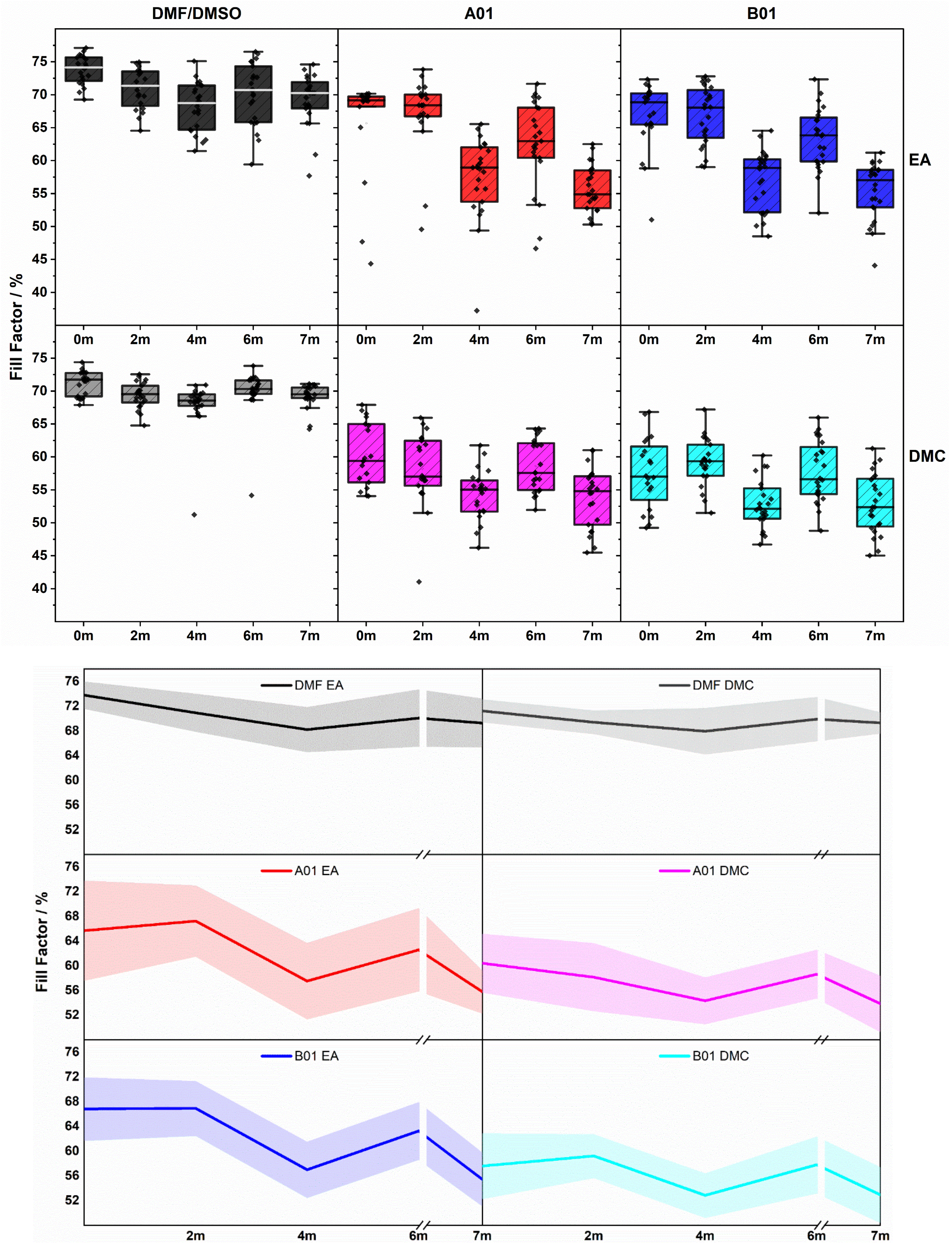

Figure 91 - Box plot and statistical plot for device Fill Factor over 7 months of measurement.

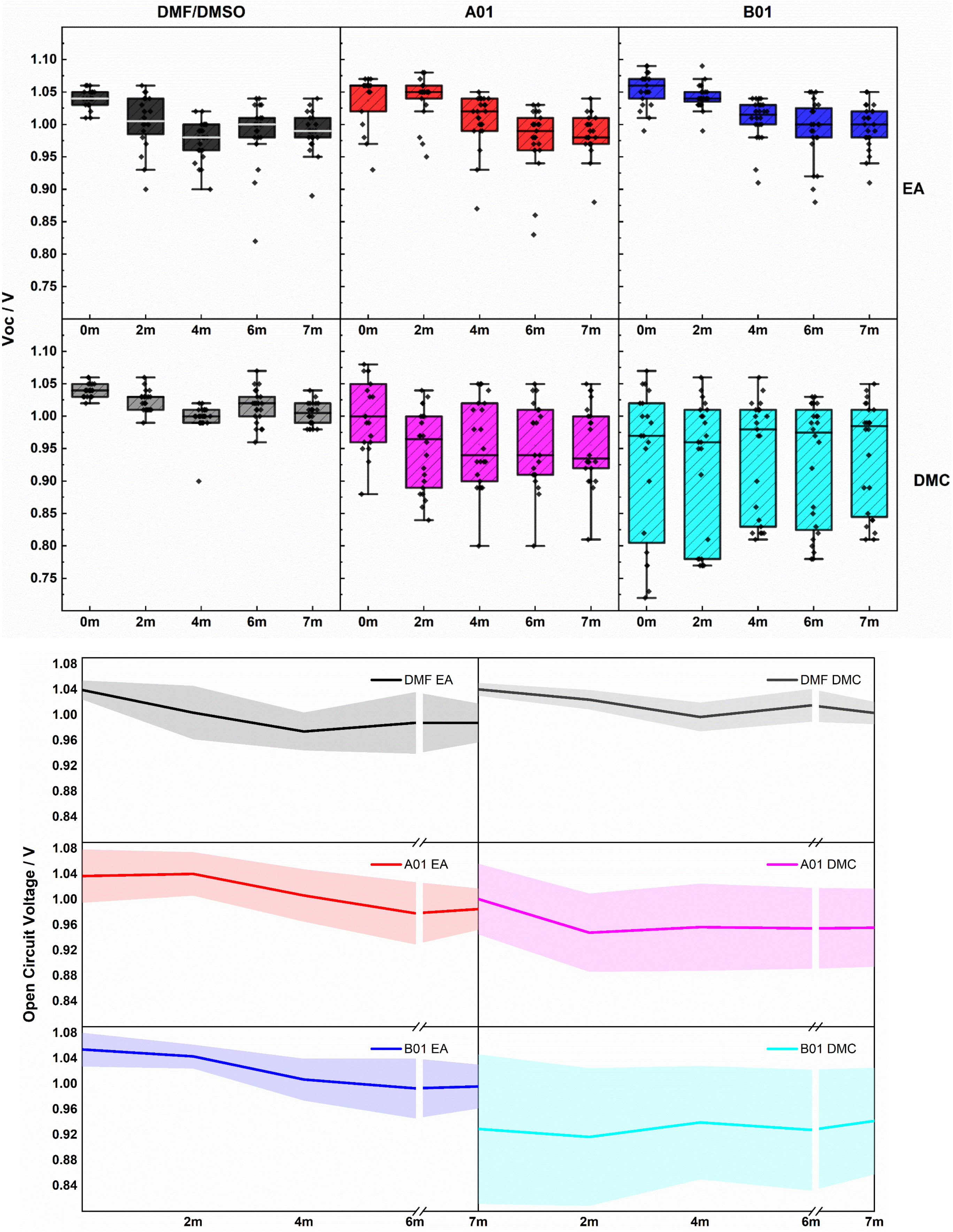

Figure 92 - Box plot and statistical plot for device Voc over 7 months of measurement.

Figure 89, Figure 90, Figure 91, and Figure 92 – a) Box plots for the four major photovoltaic parameters, power conversion efficiency (PCE, %), fill factor (FF, %), short circuit current (J_{sc}, ma cm^{-2}), open circuit voltage (V_{oc}, V) for DMF/DMSO, A01, B01 EA and DMC device builds showing pixel by pixel performance. b) Statistical plot for the sample set showing 7 months of $Cs_{0.066}(MA_{0.17}FA_{0.83})_{0.934}Pb(I_{0.83}Br_{0.17})_3$ performance evaluations. With the line representing the mean value for that data set and shaded region 1 standard deviation from the mean.

Figure 89, Figure 90, Figure 91, and Figure 92 show box plots representing 7 months of JV performance data along with a statistical representation for each of the four photovoltaic parameters recorded. All devices exhibited significant performance within this 7 month evaluation period, demonstrating the long term operability of the triple cation composition. Each precursor system was utilised to compare the novel anhydrous anti-solvent DMC.

Measurments were taken corresponding to the following dates:

Table 21 – Manufacture dates for devices measured in the PCE stability study.

Months from manufacture / m	Date	Days
0	08/08/2022	0
2	19/10/2022	72
4	13/12/2022	127
6	16/02/2023	192
7	13/03/2023	217

The DMF/DMSO control CsMAFA solution with EA as the antisolvent achieved the highest efficiency for the day zero measurement, with an average pixel result of X% +/- Y and with champion pixels > 17%. A high open circuit voltage, fill factor, and appreciable Jsc contribute to this performance. For the DMC samples, using the same precursor solution and spin conditions, performs comaprably poorly in this initial measurment averaging 12% with champion pixels > 15%. With a directly comparable V_{oc} and fill factor to the EA sample, this performance decrease can be attributed directly to the lower current exhibited by these samples. For the A01 samples, the EA set day zero measurment corresponds to previously attained device data exhibiting a lower PCE than the control samples averaging ~13% with champion pixels attaining 14% with a narrow distribution of values. The V_{oc} results indicate a similar magnitude to the DMF/DMSO control with some pixels fallling below 1 V. The FF and J_{sc} respectively show slightly lower performance for this sample set with the ~2 mA cm^{-2} decrease leading to the reduction of PCE%, The A01 DMC samples show a lower PCE averaging ~10% with champion pixels attaining 13%, with this decrease a combination of a reduction in all three parameters V_{oc}, J_{sc}, and FF. The low FF of under 60% represents a poor initial result from this combination, suggesting some retardation in the current response under illumination. With the EA anti-solvent, the performance of the B01 system is similar in trend to A01, with the major constituents of the solution remaining consistent (70 vol% DMSO/DMPU with EA initiating the crystallisation). The average PCE obtained was 13% with slightly higher champion pixels than A01, at 15%. The parameters remain consistent with the A01 devices, exhibiting a marginally higher V_{oc} than the A01 samples, consistent with the DMF-based control. Whilst a similar average J_{sc} can be seen, the higher PCE% pixels (15%) can be attributed to the higher J_{sc} values achieved for these pixels. For the synergistic combination of B01 DMC, with the inclusion of DMC within the precursor, again lower PCE% values are attained for day zero, with an average of 10% and a high degree of variability. The source for this variability can be seen in the V_{oc} values attained with mimic the PCE% spread and poor performance for this composition type, indicative of poor film formation at the ETL interferace, potentially resulting from rapid film formation due to the increased anti-solvent miscibility. The observed fill factor is also the lowest recorded for any composition with a 57.5% average, indicative of poor charge extration within the device.

The humidity and temperature of the environment during the measurment fluctuated based on the season, with the measurements spanning summer through to spring. After 72 days of aging the second measurement of the DMF/DMSO EA system shows a slight decrease in PCE, though negligible, with an increase in the J_{sc} offset by a decrease in both the V_{oc} and FF. This phenomena is explored for $MAPbI_3$ samples in chapter 5, with a low level of ageing upto 1 week, suggesting an improvement in PCE due to an increase in current. The increase in current is observed for these samples, with advanced aging (72 days) a point beyond which some level of degradation counteracts this benefit. The highests level of improvement was observed for the initially poor DMF/DMSO DMC samples, suggesting a dramatic increase in PCE of upto 2% with a consequent improvement in the champion pixels. This is accompanied by a slight reduction in both the FF and V_{oc}, with these gains solely due to a large increase in J_{sc}, of around 3 mA cm^{-2}. This result represents a far greater gain than the slight increase observed for the EA samples, highlighting the importance of ageing studies with such sensitive materials.

For the 127 day measurement, taken in december at low temperatures, a significant decrease in the ~PCE was recorded for the EA samples, with this decrease only marginal for the DMC equivalent samples, despite reduced reproducability. The decrease in the V_{oc} and FF for each sample set remains proportional in magnitude to the previous drop from day zero to day 72, with a greater reduction evident for the EA samples. This leads to a comparable FF and lower V_{oc} at day 127 for the EA samples. In terms of J_{sc}, both sample sets show similar levels of variability, indicating consistent environental influence. Despite a marginally higher J_{sc} for the DMF-based samples provides a slightly lower average PCE <0.5% with the increase in the DMC sample average attributed to higher V_{oc} values. Champion pixels are also comparable here at around ~16%. The 192 day measurement leads to an uptick in the PCE performance of the DMF/DMSO based samples, with averages around 13.75% for both anti-solvent cast device sets. All parameters improve to contribute to this value with the trend continuing during the 217 day measurement, where average PCE values remain competitive with day zero measurments for the EA samples, retaining 93% efficiency (1% decrease) compared to day zero. With the average now close to 14%, the DMC samples exhibited the greatest increase of 2%. These results highlight some of the weaknessess in current research methodologies, especially in terms of sustainable chemical substitutions. This is evidenced by the initially poor triple cation samples as deposited with DMC as the anti-solvent. Despite negative initial results, as the samples are aged and exposed to levels of environmental degradation – typically required of a solar cell material, the performance reaches parity within a 7 month period. The influence of external factors has not been throughly tested in this study, with this work suggesting there may be mechamisms involved in long term performance worth further investigation.

For the 72, 127, 192, and 217 day measurements, both the A01 and B01 samples provide similar trend profiles in terms of both PCE and J_{sc}. For the PCE this includes a similar average result for day zero and 72 days with a subsequent drop at 127 days from 13% to 10%. Slight deviation occurs at 192 days, with the A01 sample average decreasing to 9% whereas the B01 sample recovers slightly to around 12.5%, driven by an increase in J_{sc} over the A01 set. By 217 days both samples are again showing parity, with the averaging rangin from just over 11% to 11.5%, corresponding to PCE retention rates of 85% and 88% for the A01 and B01 samples respectively. The V_{oc} and FF trend is also closely aligned for both the B01 and A01 solution. With a decrease in both parameters contributing to a reduction in PCE retention as compared to the DMF-based samples. For the DMC equivalent sample sets some differences are apparent in the collected PV parameters. After 72 days the A01 DMC samples show a significant decrease in PCE and V_{oc}, with smaller decreased noted for the J_{sc} and FF. The A01 V_{oc} remains quite stable past this initial decrease, stabilising at around 0.925 V at 127 days. For B01, the DMC sample shows a wide range of values, with the Voc stable over all measurements on average, with the across all days at 0.975 V. In part as a result of this V_{oc} spread, the B01 DMC sample shows poor reproducibility amoungst pixel measurements, with the average PCE remaining relavtively consistent from day zero through to day 192, followed by a significant decrease in PCE at day 217. Conversely the PCE recovers for the A01 sample during days 127 and 192, despite a poor FF during day 127. This FF value increases in tandem with the J_{sc}, leading to higher PCE values for the 192, and 217 days, whilst remaining at around 10%. The A01 and B01 DMC sample sets suffer from reduced reproducibility per pixel, potentially resulting from issues at the ETL/PAL interface, however, the values attained show comparable consistency, with the exception of the 217 day B01 DMC value which decreases to its lowest point retaining a PCE of around 70%. The A01 DMC sample retains close to 90% of the original PCE after 217 days, with the caveat of a poor initial performance of 10%.

6.3.8 Internal Photo-Conversion Efficiency (IPCE)

In order to further investigate the perofrmance of these degraded cells, IPCE measurements were taken using champion pixels by each composition after the 217 day measurments were completed. These samples have been exposed to 1 sun (AM1.5) light during measurment. This enables verification of the J_{sc} for these achieved pixels, enlightens the potential for reverse hyseresis in certain compositions and allows analysis of the wavelength on the potential for current generation.

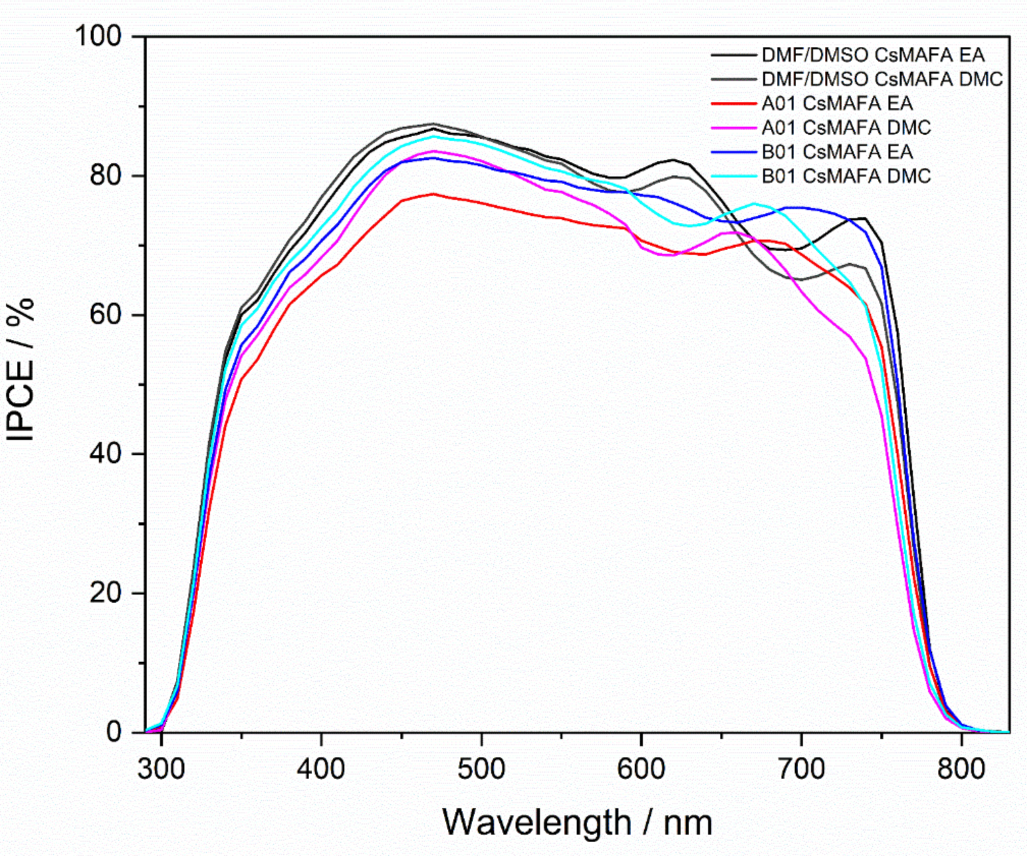

Figure 93 - Champion pixels evaluated through IPCE at 7m age for each solvent system-anti-solvent pairing.

The IPCE spectra in Figure 93 shows the percentage of each wavelength converted into current for the pixels investigated. Corroborating the device PCE measurements both the EA and DMC sample sets for the DMF/DMSO precursor suggest the highest IPCE%, approaching 90% at 450 nm. All samples suggest the highest percentage conversion efficiency at this wavelength. For the DMF-based samples the higher IPCE% at 450 nm for DMC reduces below the EA by the 625 nm peak, with an even larger discrepancy at the 750 nm peak. This provides an indication that the champion pixel for DMC has marginally higher conversion efficiency at short wavelengths and lower efficiency as the wavelength increases. The A01 and B01 EA samples show a similar spectral shape with a greater conversion efficiency for the B01 sample, with the A01 sample showing the worst conversion efficiency at 450 nm of all samples measured. Both samples show a reduced secondary peak at 600 nm, with no noticable peak at 625 nm. An increase in the spectral conversion efficiency is present for these samples instead at 725 nm in contrast to the DMF-based samples. With this peak less pronounced and extended for the poorer performing A01 measurement. This result supports observations noted in the absorptance differences between these samples, suggesting a higher capacity to absorb and convert light within the 700-750 nm range. The reduced transparency of these samples is of note here, with scattering and reabsorption possible due to the ‘cloudy appearance of these cells. The A01 and B01 DMC evuivalent samples suggest a modified spectral shape, contrasting the DMF-based DMC sample with a trough present, indicating lower conversion efficiency between 600-650 nm. The peak for these samples is extended to longer wavelengths between 640-690 nm, with the 750 nm peak not present for these samples.

6.3.9 Anti-Solvent Combinations

To investigate to further investigate the impact of the anti-solvent on the experimental triple cation perovskite inks, an optical and photochemical evaluation was undertaken with an intermediate combination of EA and DMC in a 50/50 ratio.

6.3.10 Optical and Photoluminescence Properties of the Film

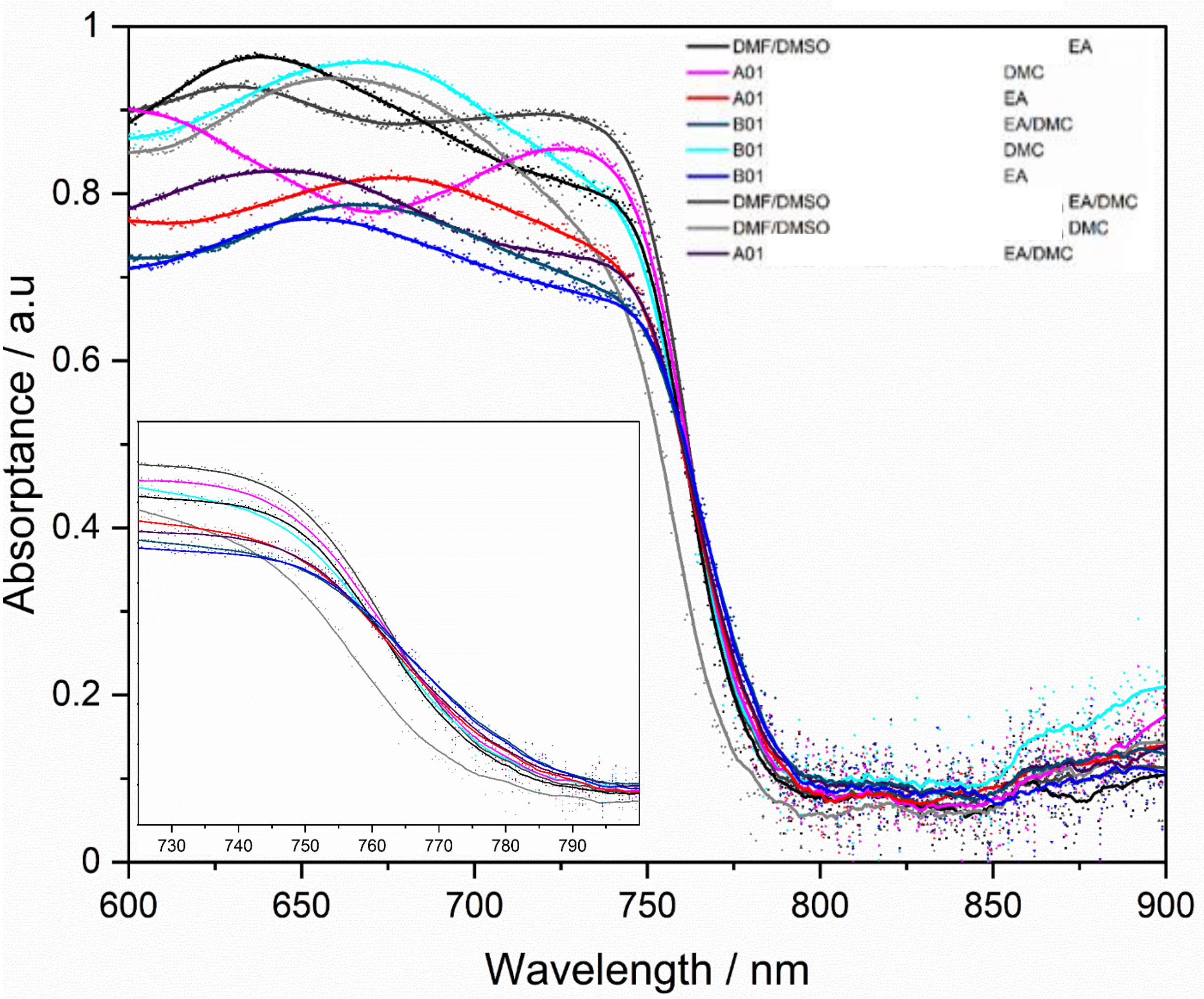

Figure 94 – Absorptance spectra for each of the films cast from the A01, B01 and DMF/DMSO solution with the anti-solvent as EA, EA/DMC, and DMC.

Absorptance spectra were taken for the films evaluated within the study (Figure 94). The triple cation composition suggests a higher degree of susceptibility to the antisolvent choice than was seen for $MAPbI_3$ perovskite. This is also evidenced by visual inspection of the films (as seen in Figure 103). The sensitivity of this complex composition, regardless of the environmental regulation, leads to films with visual disparity and modified absorptance over the band gap range.

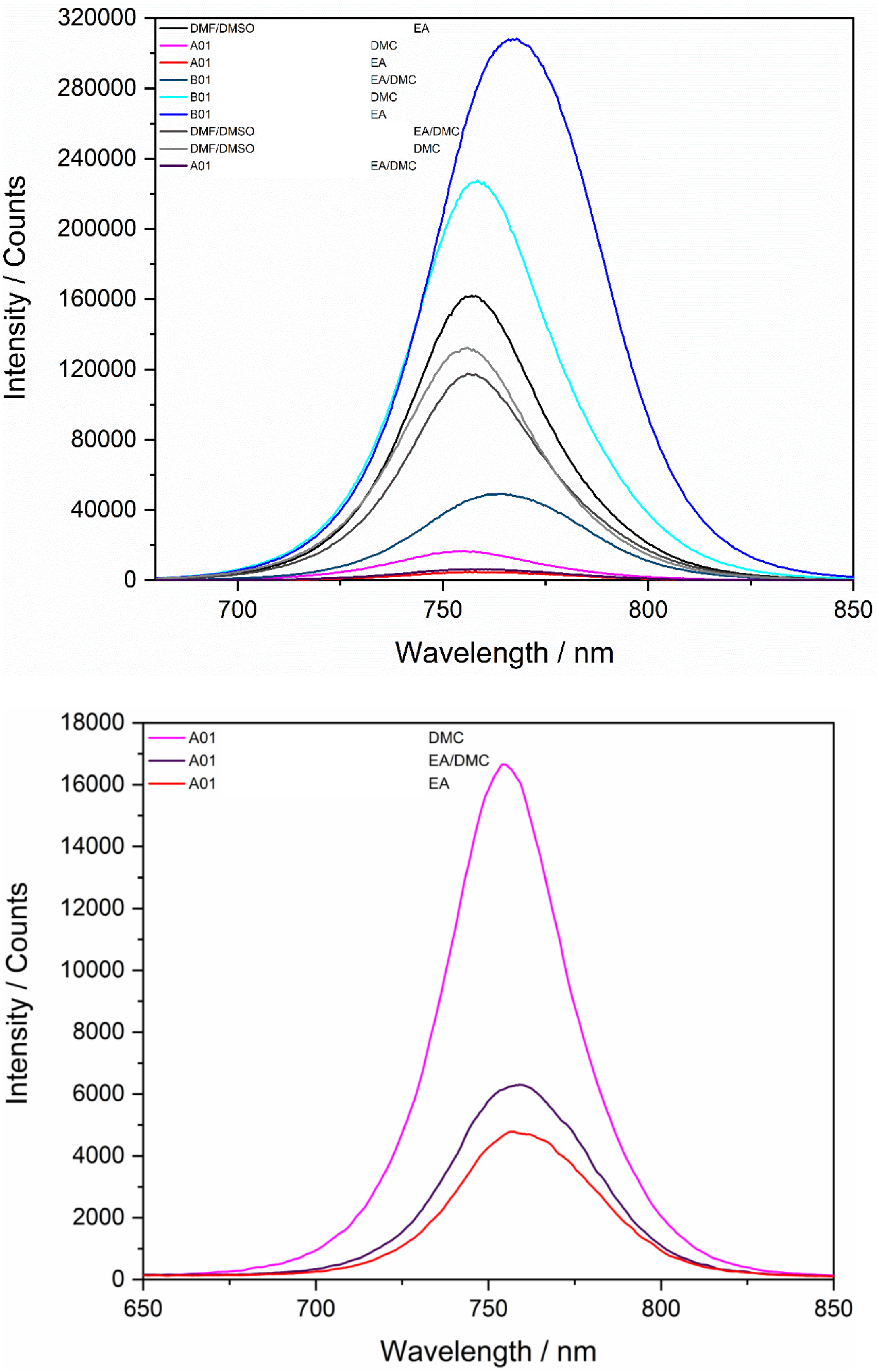

Figure 95 – Steady-state photoluminescence for the CsMAFA films deposited using pure EA, a 50/50 vol% ratio of EA/DMC and pure DMC (step 0.5nm, dwell 0.2s, BW 2.5 nm, 520BP 611LP 300 µL anti-solvent).

Films measured for SSPL (Figure 95) show highly significant changes depending on the precursor solution and anti-solvent utilised. Generally, the B01 samples, despite not showing a significant difference in absorptance, show the highest levels of PL emission. The DMF/DMSO samples retain the highest levels of reproducibility. The highlights less susceptibility to anti-solvent choice – also noted for the $MAPbI_3$ composition using this solvent system. Here the A01 system shows the lowest levels of PL emission with samples appearing visually different in Figure 103. This orange colouration is more suggestive of PbI_2 within the film, potentially due to the PbI_2 excess nature of this triple cation composition. The B01 system, however, reduces in PL as DMC is added to the precursor and upon the use of the pure component. The synergistic effect of anti-solvent addition within the precursor does not appear to benefit this system in terms of PL emission alone.

6.3.11 Small Scale Samples – An XRD Study

Samples were manufactured on a small scale (1 cm^2) to conduct and XRD study into the effects of antisolvent addition. The small sample size chosen aims to enhance the antisolvent-precursor solution interaction providing an exaggeration of the crystallographic state of a film present within a device. Three standard precursor solutions were prepared as in a device build with films prepared using the three anti-solvents noted below:

X – Pure EA

Y – EA/DMC (50/50 vol%)

Z – Pure DMC

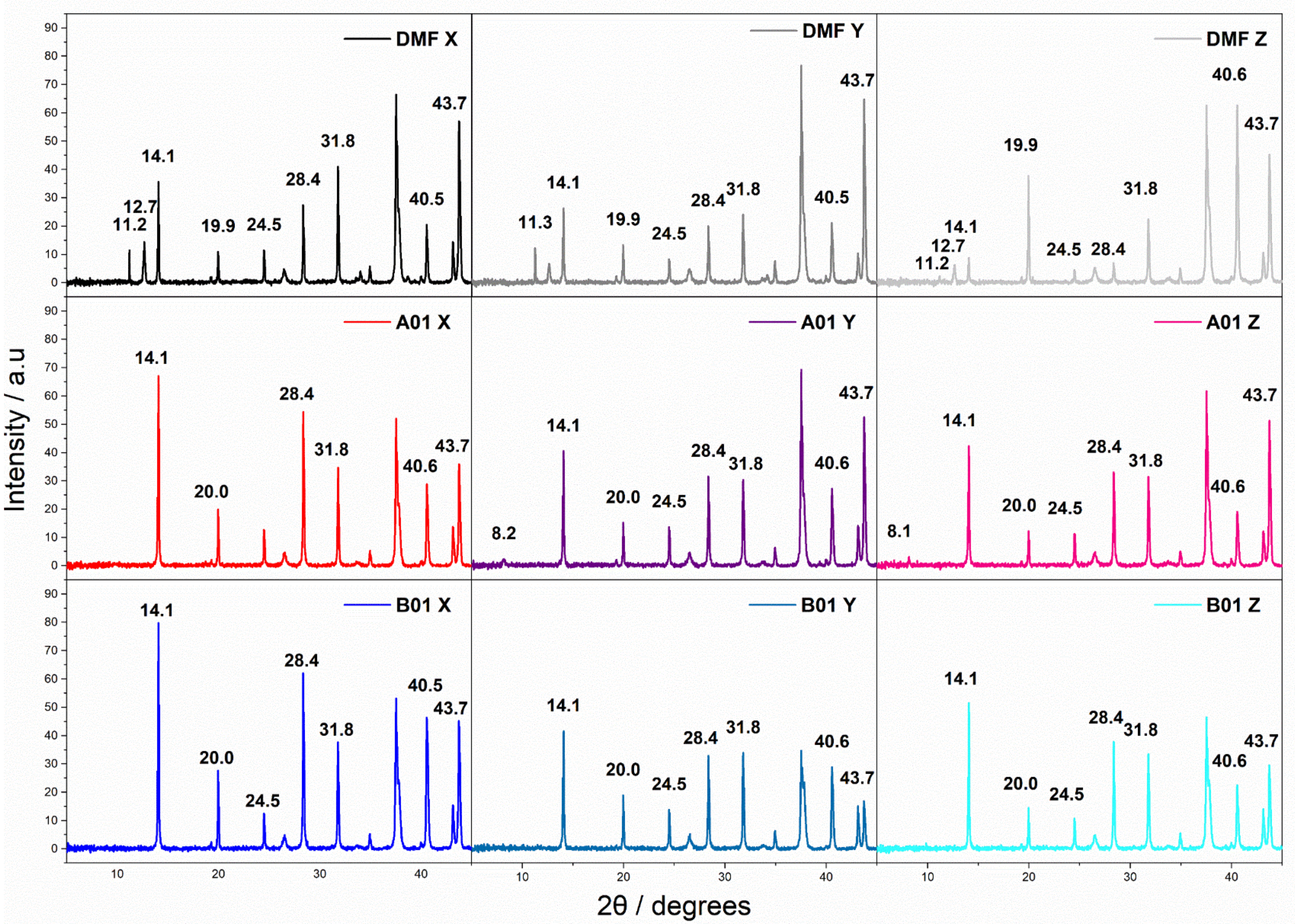

Figure 96 - 1 cm^2 Samples, exposed to atmospheric conditions during XRD scan. Evidence of photo inactive delta phase $FAPbI_3$ at 11.2 degrees in DMF/DMSO EA sample. Crystallographic changes to the DMF/DMSO DMC sample potentially favouring 200/ 400 tetragonal structure.

Figure 96 shows XRD spectra for small scale samples fabricated using the experimental antisolvents pure EA, 50/50 vol% EA/DMC and pure DMC. The DMF samples show poor plane uniformity, with a PbI_2 peak present at 12.7° and the inactive delta phase $FAPbI_3$ peak at 11.2/11.3°. No such peak is observed for the experimental solutions A01 or B01. Both A01 and B01 show a much higher intensity in the 110 direction (14.1°) than the control – indicating greater crystallinity. Transition of the anti-sovlent for these small scale samples lead to a reduction in the 110 intensity with the exception of B01 with DMC as the antisolvent.

For the case of the DMF sample, as the antisolvent DMC is introduced to crystallise the film, the 110/310 growth directions reduce in intensity with the 200/400 (20.0° and 40.6°) increase in intensity. This is most prominent for the DMF-DMC sample, with the orientation favouring the 200 and 400 planes entirely. This finding is similar to spectral differences noted in the literature for hot cast perovskite with improved charge transfer and lower trap density[233].

By fabricating devices on a small scale – enhancing the impact of the anti-solvent on film formation – large changes to the triple cation perovskite structure can be observed. This highlights the potential for selective growth processes as a result of changes to both the precursor and anti-solvent.

6.3.12 Absorptance and SSPL Studies for Aged Films and Precursor Solutions

Investigations were undertaken using absorptance measurements to investigate the effect of precursor aging and film aging on deposited films. Precursor solutions for each solvent system were aged for a 2-month period prior to deposition and initial measurement of the film. These films were then aged for one months and then remeasured. Ethyl acetate was used as the sole anti-solvent in this aging study due to the device evaluation indicating a greater performance for this system with the proposed precursor formulations.

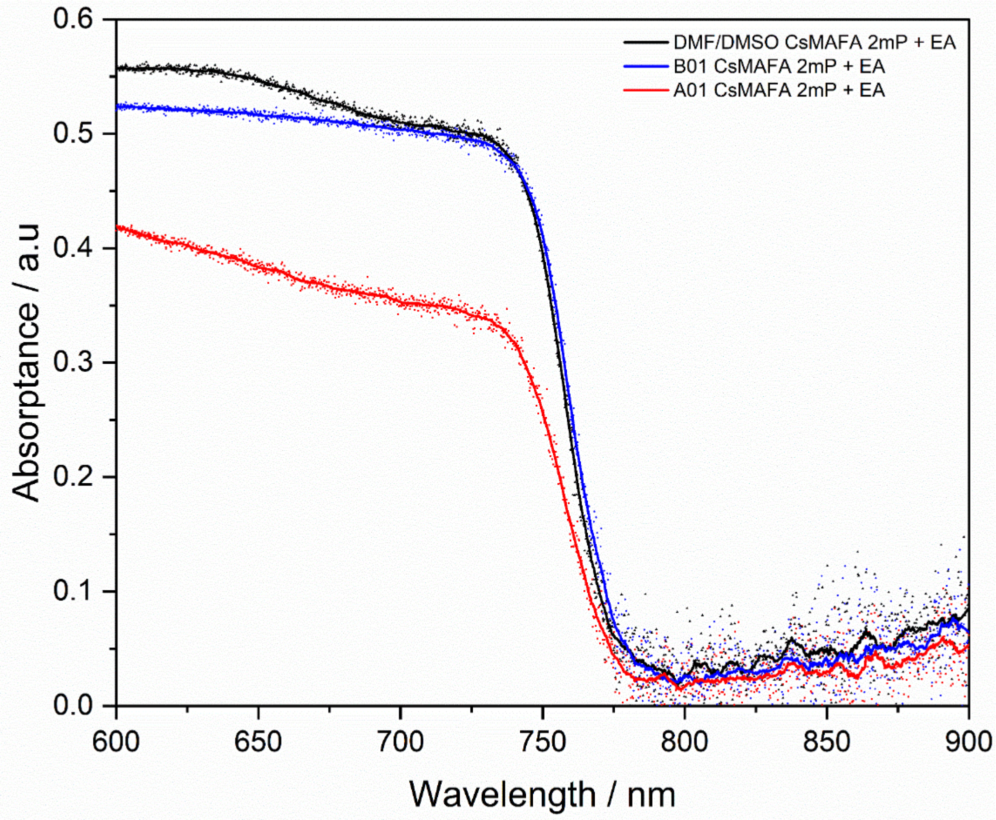

Figure 97 – Baseline subtracted absorptance scan for films deposited from the DMF/DMSO, A01 and B01 CsMAFA solutions under PMMA. Precursor solution was aged under parafilm for 2 months prior to deposition.

The initial two-month-old precursor solutions were used to spin coat films on FTO for absorptance measurements, builds were done in an ambient environment and then encapsulated with PMMA prior to initial measurement. Figure 97 provides a comparison between the ascertained absorptance for each of the films deposited from the two-month-old precursor ink. The B01 film shows the highest absorptance with a marginally longer wavelength onset than either the DMF/DMSO or A01 solutions. The aged A01 deposited film shows the lowest absorptance over the range with the DMF sample showing a similar onset but superior absorptance performance at longer wavelengths. An aged solution can therefore be used to manufacture a film with similar absorptance properties to a fresh solution, however, it can be seen that A01 shows signs of a decline in absorptance as compared to Figure 84.

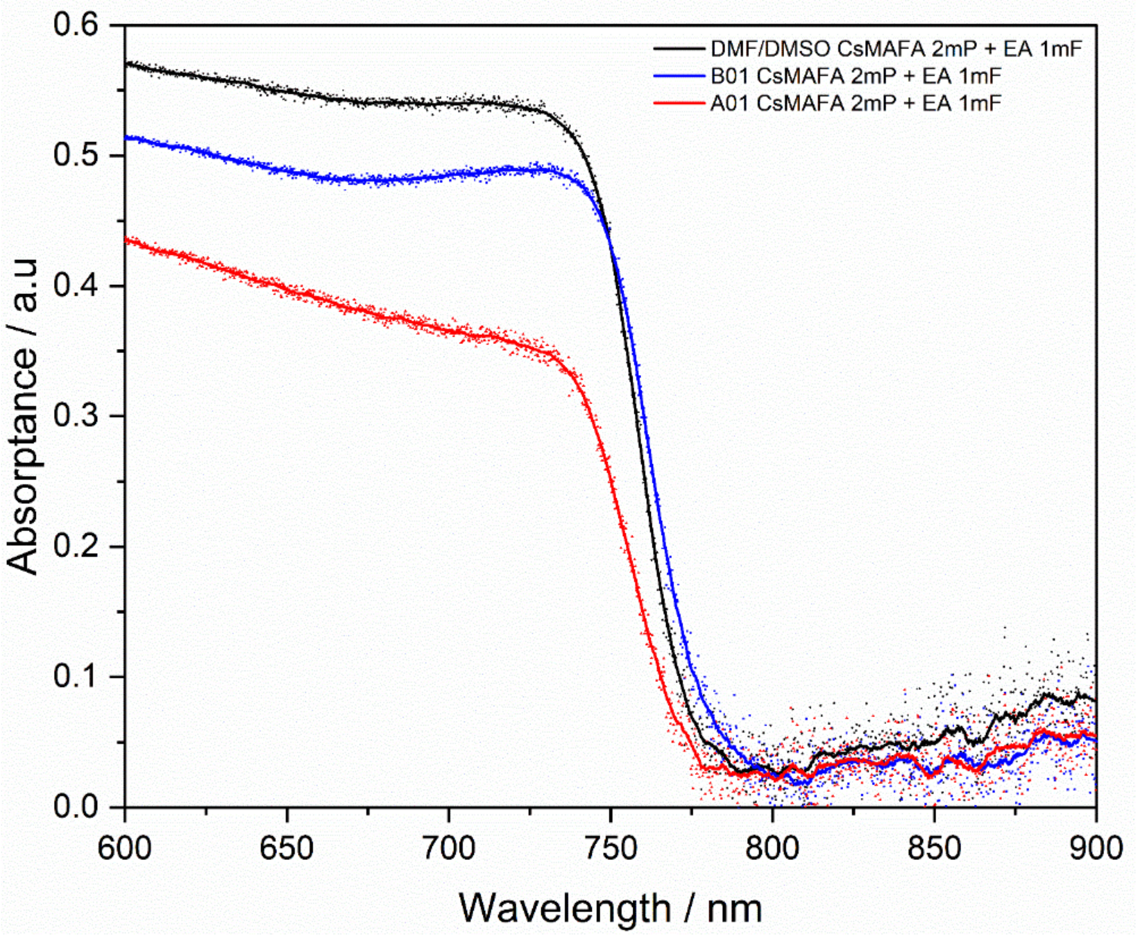

Figure 98 – Absorptance scans for the 2-month aged precursor deposited films after 1 month of aging under PMMA encapsulation.

After 1 month of aging, the films were further scanned with the result presented in Figure 98. The absorptance of the DMF/DMSO deposited film has improved marginally in the range between 600 – 750 nm. Whilst A01 shows a slightly higher absorptance, B01 shows a slight decline. This absorptance study suggests that after a substantial period of solution aging (2 months), films produced from the A01 solution show a reduced capability to absorb light through the band gap range. Furthermore, care should be taken to ensure films deposited from aged solutions retain their absorption properties after a period of film aging. Undesirable interactions between solvents and solute within the precursor are known to have a negative impact on film quality, with this effect more pronounced in the B01 film as compared to the control. Figure 86 provides XRD spectra taken for these samples with a prominent peak present at 8.2 degrees, postulated to be the result of solvent trapped within the sample. To ensure the long term absorptance of these devices this peak should be minimised where possible to avoid solvent mediated film degradation during storage. As was demonstrated previously, the long-term device performance remains stable, suggesting this artefact has minimal impact on overall PCE. It is therefore proposed that after a period of aging (1 month), independent of solvent trapping, the absorptance decreases as a result of these undesirable time dependent interactions within the precursor relative to the known mechanisms of the DMF/DMSO solution.

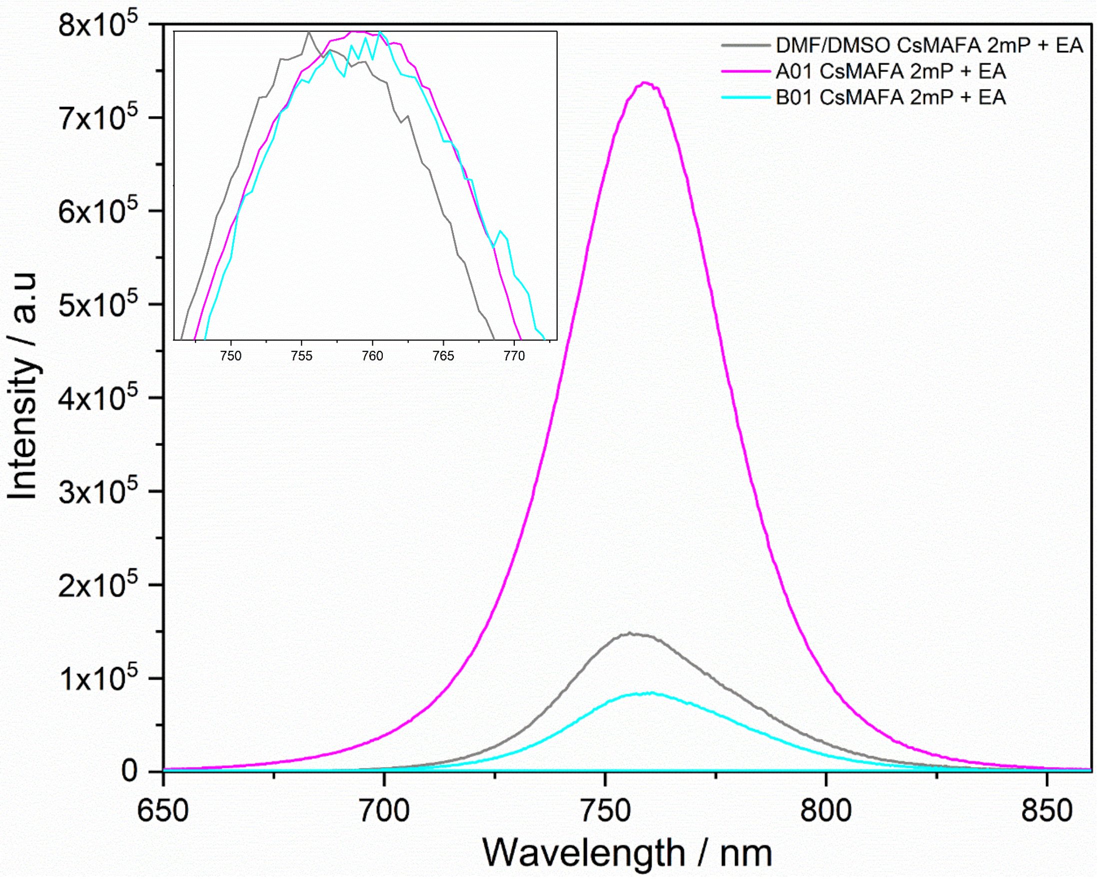

Figure 99 – Steady state photoluminescence measurements for the 2-month aged precursor solution deposited films. SSPL of the three films used to measure absorptance in Figure 97, highest PL sample was used of 3 fabricated samples. Inset shows normalised scans indicating the peak position.

SSPL measurements were also taken for the 2-month aged precursor films, with the results displayed for the initial scan in Figure 99. The highest PL sample was evaluated for each composition. This scan shows the sample with the highest PL emission was the A01 sample, followed by the DMF/DMSO control, with the B01 sample comparable in magnitude but the least emissive. The peak position is also evident showing a 760 nm peak for both A01 and B01 with a slight shift in the DMF/DMSO film peak to ~755 nm. Comparing this to fresh films produced in Figure 83 a), we can see a blue shift in all the peaks with this effect more pronounced for the A01 and B01 systems. It has been demonstrated that the addition of Cs into the structure can lead to a shift in peak position representing a slight widening of the band gap[78] (Figure *80*). Freshly made solutions have an aging time of 2 hours, with the DMF-based solution exhibiting a 760 nm peak indicative of the 5-10 % Cs addition under these conditions. The A01 and B01 solutions in Figure 83 show a red shifted peak position located at ~765 nm and 768 nm respectively. The 2 months of aging, a substantially longer period, modifies this peak position to the anticipated value of 760 nm. This result provides an indication that a longer period of dissolution is required for these solutions to fully complex the precursor cations in solution, thus depositing a composition indicative of 6.6% CsMAFA perovskite. Interestingly, while the A01 solution performed poorly in terms of absorptance after the aging period. The intensity of emission from the sample is the highest recorded.

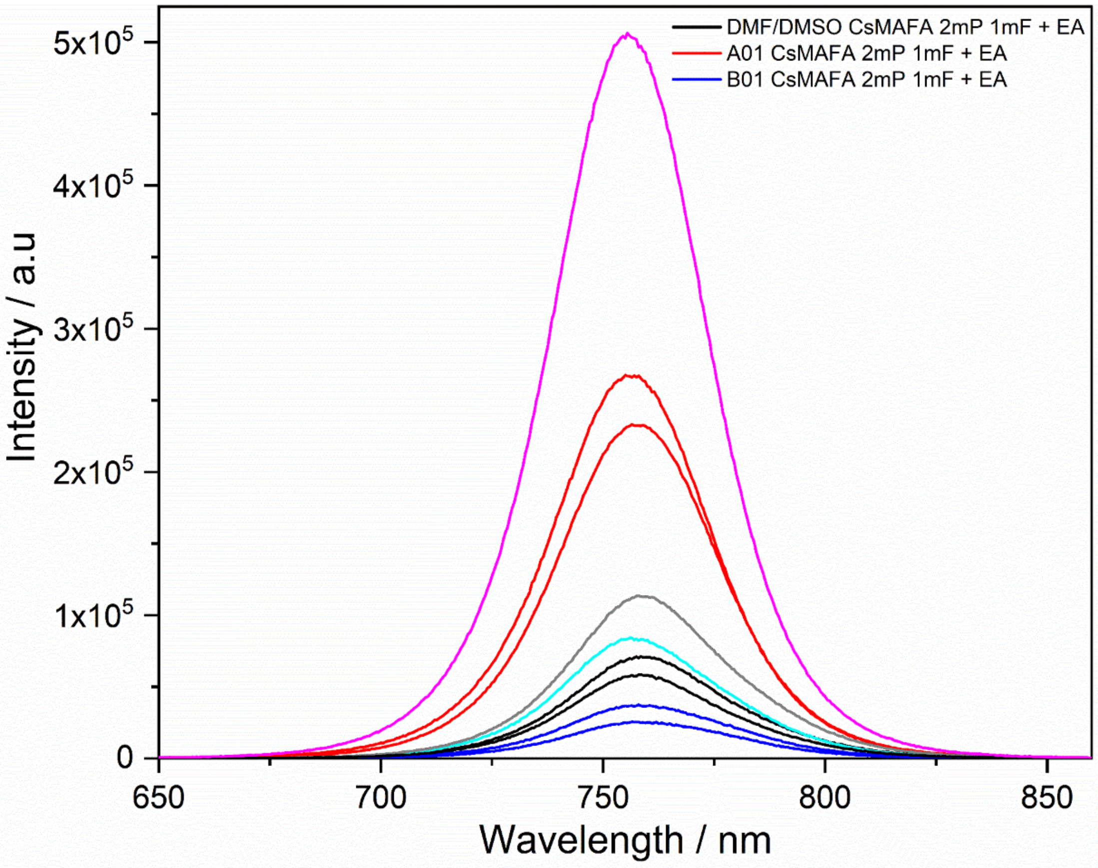

Figure 100 - SSPL of the same films measured after 31 days of aging, along with the lower PL aged samples.

This PL trend continues after 1 month of film aging. Utilising the measurement for all 3 films in Figure 100 shows the A01 samples retaining a high, reproducible PL. This result represents an anomaly when considering the more comparable performance of the DMF/DMSO and B01 formulations.

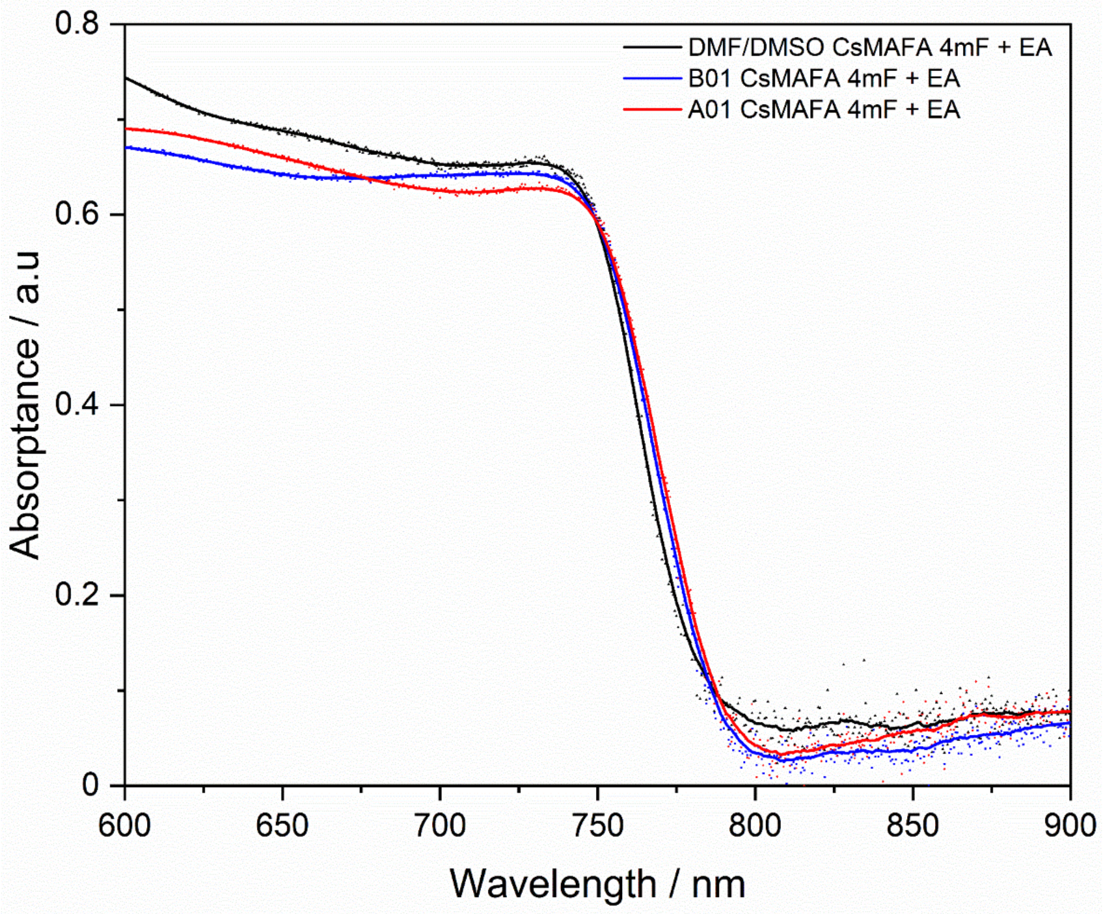

Figure 101 – Absorptance of encapsulated FTO/CsMAFA/PMMA films after four months of aging in dark, low humidity conditions.

To investigate this phenomenon, fresh samples were manufactured and aged for 4 months under PMMA in dark low humidity conditions. The results are shown in Figure 101. The spectral shape of the absorptance for each of these films is similar, with a comparable onset for freshly manufactured films. The A01 and B01 freshly made films are more comparable here, further indicating that advanced aging of the A01 precursor may lead to an increase in PL regardless of the poor film absorptance.

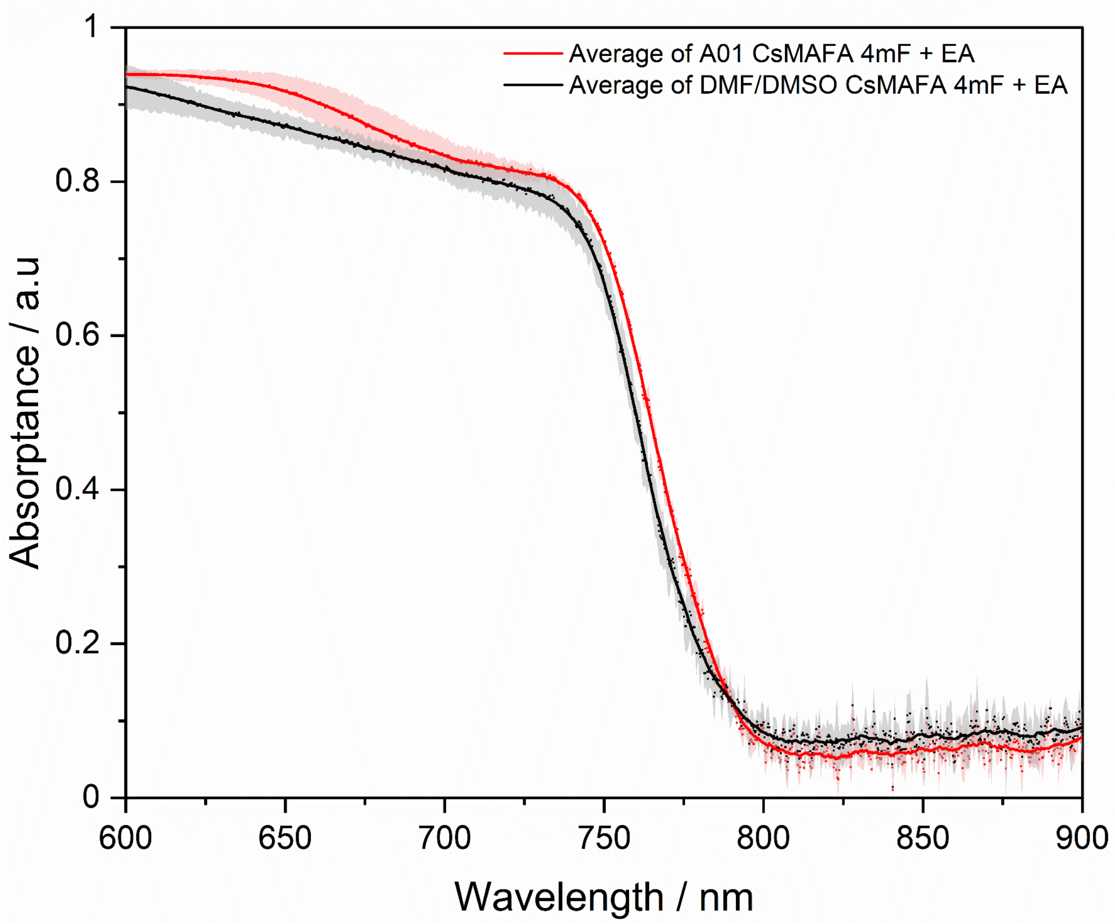

Figure 102 - a) A01 and DMF/DMSO 3 sample evaluation. Films were manufactured as fresh, encapsulated with PMMA and scanned after 4 months of aging.

To verify the reproducibility of these results, the A01 formulation was contrasted to the DMF as an average of 3 samples each after a 4-month aging period. The freshly made films again perform comparably post aging, with the A01 films showing slightly higher absorptance over the range. This result not only confirms the nature of the PL increase after aging the precursor for two months but can also be contrasted to the 4-month aged device results and 7-month IPCE spectral shape. As the devices and films measured here were manufactured under identical aging conditions, the PL comparison in Figure 83 - comparable PL, is not reflected in the device Jsc, with the slight decrease in the A01 samples unlikely to be linked to the absorption of the respective films. The IPCE spectral shape after 7 months of device aging, shows a lower IPCE for A01 devices, however the shape shows a peak for the A01 samples relative to the trough displayed for the range 600 – 750 nm. Figure 102 suggests an increase in absorptance over this range for the aged A01 films corresponding quite well to this spectral difference.

6.3.13 One Week Aged Precursor Solutions

A final study was conducted based upon the current recommended shelf life of the DMF/DMSO formulation. Methodologies suggest that this solution should be left for no longer than 1 week before a decline in performance can be anticipated. The solutions were aged for 6 days prior to deposition. Four films were manufactured on ETL substrates, with three becoming devices for measurement, and a further film deposited on FTO.

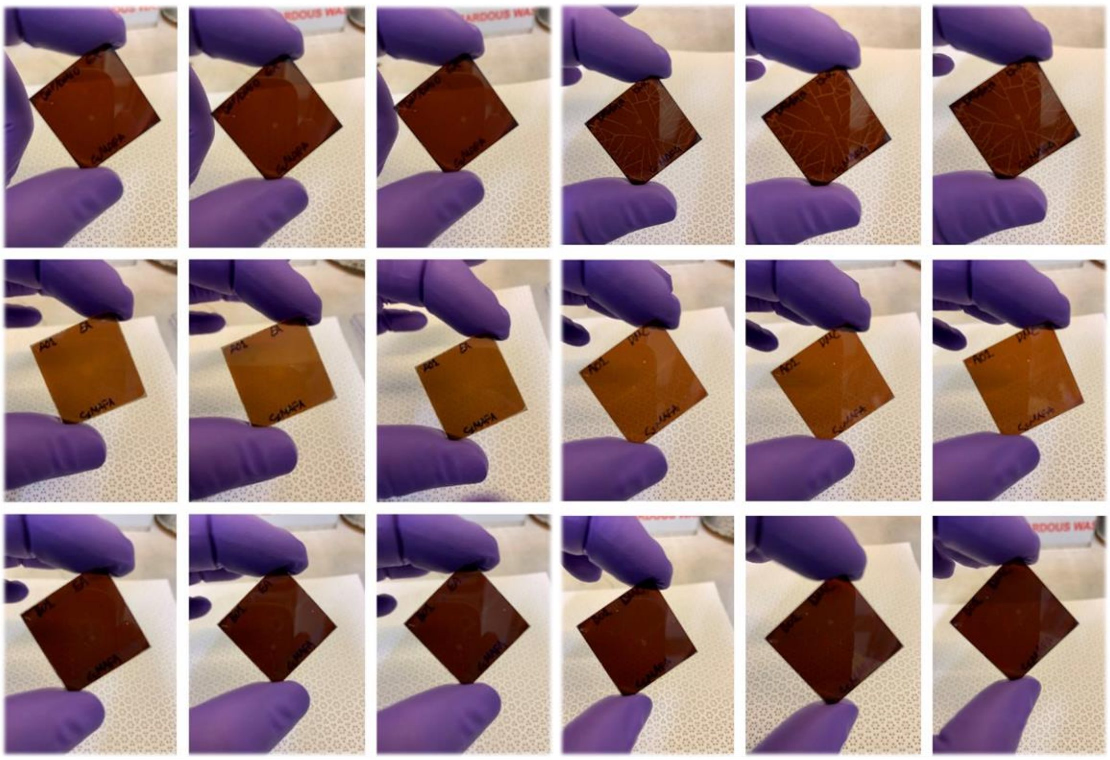

Figure 103 - Antisolvent trials with three samples of EA and DMC. Top left DMF/DMSO cast CsMAFA using EA, top right depicting DMC as the antisolvent. Middle is the A01 solution with EA on the left and DMC on the right. Bottom row shows the B01 system with EA on the left and DMC on the right.

Figure 103 provides visual example of the films cast from the 6-day aged precursor solutions, fabricated into devices.

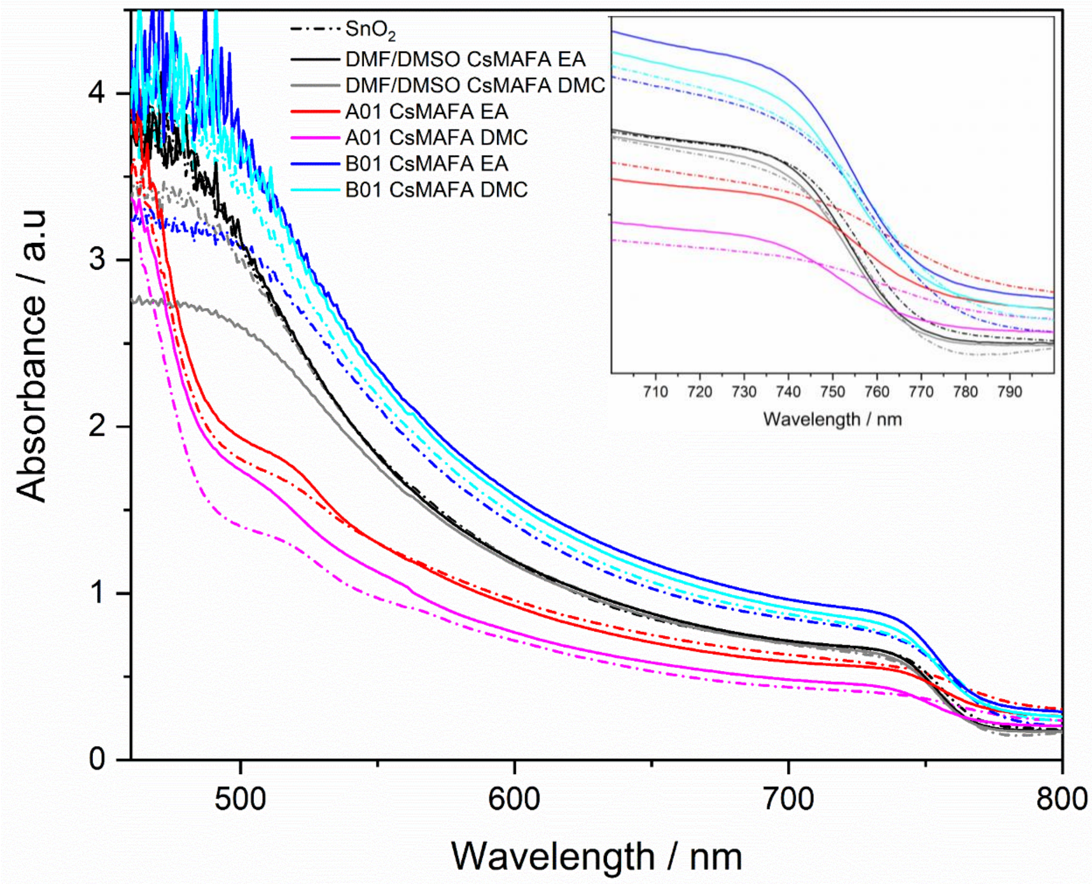

Figure 104 – UV-Vis spectroscopy for the films fabricated on bare FTO and FTO/SnO$_2$ substrates.

The absorbance for the triple cation films from the one-week-old precursor solution generally shows good agreement for the DMF/DMSO solution on FTO and FTO/SnO$_2$ for both anti-solvents (Figure 104). For the experimental solutions a slight decrease in absorbance is noted for film on SnO$_2$ as in devices.

The steady-state photoluminescence for the samples was measured for these films to determine the PL quenching behaviour for each system and anti-solvent combination.

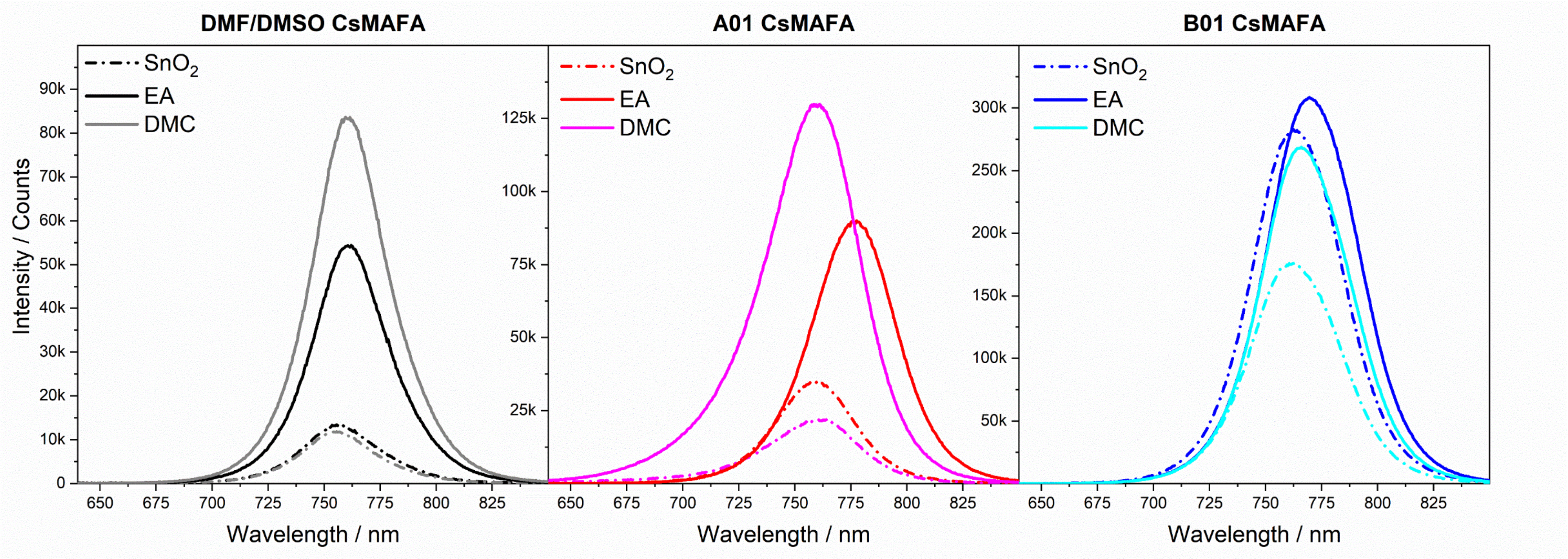

Figure 105 - Quenching behaviour for thin films deposited from the 1-week aged precursor solution.

Figure 105 indicates a clear trend for the 1-week aged DMF/DMSO precursor solution, with the DMC sample suggesting higher initial PL than EA, with the SnO_2 sample achieving parity. DMC therefore represents an opportunity to improve electron injection from perovskite to ETL. Whilst quenching from bare FTO to SnO_2 is still evident for the A01 solution, the trend is far less well defined as peak shifts are also noted. This is postulated to be the result of the aging process with the final composition of the precursor unstable. In this case switching to the anti-solvent DMC provides some quenching benefit for the film, with a more consistent peak position. The B01 solution evaluation shows significantly less quenching of the film, particularly with the EA application. DMC as the anti-solvent does appear to improve quenching when applied to both FTO and SnO_2. These results do suggest that in terms of electron generation within the perovskite active layer, and subsequent extraction, the alternative solvent DMC provides a quenching benefit to all precursor solutions evaluated. Whether this enhanced extraction can be translated into usable current in a device was investigated with full device builds.

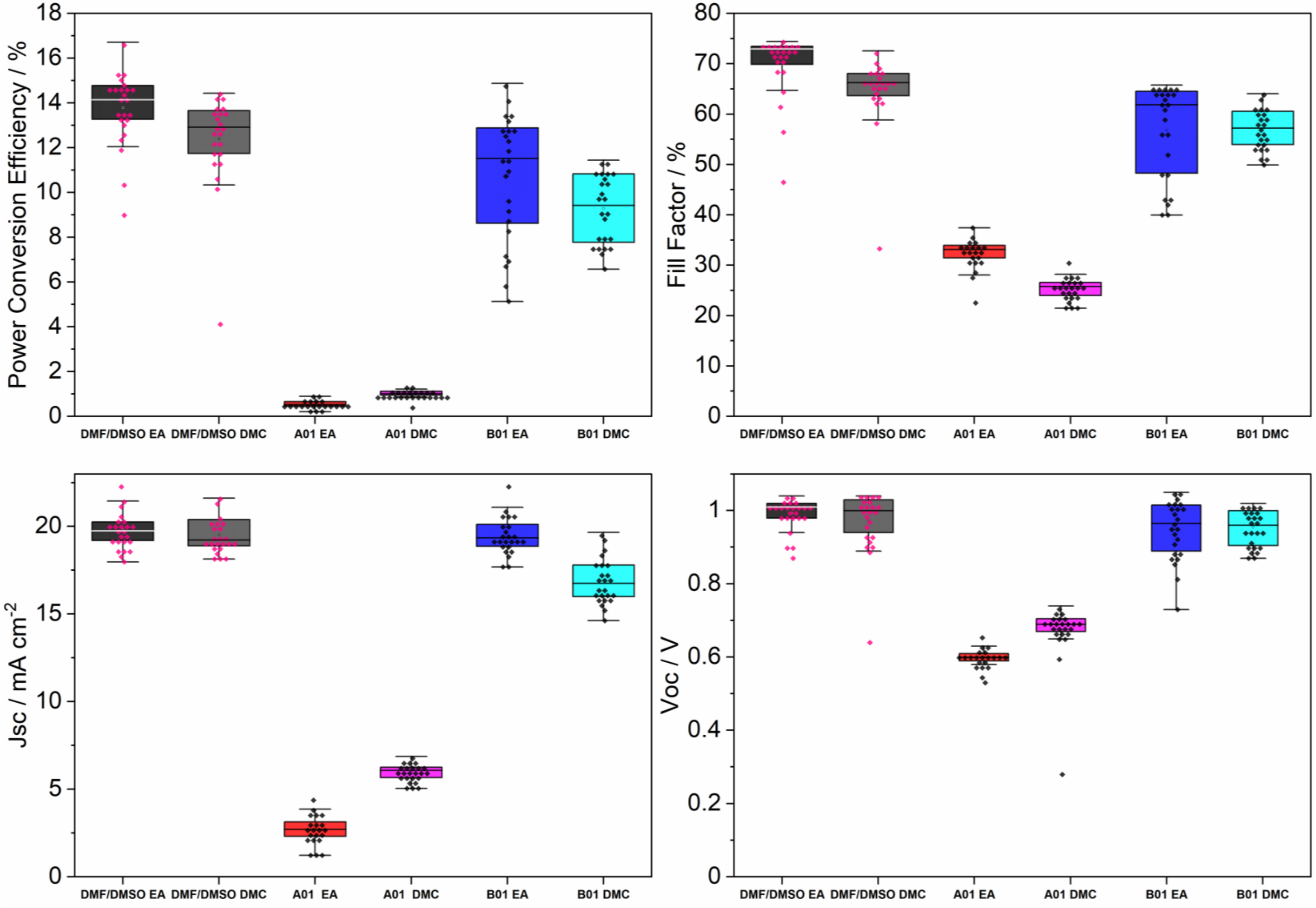

Figure 106 – Box plots showing device performance after 1 week of aging the precursor solution.

Statistical box plots can be seen in Figure 106 evaluating the performance of devices manufactured with 1-week aged precursor solutions, using both EA and DMC as antisolvents.

The DMF/DMSO solvent system results in the highest attained PCE during this evaluation. The EA sample set provides the greatest average PCE with DMC cast films marginally lower. Analysis of the main photovoltaic parameters suggests that the drawn current within the devices was comparable, with the FF lower for DMC, ultimately leading to lower PCE.

The A01 system here attains very poor PCE after 1 week of aging, with films visually appearing degraded. The transition to DMC provides uniformly higher PCE results due to a dramatic increase in the integrated current. However, the devices are barely functional.

The B01 solution outperforms the A01 candidate after the aging process, attaining an average PCE value of 12% for the EA sample set. Transition to DMC reduces performance here, despite the more promising quenching, due to lower integrated current. This result suggests that other mechanisms outside of radiative recombination and ETL injection have a greater impact on final device performance. The B01 modified solution has also proven effective in outperforming A01 in terms of long-term performance.

6.4 Conclusion

The advanced perovskite composition, CsMAFA, with increased efficiency and stability, has been evaluated along with the developed solvent systems A01 (40 vol% DMSO, 30 vol% DMPU, and 30 vol% 2-MeTHF/EtOH) and B01 (40 vol% DMSO, 30 vol% DMPU, and 30 vol% DMC. The initial film characteristics in terms of absorbance, absorptance and photoluminescence emission have been evaluated along with 'fresh' device performance. The PCE of the A01 and B01 devices was lower (*circa* 2% than the control devices, with PL investigations suggesting a much larger influence of the solvent composition on the films photochemical attributes. This is evidenced by large shifts in the peak position of the PL emission, which, when contrasted to earlier investigations of $MAPbI_3$ films is far more significant. The additional sensitivity and complexity of the triple cation films remains a significant challenge to solvent system design. Competition for complexation between novel solvents and ions, along with differing subsequent crystallisation dynamics, leads to the formation of films with varied compositional and photochemical properties. This dramatic variance can be achieved through modification of the solvent system alone, and opens pathways for extensive, facile customisation of perovskite layers – regardless of composition. This is particularly cognisant for more scalable deposition technologies – which may utilise mechanical methods for initiating nucleation. Where requirements for either nucleation or dissolution are lessened, the potential for solvent customisation increases.

The novel anti-solvent DMC has also been evaluated with the experimental triple cation precursors to investigate a synergistic effect of inclusion of the anti-solvent within the precursor. Of interest with this anti-solvent application is the ability to cause drastic changes to the crystal structure of the perovskite film, with Figure 96 showing highly modified XRD spectra for films fabricated with pure EA, a 50 vol% ratio of EA to DMC and pure DMC. This work paves the way for solvent influences structural alterations for specific perovskite structures.

Both the experimental precursor solutions and subsequently deposited films have undertaken periods of aging to assess the long-term stability of triple cation devices. Solution aging appears to have the largest detrimental impact on film performance. This was thought to be due time dependent chemical reactions occurring within the precursor. Inhibitors and stabilisers are likely to be required to extend shelf life past the period of hours and into months for premixed inks. However, efficient and scalable deposition techniques show promise engineering out this problem through optimised fabrication. This chapter also included extensive device aging, at open circuit in dark conditions. Here, experimental devices - aged over a 7-month period, retain >75% of their original PCE, remaining competitive with control devices.

As the field progresses it is vital that alternative ‘green’ chemistries are introduced whilst the technology is in the early stages of development to better the chances of successful implementation and chemical compatibility with more advanced compositions as they rise to prominence.

7. Summary of Conclusions

Within the first results chapter of this work, the literature surrounding alternative 'green' solvent formulations for perovskite inks is explored to inform a solvent selection methodology. This methodology is presented within and aims to provide a structured approach to judicious solvent selection for the most commonly used perovskite composition $MAPbI_3$. This included an evaluation of the technical properties of a processing solvent – alongside robust EHS evaluation. The selection tool allows the process of solvent screening be undertaken during the R&D phase of production, aiding in the adoption of greener chemicals during pilot scale studies. The application of this method was also summarised – with several solvents with justifiable green credentials identified for use within the perovskite sphere. This includes the use of dimethylpropyleneurea as a major processing solvent – which has since found successful application within tin-based perovskite[234] – in part due to issues surrounding the use of DMSO within these systems[234]. Finally, an alternative solvent system was proposed utilising the technical requirements and some of the identified 'greener' alternative solvents. Overall, this chapter provides the basis for the entire thesis and details a customisable methodology for solvent selection in a research area where a large amount of variety exists in terms of composition and deposition techniques.

Chapter 4 builds upon the work presented within the first results chapter, instead focussing primarily on the development of an alternative solvent system. Photochemical evaluations of the thin films are introduced here – a key characterisation within this thesis. A study comparison for films fabricated within a glovebox and in ambient conditions was also undertaken to understand the impact of environmental variables on the produced devices. After an optimisation procedure – a set of three experimental solutions were produced and evaluated. The presented characterisation incudes analysis of the film crystal structure through XRD measurements, along with peak analysis. A major effort with this chapter was to accurately characterise the size of produced crystallites. This was due to the perceived importance of large, uniform crystallites and the influence of the solvent on the size, morphology, and uniformity. A software called Zen Blue Intellesis was used to segment high resolution SEM images based on image contrast and brightness present at crystallite grain boundaries. The use of this software allowed the extrapolation of multiple parameters for films cast from each candidate solvent system – mainly the maximum ferret diameter – used as a proxy for average crystal size. Interestingly the films cast from the candidate solvents suggested smaller crystallites but with higher levels of size uniformity. A further reported result was an increase in PL intensity compared to the control, which was thought to be independent of film thickness. Finally, an analysis of multiple full device builds suggested that the candidate A system shows the greatest promise for planar architectures attaining similar results to the DMF based system.

The combined output of the first two results chapters was published in the journal green chemistry encapsulating the solvent selection methodology and the following solvent system design and application characterisation.

A secondary aspect of this research was to improve the stability of perovskite technology. This was applied to both perovskite films and precursor solutions, with the solvent the key parameter to influence the stability in both cases. Following on from the previous chapter four, it was noted that the stability of the final system is negatively impacted by precipitation of lead iodide with a 24-hour window. With a view to scalable manufacture, a study was undertaken to increase the shelf life of the precursor. The root cause of the precipitation was determined to by the perovskite antisolvent EtOH. The work contained within chapter 5 makes use of a new solvent DMC to replace the EtOH/MeTHF component. The newly developed solution was found to be stabilised comparatively with the DMF solution – with no precipitate visible. A comparison study was undertaken, fabricating fresh devices for the DMF/DMSO, A01(EtOH/MeTHF) and B01(DMC) solutions. Devices, aged at open circuit in dark conditions, were measured 4 times over 15 days. The results suggested a comparable result for the DMF-based devices after 6 days, with a gradual decline after this point. For the experimental systems the spread of results was comparable suggesting limited difference due to the change in fluid modifier. Interestingly these devices seem to suggest an improvement in performance after the initial aging period.

Chapter 5 also includes an evaluation of DMC as the anti-solvent for perovskite cells – utilising both DMF and experimental solutions. This was designed to increase the removal efficiency of the DMC present within the B01 solution. However, characterisations suggest DMC does not improve the PCE% of the experimental solutions when applied as an anti-solvent. An increase was noted using the DMF/DMSO solvent system control. This work has also been complemented by publications released in recent years[235,236], demonstrating the versatility of DMC as an anti-solvent. Solution long term stability remains an issue with perovskite precursors more generally, however, the processing window has been extended to match the control and avoid unnecessary side reactions for the proposed experimental candidate.

Moving onto chapter 6 – the fourth results chapter yields a transition to a new advanced perovskite composition designed for efficiency whilst retaining a level of stability. The solvent systems and anti-solvents developed within the three previous chapters have been implemented to the triple cation composition. Generally, this composition is much more difficult to process into a homogeneous film, with PL measurements suggesting significant changes to the optical band gap. These changes were far less pronounced with the $MAPBI_3$ composition. The selection of solvent also has a much greater role to play here due to complex interactions with multiple precursor materials. Reference material within the literature has been used to provide a baseline for this work. The scale of the changes possible to the perovskite structure using triple cation compositions and three or four component solvent systems remains a huge challenge but crucially provides an opportunity to create highly customised films. This is proven by the XRD spectra evidencing dramatic changes to the crystallographic structure for the experimental B01 triple cation perovskite samples, particularly with DMC applied as the anti-solvent. This range of customisation could open avenues for the adoption of perovskites within a wide range of optoelectronic devices, from LED displays and silicon based commercial tandems. A centre piece of the study was a prolonged aging of complete devices (stored at open circuit in dark conditions). This suggested that some experimental devices retained up to 75% of their original PCE% after 7 months – remaining competitive with the controls and providing encouragement that the transition to new solvent systems can be done with minimal impact to the long-term stability of the devices.

Throughout this work, a methodology for solvent selection has been presented, applied, characterised, and finally, this knowledge used to enhance a cutting-edge composition of perovskite achieving stable and demonstrably more sustainable devices.

8. Reference List

1 United Nations, *The climate crisis - a race we can win*, 2019.

2 G. M. MacDonald, K. D. Bennett, S. T. Jackson, L. Parducci, F. A. Smith, J. P. Smol and K. J. Willis, *Prog. Phys. Geogr.*, 2008, **32**, 139–172.

3 S. R. Weiskopf, M. A. Rubenstein, L. G. Crozier, S. Gaichas, R. Griffis, J. E. Halofsky, K. J. W. Hyde, T. L. Morelli, J. T. Morisette, R. C. Muñoz, A. J. Pershing, D. L. Peterson, R. Poudel, M. D. Staudinger, A. E. Sutton-Grier, L. Thompson, J. Vose, J. F. Weltzin and K. P. Whyte, *Sci. Total Environ.*, DOI:10.1016/j.scitotenv.2020.137782.

4 Fossil Fuels | EESI, https://www.eesi.org/topics/fossil-fuels/description, (accessed 23 May 2023).

5 Overview of Greenhouse Gases | US EPA, https://www.epa.gov/ghgemissions/overview-greenhouse-gases, (accessed 23 May 2023).

6 IPCC, *AR5 Climate Change 2014: Impacts, Adaptation, and Vulnerability*, 2014, vol. 1.

7 Climate change: evidence and causes | Royal Society, https://royalsociety.org/topics-policy/projects/climate-change-evidence-causes/basics-of-climate-change/, (accessed 23 May 2023).

8 Outlook for energy demand – World Energy Outlook 2022 – Analysis - IEA, https://www.iea.org/reports/world-energy-outlook-2022/outlook-for-energy-demand, (accessed 23 May 2023).

9 O. O. Yolcan, *Innov. Green Dev.*, 2023, **2**, 100070.

10 BEIS, *Net Zero Strategy: Build Back Greener*, 2021.

11 Renewables - Fuels & Technologies - IEA, https://www.iea.org/fuels-and-technologies/renewables, (accessed 23 May 2023).

12 IRENA, *Future of solar photovoltaic: Deployment, investment, technology, grid integration and socio-economic aspects (A Global Energy Transformation: paper)*, 2019, vol. November.

13 L. Szabó, *Proc. - 2017 Int. Conf. Mod. Power Syst. MPS 2017*, DOI:10.1109/MPS.2017.7974451.

14 R. Perez, M. Perez and D. Renné, *IEA SHC Sol. Updat.*, 2015, **62**, 4–6.

15 IRENA, *Future of Wind: Deployment, investment, grid integration and socio-economic aspects*, 2019.

16 Annual clean energy investment, 2017-2022 – Charts – Data & Statistics - IEA, https://www.iea.org/data-and-statistics/charts/annual-clean-energy-investment-2017-2022, (accessed 8 December 2023).

17 M. Tawalbeh, A. Al-Othman, F. Kafiah, E. Abdelsalam, F. Almomani and M. Alkasrawi, *Sci. Total Environ.*, DOI:10.1016/j.scitotenv.2020.143528.

18 S. W. Koch, M. Kira, G. Khitrova and H. M. Gibbs, *Nat. Mater.*, 2006, **5**, 523–531.

19 L. J. Phillips, A. M. Rashed, R. E. Treharne, J. Kay, P. Yates, I. Z. Mitrovic, A. Weerakkody, S. Hall and K. Durose, *Sol. Energy Mater. Sol. Cells*, 2016, **147**, 327–333.

20 M. Baranowski. P. Plochocka., *Adv. Energy Mater.*, DOI:10.1002/aenm.201903659.

21 C. S. De Castro, S. Dimitrov, H. D. Burrows, P. Douglas and M. L. Davies, *Sci. Prog.*, 2017, **100**, 212–230.

22 (23) What is the difference between direct and indirect band gap energies? | ResearchGate, https://www.researchgate.net/post/What_is_the_difference_between_direct_and_indirect_band_gap_energies/4, (accessed 25 May 2023).

23 Electron-Hole Recombination - Engineering LibreTexts, https://eng.libretexts.org/Bookshelves/Materials_Science/Supplemental_Modules_(Materials_Science)/Electronic_Properties/Electron-Hole_Recombination, (accessed 25 May 2023).

24 M. J. Trimpl, A. D. Wright, K. Schutt, L. R. V. Buizza, Z. Wang, M. B. Johnston, H. J. Snaith, P. Müller-Buschbaum and L. M. Herz, *Adv. Funct. Mater.*, 2020, **30**, 1–12.

25 G. Copeland, W. Otis, D, Black. A, B, *Phys. Rev.*, 1941, **74**, 463–471.

26 Early Solar History, http://solarcellcentral.com/history_page.html, (accessed 25 May 2023).

27 S. R. Wenham and M. a Green, *Prog. Photovolt Res. Appl.*, 1996, **4**, 3–33.

28 This Month in Physics History, https://www.aps.org/publications/apsnews/200904/physicshistory.cfm, (accessed 31 May 2023).

29 F. Annoni, DOI:10.13140/RG.2.2.15023.23208.

30 CIGS Solar Cells Overview | PVEducation, https://www.pveducation.org/pvcdrom/cigs-solar-cells-overview, (accessed 31 May 2023).

31 Copper Indium Gallium Diselenide Solar Cells | Photovoltaic Research | NREL, https://www.nrel.gov/pv/copper-indium-gallium-diselenide-solar-cells.html, (accessed 31 May 2023).

32 M. Nakamura, K. Yamaguchi, Y. Kimoto, Y. Yasaki, T. Kato and H. Sugimoto, *IEEE J. Photovoltaics*, 2019, **9**, 1863–1867.

33 Best Research-Cell Efficiency Chart | Photovoltaic Research | NREL, https://www.nrel.gov/pv/cell-efficiency.html, (accessed 31 May 2023).

34 M. A. Green, E. D. Dunlop, J. Hohl-Ebinger, M. Yoshita, N. Kopidakis and A. W. Y. Ho-Baillie, *Prog. Photovoltaics Res. Appl.*, 2020, **28**, 3–15.

35 Cadmium Telluride | Department of Energy, https://www.energy.gov/eere/solar/cadmium-telluride, (accessed 31 May 2023).

36 Cadmium Telluride Solar Cells | Photovoltaic Research | NREL, https://www.nrel.gov/pv/cadmium-telluride-solar-cells.html, (accessed 31 May 2023).

37 N. Papež, R. Dallaev, Ş. Ţălu and J. Kaštyl, *Materials (Basel).*, 2021, **14**, 1–16.

38 B. M. Kayes, H. Nie, R. Twist, S. G. Spruytte, F. Reinhardt, I. C. Kizilyalli and G. S. Higashi, *2011 37th IEEE Photovolt. Spec. Conf.*, 2011, 4–8.

39 A. Baiju and M. Yarema, 2022, **2022**, 1–17.

40 P. Colter, B. Hagar and S. Bedair, DOI:10.3390/cryst8120445.

41 E. Meusal, M. Baur, C. Letay, G. Bett, A. W. Warta, W. Fernandez, *Prog. Photovoltaics Res. Appl.*, DOI:10.1002/pip.514.

42 M. Kurtz, S. Myers, D. Mcmahon, W. E. Geisz, J. Steiner, *Prog. Photovoltaics Res. Appl.*, DOI:10.1002/pip.830.

43 Frauenhofer ISE, *Photovoltaics report*, 2023.

44 Indium - Element information, properties and uses | Periodic Table, https://www.rsc.org/periodic-table/element/49/indium, (accessed 31 May 2023).

45 Cadmium - Element information, properties and uses | Periodic Table, https://www.rsc.org/periodic-table/element/48/cadmium, (accessed 31 May

2023).

46 Germanium - Element information, properties and uses | Periodic Table, https://www.rsc.org/periodic-table/element/32/germanium, (accessed 31 May 2023).

47 L. Stamford and A. Azapagic, *Sci. Total Environ.*, 2019, **688**, 1092–1101.

48 C. Candelise, J. F. Spiers and R. J. K. Gross, *Renew. Sustain. Energy Rev.*, 2011, **15**, 4972–4981.

49 S. Chuangchote, M. Rachakornkij and T. Punmatharith, 2012, 1–15.

50 N. Mohr, A. Meijer, M. A. J. Huijbregts and L. Reijnders, *Int. J. Life Cycle Assess.*, 2009, **14**, 225–235.

51 B. Gratzel and O. Michael, *Nature*, 1991, **353**, 737–739.

52 K. Sharma, V. Sharma and S. S. Sharma, *Nanoscale Res. Lett.*, DOI:10.1186/s11671-018-2760-6.

53 I. Chung, B. Lee, J. He, R. P. H. Chang and M. G. Kanatzidis, *Nature*, 2012, **485**, 486–489.

54 I. Benesperi, H. Michaels and M. Freitag, *J. Mater. Chem. C*, 2018, **6**, 11903–11942.

55 M. T, K. A, T. K and S. Y, *J. Am. Chem. Soc.*, 2009, **131**, 6050–1.

56 Best Research-Cell Efficiency Chart | Photovoltaic Research | NREL, https://www.nrel.gov/pv/cell-efficiency.html, (accessed 7 April 2020).

57 F. Ma, Y. Zhao, Z. Qu and J. You, *Accounts Mater. Res.*, 2023, **4**, 716–725.

58 N. G. Park and K. Zhu, *Nat. Rev. Mater.*, DOI:10.1038/s41578-019-0176-2.

59 LONGi sets a new world record of 33.9% for the efficiency of crystalline silicon-perovskite tandem solar cells -LONGi, https://www.longi.com/en/news/new-world-record-for-the-efficiency-of-crystalline-silicon-perovskite-tandem-solar-cells/, (accessed 5 January 2025).

60 S. E. Sofia, H. Wang, A. Bruno, J. L. Cruz-Campa, T. Buonassisi and I. M. Peters, *Sustain. Energy Fuels*, 2020, **4**, 852–862.

61 L. Meng, J. You and Y. Yang, *Nat. Commun.*, 2018, **9**, 1–4.

62 R. G. Charles, M. L. Davies and P. Douglas, *Electron. Goes Green 2016+*, 2016, 1–8.

63 R. G. Charles, M. L. Davies, P. Douglas, I. L. Hallin and I. Mabbett, *Energy*,

2019, **166**, 1207–1215.

64 R. G. Charles, P. Douglas, J. A. Baker, M. J. Carnie, J. O. Douglas, D. J. Penney and T. M. Watson, *J. Clean. Prod.*, 2018, **202**, 1167–1178.

65 P. Roy, N. Kumar Sinha, S. Tiwari and A. Khare, *Sol. Energy*, 2020, **198**, 665–688.

66 M. Davis and Z. Yu, *J. Semicond. Vol.41, Issue 4, pp. 041603*, 2020, **41**, 041603-.

67 M. L. Davies, M. Carnie, P. J. Holliman, A. Connell, P. Douglas, T. Watson, C. Charbonneau, J. Troughton and D. Worsley, *Energy Mater. Mater. Sci. Eng. Energy Syst.*, 2014, **9**, 482–485.

68 Y. Wang, W. Fu, J. Yan, J. Chen, W. Yang and H. Chen, *J. Mater. Chem. A*, 2018, **6**, 13090–13095.

69 Z. Li, M. Yang, J. S. Park, S. H. Wei, J. J. Berry and K. Zhu, *Chem. Mater.*, 2016, **28**, 284–292.

70 S. Bera, A. Saha, S. Mondal, A. Biswas, S. Mallick, R. Chatterjee and S. Roy, *Mater. Adv.*, 2022, **3**, 5234–5247.

71 Y. Liu, K. Palotas, X. Yuan, T. Hou, H. Lin, Y. Li and S. T. Lee, *ACS Nano*, 2017, **11**, 2060–2065.

72 A. Maiti, S. Chatterjee, L. Peedikakkandy and A. J. Pal, *Sol. RRL*, 2020, **4**, 1–31.

73 J. Ye, M. M. Byranvand, C. O. Martínez, R. L. Z. Hoye, M. Saliba and L. Polavarapu, *Angew. Chemie - Int. Ed.*, 2021, **60**, 21636–21660.

74 M. E. Laamari, A. Cheknane, A. Benghia and H. S. Hilal, *Sol. Energy*, 2019, **182**, 9–15.

75 F. Ma, J. Li, W. Li, N. Lin, L. Wang and J. Qiao, *Chem. Sci.*, 2016, **8**, 800–805.

76 E. J. Juarez-Perez, L. K. Ono and Y. Qi, *J. Mater. Chem. A*, 2019, **7**, 16912–16919.

77 Z. Zheng, S. Wang, Y. Hu, Y. Rong, A. Mei and H. Han, *Chem. Sci.*, 2022, **13**, 2167–2183.

78 M. Saliba, T. Matsui, J. Y. Seo, K. Domanski, J. P. Correa-Baena, M. K. Nazeeruddin, S. M. Zakeeruddin, W. Tress, A. Abate, A. Hagfeldt and M. Grätzel, *Energy Environ. Sci.*, 2016, **9**, 1989–1997.

79 M. Abbas, L. Zeng, M. R. Fei Guo, X.-C. Yuan and B. Cai, *Materials (Basel).*, 2020, 6–9.

80 K. W. Tan, D. T. Moore, M. Saliba, H. Sai, L. A. Estroff, T. Hanrath, H. J. Snaith and U. Wiesner, *ACS Nano*, 2015, 4730–4739.

81 Z. Song, S. C. Watthage, A. B. Phillips and M. J. Heben, *J. Photonics Energy*, 2016, **6**, 022001.

82 A. Kheralla and N. Chetty, *Heliyon*, 2021, **7**, e06211.

83 S. Maranghi, M. L. Parisi, R. Basosi and A. Sinicropi, *Energies*, 2019, **12**, 3–7.

84 R. L. Moss, E. Tzimas, H. Kara, P. Willis and J. Kooroshy, *Energy Policy*, 2013, **55**, 556–564.

85 J. Tao and S. Yu, *Sol. Energy Mater. Sol. Cells*, 2015, **141**, 108–124.

86 C. de Castro, M. Mediavilla, L. J. Miguel and F. Frechoso, *Renew. Sustain. Energy Rev.*, 2013, **28**, 824–835.

87 A. Elshkaki and T. E. Graedel, *J. Clean. Prod.*, 2013, **59**, 260–273.

88 R. G. Charles, P. Douglas, M. Dowling and M. L. Davies, *Resour. Conserv. Recycl.*

89 M. L. Davies, *Joule*, 2020, **4**, 1626–1627.

90 P. J. Holliman, E. W. Jones, A. Connell, S. Ghosh, L. Furnell and R. J. Hobbs, *Mater. Res. Innov.*, 2015, **19**, 508–511.

91 M. Konstantakou, D. Perganti, P. Falaras and T. Stergiopoulos, *Crystals*, 2017, **7**, 1–21.

92 A. Binek, M. L. Petrus, N. Huber, H. Bristow, Y. Hu, T. Bein and P. Docampo, *ACS Appl. Mater. Interfaces*, 2016, **8**, 12881–12886.

93 K. Nishimura, M. A. Kamarudin, D. Hirotani, K. Hamada, Q. Shen, S. Iikubo, T. Minemoto, K. Yoshino and S. Hayase, *Nano Energy*, 2020, **74**, 104858.

94 K. X. Steirer, P. Schulz, G. Teeter, V. Stevanovic, M. Yang, K. Zhu and J. J. Berry, *ACS Energy Lett.*, 2016, **1**, 360–366.

95 L. Serrano-Lujan, N. Espinosa, T. T. T. T. Larsen-Olsen, J. Abad, A. Urbina and F. C. F. C. Krebs, *Adv. Energy Mater.*, DOI:10.1002/aenm.201501119.

96 B. Roose, K. Dey, Y. H. Chiang, R. H. Friend and S. D. Stranks, *J. Phys. Chem. Lett.*, 2020, **11**, 6505–6512.

97 A. Uddin and H. Yi, *Sol. RRL*, DOI:10.1002/solr.202100983.

98 Z. Wei, B. Smith, F. De Rossi, J. R. Searle, D. A. Worsley and T. M. Watson, *J. Mater. Chem. C*, 2019, **7**, 10981–10987.

99 M. Saliba, J.-P. Correa-Baena, C. M. Wolff, M. Stolterfoht, N. Phung, S. Albrecht, D. Neher and A. Abate, *Chem. Mater.*, 2018, **30**, 4193–4201.

100 A. Way, J. Luke, A. D. Evans, Z. Li, J. S. Kim, J. R. Durrant, H. K. Hin Lee and W. C. Tsoi, *AIP Adv.*, DOI:10.1063/1.5104333.

101 P. F. Méndez, S. K. M. Muhammed, E. M. Barea, S. Masi and I. Mora-Seró, *Sol. RRL*, 2019, **3**, 1900191.

102 R. A. Soni, R. S. Rana and S. S. Godara, *Nanomater. Nanocomposites*, 2021, 61–83.

103 E. V. Péan, C. S. De Castro and M. L. Davies, *Mater. Lett.*, 2019, **243**, 191–194.

104 Scanning Electron Microscope (SEM)- Definition, Principle, Parts, Images - Microbe Notes, https://microbenotes.com/scanning-electron-microscope-sem/, (accessed 10 September 2023).

105 Solar Simulator- Basic Knowledge and Working PrinciplesSolar Simulator- Basic Knowledge and Working Principles » We Enlighten Your Ideas!, https://enlitechnology.com/blog/pv/ss-x-solar-simulatior/solar-simulator-01/, (accessed 30 August 2023).

106 A. J. Doolin, R. G. Charles, C. S. P. De Castro, R. G. Rodriguez, E. V. Péan, R. Patidar, T. Dunlop, C. Charbonneau, T. Watson and M. L. Davies, *Green Chem.*, 2021, **23**, 2471–2486.

107 J. W. Lee, H. S. Kim and N. G. Park, *Acc. Chem. Res.*, 2016, **49**, 311–319.

108 K. L. Gardner, J. G. Tait, T. Merckx, W. Qiu, U. W. Paetzold, L. Kootstra, M. Jaysankar, R. Gehlhaar, D. Cheyns, P. Heremans and J. Poortmans, *Adv. Energy Mater.*, 2016, **6**, 1–8.

109 J. Wang, F. Di Giacomo, J. Brüls, H. Gorter, I. Katsouras, P. Groen, R. A. J. Janssen, R. Andriessen and Y. Galagan, *Sol. RRL*, 2017, **1**, 1700091.

110 W. Y. Tan, P. P. Cheng, Y. W. Zhang, J. M. Liang, X. Chen, Y. Liu and Y. Min, *J. Mater. Chem. C*, 2019, **7**, 6004–6011.

111 M. Lv, X. Dong, X. Fang, B. Lin, S. Zhang, J. Ding and N. Yuan, *RSC Adv.*, 2015, **5**, 20521–20529.

112 Sigma Aldrich, MSDS - 227056,

https://www.sigmaaldrich.com/MSDS/MSDS/DisplayMSDSPage.do?country=GB&language=en&productNumber=227056&brand=SIAL&PageToGoToURL=https%3A%2F%2Fwww.sigmaaldrich.com%2Fcatalog%2Fproduct%2Fsial%2F227056%3Flang%3Den, (accessed 7 April 2020).

113 J. Lee and S. Baik, *RSC Adv.*, 2018, **8**, 1005–1013.

114 J. C. Hamill, J. Schwartz and Y. L. Loo, *ACS Energy Lett.*, 2018, **3**, 92–97.

115 Z. Zhou, Z. Wang, Y. Zhou, S. Pang, D. Wang, H. Xu, Z. Liu, N. P. Padture and G. Cui, *Angew. Chemie - Int. Ed.*, 2015, **54**, 9705–9709.

116 J. Zhang, G. B. White, M. D. Ryan, A. J. Hunt and M. J. Katz, *ACS Sustain. Chem. Eng.*, 2016, **4**, 7186–7192.

117 C. Capello, U. Fischer and K. Hungerbühler, *Green Chem.*, 2007, **9**, 927–934.

118 U. Tilstam, *Org. Process Res. Dev.*, 2012, 1273–1278.

119 B. J. Kim, D. H. Kim, S. L. Kwon, S. Y. Park, Z. Li, K. Zhu and H. S. Jung, *Nat. Commun.*, 2016, **7**, 1–9.

120 C. M. Alder, J. D. Hayler, R. K. Henderson, A. M. Redman, L. Shukla, L. E. Shuster and H. F. Sneddon, *Green Chem.*, 2016, **18**, 3879–3890.

121 P. G. Jessop, *Green Chem.*, 2011, **13**, 1391–1398.

122 F. P. Byrne, S. Jin, G. Paggiola, T. H. M. Petchey, J. H. Clark, T. J. Farmer, A. J. Hunt, C. Robert McElroy and J. Sherwood, *Sustain. Chem. Process.*, 2016, **4**, 7.

123 D. Prat, O. Pardigon, H. W. Flemming, S. Letestu, V. Ducandas, P. Isnard, E. Guntrum, T. Senac, S. Ruisseau, P. Cruciani and P. Hosek, *Org. Process Res. Dev.*, 2013, **17**, 1517–1525.

124 N. G. Anderson, *Pract. Process Res. Dev.*, 2010, 81–111.

125 L. J. Diorazio, D. R. J. Hose and N. K. Adlington, *Org. Process Res. Dev.*, 2016, **20**, 760–773.

126 K. Alfonsi, J. Colberg, P. J. Dunn, T. Fevig, S. Jennings, T. A. Johnson, H. P. Kleine, C. Knight, M. A. Nagy, D. A. Perry and M. Stefaniak, *Green Chem.*, 2008, **10**, 31–36.

127 D. Prat, J. Hayler and A. Wells, *Green Chem.*, 2014, **16**, 4546–4551.

128 C. J. Clarke, W. C. Tu, O. Levers, A. Bröhl and J. P. Hallett, *Chem. Rev.*, 2018, **118**, 747–800.

129 H. F. S. J. L. Sneddon, 2018, **106**, 21–42.

130 D. Prat, A. Wells, J. Hayler, H. Sneddon, C. R. McElroy, S. Abou-Shehada and P. J. Dunn, *Green Chem.*, 2015, **18**, 288–296.

131 S. Abbott, C. M. Hansen, H. Yamamoto and R. S. Valpey, *Hansen Solubility Parameters in Practice Complete with eBook, software and data 5th Edition The HSPiP team*, 2015.

132 N. K. Noel, S. N. Habisreutinger, B. Wenger, M. T. Klug, M. T. Hörantner, M. B. Johnston, R. J. Nicholas, D. T. Moore and H. J. Snaith, *Energy Environ. Sci.*, 2017, **10**, 145–152.

133 N. J. Jeon, J. H. Noh, Y. C. Kim, W. S. Yang, S. Ryu and S. Il Seok, *Nat. Mater.*, 2014, **13**, 897–903.

134 Q. Liu, Y. Zhao, Y. Ma, X. Sun, W. Ge, Z. Fang, H. Bai, Q. Tian, B. Fan and T. Zhang, *J. Mater. Chem. A*, 2019, **7**, 18275–18284.

135 D. Burkitt, P. Greenwood, K. Hooper, D. Richards, V. Stoichkov, D. Beynon, E. Jewell and T. Watson, *MRS Adv.*, 2019, **4**, 1399–1407.

136 D. Burkitt, R. Patidar, P. Greenwood, K. Hooper, J. McGettrick, S. Dimitrov, M. Colombo, V. Stoichkov, D. Richards, D. Beynon, M. Davies and T. Watson, *Sustain. Energy Fuels*, DOI:10.1039/d0se00460j.

137 Y. Deng, C. H. van Brackle, X. Dai, J. Zhao, B. Chen and J. Huang, *Sci. Adv.*, 2019, **5**, 1–9.

138 K. H. Hendriks, J. J. Van Franeker, B. J. Bruijnaers, J. A. Anta, M. M. Wienk and R. A. J. Janssen, *J. Mater. Chem. A*, 2017, **5**, 2346–2354.

139 X. Fang, Y. Wu, Y. Lu, Y. Sun, S. Zhang, J. Zhang, W. Zhang, N. Yuan and J. Ding, *J. Mater. Chem. C*, 2017, **5**, 842–847.

140 A. Babaei, L. Albero-Blanquer, A. M. Igual-Muñoz, D. Pérez-Del-Rey, M. Sessolo, H. J. Bolink and R. Tadmouri, *Polyhedron*, 2018, **147**, 9–14.

141 H. Team, H. Yamamoto, S. Abbott and C. M. Hansen, *Hansen Solubility Parameters 50th anniversary conference, preprint PP*, 2017.

142 F. Cataldo, *Eur. Chem. Bull.*, 2015, **4**, 92–97.

143 S. D. Bergin, Z. Sun, D. Rickard, P. V. Streich, J. P. Hamilton and J. N. Coleman, *ACS Nano*, 2009, **3**, 2340–2350.

144 C. Wohlfarth, 2008, **65**, 298–298.

145 The CHEM21 Solvent Selection Guide – ACS GCI Pharmaceutical Roundtable, https://learning.acsgcipr.org/guides-and-metrics/solvent-selection-guides/the-chem21-solvent-selection-guide/, (accessed 13 December 2024).

146 P. Loubet, M. Tsang, E. Gemechu, A. Foulet and G. Sonnemann, in *Bio-based solvents*, eds. F. Jérôme and R. Luque, John Wiley & Sons, Ltd, Chichester, UK, 2017, pp. 131–148.

147 MSDS - DMF Sigma, https://www.sigmaaldrich.com/MSDS/MSDS/DisplayMSDSPage.do?country=GB&language=en&productNumber=227056&brand=SIAL&PageToGoToURL=https%3A%2F%2Fwww.sigmaaldrich.com%2Fcatalog%2Fproduct%2Fsial%2F227056%3Flang%3Den, (accessed 18 May 2020).

148 W. Fritsch and R. B. Stoughton, *Arch Dermatol.*, **90**, 512–7.

149 MSDS - DMSO sigma, https://www.sigmaaldrich.com/MSDS/MSDS/DisplayMSDSPage.do?country=GB&language=en&productNumber=276855&brand=SIAL&PageToGoToURL=https%3A%2F%2Fwww.sigmaaldrich.com%2Fcatalog%2Fproduct%2Fsial%2F276855%3Flang%3Den, (accessed 18 May 2020).

150 MSDS - GBL sigma, https://www.sigmaaldrich.com/MSDS/MSDS/DisplayMSDSPage.do?country=GB&language=en&productNumber=H7629&brand=SIGMA&PageToGoToURL=https%3A%2F%2Fwww.sigmaaldrich.com%2Fcatalog%2Fproduct%2Fsigma%2Fh7629%3Flang%3Den, (accessed 18 May 2020).

151 MSDS - Acetonitrile sigma, https://www.sigmaaldrich.com/MSDS/MSDS/DisplayMSDSPage.do?country=GB&language=en&productNumber=271004&brand=SIAL&PageToGoToURL=https%3A%2F%2Fwww.sigmaaldrich.com%2Fcatalog%2Fproduct%2Fsial%2F271004%3Flang%3Den, (accessed 18 May 2020).

152 MSDS - methylamine sigma, https://www.sigmaaldrich.com/MSDS/MSDS/DisplayMSDSPage.do?country=GB&language=en&productNumber=295531&brand=ALDRICH&PageToGoToURL=https%3A%2F%2Fwww.sigmaaldrich.com%2Fcatalog%2Fproduct%2Faldrich%2F295531%3Flang%3Den, (accessed 18 May 2020).

153 MSDS - DMAc sigma, https://www.sigmaaldrich.com/MSDS/MSDS/DisplayMSDSPage.do?country=GB&language=en&productNumber=17308&brand=ALDRICH&PageToGoToURL=https%3A%2F%2Fwww.sigmaaldrich.com%2Fcatalog%2Fproduct%2Fal

drich%2F17308%3Flang%3Den, (accessed 18 May 2020).

154 MSDS - NMP sigma, https://www.sigmaaldrich.com/MSDS/MSDS/DisplayMSDSPage.do?country=GB&language=en&productNumber=328634&brand=SIAL&PageToGoToURL=https%3A%2F%2Fwww.sigmaaldrich.com%2Fcatalog%2Fproduct%2Fsial%2F328634%3Flang%3Den, (accessed 18 May 2020).

155 (NMP) 1-methyl-2-pyrrolidone - Substance Information - ECHA, https://echa.europa.eu/cs/substance-information/-/substanceinfo/100.011.662, (accessed 28 May 2020).

156 R. Vidal, J.-A. Alberola-Borràs, G.-M. Joaquín-Luis, S. N. Habisreutinger, D. T. Moore, T. H. Schloemer, I. Mora-Seró, J. J. Berry and J. M. Luther, *Nat. Sustain.*, DOI:10.1038/s41893-020-00645-8.

157 B. S. Flowers, M. S. Mittenthal, A. H. Jenkins, D. A. Wallace, J. W. Whitley, G. P. Dennis, M. Wang, C. H. Turner, V. N. Emel'Yanenko, S. P. Verevkin and J. E. Bara, *ACS Sustain. Chem. Eng.*, 2017, **5**, 911–921.

158 D. Lundberg, *The Coordination Chemistry of Solvated Metal Ions in DMPU A Study of a Space-Demanding Solvent*, 2006.

159 S. Rahimnejad, A. Kovalenko, S. M. Forés, C. Aranda and A. Guerrero, *ChemPhysChem*, 2016, 2795–2798.

160 I. Persson, K. Lyczko, D. Lundberg, L. Eriksson and A. Pjaczek, *Inorg. Chem.*, 2011, **50**, 1058–1072.

161 H. H. Khoo, L. L. Wong, J. Tan, V. Isoni and P. Sharratt, *Resour. Conserv. Recycl.*, 2015, **95**, 174–182.

162 M. H. Wolter, R. Carron, E. Avancini, B. Bissig, T. P. Weiss, S. Nishiwaki, T. Feurer, S. Buecheler, P. Jackson, W. Witte and S. Siebentritt, *Prog. Photovoltaics Res. Appl.*, 2022, **30**, 702–712.

163 A. D. Wright, R. L. Milot, G. E. Eperon, H. J. Snaith, M. B. Johnston and L. M. Herz, *Adv. Funct. Mater.*, 2017, **27**, 1–8.

164 J. Chen, C. Zhang, X. Liu, L. Peng, J. Lin and X. Chen, *Photonics Res.*, 2021, **9**, 151.

165 Y. Guo, O. Yaffe, T. D. Hull, J. S. Owen, D. R. Reichman and L. E. Brus, *Nat. Commun.*, 2019, **10**, 1–8.

166 Y. B. Lu, W. Y. Cong, C. Guan, H. Sun, Y. Xin, K. Wang and S. Song, *J. Mater. Chem. A*, 2019, **7**, 27469–27474.

167 K. Zhang, Z. Wang, G. Wang, J. Wang, Y. Li, W. Qian, S. Zheng, S. Xiao and S. Yang, *Nat. Commun.*, 2020, **11**, 1–11.

168 K. O. Ogunniran and N. T. Martins, *IOP Conf. Ser. Earth Environ. Sci.*, DOI:10.1088/1755-1315/655/1/012049.

169 K. T. Cho, G. Grancini, Y. Lee, E. Oveisi, J. Ryu, O. Almora, M. Tschumi, P. A. Schouwink, G. Seo, S. Heo, J. Park, J. Jang, S. Paek, G. Garcia-Belmonte and M. K. Nazeeruddin, *Energy Environ. Sci.*, 2018, **11**, 952–959.

170 C. Wehrenfennig, M. Liu, H. J. Snaith, M. B. Johnston and L. M. Herz, *J. Phys. Chem. Lett.*, 2014, **5**, 1300–1306.

171 Z. Xiao, Q. Dong, C. Bi, Y. Shao, Y. Yuan and J. Huang, *Adv. Mater.*, 2014, **26**, 6503–6509.

172 H. Zhang, M. Tao, B. Gao, W. Chen, Q. Li, Q. Xu and S. Dong, *Sci. Rep.*, 2017, **7**, 1–9.

173 C. Jiang, Y. Xie, R. R. Lunt, T. W. Hamann and P. Zhang, *ACS Omega*, 2018, **3**, 3522–3529.

174 Z. Huang, D. Wang, S. Wang and T. Zhang, *Materials (Basel).*, 2018, **11**, 20–30.

175 T. S. Sherkar, C. Momblona, L. Gil-Escrig, J. Ávila, M. Sessolo, H. J. Bolink and L. J. A. Koster, *ACS Energy Lett.*, 2017, **2**, 1214–1222.

176 J. C.-B. J.P. Castro-Mendes, A.F. Hidalgo, *Adv. Energy Mater.*

177 Q. An, F. Paulus, D. Becker-Koch, C. Cho, Q. Sun, A. Weu, S. Bitton, N. Tessler and Y. Vaynzof, *Matter*, 2021, **4**, 1683–1701.

178 J. H. Im, I. H. Jang, N. Pellet, M. Grätzel and N. G. Park, *Nat. Nanotechnol.*, 2014, **9**, 927–932.

179 F. C. F. W.K. Burton, N. Cabrera, *Philos. Trans. R. Soc. London. Ser. A, Math. Phys. Sci.*, 1951, **243**, 299–358.

180 D. Liu, W. Zhou, H. Tang, P. Fu and Z. Ning, *Sci. China Chem.*, 2018, **61**, 1278–1284.

181 H. Hu, Z. Ren, P. W. K. Fong, M. Qin, D. Liu, D. Lei, X. Lu and G. Li, *Adv. Funct. Mater.*, 2019, **29**, 1–12.

182 P. Chhillar, B. P. Dhamaniya, V. Dutta and S. K. Pathak, *ACS Omega*, 2019, **4**, 11880–11887.

183 Y. Ren, B. Duan, Y. Xu, Y. Huang, Z. Li, L. Hu, T. Hayat, H. Wang, J. Zhu and S. Dai, *Sci. China Mater.*, 2017, **60**, 392–398.

184 Y. Hu, L. M. Spies, D. Alonso-Álvarez, P. Mocherla, H. Jones, J. Hanisch, T. Bein, P. R. F. Barnes and P. Docampo, *J. Mater. Chem. A*, 2018, **6**, 22215–22225.

185 D. Gedamu, I. M. Asuo, D. Benetti, M. Basti, I. Ka, S. G. Cloutier, F. Rosei and R. Nechache, *Sci. Rep.*, 2018, **8**, 1–11.

186 N. K. Noel, M. Congiu, A. J. Ramadan, S. Fearn, D. P. McMeekin, J. B. Patel, M. B. Johnston, B. Wenger and H. J. Snaith, *Joule*, 2017, **1**, 328–343.

187 S. Tian, J. Li, S. Li, T. Bu, Y. Mo, S. Wang, W. Li and F. Huang, *Sol. Energy*, 2019, **183**, 386–391.

188 E. J. Cassella, E. L. K. Spooner, J. A. Smith, T. Thornber, M. E. O’Kane, R. D. J. Oliver, T. E. Catley, S. Choudhary, C. J. Wood, D. B. Hammond, H. J. Snaith and D. G. Lidzey, *Adv. Energy Mater.*, DOI:10.1002/aenm.202203468.

189 A. M. A. Leguy, Y. Hu, M. Campoy-Quiles, M. I. Alonso, O. J. Weber, P. Azarhoosh, M. Van Schilfgaarde, M. T. Weller, T. Bein, J. Nelson, P. Docampo and P. R. F. Barnes, *Chem. Mater.*, 2015, **27**, 3397–3407.

190 J. A. Christians, P. A. Miranda Herrera and P. V. Kamat, *J. Am. Chem. Soc.*, 2015, **137**, 1530–1538.

191 B. Kelsey K. Bass, R. Eric McAnally, Shiliang Zhou, Peter I. Djurovich, Mark E. Thompson and C. Melota, *Chem Comm*, 2014, **50**, 15819–15822.

192 M. L. Petrus, Y. Hu, D. Moia, P. Calado, A. M. A. Leguy, P. R. F. Barnes and P. Docampo, *ChemSusChem*, 2016, **9**, 2699–2707.

193 G. Abdelmageed, L. Jewell, K. Hellier, L. Seymour, B. Luo, F. Bridges, J. Z. Zhang and S. Carter, *Appl. Phys. Lett.*, DOI:10.1063/1.4967840.

194 S. Kundu and T. L. Kelly, *EcoMat*, 2020, **2**, 1–22.

195 H. Gao, C. Bao, F. Li, T. Yu, J. Yang, W. Zhu, X. Zhou, G. Fu and Z. Zou, *ACS Appl. Mater. Interfaces*, 2015, **7**, 9110–9117.

196 S. Srivastava, S. Ranjan, L. Yadav, T. Sharma, S. Choudhary, D. Agarwal, A. Singh, S. Satapathi, R. K. Gupta, A. Garg and K. S. Nalwa, *Commun. Mater.*, 2023, **4**, 1–29.

197 R. Liu and K. Xu, *Micro Nano Lett.*, 2020, **15**, 349–353.

198 A. D. Taylor, Q. Sun, K. P. Goetz, Q. An, T. Schramm, Y. Hofstetter, M. Litterst,

F. Paulus and Y. Vaynzof, *Nat. Commun.*, 2021, **12**, 1–11.

199 N. Ahn, D. Y. Son, I. H. Jang, S. M. Kang, M. Choi and N. G. Park, *J. Am. Chem. Soc.*, 2015, **137**, 8696–8699.

200 S. Aldrich, *Chlorobenzene*, 2023.

201 U. Kingdom, *Encycl. Dict. Polym.*, 2007, 370–370.

202 P. Zhang, N. Gu, L. Song, X. Chen, P. Du, L. Zha, W. H. Chen and J. Xiong, *Nanoscale*, 2022, **14**, 5204–5213.

203 H. Wang, W. Zeng and R. Xia, *Thin Solid Films*, 2018, **663**, 9–13.

204 S. A. Fateev, A. A. Petrov, V. N. Khrustalev, P. V. Dorovatovskii, Y. V. Zubavichus, E. A. Goodilin and A. B. Tarasov, *Chem. Mater.*, 2018, **30**, 5237–5244.

205 M. A. Pacheco and C. L. Marshall, *Energy and Fuels*, 1997, **11**, 2–29.

206 X. Xu, C. Ma, Y. M. Xie, Y. Cheng, Y. Tian, M. Li, Y. Ma, C. S. Lee and S. W. Tsang, *J. Mater. Chem. A*, 2018, **6**, 7731–7740.

207 Z. Zhu, Y. Bai, X. Liu, C. C. Chueh, S. Yang and A. K. Y. Jen, *Adv. Mater.*, 2016, **28**, 6478–6484.

208 Z. Li, *Advanced Energy Materials*, 2016, DOI: 10.1002/aenm.201601165.

209 B. Roose, A. Ummadisingu, J. P. Correa-Baena, M. Saliba, A. Hagfeldt, M. Graetzel, U. Steiner and A. Abate, *Nano Energy*, 2017, **39**, 24–29.

210 Z. Jin, M. Yuan, H. Li, H. Yang, Q. Zhou, H. Liu, X. Lan, M. Liu, J. Wang, E. Sargent, Y. Li, *Advanced Functional Materials,* 2016, **26** 5284-5289 DOI: 10.1002/adfm.201601570.

211 J. You, L. Meng, T. Bin Song, T. F. Guo, W. H. Chang, Z. Hong, H. Chen, H. Zhou, Q. Chen, Y. Liu, N. De Marco and Y. Yang, *Nat. Nanotechnol.*, 2016, **11**, 75–81.

212 H. B. Lee, M. K. Jeon, N. Kumar, B. Tyagi, J. W. Kang, *Adv. Funct. Mater.* 2019. DOI: 10.1002/adfm.201903213

213 T. Li, Q. Li, X. Tang, Z. Chen, Y. Li, H. Zhao, S. Wang, X. Ding, Y. Zhang and J. Yao, *J. Phys. Chem. C*, 2021, **125**, 2850–2859.

214 H. Li, Y. Xia, C. Wang, G. Wang, Y. Chen, L. Guo, D. Luo and S. Wen, *ACS Appl. Mater. Interfaces*, 2019, **11**, 34989–34996.

215 A. Y. Alsalloum, B. Turedi, K. Almasabi, X. Zheng, R. Naphade, S. D. Stranks,

O. F. Mohammed and O. M. Bakr, *Energy Environ. Sci.*, 2021, **14**, 2263–2268.

216 G. Schileo and G. Grancini, *JPhys Energy*, DOI:10.1088/2515-7655/ab6cc4.

217 A. Buin, R. Comin, J. Xu, A. H. Ip and E. H. Sargent, *Chem. Mater.*, 2015, **27**, 4405–4412.

218 A. Buin, P. Pietsch, J. Xu, O. Voznyy, A. H. Ip, R. Comin and E. H. Sargent, *Nano Lett.*, 2014, **14**, 6281–6286.

219 G. E. Eperon, S. D. Stranks, C. Menelaou, M. B. Johnston, L. M. Herz and H. J. Snaith, *Energy Environ. Sci.*, 2014, **7**, 982–988.

220 N. J. Jeon, J. H. Noh, W. S. Yang, Y. C. Kim, S. Ryu, J. Seo and S. Il Seok, *Nature*, 2015, **517**, 476–480.

221 Z. Zheng, S. Wang, Y. Hu, Y. Rong, A. Mei and H. Han, *Chem. Sci.*, 2022, **13**, 2167–2183.

222 S. M. C. Jin-Wook Lee , Deok-Hwan Kim , Hui-Seon Kim , Seung-Woo Seo and and N.-G. Park, *Adv. Energy Mater.*

223 L. Xie, K. Lin, J. Lu, W. Feng, P. Song, C. Yan, K. Liu, L. Shen, C. Tian and Z. Wei, *J. Am. Chem. Soc.*, 2019, **141**, 20537–20546.

224 Q. Jiang, Y. Zhao, X. Zhang, X. Yang, Y. Chen, Z. Chu, Q. Ye, X. Li, Z. Yin and J. You, *Nat. Photonics*, 2019, **13**, 460–466.

225 H. Min, M. Kim, S. U. Lee, H. Kim, G. Kim, K. Choi, J. H. Lee and S. Il Seok, *Science (80-.).*, 2019, **366**, 749–753.

226 M. O’Kane, *ChemSusChem*, 2021, **14**, 2537–2546.

227 M. Saliba, J.-P. P. Correa-Baena, C. M. Wolff, M. Stolterfoht, N. Phung, S. Albrecht, D. Neher and A. Abate, *Chem. Mater.*, 2018, **30**, 4193–4201.

228 Y. Ren, N. Zhang, Q. Wang, J. Zhu and C. Li, *Sci. China Mater.*, 2020, **63**, 1015–1023.

229 M. Zhang, F. Zhang, Y. Wang, L. Zhu, Y. Hu, Z. Lou, Y. Hou and F. Teng, *Sci. Rep.*, 2018, **8**, 1–9.

230 H. Z. Asl and S. M. Rozati, *Appl. Phys. A Mater. Sci. Process.*, 2019, **125**, 1–8.

231 F. Giordano, A. Abate, J. P. Correa Baena, M. Saliba, T. Matsui, S. H. Im, S. M. Zakeeruddin, M. K. Nazeeruddin, A. Hagfeldt and M. Graetzel, *Nat. Commun.*, 2016, **7**, 1–6.

232 D. Bi, W. Tress, M. I. Dar, P. Gao, J. Luo, C. Renevier, K. Schenk, A. Abate, F. Giordano, J. P. Correa Baena, J. D. Decoppet, S. M. Zakeeruddin, M. K. Nazeeruddin, M. Grätzel and A. Hagfeldt, *Sci. Adv.*, DOI:10.1126/sciadv.1501170.

233 R. Lu, Y. Liu, J. Zhang, D. Zhao, X. Guo and C. Li, *Chem. Eng. J.*, 2022, **433**, 133845.

234 D. Di Girolamo, J. Pascual, M. H. Aldamasy, Z. Iqbal, G. Li, E. Radicchi, M. Li, S. H. Turren-Cruz, G. Nasti, A. Dallmann, F. De Angelis and A. Abate, *ACS Energy Lett.*, 2021, **6**, 959–968.

235 Y. W. Zhang, Z. L. Diao, J. Y. Chen, W. Y. Tan, Y. N. Qian, L. G. Xiao and Y. Min, *J. Mater. Chem. C*, 2021, **9**, 8939–8946.

236 N. Zhang, Z. Zhang, T. Liu, T. He, P. Liu, J. Li, F. Yang, G. Song, Z. Liu and M. Yuan, *Org. Electron.*, 2023, **113**, 106709.

THE END